Thin–Walled Structures 215 (2025) 113423

Contents lists available at ScienceDirect

Thin-Walled Structures

journal homepage: www.elsevier.com/locate/tws

Full length article

Hygro-thermo-electro-mechanical coupled modeling of laminated curved panels

Francesco Tornabene [a,*], Matteo Viscoti [a], Rossana Dimitri [a], Timon Rabczuk [b]

[a] *Department of Innovation Engineering, School of Engineering, University of Salento, 73100, Lecce, Italy*
[b] *Institute of Structural Mechanics, Bauhaus-Universität Weimar, 99423, Weimar, Germany*

A R T I C L E I N F O

Keywords:
Dufour and Soret effects
Equivalent Layer-Wise
Generalized differential quadrature
Hygro-thermal analysis
Navier solution
Smart structures

A B S T R A C T

The manuscript presents a generalized two-dimensional model for evaluating the stationary hygro-thermo-mechanical response of laminated shell structures made of heterogeneous piezoelectric composite materials with thermal and hygrometric properties. In particular, the static bending response of these structures is studied, along with their coupled hygro-thermo-electrical behavior. A generalized kinematic model is introduced, enabling the assessment of arbitrary temperature and mass concentration variations with respect to the unvaried configuration at the top and bottom surfaces. This is achieved through an Equivalent Layer-Wise description of the unknown field variables using higher order polynomials and zigzag functions. Furthermore, an elastic foundation is modelled according to the Winkler-Pasternak theory. The fundamental equations, derived from the total free energy of the system, are solved analytically using Navier's method. Then, the Fourier-based generalized differential quadrature numerical method is adopted to efficiently recover the through-the-thickness distribution of secondary variables, in agreement with the hygro-thermal loading conditions. The formulation is applied in some examples of investigation where the response of panels with different curvatures and lamination schemes is evaluated under external hygro-thermal fluxes and prescribed values of temperature and moisture concentration. In addition, we investigate the effect of the hygro-thermal coupling due to Dufour and Soret effect. The present formulation is verified to be a valuable tool for assessing the mechanical response of laminated structures in a thermal and hygrometric environment with reduced computational effort.

1. Introduction

In recent engineering applications, a crucial aspect of technical design is the study of the effects of environmental conditions on the response of structural components. For instance, in the aerospace industry, hygro-thermal effects can influence the deflection of curved composite panels due to hygroscopic expansion phenomena, inducing additional strains and stresses that may lead to unexpected failure [1,2]. When a composite material is exposed to temperature and humidity, it may exhibit some issues such as strength and stiffness reduction, effects on fiber-matrix interfaces [3–5], and further degradation of its mechanical properties. In addition, recent applications based on the mechanical elasticity coupling with other fields, including electricity and magnetism, have led to the development of piezoelectric and piezomagnetic sensors and actuators which are extensively used in various fields, including biomedical applications [6], structural monitoring [7], mechanical engineering [8], and wearable devices [9], among others. Piezoelectric materials are capable to generate electric voltages when subjected to mechanical loads and undergo deflections when exposed to electric loads. For this reason, novel strategies have been developed to simulate these phenomena, enhancing classical mechanical models commonly used among engineering applications [10,11]. To model hygro-thermal effects within a solid, the Fick and Fourier equations are typically employed [12–14]. However, the experimental evidence indicates that these two phenomena are correlated. The additional thermal fluxes, indeed, can arise from the mass diffusion, and the temperature variations can increase the mass diffusion within the structure [15–17]. These processes, known as thermophoretic and thermal diffusion effects, can be modelled by coupling classical heat transfer and mass diffusion equations through the Onsager principle and reciprocity relations, as detailed in Refs. [18–21]. It should also be noted that the mass diffusion is significantly slower than thermal conduction, therefore the Fourier equations may be used in their stationary form in most configurations [22]. Another important consideration regarding

* Corresponding author.
E-mail address: francesco.tornabene@unisalento.it (F. Tornabene).

https://doi.org/10.1016/j.tws.2025.113423
Received 19 February 2025; Received in revised form 18 April 2025; Accepted 6 May 2025
Available online 13 May 2025
0263-8231/© 2025 Elsevier Ltd. All rights are reserved, including those for text and data mining, AI training, and similar technologies.

the multiphysic simulations is that different physical problems must be simultaneously addressed to model accurately coupling effects. In fact, the presence of a thermal field can influence the electric response of the structure [23,24]. Therefore, the fundamental equations should be solved simultaneously in a consistent manner [25,26]. However, under the thermodynamic equlibrium, these equations can be solved in a staggered way, as certain couplings involving gradients are absent. In this way, the physical problems can be solved independently, thus reducing the computational effort. As far as the modelling strategies are concerned, three-dimensional (3D) approaches are typically adopted to accurately evaluate all interactions between these phenomena [27,28]. However, to analyze laminated panels using two-dimensional (2D) theories, the uncoupled multifield simulations are often performed, where a pre-determined distribution of scalar multifield variables such as temperature variation, electric potential, and moisture concentration, is assumed. This approach is suitable only for thin laminates, where the thickness of the panel is negligible compared to the size of the structure. However, in moderately thick laminates with a significant variation of the consitutive properties for each layer, these quantities may exhibit arbitrary through-the-thickness distributions [29,30], thus requiring coupled simulations for accurate predictions. In the exisiting literature on this topic, the thermal conduction and mass diffusion equations are typically solved only along the thickness direction in their one-dimensional form. Then, the additional strains induced by temperature or moisture variations are evaluated and included in the classical mechanical analysis.

The introduction of additional physical phenomena into the model introduces new variables that can increase the computational cost of the simulation [31]. For this reason, 2D approaches [32,33] are often preferred in lieu of 3D simulations, to increase the efficiency of the theory. Among 2D approaches, various theories are found in literature, which can be classified into Equivalent Single Layer (ESL) or Layer-Wise (LW) theories, as detailed in the review papers in Ref. [34,35]. In ESL theories, a reference surface is defined at the middle thickness of the structure, treating the entire laminate as an equivalent continuum material [36,37]. This approach allows for the introduction of a kinematic model to expand unknown variables along the thickness direction. In contrast, in LW models the fundamental equations are developed within each lamina, with kinematic compatibility conditions applied to assemble the relations for the entire laminate [38,39]. Classical theories, such as the Classical Plate Theory (CPT) and the First-order Shear Deformation Theory (FSDT), belong to the ESL category [40–42] and are extensively adopted in literature for several applications. However, as demonstrated in Ref. [43], these theories are insufficient in their accuracy for laminates made of advanced materials, because their kinematic models lack the necessary Degrees of Freedom (DOFs) to capture the non-uniform distribution of bending induced by the stretching effect.To model this particular effect in deflection, indeed, higher-order polynomials are required in the kinematic model. To this end, the Third-order Shear Deformation Theory (TSDT) [44,45] was introduced in literature which adopts higher-order distributions of in-plane unknown variables. On the other hand, TSDT assumes a uniform through-the-thickness distribution of the out-of-plane displacement component, which limits its ability to predict the stretching effect. To overcome these limitations, Higher-order Shear Deformation Theories (HSDTs) have been developed which incorporate higher-order polynomials within the kinematic model [46–48]. In addition, zigzag functions were introduced to efficiently capture the interaction between adjacent laminae in a 2D theory. Following the pioneering works by Murakami [49,50], where zigzag functions are applied for in-plane variables, further zigzag theories have been developed. For example, in Ref. [51] the Murakami function has been applied to each displacement field component to investigate the vibration of generally anisotropic laminates. Moreover, refined zigzag theories [52,53] have been developed for composite materials, based on some considerations regarding the shear properties of the specific panel under investigation. It should be noted that HSDTs, along with zigzag functions, introduce different terms within the theory which can complicate the theory. A significant advancement in this field is the generalized formulation [54,55], which considers arbitrary thickness functions, and derives the fundamental equations independently of the specific expression of the thickness function itself. In addition, Equivalent Layer-Wise (ELW) theories [56] have been developed to enable the possibility to prescribe arbitrary values of the unknown variables at the top and bottom surfaces of laminates. The generalized formulation, developed for the mechanical case, was later adopted in Ref. [57] for electro-mechanical simulations to model arbitrary distributions of the electric potential within the solid. In Ref. [58,59], this approach was further expanded to multifield simulations to develop a comprehensive model that accounts for all possible couplings between different physical phenomena. The use of refined kinematic models is crucial when advanced materials are included within the lamination scheme. These materials frequently contain multiple phases within the same layer, each contributing to the overall behavior of the lamina. A wide class of composite material exhibiting coupled multifield properties can be obtained, from a manufacturing point of view, by introducing inclusions within an isotropic matrix. In this way, the unit cells that can be traced are that of the spherical inclusion within an isotropic matrix, or vertically aligned nanostructures, as well as heterogeneous laminates, as extensively detailed in Ref. [60]. As a result, it is important to derive the constitutive properties of an equivalent continuum material through effective homogenization procedures. A widely used method is the well-known rule of mixture [61], which relates the overall properties of the homogenized material to the volume or mass fractions of each phase. However, this method does not take into account the influence of the shape of various phases within the material, which may cause localized deformation effects. To overcome these drawbacks, the well-known Mori-Tanaka procedure was developed [62], which employs the Eshelby tensor of an equivalent inclusion problem [63]. Generally speaking, the elements of this tensor are computed numerically [64]. However, closed-form expressions of these quantitites have been recently derived for ellipsoidal [65–67] and polygonal [68,69] inclusions. The Mori-Tanaka homogenization method has been adopted to determine the homogenized properties of advanced materials across various physical problems, including fiber-reinforced composites and carbon nanotubes [70–72]. In addition, in Refs. [73,74] this procedure has been extended to obtain the homogenized multifield properties of smart laminae with piezoelectric and piezomagnetic phases, considering the effects of temperature variations within the solid.

The derivation of an analytical homogenization is essential for modelling graded variations in the material properties within a solid. Indeed, a variation in these quantities can be achieved by varying the governing parameters of the unit cell, such as the volume fraction of each constituent material, the shape parameters of inclusions, and their orientation with respect to the material reference system [75]. In this context, the laminate is made of Functionally Graded Matetials (FGMs). Referring to laminated structures, most applications consider the material variability along the thickness direction, modelled using one-dimensional power and trigonometric expressions [76–79]. In manufacturing industry, FGMs are typically developed by combining ceramic and metal phases, and they are extensively studied in literature as they offer good mechanical and thermal insulation properties within a single material [80]. Modelling strategies for FGMs can also be applied to other problems, as happens for instance for the material porosity, where the presence of voids is represented as inclusions within the unit cell that exhibit null constitutive properties [81].

In multifield analyses, the number of variables increases compared to those ones involved in mechanical simulations. This increases the necessity of using efficient numerical methods to obtain solutions with a reduced computational effort. Among these methods, the classical Finite Element Method (FEM) is widely used in most commercial software and is known for its stability [82,83]. As it is well-known, in FEM implementations of a differential problem, the domain is discretized into finite elements, with fixed shape functions introduced to express the variation of the unknown variables within this region. However, this approach does not inherently guarantee a smooth continuity in the solution [84], therefore accurate results require a finer mesh, which increases, in turn, the computational cost of the simulation. To overcome these limitations, collocation methods have been recently developed in Refs. [85,86], that use a global interpolation of the solution across the entire domain. Among these numerical procedures, the Generalized Differential Quadrature (GDQ) method has been extensively applied in various engineering problems, including structural mechanics [87–90], fracture analysis [91], and time-history simulations [92], as well as vibration analysis [93,94], among others. Based on the GDQ method, the derivatives are approximated as a weighted sum of the values assumed by a function at specific sample points. The weighting coefficients can be derived through several approaches, as detailed in Refs. [95,96]. The most common methodology uses a recursive procedure, based on Lagrange polynomials, to determine the quadrature coefficients. Recent studies, however, have shown that similar accuracy can be reached using trigonometric series instead of Lagrange polynomials [97]. Overall, the GDQ method has proven to be very accurate and requires a lower computational effort than FEM, especially for non-uniform grids [98, 99].

The validation of the numerical model is typically performed by comparing the numerical results to a closed-form analytical solution of the differential equation set, derived for some specific cases. This solution can be obtained, for example, by assuming a specific expression of the unknown variables that satisfies the given boundary conditions. In this context, the Navier approach, adopted for instance in Ref. [100], uses a trigonometric expression to describe the unknown variables within the physical domain. This method has been widely applied to various problems, including simply-supported plates and shells under mechanical pressures, as well as multiphysics simulations, involving 2D or 3D cases [101,102]. Furthermore, in Refs. [103,104] this procedure has been generalized into the boundary discontinuous method which addresses clamped laminated panels using analytical solutions. However, as demonstrated in Ref. [105], the results from 2D analytical solutions must be adjusted through a post-processing recovery procedure that employs a numerical method to solve the equilibrium equations. This ensures that the results align with those from 3D simulations.

This work presents a novel formulation based on the ELW, for evaluating the hygro-thermal effects on a laminated curved panel under mechanical, electric, and magnetic loads for thermodynamic equilibrium conditions. The theory is based on a general curvilinear reference system with principal coordinates and adopts a generalized kinematic model to describe the unknown variables along the thickness direction, taking into account higher-order theories and a zigzag function to model the 3D multifield behavior of laminated structures with various lamination schemes. A fully-coupled constitutive relationship is provided, accounting for the strains induced by other fields on the structures, as well as the piezoelectric effect. The influence of temperature and moisture variations on the electric response within each layer is modelled through pyroelectric and hygroelectric terms, while hygro-thermal coupling accounts for thermophoretic and thermal diffusion phenomena. The consitutive coefficients are derived from an analytical procedure based on the Mori-Tanaka approach for a two-phase smart material. Furthermore, an arbitrary variation of the material properties is modelled within each layer. The fundamental relations are derived from the stationary configuration of the total energy of the system, taking into account various multifield loads with surface distributions. A semi-analytical Navier solution is derived for simply-supported spherical panels with cross-ply lamination schemes and uniform curvatures. Then, a post-processing procedure is presented herein, which enables the reconstruction of the 3D distribution of multifield primary and secondary variables within the 3D solid. With respect to the comprehensive theory reported in Ref. [58], this paper focuses on hygro-thermo-electro-elastic multifield coupling, and introduces a general kinematic model based on Jacobi polynomials, while in Ref. [58] only power functions are adopted. In addition, the recovery procedure for the post-processing is here based on T-GIQ numerical method, while in this reference the reconstruction of primary and secondary variables is performed by discretizing the balance equations with the GDQ method. Furthermore, an arbitrary variation of the material properties is introduced which cannot be traced in the previous research on the topic. The model is applied in numerical examples, where the multifield response is evaluated for various loading conditions in terms of mechanical pressures and multifield fluxes, as well as arbitrary values of electric potential, temperature and moisture concentration variations. The results are compared with outcomes from 3D numerical simulations using a finite element code. Additional simulations are also performed to investigate other coupling effects that cannot be predicted with classical 3D FEM, and a parametric investigation shows the effect of the material distribution parameters. The formulation presented in this paper can be a valid tool for practical engineering applications involving multiphysics modeling of curved laminated structures, accounting for effects that are not predicted by most existing theoretical and numerical approaches. Furthermore, due to its high accuracy and computaitonal efficiency, it can be adopted in optimization procedures [106], and it can be expanded to investigate the vibration characteristics of multilayered piezoelectric structures [107].

2. Theoretical analysis

In line with the ELW approach, the geometry of a doubly-curved shell structure, defined by the position vector $\mathbf{R}(\alpha_1, \alpha_2, \zeta)$, with $(\alpha_1, \alpha_2, \zeta) \in [\alpha_1^0, \alpha_1^1] \times [\alpha_2^0, \alpha_2^1] \times [-h/2, h/2]$ is described by the quantity $\mathbf{r}(\alpha_1, \alpha_2)$, representing the surface position vector of the shell located at $\zeta = 0$. The position vector $\mathbf{R}$ is, thus, expressed as follows [58]:

$$\mathbf{R}(\alpha_1, \alpha_2, \zeta) = \mathbf{r}(\alpha_1, \alpha_2) + \frac{h}{2} z \mathbf{n}(\alpha_1, \alpha_2) \tag{1}$$

where $z = 2\zeta/h$ is a dimensionless variable identifying points along the thickness direction. The reference surface, $\mathbf{r}$, is expressed through the curvilinear principal coordinates α_1, α_2. The thickness of the laminated shell, denoted by h, is evaluated as summation of thicknesses $h_k = \zeta_{k+1} - \zeta_k$, with $k = 1, ..., l$ of each k-th lamina in the stacking sequence, being l the total number of laminae. The outward normal unit vector $\mathbf{n}(\alpha_1, \alpha_2)$ at an arbitrary point of the reference surface belonging to the parametric domain $[\alpha_1^0, \alpha_1^1] \times [\alpha_2^0, \alpha_2^1]$, is determined by the following relation, derived in Ref. [58]:

$$\mathbf{n}(\alpha_1, \alpha_2) = \frac{\mathbf{r}_{,1} \wedge \mathbf{r}_{,2}}{|\mathbf{r}_{,1} \wedge \mathbf{r}_{,2}|} \tag{2}$$

being $\mathbf{r}_{,i}$, with $i = 1, 2$, the first-order partial derivative of the reference surface equation with respect to $\alpha_i = \alpha_1, \alpha_2$ principal coordinate, while the symbol $\wedge$ represents the well-known vector cross product. In addition, the second-order partial derivatives of $\mathbf{r}$ with respect to $\alpha_i, \alpha_j = \alpha_1, \alpha_2$ are denoted by $\mathbf{r}_{,ij}$. From Eq. (1), it is possible to derive the geometric properties of the 3D solid, based on those ones of the reference surface $\mathbf{r}(\alpha_1, \alpha_2)$. More specifically, the Lamé parameters $A_i = A_1, A_2$ refer to the metric coefficients, and the principal radii of curvature $R_i = R_1, R_2$ refer to the principal directions $\alpha_i = \alpha_1, \alpha_2$. They are evaluated at any point within the rectangular parametric domain $[\alpha_1^0, \alpha_1^1] \times [\alpha_2^0, \alpha_2^1]$ as follows:

$$\begin{aligned} A_i(\alpha_1, \alpha_2) &= \sqrt{\mathbf{r}_{,i} \cdot \mathbf{r}_{,i}} \\ R_i(\alpha_1, \alpha_2) &= -\frac{\mathbf{r}_{,i} \cdot \mathbf{r}_{,i}}{\mathbf{r}_{,ii} \cdot \mathbf{n}} \end{aligned} \tag{3}$$

At this point, it is useful to define the curvilinear coordinate $s_i = s_1$,

s_2 along each principal direction. The infinitesimal variation ds_i of this coordinate is related to the corresponding infinitesimal change, denoted by $d\alpha_i$, associated with $\alpha_i = \alpha_1, \alpha_2$ curvilinear coordinates, through the Lamé parameters introduced in Eq. (3). This relationship is given by $ds_i = A_i d\alpha_i$. The curvilinear abscissa $s_i = s_1, s_2$, with $s_i \in [s_i^0, s_i^1]$, is obtained by integrating this relation over the interval $[\alpha_i^0, \alpha_i]$, and it refers to the reference surface. To compute lengths at an arbitrary height ζ within the 3D solid, scaling parameters H_1 and H_2 are introduced, which account for the metrics changes due to height ζ. They are defined as follows:

$$H_i(\alpha_1, \alpha_2, \zeta) = 1 + \frac{\zeta}{R_i} \tag{4}$$

Following the ELW approach, a generalized kinematic model is developed to characterize the unknown configuration variables of the 3D structure, taking into account $N+2$ terms for the kinematic expansion. The following compact notation expresses this relationship [58]:

$$\mathbf{\Delta}^{(k)} = \sum_{\tau=0}^{N+1} \mathbf{F}_\tau^{(k)} \boldsymbol{\delta}^{(\tau)} \tag{5}$$

dry solid $[\mathrm{kg/m^3}]$, respectively. The use of the generalized kinematic model of Eq. (5) enables to obtain refined descriptions of the unknown variables depending on the specific simulation requirements. Furthermore, selecting particular expressions for the thickness functions allows the model to include classical theories such as CPT, FSDT and TSDT. In this study, the thickness functions are selected within the ELW framework. In particular, the following expressions are adopted for any $i = 1, \ldots, 6$, depending on the normalized thickness coordinate $\tilde{z} = 2\zeta/h$ with $\tilde{z} \in [-1, 1]$ and for $\tau = 1, \ldots, N-1$:

$$F_\tau^{(k)\alpha_i}(\tilde{z}) = \begin{cases} \dfrac{1-\tilde{z}}{2} & \text{for } \tau = 0 \\ J_{\tau+2}^{(\gamma,\delta)}(\tilde{z}) - J_\tau^{(\gamma,\delta)}(\tilde{z}) & \text{for } \tau = 1, .., N-1 \\ \dfrac{1+\tilde{z}}{2} & \text{for } \tau = N \end{cases} \tag{7}$$

Here, $J_\tau^{(\gamma,\delta)}(\tilde{z})$ denote the Jacobi orthogonal polynomial of the τ-th order [85], with characteristic parameters γ, δ. These polynomials are recursively calculated using the following relation:

$$J_\tau^{(\gamma,\delta)}(\tilde{z}) = \begin{cases} 1 & \text{for } \tau = 1 \\ \dfrac{1}{2}(2(\gamma+1) + (\gamma+\delta+2)(\tilde{z}-1)) & \text{for } \tau = 2 \\ \dfrac{C(AB\tilde{z} + \gamma^2 - \delta^2) J_{\tau-1}^{(\gamma,\delta)}(\tilde{z}) - 2(\tau+\gamma-2)(\tau+\delta-2) A J_{\tau-2}^{(\gamma,\delta)}(\tilde{z})}{D} & \text{for } \tau = 3, \ldots N \end{cases} \tag{8}$$

In the previous relation, the vector $\mathbf{\Delta}^{(k)}$ of size 6×1 contains the unknown variables at an arbitrary point within the doubly-curved 3D solid. The vector $\boldsymbol{\delta}^{(\tau)}$ of size 6×1 collects the generalized configuration variables, defined at each (α_1, α_2) point within the physical domain, for an arbitrary τ-th kinematic expansion order with $\tau = 0, \ldots, N+1$. The matrix $\mathbf{F}_\tau^{(k)}$ of size 6×6 depends on the thickness coordinate ζ. This matrix is defined for each $\tau = 0, \ldots, N+1$, and collects the thickness functions $F_\tau^{(k)\alpha_i} = F_\tau^{(k)\alpha_i}(\zeta)$ for $i = 1, \ldots, 6$ corresponding to each τ-th kinematic expansion order. The previous relation can be expressed in the following expanded form:

$$\mathbf{\Delta}^{(k)} = \begin{bmatrix} U_1^{(k)} \\ U_2^{(k)} \\ U_3^{(k)} \\ \Delta\phi^{(k)} \\ \Delta\mathrm{T}^{(k)} \\ \Delta\mathrm{C}^{(k)} \end{bmatrix} = \sum_{\tau=0}^{N+1} \begin{bmatrix} F_\tau^{(k)\alpha_1} & 0 & 0 & 0 & 0 & 0 \\ 0 & F_\tau^{(k)\alpha_2} & 0 & 0 & 0 & 0 \\ 0 & 0 & F_\tau^{(k)\alpha_3} & 0 & 0 & 0 \\ 0 & 0 & 0 & F_\tau^{(k)\alpha_4} & 0 & 0 \\ 0 & 0 & 0 & 0 & F_\tau^{(k)\alpha_5} & 0 \\ 0 & 0 & 0 & 0 & 0 & F_\tau^{(k)\alpha_6} \end{bmatrix} \begin{bmatrix} u_1^{(\tau)} \\ u_2^{(\tau)} \\ u_3^{(\tau)} \\ \phi^{(\tau)} \\ \xi^{(\tau)} \\ \kappa^{(\tau)} \end{bmatrix} \tag{6}$$

Referring to the 3D solid, the unknown variables of the multifield problem include the displacement field components $U_1^{(k)}$, $U_2^{(k)}$, $U_3^{(k)}$, expressed in meters [m] and defined with respect to the shell geometric reference system $O'\alpha_1\alpha_2\zeta$. Variations in electric potential, temperature, and moisture concentration, denoted by $\Delta\phi^{(k)} = \phi^{(k)} - \phi_0$, $\Delta\mathrm{T}^{(k)} = \mathrm{T}^{(k)} - \mathrm{T}_0$ and $\Delta\mathrm{C}^{(k)} = \mathrm{C}^{(k)} - \mathrm{C}_0$, are also evaluated with respect to the reference state of the system, defined by the reference values ϕ_0, T_0 and C_0. According to the International Standards, these scalar quantities are expressed in volt [V], kelvin [K], and moisture mass per unit volume of

with $A = 2\tau + \gamma + \delta - 2$, $B = A - 2$, $C = A - 1$ and $D = 2(\tau - 1)(\tau + \gamma + \delta - 1)B$. As is well-known, the selection of specific values for parameters γ, δ within Eq. (8), leads to a wide range of polynomial families, including Legendre ($\gamma = \delta = 0$), Lobatto ($\gamma = \delta = 1$), and Chebyshev polynomials of the first, second, third, and fourth kinds, while selecting $\gamma = \delta = -1/2$, $\gamma = \delta = 1/2$, $\gamma = -\delta = -1/2$, and $\gamma = -\delta = 1/2$, respectively. Note that the first-order derivative of these polynomials with respect to the dimensionless coordinate $\tilde{z}$ must be derived accordingly. It should be noted that the thickness function in Eq. (7), for $\tau = 0$, assumes a null value at $\zeta = h/2$, while it is equal to 1 at $\zeta = -h/2$. Conversely, the thickness function associated with $\tau = N$ is equal to 1 at the top surface, while it assumes a null value at $\zeta = -h/2$. This behavior ensures that the kinematic expansion in Eq. (5), combined with Eq. (7), allows for the specification of arbitrary values of the unknown configuration variables at the top and bottom surface, namely at the bottom of the $k = 1$ lamina and at the top of the l-th layer within the stacking sequence [58]:

$$\begin{aligned} \Delta_i^{(1)}\left(\alpha_1, \alpha_2, \zeta = -\frac{h}{2}\right) &= \Delta_i^{(-)} = \delta_i^{(0)}(\alpha_1, \alpha_2) \\ \Delta_i^{(l)}\left(\alpha_1, \alpha_2, \zeta = \frac{h}{2}\right) &= \Delta_i^{(+)} = \delta_i^{(N)}(\alpha_1, \alpha_2) \end{aligned} \tag{9}$$

Finally, the following thickness functions are introduced for the $\tau = N+1$ kinematic order, introduced for the first time in Ref. [58]:

$$F_{N+1}^{(k)\alpha_i} = \begin{cases} z_1 = -\dfrac{\zeta - \zeta_1}{\zeta_2 - \zeta_1} \\ z_k = (-1)^k (2\bar{z}_k - 1), \quad k = 2, \ldots, l-1 \\ z_l = (-1)^l \dfrac{\zeta - \zeta_{l+1}}{\zeta_{l+1} - \zeta_l} \end{cases} \tag{10}$$

with $\bar{z}_k = (\zeta - \zeta_k)/(\zeta_{k+1} - \zeta_k)$, for any $k = 1, \ldots, l$. The thickness function in Eq. (10) refers to the modified zigzag function, which is developed to simulate the interaction between adjacent laminae in the stacking sequence. This expression assumes a null value at $\zeta = h/2$ and $\zeta = -h/2$. The kinematic model adopted in each simulation is rapidly identified by using the specific acronyms ELD $-N$ and ELDZL $-N$. In particular, "EL" indicates that the model is based on the ELW theory, where the displacement field components (D) are the unknown configuration variables. The acronym also accounts for the maximum N-th order of the kinematic expansion. Furthermore, when the zigzag function from Eq. (10) is used, the acronym "ZL" is added to the nomenclature.

To derive the governing equations for the hygro-thermo-electro-elastic problem, the higher-order kinematic model is used to express the definition equations from those derived for a doubly-curved 3D solid, reported below in compact matrix form, for the sake of completeness. These equations relate vector $\mathbf{\Delta}^{(k)}$ already introduced in Eqs. (5)-(6) with vector $\boldsymbol{\pi}^{(k)} = \left[\boldsymbol{\varepsilon}^{(k)T} \;\; \mathscr{E}^{(k)T} \;\; \widehat{\Delta \mathrm{T}}^{(k)} \;\; \widehat{\Delta \mathrm{C}}^{(k)} \;\; \boldsymbol{\theta}^{(k)T} \;\; \boldsymbol{\lambda}^{(k)T}\right]^T$ of the 3D multifield primary variables [58]:

$$\boldsymbol{\pi}^{(k)} = \mathbf{D}\mathbf{\Delta}^{(k)} = \mathbf{D}_{\zeta}\mathbf{D}_{\Omega}\mathbf{\Delta}^{(k)} \tag{11}$$

The definition equation is expressed in the previous relation in terms of a multifield kinematic operator $\mathbf{D}$, which is composed by the sub-operators corresponding to each specific physical problem. This includes the symmetric part of the strain tensor and the gradient of a scalar field. Further details can be found in Ref. [58]. The sub-vectors of the 3D primary variables for mechanical elasticity, electrostatics, thermal conduction, and mass diffusion, are presented in extended form as $\boldsymbol{\varepsilon}^{(k)} = \left[\varepsilon_1^{(k)} \;\; \varepsilon_2^{(k)} \;\; \gamma_{12}^{(k)} \;\; \gamma_{13}^{(k)} \;\; \gamma_{23}^{(k)} \;\; \varepsilon_3^{(k)}\right]^T$, $\mathscr{E}^{(k)} = \left[\mathscr{E}_1^{(k)} \;\; \mathscr{E}_2^{(k)} \;\; \mathscr{E}_3^{(k)}\right]^T$, $\boldsymbol{\theta}^{(k)} = \left[\theta_1^{(k)} \;\; \theta_2^{(k)} \;\; \theta_3^{(k)}\right]^T$, and $\boldsymbol{\lambda}^{(k)} = \left[\lambda_1^{(k)} \;\; \lambda_2^{(k)} \;\; \lambda_3^{(k)}\right]^T$. Since the present formulation is derived for a doubly-curved 3D solid in curvilinear principal coordinates according to Eq. (1), it is convenient to split the operator $\mathbf{D}$ in two parts, denoted by $\mathbf{D}_{\zeta}$ and $\mathbf{D}_{\Omega}$, which contain the derivatives with respect to the thickness coordinate ζ and the partial derivatives with respect to the in-plane quantities α_1, α_2, respectively. The operator $\mathbf{D}_{\zeta}$ assumes the following representation:

$$\mathbf{D}_{\zeta} = \begin{bmatrix} \mathbf{D}_{\zeta(1)} & \mathbf{0} & \mathbf{0} & \mathbf{0} & \mathbf{0} & \mathbf{0} \\ \mathbf{0} & \mathbf{D}_{\zeta(2)} & \mathbf{0} & \mathbf{0} & \mathbf{0} & \mathbf{0} \\ \mathbf{0} & \mathbf{0} & \mathbf{D}_{\zeta(3)} & 0 & \mathbf{0} & \mathbf{0} \\ \mathbf{0} & \mathbf{0} & 0 & \mathbf{D}_{\zeta(3)} & \mathbf{0} & \mathbf{0} \\ \mathbf{0} & \mathbf{0} & \mathbf{0} & \mathbf{0} & \mathbf{D}_{\zeta(2)} & \mathbf{0} \\ \mathbf{0} & \mathbf{0} & \mathbf{0} & \mathbf{0} & \mathbf{0} & \mathbf{D}_{\zeta(2)} \end{bmatrix} \tag{12}$$

where the quantities $\mathbf{D}_{\zeta(1)}, \mathbf{D}_{\zeta(2)}$ and $\mathbf{D}_{\zeta(3)}$ are expressed as follows [58]:

$$\mathbf{D}_{\zeta(1)} = \begin{bmatrix} \frac{1}{H_1} & 0 & 0 & 0 & 0 & 0 & 0 & 0 & 0 \\ 0 & \frac{1}{H_2} & 0 & 0 & 0 & 0 & 0 & 0 & 0 \\ 0 & 0 & \frac{1}{H_1} & \frac{1}{H_2} & 0 & 0 & 0 & 0 & 0 \\ 0 & 0 & 0 & 0 & \frac{1}{H_1} & 0 & \frac{\partial}{\partial \zeta} & 0 & 0 \\ 0 & 0 & 0 & 0 & 0 & \frac{1}{H_2} & 0 & \frac{\partial}{\partial \zeta} & 0 \\ 0 & 0 & 0 & 0 & 0 & 0 & 0 & 0 & \frac{\partial}{\partial \zeta} \end{bmatrix}$$

$$\mathbf{D}_{\zeta(2)} = \begin{bmatrix} \frac{1}{H_1} & 0 & 0 \\ 0 & \frac{1}{H_2} & 0 \\ 0 & 0 & \frac{\partial}{\partial \zeta} \end{bmatrix}, \quad \mathbf{D}_{\zeta(3)} = 1 \tag{13}$$

The differential operator $\mathbf{D}_{\Omega}$, introduced in Eq. (11), is associated to derivatives with respect to α_1, α_2, and it is defined from the following relation:

$$\mathbf{D}_{\Omega} = \sum_{i=1}^{6} \mathbf{D}_{\Omega}^{\alpha_i} = \begin{bmatrix} \mathbf{D}_{\Omega(1)} & \mathbf{0} & \mathbf{0} & \mathbf{0} \\ \mathbf{0} & \mathbf{D}_{\Omega(2)} & \mathbf{0} & \mathbf{0} \\ \mathbf{0} & \mathbf{0} & \mathbf{D}_{\Omega(3)} & \mathbf{0} \\ \mathbf{0} & \mathbf{0} & \mathbf{0} & \mathbf{D}_{\Omega(3)} \\ \mathbf{0} & \mathbf{0} & \mathbf{D}_{\Omega(2)} & \mathbf{0} \\ \mathbf{0} & \mathbf{0} & \mathbf{0} & \mathbf{D}_{\Omega(2)} \end{bmatrix} \tag{14}$$

The sub-operators $\mathbf{D}_{\Omega(1)}, \mathbf{D}_{\Omega(2)}$ and $\mathbf{D}_{\Omega(3)}$ in the previous equation are presented below in extended form:

$$\begin{gathered} \mathbf{D}_{\Omega(1)} = \left[\overline{\mathbf{D}}_{\Omega}^{\alpha_1} \;\; \overline{\mathbf{D}}_{\Omega}^{\alpha_2} \;\; \overline{\mathbf{D}}_{\Omega}^{\alpha_3}\right] \\ \mathbf{D}_{\Omega(2)} = \left[-\frac{1}{A_1}\frac{\partial}{\partial \alpha_1} \quad -\frac{1}{A_2}\frac{\partial}{\partial \alpha_2} \quad -1\right]^T \\ \mathbf{D}_{\Omega(3)} = 1 \end{gathered} \tag{15}$$

The quantities $\overline{\mathbf{D}}_{\Omega}^{\alpha_1}, \overline{\mathbf{D}}_{\Omega}^{\alpha_2}$ and $\overline{\mathbf{D}}_{\Omega}^{\alpha_3}$ are expressed as follows [58]:

$$\overline{\mathbf{D}}_{\Omega}^{\alpha_1} = \begin{bmatrix} \frac{1}{A_1}\frac{\partial}{\partial \alpha_1} \\ \frac{1}{A_1 A_2}\frac{\partial A_2}{\partial \alpha_1} \\ -\frac{1}{A_1 A_2}\frac{\partial A_1}{\partial \alpha_2} \\ \frac{1}{A_2}\frac{\partial}{\partial \alpha_2} \\ -\frac{1}{R_1} \\ 0 \\ 1 \\ 0 \\ 0 \end{bmatrix}, \quad \overline{\mathbf{D}}_{\Omega}^{\alpha_2} = \begin{bmatrix} \frac{1}{A_1 A_2}\frac{\partial A_1}{\partial \alpha_2} \\ \frac{1}{A_2}\frac{\partial}{\partial \alpha_2} \\ \frac{1}{A_1}\frac{\partial}{\partial \alpha_1} \\ -\frac{1}{A_1 A_2}\frac{\partial A_2}{\partial \alpha_1} \\ 0 \\ -\frac{1}{R_2} \\ 0 \\ 1 \\ 0 \end{bmatrix}, \quad \overline{\mathbf{D}}_{\Omega}^{\alpha_3} = \begin{bmatrix} \frac{1}{R_1} \\ \frac{1}{R_2} \\ 0 \\ 0 \\ \frac{1}{A_1}\frac{\partial}{\partial \alpha_1} \\ \frac{1}{A_2}\frac{\partial}{\partial \alpha_2} \\ 0 \\ 0 \\ 1 \end{bmatrix} \tag{16}$$

Finally, the operators $\mathbf{D}_{\Omega}^{\alpha_i}$, with $i = 1,\ldots,6$, introduced in Eq. (14), are defined in terms of the operators $\overline{\mathbf{D}}_{\Omega}^{\alpha_i}$ from Eq. (16) as follows, with $\overline{\mathbf{D}}_{\Omega}^{\alpha_4} = \overline{\mathbf{D}}_{\Omega}^{\alpha_5} = \overline{\mathbf{D}}_{\Omega}^{\alpha_6} = \mathbf{D}_{\Omega(2)}$ and $\widetilde{\mathbf{D}}_{\Omega}^{\alpha_5} = \widetilde{\mathbf{D}}_{\Omega}^{\alpha_6} = \mathbf{D}_{\Omega(3)}$:

$$\mathbf{D}_{\Omega}^{\alpha_1} = \begin{bmatrix} \overline{\mathbf{D}}_{\Omega}^{\alpha_1} & \mathbf{0} & \mathbf{0} & \mathbf{0} & \mathbf{0} & \mathbf{0} \\ \mathbf{0} & \mathbf{0} & \mathbf{0} & \mathbf{0} & \mathbf{0} & \mathbf{0} \\ \mathbf{0} & \mathbf{0} & \mathbf{0} & \mathbf{0} & \mathbf{0} & \mathbf{0} \\ \mathbf{0} & \mathbf{0} & \mathbf{0} & \mathbf{0} & \mathbf{0} & \mathbf{0} \\ \mathbf{0} & \mathbf{0} & \mathbf{0} & \mathbf{0} & \mathbf{0} & \mathbf{0} \\ \mathbf{0} & \mathbf{0} & \mathbf{0} & \mathbf{0} & \mathbf{0} & \mathbf{0} \end{bmatrix}, \quad \mathbf{D}_{\Omega}^{\alpha_2} = \begin{bmatrix} \mathbf{0} & \overline{\mathbf{D}}_{\Omega}^{\alpha_2} & \mathbf{0} & \mathbf{0} & \mathbf{0} & \mathbf{0} \\ \mathbf{0} & \mathbf{0} & \mathbf{0} & \mathbf{0} & \mathbf{0} & \mathbf{0} \\ \mathbf{0} & \mathbf{0} & \mathbf{0} & \mathbf{0} & \mathbf{0} & \mathbf{0} \\ \mathbf{0} & \mathbf{0} & \mathbf{0} & \mathbf{0} & \mathbf{0} & \mathbf{0} \\ \mathbf{0} & \mathbf{0} & \mathbf{0} & \mathbf{0} & \mathbf{0} & \mathbf{0} \\ \mathbf{0} & \mathbf{0} & \mathbf{0} & \mathbf{0} & \mathbf{0} & \mathbf{0} \end{bmatrix},$$

$$\mathbf{D}_{\Omega}^{\alpha_3} = \begin{bmatrix} \mathbf{0} & \mathbf{0} & \overline{\mathbf{D}}_{\Omega}^{\alpha_3} & \mathbf{0} & \mathbf{0} & \mathbf{0} \\ \mathbf{0} & \mathbf{0} & \mathbf{0} & \mathbf{0} & \mathbf{0} & \mathbf{0} \\ \mathbf{0} & \mathbf{0} & \mathbf{0} & \mathbf{0} & \mathbf{0} & \mathbf{0} \\ \mathbf{0} & \mathbf{0} & \mathbf{0} & \mathbf{0} & \mathbf{0} & \mathbf{0} \\ \mathbf{0} & \mathbf{0} & \mathbf{0} & \mathbf{0} & \mathbf{0} & \mathbf{0} \\ \mathbf{0} & \mathbf{0} & \mathbf{0} & \mathbf{0} & \mathbf{0} & \mathbf{0} \end{bmatrix}, \quad \mathbf{D}_{\Omega}^{\alpha_4} = \begin{bmatrix} \mathbf{0} & \mathbf{0} & \mathbf{0} & \mathbf{0} & \mathbf{0} & \mathbf{0} \\ \mathbf{0} & \mathbf{0} & \mathbf{0} & \overline{\mathbf{D}}_{\Omega}^{\alpha_4} & \mathbf{0} & \mathbf{0} \\ \mathbf{0} & \mathbf{0} & \mathbf{0} & \mathbf{0} & \mathbf{0} & \mathbf{0} \\ \mathbf{0} & \mathbf{0} & \mathbf{0} & \mathbf{0} & \mathbf{0} & \mathbf{0} \\ \mathbf{0} & \mathbf{0} & \mathbf{0} & \mathbf{0} & \mathbf{0} & \mathbf{0} \\ \mathbf{0} & \mathbf{0} & \mathbf{0} & \mathbf{0} & \mathbf{0} & \mathbf{0} \end{bmatrix}$$

$$\mathbf{D}_{\Omega}^{\alpha_5} = \begin{bmatrix} \mathbf{0} & \mathbf{0} & \mathbf{0} & \mathbf{0} & \mathbf{0} & \mathbf{0} \\ \mathbf{0} & \mathbf{0} & \mathbf{0} & \mathbf{0} & \mathbf{0} & \mathbf{0} \\ \mathbf{0} & \mathbf{0} & \mathbf{0} & \mathbf{0} & \widetilde{\mathbf{D}}_{\Omega}^{\alpha_5} & \mathbf{0} \\ \mathbf{0} & \mathbf{0} & \mathbf{0} & \mathbf{0} & \mathbf{0} & \mathbf{0} \\ \mathbf{0} & \mathbf{0} & \mathbf{0} & \mathbf{0} & \overline{\mathbf{D}}_{\Omega}^{\alpha_5} & \mathbf{0} \\ \mathbf{0} & \mathbf{0} & \mathbf{0} & \mathbf{0} & \mathbf{0} & \mathbf{0} \end{bmatrix}, \quad \mathbf{D}_{\Omega}^{\alpha_6} = \begin{bmatrix} \mathbf{0} & \mathbf{0} & \mathbf{0} & \mathbf{0} & \mathbf{0} & \mathbf{0} \\ \mathbf{0} & \mathbf{0} & \mathbf{0} & \mathbf{0} & \mathbf{0} & \mathbf{0} \\ \mathbf{0} & \mathbf{0} & \mathbf{0} & \mathbf{0} & \mathbf{0} & \mathbf{0} \\ \mathbf{0} & \mathbf{0} & \mathbf{0} & \mathbf{0} & \mathbf{0} & \widetilde{\mathbf{D}}_{\Omega}^{\alpha_6} \\ \mathbf{0} & \mathbf{0} & \mathbf{0} & \mathbf{0} & \mathbf{0} & \mathbf{0} \\ \mathbf{0} & \mathbf{0} & \mathbf{0} & \mathbf{0} & \mathbf{0} & \overline{\mathbf{D}}_{\Omega}^{\alpha_6} \end{bmatrix} \tag{17}$$

By introducing the higher-order kinematic model from Eq. (5) into Eq. (11), the elements of vector $\boldsymbol{\pi}^{(k)}$ are expanded and expressed in terms of the generalized configuration variables vector $\boldsymbol{\delta}^{(\tau)}$. This results in the introduction of vector $\boldsymbol{\pi}^{(\tau)\alpha_i} = \mathbf{D}_{\Omega}^{\alpha_i}\boldsymbol{\delta}^{(\tau)}$ of generalized primary variables for each τ-th order of the kinematic expansion:

$$\boldsymbol{\pi}^{(k)} = \mathbf{D}\boldsymbol{\Delta}^{(k)} = \mathbf{D}_{\zeta}\sum_{i=1}^{6}\mathbf{D}_{\Omega}^{\alpha_i}\boldsymbol{\Delta}^{(k)} = \sum_{\tau=0}^{N+1}\sum_{i=1}^{6}\mathbf{Z}^{(k\tau)\alpha_i}\mathbf{D}_{\Omega}^{\alpha_i}\boldsymbol{\delta}^{(\tau)} = \sum_{\tau=0}^{N+1}\sum_{i=1}^{6}\mathbf{Z}^{(k\tau)\alpha_i}\boldsymbol{\pi}^{(\tau)\alpha_i} \tag{18}$$

where $\boldsymbol{\pi}^{(\tau)\alpha_i} = \left[\boldsymbol{\varepsilon}^{(\tau)\alpha_i T} \quad \boldsymbol{\mathscr{E}}^{(\tau)\alpha_i T} \quad \widehat{\Delta \mathrm{T}}^{(k)} \quad \widehat{\Delta \mathrm{C}}^{(k)} \quad \boldsymbol{\theta}^{(k)T} \quad \boldsymbol{\lambda}^{(k)T}\right]^T$ contains the generalized vectors of the primary variables corresponding to each physical problem. These vectors are defined as follows:

$$\begin{gathered}\boldsymbol{\varepsilon}^{(\tau)\alpha_i}(\alpha_1,\alpha_2) = \left[\varepsilon_1^{(\tau)\alpha_i} \quad \varepsilon_2^{(\tau)\alpha_i} \quad \gamma_1^{(\tau)\alpha_i} \quad \gamma_2^{(\tau)\alpha_i} \quad \gamma_{13}^{(\tau)\alpha_i} \quad \gamma_{23}^{(\tau)\alpha_i} \quad \omega_{13}^{(\tau)\alpha_i} \quad \omega_{23}^{(\tau)\alpha_i} \quad \varepsilon_3^{(\tau)\alpha_i}\right]^T \\ \boldsymbol{\mathscr{E}}^{(\tau)\alpha_i}(\alpha_1,\alpha_2) = \left[\mathscr{E}_1^{(\tau)\alpha_i} \quad \mathscr{E}_2^{(\tau)\alpha_i} \quad \mathscr{E}_3^{(\tau)\alpha_i}\right]^T \\ \widehat{\Delta \mathrm{T}}^{(\tau)\alpha_i}(\alpha_1,\alpha_2) = \widehat{\Delta \mathrm{T}}^{(\tau)\alpha_i}, \quad \widehat{\Delta \mathrm{C}}^{(\tau)\alpha_i}(\alpha_1,\alpha_2) = \widehat{\Delta \mathrm{C}}^{(\tau)\alpha_i} \\ \boldsymbol{\theta}^{(\tau)\alpha_i}(\alpha_1,\alpha_2) = \left[\theta_1^{(\tau)\alpha_i} \quad \theta_2^{(\tau)\alpha_i} \quad \theta_3^{(\tau)\alpha_i}\right]^T, \quad \boldsymbol{\lambda}^{(\tau)\alpha_i}(\alpha_1,\alpha_2) = \left[\lambda_1^{(\tau)\alpha_i} \quad \lambda_2^{(\tau)\alpha_i} \quad \lambda_3^{(\tau)\alpha_i}\right]^T\end{gathered} \tag{19}$$

A key aspect in the previous equation is the introduction of matrix $\mathbf{Z}^{(k\tau)\alpha_i}$ for each $\tau = 0,\dots,N+1$ and $i = 1,\dots,6$, depending on the thickness coordinate ζ, which incorporates the thickness function matrix $\mathbf{F}_{\tau}^{(k)}$ of Eq. (5) into its definition. This matrix takes the following extended form [58]:

$$\mathbf{Z}^{(k\tau)\alpha_i} = \begin{bmatrix} \mathbf{Z}_1^{(k\tau)\alpha_i} & \mathbf{0} & \mathbf{0} & \mathbf{0} & \mathbf{0} & \mathbf{0} \\ \mathbf{0} & \mathbf{Z}_2^{(k\tau)\alpha_i} & \mathbf{0} & \mathbf{0} & \mathbf{0} & \mathbf{0} \\ \mathbf{0} & \mathbf{0} & \mathbf{Z}_3^{(k\tau)\alpha_i} & \mathbf{0} & \mathbf{0} & \mathbf{0} \\ \mathbf{0} & \mathbf{0} & \mathbf{0} & \mathbf{Z}_3^{(k\tau)\alpha_i} & \mathbf{0} & \mathbf{0} \\ \mathbf{0} & \mathbf{0} & \mathbf{0} & \mathbf{0} & \mathbf{Z}_2^{(k\tau)\alpha_i} & \mathbf{0} \\ \mathbf{0} & \mathbf{0} & \mathbf{0} & \mathbf{0} & \mathbf{0} & \mathbf{Z}_2^{(k\tau)\alpha_i} \end{bmatrix} \tag{20}$$

where the sub-matrices $\mathbf{Z}_m^{(k\tau)\alpha_i} = \mathbf{Z}_1^{(k\tau)\alpha_i}, \mathbf{Z}_2^{(k\tau)\alpha_i}, \mathbf{Z}_3^{(k\tau)\alpha_i}$ are defined as follows:

$$\mathbf{Z}_m^{(k\tau)\alpha_i} = \mathbf{D}_{\zeta(m)}F_{\tau}^{(k)\alpha_i} \tag{21}$$

for $m = 1, 2, 3$. At this point, the coupled constitutive equation is introduced, accounting for the interaction effects between mechanical elasticity, electrostatics, and hygro-thermal phenomena. If the vector of multifield 3D secondary variables is denoted by $\boldsymbol{\chi}^{(k)}$, the following relation is obtained for an arbitrary k-th lamina of the stacking sequence [58]:

$$\begin{gathered}\boldsymbol{\chi}^{(k)} = \overline{\boldsymbol{\Gamma}}^{(k)}\boldsymbol{\pi}^{(k)} \quad \Leftrightarrow \quad \begin{bmatrix} \boldsymbol{\sigma}^{(k)} \\ \boldsymbol{\mathscr{D}}^{(k)} \\ \upeta^{(k)} \\ \upmu^{(k)} \\ \mathbf{h}^{(k)} \\ \mathbf{c}^{(k)} \end{bmatrix} \\ = \begin{bmatrix} \overline{\boldsymbol{\Gamma}}_{\mathrm{C}}^{(k)} & -\overline{\boldsymbol{\Gamma}}_{\mathrm{P}}^{(k)T} & -\overline{\boldsymbol{\Gamma}}_{\mathrm{z}}^{(k)T} & -\overline{\boldsymbol{\Gamma}}_{\mathrm{e}}^{(k)T} & \mathbf{0} & \mathbf{0} \\ \overline{\boldsymbol{\Gamma}}_{\mathrm{P}}^{(k)} & \overline{\boldsymbol{\Gamma}}_{\mathrm{L}}^{(k)} & \overline{\boldsymbol{\Gamma}}_{\mathrm{o}}^{(k)T} & \overline{\boldsymbol{\Gamma}}_{\mathrm{g}}^{(k)T} & \mathbf{0} & \mathbf{0} \\ \overline{\boldsymbol{\Gamma}}_{\mathrm{z}}^{(k)} & \overline{\boldsymbol{\Gamma}}_{\mathrm{o}}^{(k)} & \overline{\boldsymbol{\Gamma}}_{\mathrm{TT}}^{(k)} & \overline{\boldsymbol{\Gamma}}_{\mathrm{TC}}^{(k)} & \mathbf{0} & \mathbf{0} \\ \overline{\boldsymbol{\Gamma}}_{\mathrm{e}}^{(k)} & \overline{\boldsymbol{\Gamma}}_{\mathrm{g}}^{(k)} & \overline{\boldsymbol{\Gamma}}_{\mathrm{TC}}^{(k)} & \overline{\boldsymbol{\Gamma}}_{\mathrm{CC}}^{(k)} & \mathbf{0} & \mathbf{0} \\ \mathbf{0} & \mathbf{0} & \mathbf{0} & \mathbf{0} & \overline{\boldsymbol{\Gamma}}_{\mathrm{K}}^{(k)} & \overline{\boldsymbol{\Gamma}}_{\mathrm{Y}}^{(k)} \\ \mathbf{0} & \mathbf{0} & \mathbf{0} & \mathbf{0} & \overline{\boldsymbol{\Gamma}}_{\mathrm{X}}^{(k)} & \overline{\boldsymbol{\Gamma}}_{\mathrm{S}}^{(k)} \end{bmatrix} \begin{bmatrix} \boldsymbol{\varepsilon}^{(k)} \\ \boldsymbol{\mathscr{E}}^{(k)} \\ \widehat{\Delta \mathrm{T}}^{(k)} \\ \widehat{\Delta \mathrm{C}}^{(k)} \\ \boldsymbol{\theta}^{(k)} \\ \boldsymbol{\lambda}^{(k)} \end{bmatrix}\end{gathered} \tag{22}$$

In the previous relation, $\boldsymbol{\sigma}^{(k)} = \left[\sigma_1^{(k)} \quad \sigma_2^{(k)} \quad \tau_{12}^{(k)} \quad \tau_{13}^{(k)} \quad \tau_{23}^{(k)} \quad \sigma_3^{(k)}\right]^T$ collects the 3D stress components, while $\boldsymbol{\mathscr{D}}^{(k)} = \left[\mathscr{D}_1^{(k)} \quad \mathscr{D}_2^{(k)} \quad \mathscr{D}_3^{(k)}\right]^T$ represents the vector of electric flux components. In addition, $\mathbf{h}^{(k)} = \left[h_1^{(k)} \quad h_2^{(k)} \quad h_3^{(k)}\right]^T$ and $\mathbf{c}^{(k)} = \left[c_1^{(k)} \quad c_2^{(k)} \quad c_3^{(k)}\right]^T$ are the thermal flux and mass flux vector, respectively, while $\eta^{(k)}$ denotes the specific entropy of the shell solid. Finally, $\upmu^{(k)}$ represents the specific entropy of the system. The matrices $\overline{\boldsymbol{\Gamma}}_{\mathrm{C}}^{(k)}, \overline{\boldsymbol{\Gamma}}_{\mathrm{L}}^{(k)}, \overline{\boldsymbol{\Gamma}}_{\mathrm{P}}^{(k)}, \overline{\boldsymbol{\Gamma}}_{\mathrm{z}}^{(k)}, \overline{\boldsymbol{\Gamma}}_{\mathrm{e}}^{(k)}, \overline{\boldsymbol{\Gamma}}_{\mathrm{o}}^{(k)}, \overline{\boldsymbol{\Gamma}}_{\mathrm{g}}^{(k)}, \overline{\boldsymbol{\Gamma}}_{\mathrm{K}}^{(k)}, \overline{\boldsymbol{\Gamma}}_{\mathrm{X}}^{(k)}, \overline{\boldsymbol{\Gamma}}_{\mathrm{Y}}^{(k)}, \overline{\boldsymbol{\Gamma}}_{\mathrm{S}}^{(k)}, \overline{\boldsymbol{\Gamma}}_{\mathrm{TT}}^{(k)}, \overline{\boldsymbol{\Gamma}}_{\mathrm{TC}}^{(k)}$ and $\overline{\boldsymbol{\Gamma}}_{\mathrm{CC}}^{(k)}$ occurring in Eq. (22) take the following extended form, for generally anisotropic materials:

$$
\begin{aligned}
&\overline{\boldsymbol{\Gamma}}_{\mathrm{C}}^{(k)}=\begin{bmatrix}
\overline{C}_{11}^{(k)} & \overline{C}_{12}^{(k)} & \overline{C}_{16}^{(k)} & \overline{C}_{14}^{(k)} & \overline{C}_{15}^{(k)} & \overline{C}_{13}^{(k)}\\
\overline{C}_{12}^{(k)} & \overline{C}_{22}^{(k)} & \overline{C}_{26}^{(k)} & \overline{C}_{24}^{(k)} & \overline{C}_{25}^{(k)} & \overline{C}_{23}^{(k)}\\
\overline{C}_{16}^{(k)} & \overline{C}_{26}^{(k)} & \overline{C}_{66}^{(k)} & \overline{C}_{46}^{(k)} & \overline{C}_{56}^{(k)} & \overline{C}_{36}^{(k)}\\
\overline{C}_{14}^{(k)} & \overline{C}_{24}^{(k)} & \overline{C}_{46}^{(k)} & \overline{C}_{44}^{(k)} & \overline{C}_{45}^{(k)} & \overline{C}_{34}^{(k)}\\
\overline{C}_{15}^{(k)} & \overline{C}_{25}^{(k)} & \overline{C}_{56}^{(k)} & \overline{C}_{45}^{(k)} & \overline{C}_{55}^{(k)} & \overline{C}_{35}^{(k)}\\
\overline{C}_{13}^{(k)} & \overline{C}_{23}^{(k)} & \overline{C}_{36}^{(k)} & \overline{C}_{34}^{(k)} & \overline{C}_{35}^{(k)} & \overline{C}_{33}^{(k)}
\end{bmatrix}\\
&\overline{\boldsymbol{\Gamma}}_{\mathrm{L}}^{(k)}=\begin{bmatrix}
\overline{l}_{11}^{(k)} & \overline{l}_{12}^{(k)} & \overline{l}_{13}^{(k)}\\
\overline{l}_{12}^{(k)} & \overline{l}_{22}^{(k)} & \overline{l}_{23}^{(k)}\\
\overline{l}_{13}^{(k)} & \overline{l}_{23}^{(k)} & \overline{l}_{33}^{(k)}
\end{bmatrix}\\
&\overline{\boldsymbol{\Gamma}}_{\mathrm{P}}^{(k)}=\begin{bmatrix}
\overline{p}_{11}^{(k)} & \overline{p}_{12}^{(k)} & \overline{p}_{16}^{(k)} & \overline{p}_{14}^{(k)} & \overline{p}_{15}^{(k)} & \overline{p}_{13}^{(k)}\\
\overline{p}_{21}^{(k)} & \overline{p}_{22}^{(k)} & \overline{p}_{26}^{(k)} & \overline{p}_{24}^{(k)} & \overline{p}_{25}^{(k)} & \overline{p}_{23}^{(k)}\\
\overline{p}_{31}^{(k)} & \overline{p}_{32}^{(k)} & \overline{p}_{36}^{(k)} & \overline{p}_{34}^{(k)} & \overline{p}_{35}^{(k)} & \overline{p}_{33}^{(k)}
\end{bmatrix}\\
&\overline{\boldsymbol{\Gamma}}_{\mathrm{z}}^{(k)}=\begin{bmatrix}\overline{z}_{11}^{(k)} & \overline{z}_{22}^{(k)} & \overline{z}_{12}^{(k)} & \overline{z}_{13}^{(k)} & \overline{z}_{23}^{(k)} & \overline{z}_{33}^{(k)}\end{bmatrix}\\
&\overline{\boldsymbol{\Gamma}}_{\mathrm{e}}^{(k)}=\begin{bmatrix}\overline{e}_{11}^{(k)} & \overline{e}_{22}^{(k)} & \overline{e}_{12}^{(k)} & \overline{e}_{13}^{(k)} & \overline{e}_{23}^{(k)} & \overline{e}_{33}^{(k)}\end{bmatrix}\\
&\overline{\boldsymbol{\Gamma}}_{\mathrm{o}}^{(k)}=\begin{bmatrix}\overline{o}_{11}^{(k)} & \overline{o}_{22}^{(k)} & \overline{o}_{33}^{(k)}\end{bmatrix}\\
&\overline{\boldsymbol{\Gamma}}_{\mathrm{g}}^{(k)}=\begin{bmatrix}\overline{g}_{11}^{(k)} & \overline{g}_{22}^{(k)} & \overline{g}_{33}^{(k)}\end{bmatrix}\\
&\overline{\boldsymbol{\Gamma}}_{\mathrm{K}}^{(k)}=\begin{bmatrix}
\overline{k}_{11}^{(k)} & \overline{k}_{12}^{(k)} & \overline{k}_{13}^{(k)}\\
\overline{k}_{12}^{(k)} & \overline{k}_{22}^{(k)} & \overline{k}_{23}^{(k)}\\
\overline{k}_{13}^{(k)} & \overline{k}_{23}^{(k)} & \overline{k}_{33}^{(k)}
\end{bmatrix},\quad
\overline{\boldsymbol{\Gamma}}_{\mathrm{X}}^{(k)}=\begin{bmatrix}
\overline{x}_{11}^{(k)} & \overline{x}_{12}^{(k)} & \overline{x}_{13}^{(k)}\\
\overline{x}_{12}^{(k)} & \overline{x}_{22}^{(k)} & \overline{x}_{23}^{(k)}\\
\overline{x}_{13}^{(k)} & \overline{x}_{23}^{(k)} & \overline{x}_{33}^{(k)}
\end{bmatrix}\\
&\overline{\boldsymbol{\Gamma}}_{\mathrm{Y}}^{(k)}=\begin{bmatrix}
\overline{y}_{11}^{(k)} & \overline{y}_{12}^{(k)} & \overline{y}_{13}^{(k)}\\
\overline{y}_{12}^{(k)} & \overline{y}_{22}^{(k)} & \overline{y}_{23}^{(k)}\\
\overline{y}_{13}^{(k)} & \overline{y}_{23}^{(k)} & \overline{y}_{33}^{(k)}
\end{bmatrix},\quad
\overline{\boldsymbol{\Gamma}}_{\mathrm{S}}^{(k)}=\begin{bmatrix}
\overline{s}_{11}^{(k)} & \overline{s}_{12}^{(k)} & \overline{s}_{13}^{(k)}\\
\overline{s}_{12}^{(k)} & \overline{s}_{22}^{(k)} & \overline{s}_{23}^{(k)}\\
\overline{s}_{13}^{(k)} & \overline{s}_{23}^{(k)} & \overline{s}_{33}^{(k)}
\end{bmatrix}\\
&\overline{\boldsymbol{\Gamma}}_{\mathrm{TT}}^{(k)}=\overline{\xi}_{11}^{(k)},\quad \overline{\boldsymbol{\Gamma}}_{\mathrm{TC}}^{(k)}=\overline{\xi}_{12}^{(k)},\quad \overline{\boldsymbol{\Gamma}}_{\mathrm{CC}}^{(k)}=\overline{\xi}_{22}^{(k)}
\end{aligned}
\tag{23}
$$

Note that matrices $\overline{\boldsymbol{\Gamma}}_{\mathrm{z}}^{(k)}$ and $\overline{\boldsymbol{\Gamma}}_{\mathrm{e}}^{(k)}$ account for the stresses associated with thermal expansion and hygroscopic expansion phenomena, and

$$
\overline{\boldsymbol{\Gamma}}^{(k)}=\begin{bmatrix}
\mathbf{T}^{(k)}\overline{\boldsymbol{\Gamma}}_{\mathrm{C}}^{(k)}\mathbf{T}^{(k)T} & -\mathbf{T}^{(k)}\overline{\boldsymbol{\Gamma}}_{\mathrm{P}}^{(k)T}\mathbf{H}^{(k)} & -\mathbf{T}^{(k)}\overline{\boldsymbol{\Gamma}}_{\mathrm{C}}^{(k)}\mathbf{T}^{(k)T}\overline{\boldsymbol{\Gamma}}_{\mathrm{a}}^{(k)} & -\mathbf{T}^{(k)}\overline{\boldsymbol{\Gamma}}_{\mathrm{C}}^{(k)}\mathbf{T}^{(k)T}\overline{\boldsymbol{\Gamma}}_{\mathrm{b}}^{(k)} & \mathbf{0} & \mathbf{0}\\
\mathbf{H}^{(k)T}\overline{\boldsymbol{\Gamma}}_{\mathrm{P}}^{(k)}\mathbf{T}^{(k)T} & \mathbf{H}^{(k)T}\overline{\boldsymbol{\Gamma}}_{\mathrm{L}}^{(k)}\mathbf{H}^{(k)} & \mathbf{H}^{(k)T}\overline{\boldsymbol{\Gamma}}_{\mathrm{o}}^{(k)T} & \mathbf{H}^{(k)T}\overline{\boldsymbol{\Gamma}}_{\mathrm{g}}^{(k)T} & \mathbf{0} & \mathbf{0}\\
\overline{\boldsymbol{\Gamma}}_{\mathrm{a}}^{(k)T}\mathbf{T}^{(k)T}\overline{\boldsymbol{\Gamma}}_{\mathrm{C}}^{(k)}\mathbf{T}^{(k)} & \overline{\boldsymbol{\Gamma}}_{\mathrm{o}}^{(k)}\mathbf{H}^{(k)} & \overline{\boldsymbol{\Gamma}}_{\mathrm{TT}}^{(k)} & \overline{\boldsymbol{\Gamma}}_{\mathrm{TC}}^{(k)} & \mathbf{0} & \mathbf{0}\\
\overline{\boldsymbol{\Gamma}}_{\mathrm{b}}^{(k)T}\mathbf{T}^{(k)T}\overline{\boldsymbol{\Gamma}}_{\mathrm{C}}^{(k)}\mathbf{T}^{(k)} & \overline{\boldsymbol{\Gamma}}_{\mathrm{g}}^{(k)}\mathbf{H}^{(k)} & \overline{\boldsymbol{\Gamma}}_{\mathrm{TC}}^{(k)} & \overline{\boldsymbol{\Gamma}}_{\mathrm{CC}}^{(k)} & \mathbf{0} & \mathbf{0}\\
\mathbf{0} & \mathbf{0} & \mathbf{0} & \mathbf{0} & \mathbf{H}^{(k)T}\overline{\boldsymbol{\Gamma}}_{\mathrm{K}}^{(k)}\mathbf{H}^{(k)} & \mathbf{H}^{(k)T}\overline{\boldsymbol{\Gamma}}_{\mathrm{Y}}^{(k)}\mathbf{H}^{(k)}\\
\mathbf{0} & \mathbf{0} & \mathbf{0} & \mathbf{0} & \mathbf{H}^{(k)T}\overline{\boldsymbol{\Gamma}}_{\mathrm{X}}^{(k)}\mathbf{H}^{(k)} & \mathbf{H}^{(k)T}\overline{\boldsymbol{\Gamma}}_{\mathrm{S}}^{(k)}\mathbf{H}^{(k)}
\end{bmatrix}
\tag{25}
$$

they are calculated in terms of the elastic stiffness matrix $\overline{\boldsymbol{\Gamma}}_{\mathrm{C}}^{(k)}$ of the mechanical elasticity. More specifically, vectors, $\overline{\boldsymbol{\Gamma}}_{\mathrm{a}}^{(k)}=\begin{bmatrix}\overline{a}_{11} & \overline{a}_{22} & \overline{a}_{12}\,\overline{a}_{13} & \overline{a}_{23} & \overline{a}_{33}\end{bmatrix}^T$ and $\overline{\boldsymbol{\Gamma}}_{\mathrm{b}}^{(k)}=\begin{bmatrix}\overline{b}_{11} & \overline{b}_{22} & \overline{b}_{12}\,\overline{b}_{13} & \overline{b}_{23} & \overline{b}_{33}\end{bmatrix}^T$ of size 6×1, collect the rotated thermal expansion coefficients and the hygroscopic expansion coefficients, $\overline{a}_{ij}^{(k)}$ and $\overline{b}_{ij}^{(k)}$, respectively, with $i,j=1,\dots,3$ [58]:

$$
\overline{\boldsymbol{\Gamma}}_{\mathrm{z}}^{(k)T}=\overline{\boldsymbol{\Gamma}}_{\mathrm{C}}^{(k)}\overline{\boldsymbol{\Gamma}}_{\mathrm{a}}^{(k)},\quad \overline{\boldsymbol{\Gamma}}_{\mathrm{e}}^{(k)T}=\overline{\boldsymbol{\Gamma}}_{\mathrm{C}}^{(k)}\overline{\boldsymbol{\Gamma}}_{\mathrm{b}}^{(k)}
\tag{24}
$$

The coupled hygro-thermo-electro-elastic constitutive relation in Eq. (22) is referred to the geometric reference system of the solid. However,

Table 1

Analytical expressions adopted in the simulation for the variation of the material properties within an arbitrary layer of the shell. Symmetric and unsymmetric distributions are considered, taking into account both polynomial and trigonometric functions. Further material distributions can be found in Ref. [58].

Symbol	Denomination	Analytical expression
U	Uniform	$g(\widehat{z}_k)=1$
UC – I	Unsymmetric cosine I	$g(\widehat{z}_k)=1-\cos\left(\frac{\pi}{2}\widehat{z}_k+\frac{\pi}{4}\right)$
UC – II	Unsymmetric cosine II	$g(\widehat{z}_k)=\cos\left(\frac{\pi}{2}\widehat{z}_k+\frac{\pi}{4}\right)$
UC – III	Unsymmetric cosine III	$g(\widehat{z}_k)=1-\cos\left(\frac{\pi}{2}\widehat{z}_k-\frac{\pi}{4}\right)$
UC – IV	Unsymmetric cosine IV	$g(\widehat{z}_k)=\cos\left(\frac{\pi}{2}\widehat{z}_k-\frac{\pi}{4}\right)$
SC – I	Symmetric cosine I	$g(\widehat{z}_k)=1-\cos(\pi\widehat{z}_k)^{\frac{1}{p}}$
SC – II	Symmetric cosine II	$g(\widehat{z}_k)=(\cos(\pi\widehat{z}_k))^{\frac{1}{p}}$
HS – I	Hyperbolic sine I	$g(\widehat{z}_k)=\frac{1}{2}\left(1-\left(\frac{\sinh\widehat{z}_k}{\sinh\frac{1}{2}}\right)^{2p+1}\right)$
HS – II	Hyperbolic sine II	$g(\widehat{z}_k)=\frac{1}{2}\left(1+\left(\frac{\sinh\widehat{z}_k}{\sinh\frac{1}{2}}\right)^{2p+1}\right)$
HT – I	Hyperbolic tangent I	$g(\widehat{z}_k)=\frac{1}{2}\left(1-\left(\frac{\tanh\widehat{z}_k}{\tanh\frac{1}{2}}\right)^{3}\right)$
HT – II	Hyperbolic tangent II	$g(\widehat{z}_k)=\frac{1}{2}\left(1+\left(\frac{\tanh\widehat{z}_k}{\tanh\frac{1}{2}}\right)^{3}\right)$

the elements of the matrices in Eq. (23) are derived, for each k-th layer, with respect to the so-called material reference system, denoted as $O'\widehat{\alpha}_1^{(k)}\widehat{\alpha}_2^{(k)}\widehat{\zeta}^{(k)}$, which depends on the symmetry axes of the constituent material. For this reason, the multifield constitutive matrix $\overline{\boldsymbol{\Gamma}}^{(k)}$ in Eq. (22) is expressed in terms of the matrices $\boldsymbol{\Gamma}_{\mathrm{C}}^{(k)},\boldsymbol{\Gamma}_{\mathrm{L}}^{(k)},\boldsymbol{\Gamma}_{\mathrm{P}}^{(k)},\boldsymbol{\Gamma}_{\mathrm{o}}^{(k)},\boldsymbol{\Gamma}_{\mathrm{g}}^{(k)},\boldsymbol{\Gamma}_{\mathrm{K}}^{(k)},\boldsymbol{\Gamma}_{\mathrm{X}}^{(k)}$, $\boldsymbol{\Gamma}_{\mathrm{Y}}^{(k)},\boldsymbol{\Gamma}_{\mathrm{S}}^{(k)},\boldsymbol{\Gamma}_{\mathrm{TT}}^{(k)},\boldsymbol{\Gamma}_{\mathrm{TC}}^{(k)}$ and $\boldsymbol{\Gamma}_{\mathrm{CC}}^{(k)}$ written in the material reference system as follows:

The multifield relation in Eq. (22) is, thus, derived from Eq. (25) by introducing a transformation matrix, denoted by $\mathbf{H}^{(k)}$, which accounts for the rotation angles of the material reference axes $\widehat{\alpha}_1^{(k)}\widehat{\alpha}_2^{(k)}\widehat{\zeta}^{(k)}$ with respect to the geometric reference system of the solid. If the planes $\widehat{\alpha}_1^{(k)}-\widehat{\alpha}_2^{(k)}$ and $\alpha_1-\alpha_2$ are assumed to be parallel, the transformation matrix $\mathbf{H}^{(k)}$ depends only on the angle $\vartheta^{(k)}$ between $\widehat{\alpha}_1^{(k)}$ and α_1 material and geometric axes, and takes the following aspect [58]:

$$
\mathbf{H}^{(k)}=\begin{bmatrix}
\cos\vartheta^{(k)} & \sin\vartheta^{(k)} & 0\\
-\sin\vartheta^{(k)} & \cos\vartheta^{(k)} & 0\\
0 & 0 & 1
\end{bmatrix}
\tag{26}
$$

Table 2
Constitutive coefficients of smart materials with multifield properties adopted in the simulations.

Material	$CoFe_2O_4$	MAT – I	MAT – II	MAT – III	$BaTiO_3$
V_f	0	0.2	0.4 [× 1/3]	0.6	1
T_0[K]	297	297	297	297	297
$\rho\,[\mathrm{kg/m^3}]$	5300	5400	1833	5600	5800
$M_\infty[\%]$	0.01	0.01	0.02	0.01	0.03
c [J/kgK]	377.36	414.58	450.45	357.14	550.62
$C_{11}=C_{22}\,[\times 10^9\,\mathrm{N/m^2}]$	286	252.38	74.98	202.08	166
$C_{12}\,[\times 10^9\,\mathrm{N/m^2}]$	173	144.72	40.78	104.26	77
$C_{13}=C_{23}\,[\times 10^9\,\mathrm{N/m^2}]$	170.5	143.99	40.89	105.13	78
$C_{66}=(C_{11}-C_{12})/2\,[\times 10^9\,\mathrm{N/m^2}]$	56.5	53.83	17.10	48.91	44.5
$C_{44}=C_{55}\,[\times 10^9\,\mathrm{N/m^2}]$	45.3	47.15	16.33	50.81	43
$C_{33}\,[\times 10^9\,\mathrm{N/m^2}]$	269.5	24.11	72.41	196.54	162
$p_{14}=p_{25}\,[\mathrm{C/m^2}]$	0	0.04	0.03	0.23	11.6
$p_{31}=p_{32}\,[\mathrm{C/m^2}]$	0	-1.26	-0.76	-3.11	-4.4
$p_{33}\,[\mathrm{C/m^2}]$	0	3.39	2.33	10.76	18.6
$q_{14}=q_{25}\,[\mathrm{Wb/m^2}]$	550	367.81	79.00	138.50	0
$q_{31}=q_{32}\,[\mathrm{Wb/m^2}]$	580.3	414.00	93.39	170.17	0
$q_{33}\,[\mathrm{Wb/m^2}]$	-699.7	-602.79	-159.35	-332.94	0
$a_{11}=a_{22}\,[\times 10^{-6}\,1/\mathrm{K}]$	10	11.02	12.09	13.22	15.7
$a_{33}\,[\times 10^{-6}\,1/\mathrm{K}]$	5	5.17	5.39	5.65	6.4
$b_{11}=b_{22}\,[\times 10^{-4}\,\mathrm{m^3/kg}]$	1.1	0.90	0.70	0.48	0
$b_{33}\,[\times 10^{-4}\,\mathrm{m^3/kg}]$	0	0.01	0.17	0.02	0
$l_{11}=l_{22}\,[\times 10^{-9}\,\mathrm{F/m}]$	0.08	11.94	0.06	0.31	11.2
$l_{33}\,[\times 10^{-9}\,\mathrm{F/m}]$	0.093	26.10	1.71	7.62	12.6
$d_{11}=d_{22}\,[\times 10^{-12}\,\mathrm{s/m}]$	0	-2.56	-1.49	-5.91	0
$d_{33}\,[\times 10^{-9}\,\mathrm{s/m}]$	0	2.05	0.92	2.52	0
$m_{11}=m_{22}\,[\times 10^{-6}\,\mathrm{H/m}]$	590	396.10	85.6	152.2	5
$m_{33}\,[\times 10^{-6}\,\mathrm{H/m}]$	157	127.87	32.86	69.1	10
$o_{33}\,[\times 10^{-5}\,\mathrm{C/m^2K}]$	0	3.60	0.27	11.51	20
$g_{33}\,[\times 10^{-4}\,\mathrm{Cm/kg}]$	0	-1.78	0	-2.20	0
$w_{33}\,[\times 10^{-4}\,\mathrm{T/K}]$	3.2	-2.69	-1.73	-5.19	0
$f_{33}\,[\mathrm{Tm^3/kg}]$	0	-0.02	-0.01	-0.03	0
$k_{11}=k_{22}\,[\mathrm{J/mK}]$	3.2	3.03	0.96	2.74	2.5
$k_{33}\,[\mathrm{J/mK}]$	3.2	3.06	0.97	2.78	2.5
$s_{11}=s_{22}\,[\times 10^{-8}\,\mathrm{m^2}]\,(u_d=0.1,\ \lambda\nu=0.25)$	16	13.24	3.76	9.84	7.83
$s_{33}\,[\times 10^{-8}\,\mathrm{m^2}]\,(u_d=0.1,\ \lambda\nu=0.25)$	16	14.37	4.24	11.1	7.83
$x_{11}=x_{22}\,[\times 10^{-8}\,\mathrm{kg/mK}]\,(u_d=0.1,\ \lambda\nu=0.25)$	4.08	4.46	1.54	4.66	4.57
$x_{33}\,[\times 10^{-8}\,\mathrm{kg/mK}]\,(u_d=0.1,\ \lambda\nu=0.25)$	4.08	4.50	1.56	4.73	4.57
$y_{11}=y_{22}\,[\mathrm{J/m^2K}]\,(u_d=0.1,\ \lambda\nu=0.25)$	3.14	2.25	0.59	1.45	1.07
$y_{33}\,[\mathrm{J/m^2K}]\,(u_d=0.1,\ \lambda\nu=0.25)$	3.14	2.44	0.66	1.63	1.07

It is useful to introduce an additional transformation matrix of size 6 × 6, denoted by $\mathbf{T}^{(k)}$, which is defined by appropriately expanding the matrix $\mathbf{H}^{(k)}$ through the Kronecker product $\otimes$:

$$\begin{aligned}\mathbf{T}^{(k)} &= \overline{\mathbf{T}}^{(k)}_{([1,5,4,7,8,9]\times[1,5,2+4,3+7,6+8,9])}\\ &= \left(\mathbf{H}^{(k)T}\otimes\left(\mathbf{H}^{(k)}\right)^{-1}\right)_{([1,5,4,7,8,9]\times[1,5,2+4,3+7,6+8,9])}\end{aligned} \tag{27}$$

The elements of the vectors $\overline{\boldsymbol{\Gamma}}_{\mathrm{a}}^{(k)}$ and $\overline{\boldsymbol{\Gamma}}_{\mathrm{b}}^{(k)}$, of size 6 × 1, and denoted by $\overline{a}_{ij}^{(k)}$ and $\overline{b}_{ij}^{(k)}$ with $i,j=1,2,3$, are collected into matrices $\overline{\mathbf{A}}^{(k)}$ and $\overline{\mathbf{B}}^{(k)}$, and they are calculated as follows:

$$\begin{aligned}\overline{\mathbf{A}}^{(k)} &= \mathbf{Y}_\varepsilon\odot\left(\mathbf{H}^{(k)T}\widehat{\mathbf{A}}^{(k)}\mathbf{H}^{(k)}\right)\\ \overline{\mathbf{B}}^{(k)} &= \mathbf{Y}_\varepsilon\odot\left(\mathbf{H}^{(k)T}\widehat{\mathbf{B}}^{(k)}\mathbf{H}^{(k)}\right)\end{aligned} \tag{28}$$

where the symbol $\odot$ denotes the Hadamard product. The arbitrary elements of matrices $\widehat{\mathbf{A}}^{(k)},\widehat{\mathbf{B}}^{(k)}$ are denoted by $\widehat{a}_{ij}^{(k)}$ and $\widehat{b}_{ij}^{(k)}$ with $i,j=1,2,3$, while the thermal expansion coefficients and hygroscopic expansion coefficients are denoted by $a_{ij}^{(k)}$ and $b_{ij}^{(k)}$, respectively, and are collected into matrices $\mathbf{A}^{(k)},\mathbf{B}^{(k)}$ of size 3 × 3. The matrix $\mathbf{Y}_\varepsilon$ of size 3 × 3 allows for the conversion between the 3D strain components and the engineering strain components. All these coefficients are, thus, related to each other according to the following relations [58]:

$$\begin{aligned}\mathbf{A}^{(k)} &= \begin{bmatrix} a_{11}^{(k)} & a_{12}^{(k)} & a_{13}^{(k)}\\ a_{12}^{(k)} & a_{22}^{(k)} & a_{23}^{(k)}\\ a_{13}^{(k)} & a_{23}^{(k)} & a_{33}^{(k)}\end{bmatrix} = \begin{bmatrix}1&2&2\\2&1&2\\2&2&1\end{bmatrix}\odot\begin{bmatrix} \widehat{a}_{11}^{(k)} & \widehat{a}_{12}^{(k)} & \widehat{a}_{13}^{(k)}\\ \widehat{a}_{12}^{(k)} & \widehat{a}_{22}^{(k)} & \widehat{a}_{23}^{(k)}\\ \widehat{a}_{13}^{(k)} & \widehat{a}_{23}^{(k)} & \widehat{a}_{33}^{(k)}\end{bmatrix} = \mathbf{Y}_\varepsilon\odot\widehat{\mathbf{A}}^{(k)}\\ \mathbf{B}^{(k)} &= \begin{bmatrix} b_{11}^{(k)} & b_{12}^{(k)} & b_{13}^{(k)}\\ b_{12}^{(k)} & b_{22}^{(k)} & b_{23}^{(k)}\\ b_{13}^{(k)} & b_{23}^{(k)} & b_{33}^{(k)}\end{bmatrix} = \begin{bmatrix}1&2&2\\2&1&2\\2&2&1\end{bmatrix}\odot\begin{bmatrix} \widehat{b}_{11}^{(k)} & \widehat{b}_{12}^{(k)} & \widehat{b}_{13}^{(k)}\\ \widehat{b}_{12}^{(k)} & \widehat{b}_{22}^{(k)} & \widehat{b}_{23}^{(k)}\\ \widehat{b}_{13}^{(k)} & \widehat{b}_{23}^{(k)} & \widehat{b}_{33}^{(k)}\end{bmatrix} = \mathbf{Y}_\varepsilon\odot\widehat{\mathbf{B}}^{(k)}\end{aligned} \tag{29}$$

The matrices $\boldsymbol{\Gamma}_{\mathrm{Y}}^{(k)}$ and $\boldsymbol{\Gamma}_{\mathrm{X}}^{(k)}$, couple the Fourier heat conduction model and Fick mass diffusion equations, are derived from the thermal conductivity matrix $\boldsymbol{\Gamma}_{\mathrm{K}}^{(k)}$ and the mass diffusivity matrix $\boldsymbol{\Gamma}_{\mathrm{S}}^{(k)}$, both expressed in the material reference system. These matrices are obtained by applying the Onsager reciprocity theorem and by defining some appropriate generalized hygro-thermal variables, with the coupling coefficients set as $\lambda^{(k)},\nu^{(k)}$, as detailed in Ref. [58]:

$$\begin{aligned}\boldsymbol{\Gamma}_{\mathrm{Y}}^{(k)} &= \nu^{(k)}\rho^{(k)}c^{(k)}\boldsymbol{\Gamma}_{\mathrm{S}}^{(k)}\\ \boldsymbol{\Gamma}_{\mathrm{X}}^{(k)} &= \frac{\lambda^{(k)}}{\rho^{(k)}c^{(k)}}\boldsymbol{\Gamma}_{\mathrm{K}}^{(k)}\end{aligned} \tag{30}$$

Here, $\rho^{(k)}$ denotes the density of the constituent material, while $c^{(k)}$ represents the specific heat. In addition, the coupling coefficients $\lambda^{(k)}$ and $\nu^{(k)}$ in Eq. (30) are derived from the following relations:

$$\nu^{(k)} = \frac{Q_h^{(k)}}{\rho^{(k)}c^{(k)}} \tag{31}$$

where $Q_h^{(k)}$ represents the amount of heat transferred due to the mass diffusion. This quantity is evaluated as follows:

$$Q_h^{(k)} = \mathrm{T}_0\sqrt{\frac{\rho^{(k)}c^{(k)}\lambda^{(k)}\nu^{(k)}R_g}{u_d^{(k)}C_\infty^{(k)}}} = \mathrm{T}_0\sqrt{\frac{c^{(k)}\lambda^{(k)}\nu^{(k)}R_g}{u_d^{(k)}M_\infty^{(k)}}} \tag{32}$$

In the previous relation, T_0 denotes the reference temperature, previously introduced for defining the absolute temperature variation in Eq. (6), while $R_g=461.9\,\mathrm{J/(kg\,K)}$ is the universal gas constant for water vapor. Furthermore, the parameter $u_d^{(k)}$ is set to 0.1, while the product $\lambda^{(k)}\nu^{(k)}$ is typically calibrated through experimental tests. For hygro-thermal coupled simulations, the value 0.25 is used for this product, based on the experimental results from Ref. [18] and the theory reported in Ref. [58]. Finally, the quantity $M_\infty^{(k)}$ is the equilibrium moisture content within the solid, dependent on the relative humidity and determined through experimental measurements. It should be noted that the constitutive relation in Eq. (30) is derived directly from the Onsager principle, which relates the moisture flux vector and the heat flux vector through the kinetic coefficients, which are derived from the physical parameters of the material, as well as the temperature gradient and the

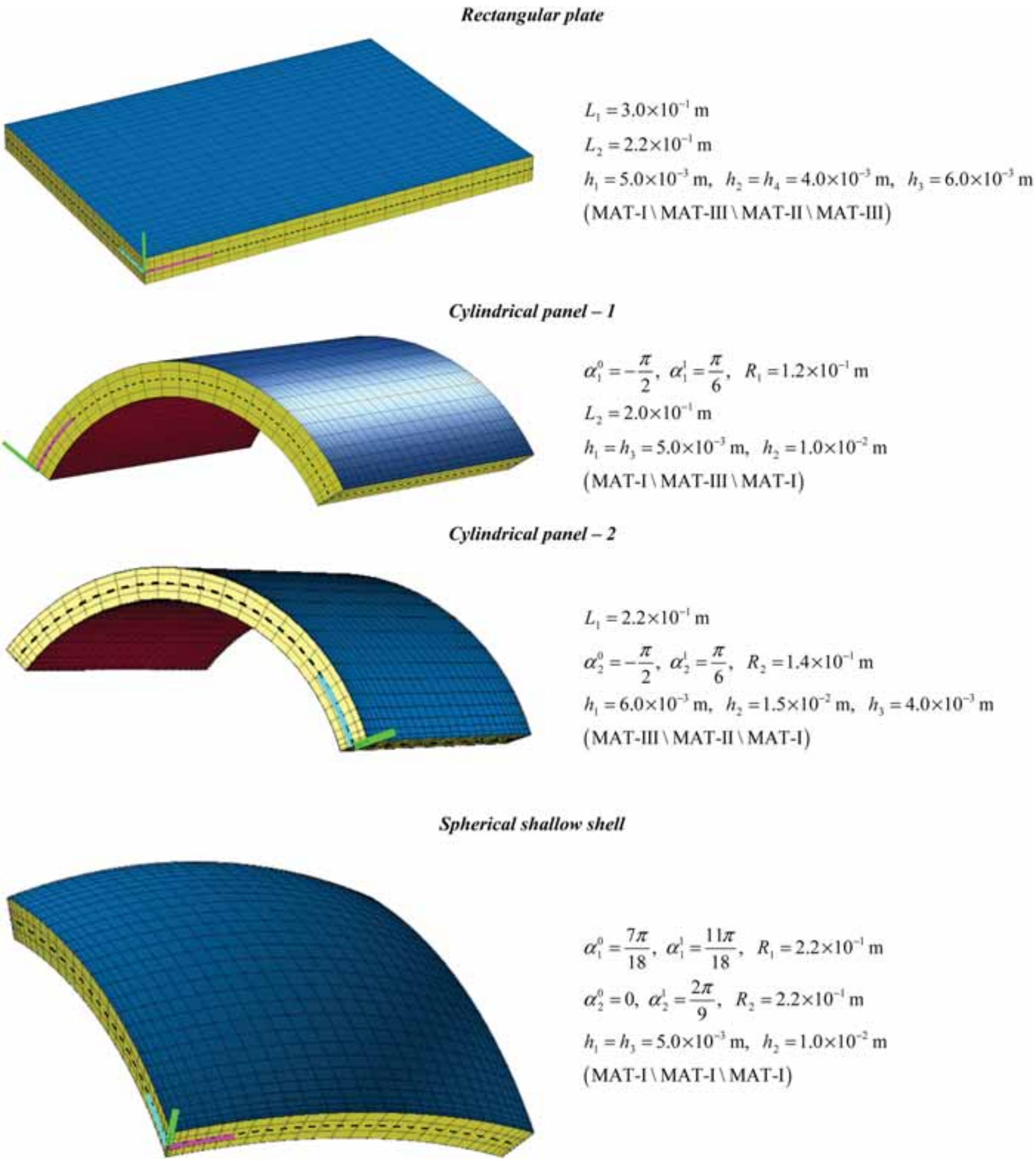

Fig. 1. Geometric and material inputs for laminated panels with different curvatures. Representation of the 3D solids and their geometric reference system in principal coordinates.

gradient of the ratio between the chemical potential and the temperature. This heat and moisture change must satisfy the second principle of thermodynamics. The coupling coefficients $\lambda^{(k)}, \nu^{(k)}$ are defined to simplify the expression of the constitutive relation. Their expression is derived under the assumption that moisture diffusion rate is much slower than the temperature variation rate. In any case, these values must be calibrated with experimental data. If the values cited above are adopted, an acceptable agreement is observed with experimental tests, remaining in ten percent of maximum discrepancy. The coefficients $\overline{\boldsymbol{\Gamma}}_{TT}^{(k)} = \boldsymbol{\Gamma}_{TT}^{(k)} = \xi_{11}^{(k)}$, $\overline{\boldsymbol{\Gamma}}_{CC}^{(k)} = \boldsymbol{\Gamma}_{CC}^{(k)} = \xi_{22}^{(k)}$ and $\overline{\boldsymbol{\Gamma}}_{TC}^{(k)} = \boldsymbol{\Gamma}_{TC}^{(k)} = \xi_{12}^{(k)}$ within the constitutive matrix in Eq. (25) are derived from the following expression [58] for the variation of the specific chemical potential $\Delta\mu^{(k)}$ with respect to $\mu_0^{(k)}$:

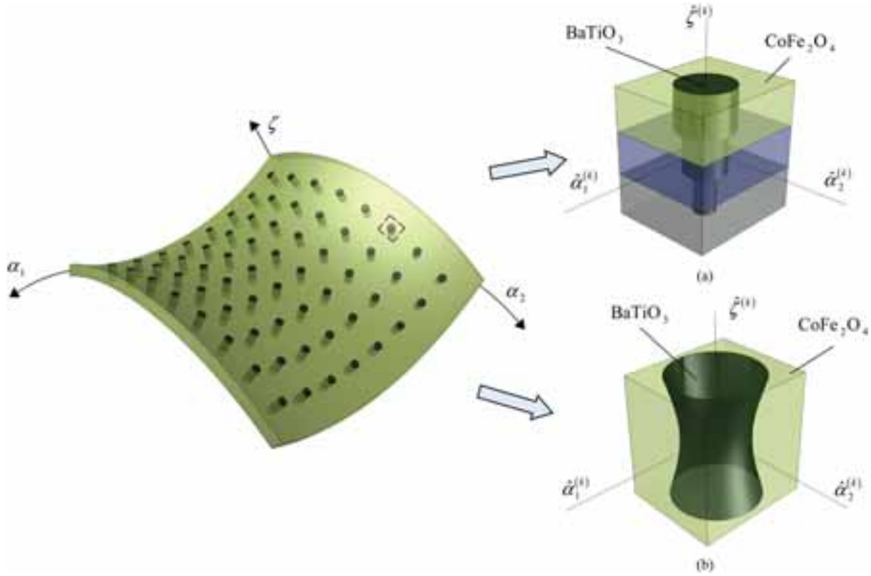

Fig. 2. Schematic representation of a doubly-curved shell panel with multifield properties. The unit cell of the constituent material is obtained from cylindrical fibers oriented along the thickness direction. (a) Layered configuration, (b) Smooth variation of the unit cell along the thickness direction.

$$\Delta\mu^{(k)} = \mu^{(k)} - \mu_0^{(k)} = R_g \mathrm{T}^{(k)} \log \Delta \mathrm{C}^{(k)} \tag{33}$$

In this way, the following definitions can be introduced:

$$\begin{aligned}
\xi_{11}^{(k)} &= \left(\frac{\partial \eta^{(k)}}{\partial \mathrm{T}}\right)_{\boldsymbol{\varepsilon},\Delta\mathrm{C}} = \left(\frac{\partial \eta^{(k)}}{\partial \mathrm{T}}\right)_{\boldsymbol{\varepsilon},\mathrm{C}_\infty} = \frac{\rho^{(k)} c^{(k)}}{\mathrm{T}_0} \\
\xi_{22}^{(k)} &= \left(\frac{\partial \mu^{(k)}}{\partial \mathrm{C}}\right)_{\boldsymbol{\varepsilon},\Delta\mathrm{T}} = \left(\frac{\partial \mu^{(k)}}{\partial \mathrm{C}}\right)_{\boldsymbol{\varepsilon},\mathrm{T}_0} = \frac{R_g \mathrm{T}_0}{\mathrm{C}_\infty^{(k)} - \mathrm{C}_0^{(k)}} \cong \frac{R_g \mathrm{T}_0}{\mathrm{C}_\infty^{(k)}} = \frac{R_g \mathrm{T}_0}{\rho^{(k)} M_\infty^{(k)}} \\
\xi_{12}^{(k)} &= \left(\frac{\partial \mu^{(k)}}{\partial \mathrm{T}}\right)_{\boldsymbol{\varepsilon},\Delta\mathrm{C}} = \left(\frac{\partial \mu^{(k)}}{\partial \mathrm{T}}\right)_{\boldsymbol{\varepsilon},\mathrm{C}_\infty} = \left(\frac{\partial \eta^{(k)}}{\partial \mathrm{C}}\right)_{\boldsymbol{\varepsilon},\Delta\mathrm{T}} = \left(\frac{\partial \eta^{(k)}}{\partial \mathrm{C}}\right)_{\boldsymbol{\varepsilon},\mathrm{T}_0} = \\
&= -\frac{\Delta\mu^{(k)}}{\mathrm{T}_0} = -R_g \log\left(\mathrm{C}_\infty^{(k)} - \mathrm{C}_0^{(k)}\right) \cong -R_g \log \mathrm{C}_\infty^{(k)} = -R_g \log\left(\rho^{(k)} M_\infty^{(k)}\right)
\end{aligned} \tag{34}$$

It should be noted that $\mathrm{C}_\infty^{(k)} = \rho^{(k)} M_\infty^{(k)}$ and $\mathrm{C}_0^{(k)} = 0$. Referring to Eq. (25), an arbitrary variation in the material properties along the thickness direction can be modelled using the following relations:

$$\begin{aligned}
\rho^{(k)}(\zeta) &= \rho_0^{(k)} f_k(\zeta) = \rho_0^{(k)} f_k(\widehat{z}_k) = \rho_0^{(k)}\left(1 + \delta^{(k)}\left(\delta_0^{(k)} + g(\widehat{z}_k)\right)\right) \\
\overline{\Gamma}_{ij}^{(k)}(\zeta) &= \overline{\Gamma}_{0ij}^{(k)} f_k(\zeta) = \overline{\Gamma}_{0ij}^{(k)} f_k(\widehat{z}_k) = \overline{\Gamma}_{0ij}^{(k)}\left(1 + \delta^{(k)}\left(\delta_0^{(k)} + g(\widehat{z}_k)\right)\right)
\end{aligned} \tag{35}$$

As can be seen, $\overline{\Gamma}_{0ij}^{(k)}$ and $\rho_0^{(k)}$ denote the reference values of the constitutive coefficients and density, respectively, while $g = g(\widehat{z}_k)$ represents the material grading function. Some typical expressions for g are collected in Table 1. In addition, $\delta^{(k)}$ and $\delta_0^{(k)}$ are the scaling and position parameters of the distribution, respectively. This variation is described using the coordinate $\widehat{z}_k \in [-1/2, 1/2]$, defined for each k-th layer as follows:

$$\widehat{z}_k = \frac{\zeta - \zeta_k}{\zeta_{k+1} - \zeta_k} - \frac{1}{2} = \frac{\zeta - \zeta_k}{h_k} - \frac{1}{2} \tag{36}$$

At this point, the 3D constitutive relationship in Eq. (22) is formulated within the ELW framework. For this purpose, the modified vector of secondary variables, denoted by $\overline{\chi}^{(k)}$, is conveniently introduced:

$$\overline{\chi}^{(k)} = \mathbf{B}\chi^{(k)} \quad \Leftrightarrow \quad \begin{bmatrix} \boldsymbol{\sigma}^{(k)} \\ \mathbf{D}^{(k)} \\ \eta^{(k)} \\ \mu^{(k)} \\ \overline{\mathbf{h}}^{(k)} \\ \overline{\mathbf{c}}^{(k)} \end{bmatrix} = \begin{bmatrix} \widehat{\mathbf{I}} & \mathbf{0} & \mathbf{0} & \mathbf{0} & \mathbf{0} & \mathbf{0} \\ \mathbf{0} & \mathbf{I} & \mathbf{0} & \mathbf{0} & \mathbf{0} & \mathbf{0} \\ \mathbf{0} & \mathbf{0} & 1 & 0 & \mathbf{0} & \mathbf{0} \\ \mathbf{0} & \mathbf{0} & 0 & 1 & \mathbf{0} & \mathbf{0} \\ \mathbf{0} & \mathbf{0} & \mathbf{0} & \mathbf{0} & \frac{1}{\mathrm{T}_0}\mathbf{I} & \frac{\mu_\infty}{\mathrm{T}_0}\mathbf{I} \\ \mathbf{0} & \mathbf{0} & \mathbf{0} & \mathbf{0} & \mathbf{0} & \frac{\mu_\infty}{\mathrm{C}_\infty}\mathbf{I} \end{bmatrix} \begin{bmatrix} \boldsymbol{\sigma}^{(k)} \\ \mathbf{D}^{(k)} \\ \eta^{(k)} \\ \mu^{(k)} \\ \mathbf{h}^{(k)} \\ \mathbf{c}^{(k)} \end{bmatrix} \tag{37}$$

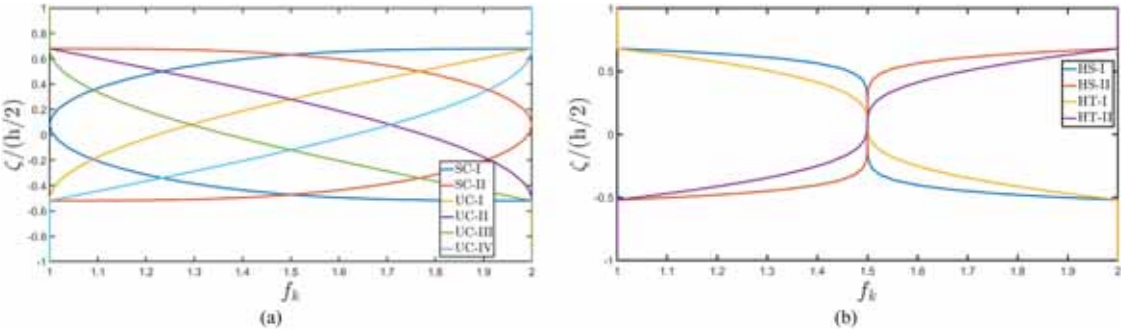

Fig. 3. Trigonometric (a) and hyperbolic (b) variations of the multifield material properties within the lamination scheme of shallow spherical shell. The first and third lamina are characterized by a null or uniform variation to ensure continuity of the profile.

Table 3
Through-the-thickness distribution of the displacement field components and the electric potential variation, of a sinusoidally loaded rectangular plate in E-D simulation employing higher-order ELW theories. A reference 3D FEM solution is provided for validation. The results are provided at $(0.25L_1, 0.75L_2)$.

	$U_1\ [\times 10^{-7}\mathrm{m}]$		$U_2\ [\times 10^{-7}\mathrm{m}]$		$U_3\ [\times 10^{-6}\mathrm{m}]$		$\Delta\phi\ [\times 10^{3}\mathrm{V}]$	
$\zeta\ [10^{-3}\mathrm{m}]$	3D FEM	ELDZL7	3D FEM	ELDZL7	3D FEM	ELDZL7	3D FEM	ELDZL7
-0.95	-4.06	-4.07	5.54	5.55	-4.30	-4.30	1.82	1.82
-0.88	-3.74	-3.75	5.10	5.12	-4.31	-4.31	1.81	1.81
-0.81	-3.42	-3.44	4.67	4.69	-4.31	-4.31	1.80	1.80
-0.70	-2.95	-2.95	4.02	4.02	-4.32	-4.32	1.78	1.78
-0.59	-2.47	-2.46	3.37	3.36	-4.33	-4.33	1.77	1.77
-0.52	-2.16	-2.16	2.94	2.94	-4.33	-4.33	1.76	1.76
-0.45	-1.84	-1.86	2.52	2.53	-4.33	-4.33	1.75	1.75
-0.45	-1.84	-1.86	2.52	2.53	-4.33	-4.33	1.75	1.75
-0.37	-1.49	-1.50	2.04	2.04	-4.34	-4.34	1.75	1.75
-0.25	-0.97	-0.97	1.32	1.32	-4.34	-4.34	1.74	1.74
-0.13	-0.44	-0.45	0.61	0.61	-4.34	-4.34	1.74	1.74
-0.05	-0.10	-0.10	0.13	0.14	-4.34	-4.34	1.73	1.73
-0.05	-0.10	-0.10	0.13	0.14	-4.34	-4.34	1.73	1.73
0.04	0.25	0.26	-0.34	-0.36	-4.35	-4.35	1.73	1.73
0.12	0.59	0.59	-0.81	-0.80	-4.35	-4.35	1.72	1.73
0.25	1.11	1.12	-1.52	-1.52	-4.35	-4.35	1.72	1.72
0.38	1.64	1.64	-2.23	-2.25	-4.35	-4.35	1.72	1.72
0.46	1.99	1.98	-2.71	-2.70	-4.35	-4.35	1.72	1.72
0.55	2.34	2.35	-3.19	-3.21	-4.35	-4.35	1.72	1.72
0.55	2.34	2.35	-3.19	-3.21	-4.35	-4.35	1.72	1.72
0.63	2.70	2.70	-3.68	-3.69	-4.35	-4.35	1.73	1.73
0.75	3.23	3.24	-4.41	-4.41	-4.35	-4.35	1.74	1.74
0.87	3.77	3.78	-5.14	-5.15	-4.34	-4.34	1.75	1.75
0.95	4.13	4.14	-5.63	-5.64	-4.34	-4.34	1.76	1.76

Here, the matrix $\mathbf{B}$ depends on the identity matrices $\widehat{\mathbf{I}}$ and $\mathbf{I}$ of sizes 6×6 and 3×3, respectively. The relation introduced in Eq. (37) is used to evaluate the virtual variation of the total free energy, denoted by Y, of the doubly-curved shell solid. If $\delta\overline{\boldsymbol{\pi}}^{(k)}$ is the virtual variation of the vector of the 3D primary variables, one obtains the following expression after some mathematical manipulations, which are detailed in Ref. [58]:

$$\begin{aligned}\delta Y &= \sum_{k=1}^{l}\int_{\alpha_1}\int_{\alpha_2}\int_{\zeta_k}^{\zeta_{k+1}}\left(\delta\overline{\boldsymbol{\pi}}^{(k)T}\overline{\boldsymbol{\chi}}^{(k)}\right)A_1A_2H_1H_2\,d\alpha_1 d\alpha_2 d\zeta \\ &= \sum_{\tau=0}^{N+1}\sum_{i=1}^{6}\int_{\alpha_1}\int_{\alpha_2}\left(\delta\overline{\boldsymbol{\pi}}^{(\tau)\alpha_i}\right)^T\overline{\mathbf{B}}\boldsymbol{\Sigma}^{(\tau)\alpha_i}A_1A_2\,d\alpha_1 d\alpha_2\end{aligned} \tag{38}$$

Note that, in the previous equation, the modified vector of secondary variables $\overline{\boldsymbol{\chi}}^{(k)}$ from Eq. (37) is expressed in terms of the multifield constitutive relationship in Eq. (22), incorporating the higher-order

Table 4
Through-the-thickness distribution of 3D strain components of a sinusoidally loaded rectangular plate in E-D simulation employing higher-order ELW theories. A reference 3D FEM solution is provided for validation. The results are provided at $(0.25L_1, 0.75L_2)$.

	$\varepsilon_1\ [\times 10^{-6}\mathrm{m/m}]$		$\varepsilon_2\ [\times 10^{-6}\mathrm{m/m}]$		$\gamma_{12}\ [\times 10^{-5}\mathrm{m/m}]$		$\gamma_{13}\ [\times 10^{-6}\mathrm{m/m}]$		$\gamma_{23}\ [\times 10^{-6}\mathrm{m/m}]$		$\varepsilon_3\ [\times 10^{-6}\mathrm{m/m}]$	
$\zeta\ [10^{-3}\mathrm{m}]$	3D FEM	ELDZL7	3D FEM	ELDZL7	3D FEM	ELDZL7	3D FEM	ELDZL7	3D FEM	ELDZL7	3D FEM	ELDZL7
-0.95	4.25	4.26	7.91	7.92	1.16	1.16	-0.02	-0.02	0.04	0.02	-7.91	-7.91
-0.88	3.92	3.93	7.29	7.31	1.07	1.07	-0.32	-0.31	0.44	0.42	-7.35	-7.37
-0.81	3.58	3.60	6.67	6.69	0.98	0.98	-0.59	-0.57	0.81	0.78	-6.80	-6.82
-0.70	3.09	3.09	5.74	5.74	0.84	0.84	-0.95	-0.94	1.30	1.29	-5.98	-5.98
-0.59	2.59	2.58	4.82	4.80	0.71	0.70	-1.25	-1.25	1.71	1.71	-5.16	-5.15
-0.52	2.26	2.26	4.20	4.20	0.62	0.62	-1.42	-1.41	1.94	1.92	-4.62	-4.62
-0.45	1.93	1.94	3.59	3.61	0.53	0.53	-1.56	-1.55	2.13	2.11	-4.08	-4.10
-0.45	1.93	1.94	3.59	3.61	0.53	0.53	-1.52	-1.51	2.08	2.05	-3.65	-3.66
-0.37	1.56	1.57	2.91	2.92	0.43	0.43	-1.63	-1.63	2.23	2.22	-3.16	-3.17
-0.25	1.01	1.02	1.89	1.89	0.28	0.28	-1.74	-1.74	2.38	2.38	-2.43	-2.43
-0.13	0.47	0.47	0.87	0.87	0.13	0.13	-1.80	-1.80	2.46	2.45	-1.70	-1.70
-0.05	0.10	0.11	0.19	0.20	0.03	0.03	-1.80	-1.80	2.46	2.45	-1.21	-1.22
-0.05	0.10	0.11	0.19	0.20	0.03	0.03	-5.37	-5.36	7.34	7.31	-3.16	-3.17
0.04	-0.26	-0.28	-0.48	-0.51	-0.07	-0.08	-5.30	-5.29	7.24	7.21	-2.64	-2.62
0.12	-0.62	-0.62	-1.16	-1.15	-0.17	-0.17	-5.20	-5.20	7.09	7.08	-2.13	-2.14
0.25	-1.17	-1.17	-2.17	-2.17	-0.32	-0.32	-4.98	-4.98	6.80	6.79	-1.35	-1.35
0.38	-1.72	-1.72	-3.19	-3.21	-0.47	-0.47	-4.70	-4.69	6.41	6.40	-0.56	-0.55
0.46	-2.08	-2.07	-3.87	-3.85	-0.57	-0.56	-4.47	-4.48	6.10	6.11	-0.04	-0.05
0.55	-2.45	-2.46	-4.56	-4.58	-0.67	-0.67	-4.20	-4.21	5.74	5.74	0.50	0.52
0.55	-2.45	-2.46	-4.56	-4.58	-0.67	-0.67	-1.43	-1.42	1.95	1.94	2.20	2.21
0.63	-2.82	-2.83	-5.25	-5.27	-0.77	-0.77	-1.22	-1.21	1.66	1.65	2.69	2.70
0.75	-3.38	-3.39	-6.29	-6.30	-0.92	-0.92	-0.84	-0.84	1.16	1.14	3.44	3.45
0.87	-3.95	-3.95	-7.34	-7.35	-1.08	-1.08	-0.41	-0.41	0.57	0.56	4.21	4.22
0.95	-4.33	-4.33	-8.05	-8.06	-1.18	-1.18	-0.09	-0.08	0.13	0.12	4.72	4.73

Table 5
Through-the-thickness distribution of 3D stress components of a sinusoidally loaded rectangular plate in E-D simulation employing higher-order ELW theories. A reference 3D FEM solution is provided for validation. The results are provided at $(0.25L_1, 0.75L_2)$.

	$\sigma_1\left[\times 10^6\,\mathrm{N/m^2}\right]$		$\sigma_2\left[\times 10^6\,\mathrm{N/m^2}\right]$		$\tau_{12}\left[\times 10^5\,\mathrm{N/m^2}\right]$		$\tau_{13}\left[\times 10^4\,\mathrm{N/m^2}\right]$		$\tau_{23}\left[\times 10^5\,\mathrm{N/m^2}\right]$		$\sigma_3\left[\times 10^5\,\mathrm{N/m^2}\right]$	
$\zeta\left[10^{-3}\mathrm{m}\right]$	3D FEM	ELDZL7	3D FEM	ELDZL7	3D FEM	ELDZL7	3D FEM	ELDZL7	3D FEM	ELDZL7	3D FEM	ELDZL7
-0.95	1.10	1.10	1.50	1.49	6.25	6.25	-0.03	0.00	0.01	0.00	-2.15	-2.15
-0.88	1.01	1.01	1.37	1.37	5.75	5.77	-1.44	-1.37	0.20	1.87	-2.15	-2.15
-0.81	0.91	0.92	1.24	1.25	5.26	5.29	-2.72	-2.63	0.37	3.59	-2.15	-2.16
-0.70	0.77	0.77	1.05	1.06	4.53	4.53	-4.40	-4.38	0.60	5.97	-2.17	-2.17
-0.59	0.62	0.61	0.86	0.85	3.80	3.79	-5.82	-5.82	0.80	7.94	-2.18	-2.19
-0.52	0.53	0.50	0.74	0.71	3.32	3.32	-6.62	-6.59	0.91	8.98	-2.20	-2.20
-0.45	0.43	0.39	0.61	0.57	2.84	2.85	-7.29	-7.22	1.00	9.85	-2.21	-2.21
-0.45	0.41	0.45	0.57	0.61	2.58	2.59	-7.29	-7.22	1.00	9.85	-2.21	-2.21
-0.37	0.31	0.34	0.44	0.47	2.09	2.09	-7.86	-7.82	1.07	10.66	-2.23	-2.23
-0.25	0.16	0.17	0.25	0.25	1.35	1.35	-8.43	-8.43	1.15	11.49	-2.26	-2.26
-0.13	0.02	0.00	0.06	0.04	0.62	0.63	-8.73	-8.70	1.19	11.86	-2.29	-2.29
-0.05	-0.08	-0.11	-0.07	-0.10	0.13	0.14	-8.74	-8.70	1.19	11.86	-2.31	-2.31
-0.05	-0.11	-0.10	-0.11	-0.10	0.05	0.05	-8.72	-8.70	1.19	11.86	-2.31	-2.31
0.04	-0.14	-0.14	-0.15	-0.15	-0.12	-0.13	-8.60	-8.58	1.17	11.70	-2.33	-2.34
0.12	-0.18	-0.18	-0.20	-0.19	-0.29	-0.29	-8.43	-8.42	1.15	11.49	-2.36	-2.36
0.25	-0.23	-0.23	-0.26	-0.26	-0.54	-0.54	-8.07	-8.07	1.10	11.01	-2.39	-2.39
0.38	-0.28	-0.28	-0.33	-0.33	-0.80	-0.80	-7.61	-7.60	1.04	10.36	-2.42	-2.42
0.46	-0.32	-0.31	-0.38	-0.37	-0.97	-0.97	-7.23	-7.26	0.99	9.89	-2.44	-2.44
0.55	-0.35	-0.34	-0.42	-0.41	-1.14	-1.15	-6.80	-6.82	0.93	9.30	-2.46	-2.46
0.55	-0.76	-0.79	-0.96	-1.00	-3.27	-3.29	-6.83	-6.82	0.93	9.30	-2.46	-2.46
0.63	-0.86	-0.87	-1.09	-1.11	-3.77	-3.78	-5.75	-5.72	0.79	7.80	-2.47	-2.47
0.75	-1.00	-1.00	-1.29	-1.29	-4.51	-4.52	-3.86	-3.83	0.53	5.22	-2.49	-2.49
0.87	-1.15	-1.15	-1.48	-1.48	-5.27	-5.28	-1.68	-1.64	0.23	2.24	-2.50	-2.50
0.95	-1.25	-1.27	-1.62	-1.63	-5.77	-5.78	-0.04	0.00	0.01	0.00	-2.50	-2.50

Table 6
Through-the-thickness distribution of 3D electric field components and of the electric flux components of a sinusoidally loaded rectangular plate in E-D simulation employing higher-order ELW theories. A reference 3D FEM solution is provided for validation. The results are provided at $(0.25L_1, 0.75L_2)$.

	$\mathscr{E}_1\left[\times 10^4\mathrm{V/m}\right]$		$\mathscr{E}_2\left[\times 10^4\mathrm{V/m}\right]$		$\mathscr{E}_3\left[\times 10^4\mathrm{V/m}\right]$		$\mathscr{D}_1\left[\times 10^{-6}\mathrm{C/m^2}\right]$		$\mathscr{D}_2\left[\times 10^{-6}\mathrm{C/m^2}\right]$		$\mathscr{D}_3\left[\times 10^{-6}\mathrm{C/m^2}\right]$	
$\zeta\left[10^{-3}\mathrm{m}\right]$	3D FEM	ELDZL7	3D FEM	ELDZL7	3D FEM	ELDZL7	3D FEM	ELDZL7	3D FEM	ELDZL7	3D FEM	ELDZL7
-0.95	-1.91	-1.91	2.60	2.60	1.77	1.77	-2.28	-2.29	3.11	3.12	3.99	4.00
-0.88	-1.89	-1.90	2.58	2.58	1.65	1.65	-2.27	-2.27	3.10	3.10	3.94	3.95
-0.81	-1.88	-1.88	2.57	2.57	1.53	1.53	-2.27	-2.26	3.10	3.09	3.90	3.90
-0.70	-1.87	-1.87	2.55	2.55	1.35	1.35	-2.26	-2.26	3.09	3.09	3.83	3.83
-0.59	-1.85	-1.85	2.53	2.53	1.17	1.17	-2.26	-2.27	3.08	3.09	3.75	3.76
-0.52	-1.84	-1.84	2.51	2.52	1.06	1.06	-2.25	-2.27	3.07	3.10	3.70	3.71
-0.45	-1.84	-1.84	2.50	2.50	0.94	0.94	-2.25	-2.28	3.07	3.11	3.66	3.66
-0.45	-1.84	-1.84	2.50	2.50	0.79	0.79	-6.08	-5.86	8.30	7.99	3.66	3.66
-0.37	-1.83	-1.83	2.50	2.50	0.67	0.68	-6.09	-5.95	8.31	8.12	3.51	3.51
-0.25	-1.82	-1.82	2.49	2.49	0.50	0.50	-6.09	-6.08	8.31	8.30	3.29	3.30
-0.13	-1.82	-1.82	2.48	2.48	0.33	0.34	-6.09	-6.20	8.31	8.45	3.08	3.09
-0.05	-1.82	-1.82	2.48	2.48	0.22	0.22	-6.08	-6.25	8.30	8.53	2.93	2.93
-0.05	-1.82	-1.82	2.48	2.48	0.62	0.62	-1.30	-1.28	1.77	1.74	2.93	2.93
0.04	-1.81	-1.81	2.47	2.47	0.50	0.49	-1.29	-1.28	1.76	1.75	2.90	2.89
0.12	-1.81	-1.81	2.46	2.46	0.38	0.38	-1.29	-1.28	1.76	1.75	2.87	2.87
0.25	-1.80	-1.80	2.46	2.46	0.20	0.20	-1.28	-1.27	1.74	1.74	2.82	2.82
0.38	-1.80	-1.80	2.46	2.46	0.02	0.02	-1.27	-1.26	1.73	1.72	2.77	2.77
0.46	-1.80	-1.80	2.46	2.46	-0.10	-0.10	-1.26	-1.25	1.72	1.70	2.74	2.74
0.55	-1.80	-1.80	2.46	2.46	-0.22	-0.23	-1.25	-1.23	1.71	1.68	2.70	2.70
0.55	-1.80	-1.80	2.46	2.46	-0.56	-0.56	-5.96	-6.10	8.13	8.32	2.70	2.70
0.63	-1.81	-1.81	2.47	2.47	-0.68	-0.68	-5.92	-5.99	8.08	8.16	2.56	2.56
0.75	-1.82	-1.82	2.48	2.48	-0.85	-0.85	-5.87	-5.84	8.00	7.97	2.35	2.35
0.87	-1.83	-1.83	2.49	2.50	-1.03	-1.03	-5.80	-5.78	7.92	7.89	2.14	2.14
0.95	-1.84	-1.84	2.51	2.51	-1.15	-1.15	-5.76	-5.84	7.85	7.96	2.00	2.00

generalized definition equations introduced in Eq. (18). This approach allows for defining the vector of generalized secondary variables, denoted by $\mathbf{\Sigma}^{(\tau)\alpha_i} = \left[\mathbf{S}^{(\tau)\alpha_i T} \quad \mathbf{D}^{(\tau)\alpha_i T} \quad E^{(\tau)\alpha_i} \quad M^{(\tau)\alpha_i} \quad \mathbf{H}^{(\tau)\alpha_i T} \quad \mathbf{C}^{(\tau)\alpha_i T}\right]^T$, for each τ-th kinematic expansion order. The matrix $\overline{\mathbf{B}}$ is then defined as follows in terms of the identity matrices $\breve{\mathbf{I}}$ and $\mathbf{I}$ of sizes 9×9 and 3×3, respectively:

Table 7
Through-the-thickness distribution of the displacement field components and of the absolute temperature variation of a sinusoidally loaded rectangular plate in T-D simulation, employing higher-order ELW theories. A reference 3D FEM solution is provided for validation. The results are provided at $(0.25L_1, 0.75L_2)$.

	$U_1\ [\times 10^{-6}\mathrm{m}]$		$U_2\ [\times 10^{-6}\mathrm{m}]$		$U_3\ [\times 10^{-6}\mathrm{m}]$		ΔT [K]	
$\zeta\ [10^{-3}\mathrm{m}]$	3D FEM	ELDZL7	3D FEM	ELDZL7	3D FEM	ELDZL7	3D FEM	ELDZL7
-0.95	-1.86	-1.86	2.53	2.53	-4.03	-4.04	2.59	2.59
-0.88	-1.83	-1.83	2.49	2.50	-4.02	-4.03	2.59	2.59
-0.81	-1.80	-1.80	2.45	2.45	-4.01	-4.02	2.59	2.60
-0.70	-1.75	-1.75	2.39	2.39	-4.00	-4.00	2.60	2.60
-0.59	-1.71	-1.71	2.33	2.33	-3.98	-3.98	2.61	2.61
-0.52	-1.68	-1.68	2.29	2.29	-3.97	-3.97	2.61	2.62
-0.45	-1.65	-1.66	2.25	2.26	-3.95	-3.96	2.62	2.63
-0.45	-1.65	-1.66	2.25	2.26	-3.95	-3.96	2.62	2.63
-0.37	-1.62	-1.62	2.21	2.21	-3.94	-3.94	2.63	2.63
-0.25	-1.58	-1.58	2.15	2.15	-3.90	-3.91	2.64	2.64
-0.13	-1.53	-1.53	2.09	2.09	-3.87	-3.88	2.65	2.65
-0.05	-1.50	-1.50	2.04	2.05	-3.85	-3.85	2.66	2.67
-0.05	-1.50	-1.50	2.04	2.05	-3.85	-3.85	2.66	2.67
0.04	-1.47	-1.47	2.01	2.00	-3.83	-3.83	2.69	2.70
0.12	-1.44	-1.44	1.97	1.97	-3.81	-3.81	2.73	2.73
0.25	-1.40	-1.40	1.91	1.91	-3.78	-3.78	2.77	2.78
0.38	-1.36	-1.36	1.85	1.85	-3.74	-3.75	2.82	2.83
0.46	-1.33	-1.33	1.81	1.82	-3.72	-3.73	2.86	2.85
0.55	-1.30	-1.30	1.77	1.77	-3.70	-3.70	2.89	2.88
0.55	-1.30	-1.30	1.77	1.77	-3.70	-3.70	2.89	2.88
0.63	-1.27	-1.27	1.73	1.73	-3.67	-3.67	2.91	2.90
0.75	-1.23	-1.23	1.67	1.67	-3.62	-3.63	2.92	2.92
0.87	-1.18	-1.18	1.61	1.61	-3.58	-3.58	2.94	2.94
0.95	-1.15	-1.15	1.57	1.57	-3.55	-3.55	2.96	2.95

Table 8
Through-the-thickness distribution of 3D strain components for a sinusoidally loaded rectangular plate in T-D simulation employing higher-order ELW theories. A reference 3D FEM solution is provided for validation. The results are provided at $(0.25L_1, 0.75L_2)$.

	$\varepsilon_1\ [\times 10^{-6}\mathrm{m/m}]$		$\varepsilon_2\ [\times 10^{-6}\mathrm{m/m}]$		$\gamma_{12}\ [\times 10^{-5}\mathrm{m/m}]$		$\gamma_{13}\ [\times 10^{-5}\mathrm{m/m}]$		$\gamma_{23}\ [\times 10^{-5}\mathrm{m/m}]$		$\varepsilon_3\ [\times 10^{-6}\mathrm{m/m}]$	
$\zeta\ [10^{-3}\mathrm{m}]$	3D FEM	ELDZL7	3D FEM	ELDZL7	3D FEM	ELDZL7	3D FEM	ELDZL7	3D FEM	ELDZL7	3D FEM	ELDZL7
-0.95	1.94	1.95	3.62	3.62	5.30	5.31	-0.01	0.00	0.01	0.00	1.34	1.34
-0.88	1.91	1.92	3.56	3.56	5.22	5.22	-0.43	-0.41	0.59	0.56	1.40	1.40
-0.81	1.88	1.88	3.50	3.51	-0.18	5.14	2.51	-0.79	-4.03	1.08	1.46	1.46
-0.70	1.84	1.84	3.41	3.42	-0.18	5.01	2.45	-1.35	-4.01	1.84	1.55	1.55
-0.59	1.79	1.79	3.33	3.33	-0.18	4.88	2.39	-1.85	-4.00	2.52	1.64	1.65
-0.52	1.76	1.76	3.28	3.28	-0.17	4.81	2.35	-2.14	-3.98	2.92	1.70	1.70
-0.45	1.73	1.73	3.22	3.22	-0.17	4.73	2.31	-2.41	-3.97	3.28	1.76	1.77
-0.45	1.73	1.73	3.22	3.22	-0.17	4.73	2.29	-2.24	-3.97	3.05	2.43	2.44
-0.37	1.70	1.70	3.16	3.16	-0.17	4.63	2.25	-2.28	-3.95	3.11	2.49	2.50
-0.25	1.65	1.65	3.07	3.07	-0.16	4.50	2.19	-2.30	-3.93	3.14	2.59	2.59
-0.13	1.60	1.60	2.98	2.98	-0.16	4.37	2.13	-2.28	-3.89	3.11	2.69	2.69
-0.05	1.57	1.57	2.92	2.92	-0.15	4.29	2.09	-2.23	-3.87	3.05	2.76	2.76
-0.05	1.57	1.57	2.92	2.92	-0.15	4.29	2.07	-6.95	-3.86	9.47	2.22	2.23
0.04	1.54	1.54	2.86	2.86	-0.15	4.20	2.02	-6.89	-3.84	9.39	2.33	2.34
0.12	1.51	1.51	2.81	2.81	-0.15	4.12	1.99	-6.80	-3.82	9.27	2.43	2.43
0.25	1.47	1.47	2.73	2.73	-0.14	4.00	1.93	-6.59	-3.79	8.99	2.59	2.59
0.38	1.42	1.42	2.64	2.64	-0.14	3.87	1.87	-6.30	-3.76	8.59	2.75	2.76
0.46	1.39	1.40	2.59	2.59	-0.13	3.80	1.83	-6.08	-3.73	8.30	2.86	2.85
0.55	1.36	1.36	2.53	2.53	-0.13	3.71	1.79	-5.80	-3.71	7.91	2.97	2.96
0.55	1.36	1.36	2.53	2.53	-0.13	3.71	1.77	-1.87	-3.70	2.54	3.52	3.50
0.63	1.33	1.33	2.48	2.47	3.63	3.63	-1.56	-1.54	2.13	2.10	3.59	3.58
0.75	1.29	1.28	2.39	2.39	3.51	3.50	-1.02	-1.01	1.40	1.38	3.70	3.69
0.87	1.24	1.24	2.30	2.30	3.38	3.38	-0.43	-0.43	0.60	0.58	3.81	3.79
0.95	1.21	1.21	2.25	2.24	3.29	3.29	-0.01	0.00	0.01	0.00	3.88	3.87

$$\overline{\mathbf{B}} = \begin{bmatrix} \breve{\mathbf{I}} & \mathbf{0} & \mathbf{0} & \mathbf{0} & \mathbf{0} & \mathbf{0} \\ \mathbf{0} & \mathbf{I} & \mathbf{0} & \mathbf{0} & \mathbf{0} & \mathbf{0} \\ \mathbf{0} & \mathbf{0} & 1 & 0 & \mathbf{0} & \mathbf{0} \\ \mathbf{0} & \mathbf{0} & 0 & 1 & \mathbf{0} & \mathbf{0} \\ \mathbf{0} & \mathbf{0} & \mathbf{0} & \mathbf{0} & \frac{1}{\mathrm{T}_0}\mathbf{I} & \frac{\mu_\infty}{\mathrm{T}_0}\mathbf{I} \\ \mathbf{0} & \mathbf{0} & \mathbf{0} & \mathbf{0} & \mathbf{0} & \frac{\mu_\infty}{\mathrm{C}_\infty}\mathbf{I} \end{bmatrix} \tag{39}$$

The sub-vectors within the vector $\boldsymbol{\Sigma}^{(\tau)\alpha_i}$ in Eq. (38) are expressed in detailed form as $\mathbf{S}^{(\tau)\alpha_i} = \left[N_1^{(\tau)\alpha_i}\ \ N_2^{(\tau)\alpha_i}\ \ N_{12}^{(\tau)\alpha_i}\ \ N_{21}^{(\tau)\alpha_i}\ \ T_1^{(\tau)\alpha_i}\ \ T_2^{(\tau)\alpha_i}\ \ P_1^{(\tau)\alpha_i} P_2^{(\tau)\alpha_i} S_3^{(\tau)\alpha_i}\right]^T$, $\mathbf{D}^{(\tau)\alpha_i} = \left[D_1^{(\tau)\alpha_i}\ \ D_2^{(\tau)\alpha_i}\ \ D_3^{(\tau)\alpha_i}\right]^T$, $\mathbf{H}^{(\tau)\alpha_i} = \left[H_1^{(\tau)\alpha_i}\ \ H_2^{(\tau)\alpha_i}\ \ H_3^{(\tau)\alpha_i}\right]^T$ and $\mathbf{C}^{(\tau)\alpha_i} = \left[C_1^{(\tau)\alpha_i}\ \ C_2^{(\tau)\alpha_i}\ \ C_3^{(\tau)\alpha_i}\right]^T$. The elements of the vector $\boldsymbol{\Sigma}^{(\tau)\alpha_i}$, are evaluated using the relations reported in Appendix I, which are derived through the procedure extensively outlined in Ref. [58]. From Eq. (38), the generalized expression of the multifield constitutive relationship for the entire laminate can be derived, considering the generalized description of unknown field variables through the unified

Table 9
Through-the-thickness distribution of 3D stress components of a sinusoidally loaded rectangular plate in T-D simulation employing higher-order ELW theories. A reference 3D FEM solution is provided for validation. The results are provided at $(0.25L_1, 0.75L_2)$.

	σ_1 $[\times 10^6\,\mathrm{N/m^2}]$		σ_2 $[\times 10^6\,\mathrm{N/m^2}]$		τ_{12} $[\times 10^6\,\mathrm{N/m^2}]$		τ_{13} $[\times 10^5\,\mathrm{N/m^2}]$		τ_{23} $[\times 10^5\,\mathrm{N/m^2}]$		σ_3 $[\times 10^5\,\mathrm{N/m^2}]$	
ζ $[10^{-3}\mathrm{m}]$	3D FEM	ELDZL7	3D FEM	ELDZL7	3D FEM	ELDZL7	3D FEM	ELDZL7	3D FEM	ELDZL7	3D FEM	ELDZL7
-0.95	-1.18	-1.16	0.62	0.64	2.85	2.86	0.00	0.00	0.01	0.00	-2.02	-2.02
-0.88	-1.27	-1.28	0.50	0.49	2.81	2.81	-0.20	-0.19	0.28	0.26	-2.03	-2.02
-0.81	-1.37	-1.38	0.37	0.36	2.76	2.77	-0.39	-0.37	0.53	0.51	-2.04	-2.03
-0.70	-1.51	-1.52	0.18	0.18	2.70	2.70	-0.64	-0.64	0.88	0.87	-2.07	-2.04
-0.59	-1.66	-1.65	0.00	0.01	2.63	2.63	-0.87	-0.87	1.19	1.19	-2.09	-2.07
-0.52	-1.75	-1.73	-0.12	-0.10	2.59	2.59	-1.01	-1.01	1.38	1.38	-2.11	-2.09
-0.45	-1.85	-1.82	-0.25	-0.22	2.54	2.55	-1.14	-1.14	1.55	1.55	-2.14	-2.11
-0.45	-2.76	-2.84	-1.30	-1.39	2.31	2.31	-1.14	-1.14	1.55	1.55	-2.14	-2.11
-0.37	-2.86	-2.91	-1.43	-1.47	2.27	2.27	-1.16	-1.16	1.59	1.58	-2.17	-2.14
-0.25	-3.00	-3.00	-1.62	-1.61	2.20	2.20	-1.18	-1.17	1.61	1.59	-2.21	-2.18
-0.13	-3.16	-3.11	-1.81	-1.76	2.14	2.14	-1.16	-1.16	1.59	1.58	-2.24	-2.22
-0.05	-3.26	-3.19	-1.94	-1.87	2.09	2.10	-1.14	-1.13	1.55	1.55	-2.27	-2.25
-0.05	-1.04	-1.07	-0.58	-0.61	0.73	0.73	-1.14	-1.13	1.55	1.55	-2.26	-2.25
0.04	-1.09	-1.12	-0.64	-0.67	0.72	0.72	-1.13	-1.12	1.54	1.53	-2.29	-2.28
0.12	-1.14	-1.16	-0.70	-0.72	0.70	0.70	-1.12	-1.11	1.52	1.51	-2.32	-2.31
0.25	-1.22	-1.23	-0.79	-0.80	0.68	0.68	-1.08	-1.08	1.48	1.47	-2.36	-2.35
0.38	-1.31	-1.30	-0.89	-0.88	0.66	0.66	-1.04	-1.03	1.41	1.40	-2.40	-2.39
0.46	-1.36	-1.34	-0.95	-0.93	0.65	0.65	-1.00	-0.99	1.36	1.36	-2.43	-2.41
0.55	-1.42	-1.39	-1.02	-0.99	0.64	0.63	-0.95	-0.95	1.30	1.29	-2.46	-2.44
0.55	-4.35	-4.35	-3.20	-3.20	1.82	1.82	-0.95	-0.95	1.30	1.29	-2.46	-2.44
0.63	-4.45	-4.45	-3.33	-3.33	1.78	1.78	-0.79	-0.78	1.08	1.07	-2.49	-2.46
0.75	-4.61	-4.60	-3.53	-3.52	1.71	1.71	-0.52	-0.52	0.71	0.70	-2.51	-2.48
0.87	-4.77	-4.75	-3.73	-3.71	1.65	1.65	-0.22	-0.22	0.30	0.30	-2.51	-2.50
0.95	-4.88	-4.86	-3.86	-3.85	1.61	1.61	0.00	0.00	0.01	0.00	-2.51	-2.50

Table 10
Through-the-thickness distribution of the temperature gradient components and of the thermal flux components of a sinusoidally loaded rectangular plate in T-D simulation employing higher-order ELW theories. A reference 3D FEM solution is provided for validation. The results are provided at $(0.25L_1, 0.75L_2)$.

	θ_1 $[\times 10^1\,\mathrm{K/m}]$		θ_2 $[\times 10^1\,\mathrm{K/m}]$		θ_3 $[\times 10^1\,\mathrm{K/m}]$		h_1 $[\times 10^1\,\mathrm{J/m^2}]$		h_2 $[\times 10^2\,\mathrm{J/m^2}]$		h_3 $[\times 10^1\,\mathrm{J/m^2}]$	
ζ $[10^{-3}\mathrm{m}]$	3D FEM	ELDZL7	3D FEM	ELDZL7	3D FEM	ELDZL7	3D FEM	ELDZL7	3D FEM	ELDZL7	3D FEM	ELDZL7
-0.95	-2.71	-2.71	3.69	3.70	-0.47	-0.44	-8.21	-8.22	1.12	1.12	-1.44	-1.35
-0.88	-2.71	-2.72	3.70	3.71	-0.50	-0.50	-8.22	-8.23	1.12	1.12	-1.53	-1.52
-0.81	-2.72	-2.72	3.70	3.71	-0.56	-0.55	-8.23	-8.24	1.12	1.12	-1.70	-1.70
-0.70	-2.72	-2.73	3.71	3.72	-0.64	-0.64	-8.25	-8.26	1.12	1.13	-1.97	-1.97
-0.59	-2.73	-2.73	3.72	3.73	-0.73	-0.73	-8.27	-8.29	1.13	1.13	-2.23	-2.24
-0.52	-2.74	-2.74	3.73	3.74	-0.79	-0.79	-8.29	-8.31	1.13	1.13	-2.41	-2.41
-0.45	-2.74	-2.75	3.74	3.75	-0.82	-0.85	-8.31	-8.34	1.13	1.14	-2.50	-2.59
-0.45	-2.74	-2.75	3.74	3.75	-0.96	-0.93	-7.51	-7.54	1.02	1.03	-2.68	-2.59
-0.37	-2.75	-2.75	3.75	3.76	-1.00	-1.00	-7.54	-7.55	1.03	1.03	-2.77	-2.77
-0.25	-2.76	-2.76	3.77	3.77	-1.09	-1.09	-7.57	-7.57	1.03	1.03	-3.04	-3.04
-0.13	-2.78	-2.78	3.79	3.79	-1.19	-1.19	-7.61	-7.62	1.04	1.04	-3.31	-3.31
-0.05	-2.79	-2.79	3.80	3.81	-1.22	-1.26	-7.64	-7.66	1.04	1.04	-3.40	-3.50
-0.05	-0.98	-2.79	1.33	3.81	-1.27	-3.59	-2.67	-2.68	0.36	0.37	-3.53	-3.50
0.04	-0.99	-2.83	1.35	3.85	-1.28	-3.67	-2.71	-2.71	0.37	0.37	-3.56	-3.57
0.12	-2.85	-2.86	3.89	3.90	-3.73	-3.73	-2.74	-2.74	0.37	0.37	-3.63	-3.63
0.25	-2.91	-2.91	3.96	3.96	-3.84	-3.84	-2.79	-2.79	0.38	0.38	-3.74	-3.74
0.38	-2.96	-2.96	4.03	4.03	-3.95	-3.96	-2.84	-2.84	0.39	0.39	-3.85	-3.85
0.46	-2.99	-2.99	4.08	4.08	-4.03	-4.03	-2.87	-2.86	0.39	0.39	-3.92	-3.92
0.55	-3.03	-3.02	4.13	4.12	-4.07	-4.11	-2.91	-2.90	0.40	0.40	-3.96	-4.00
0.55	-3.03	-3.02	4.13	4.12	-1.47	-1.44	-8.30	-8.27	1.13	1.13	-4.10	-4.00
0.63	-3.04	-3.04	4.15	4.14	-1.51	-1.51	-8.33	-8.32	1.14	1.13	-4.20	-4.19
0.75	-3.06	-3.06	4.17	4.17	-1.62	-1.62	-8.39	-8.38	1.14	1.14	-4.50	-4.50
0.87	-3.08	-3.08	4.20	4.19	-1.73	-1.73	-8.45	-8.43	1.15	1.15	-4.80	-4.80
0.95	-3.10	-3.09	4.22	4.22	-1.76	-1.80	-8.49	-8.47	1.16	1.15	-4.90	-5.00

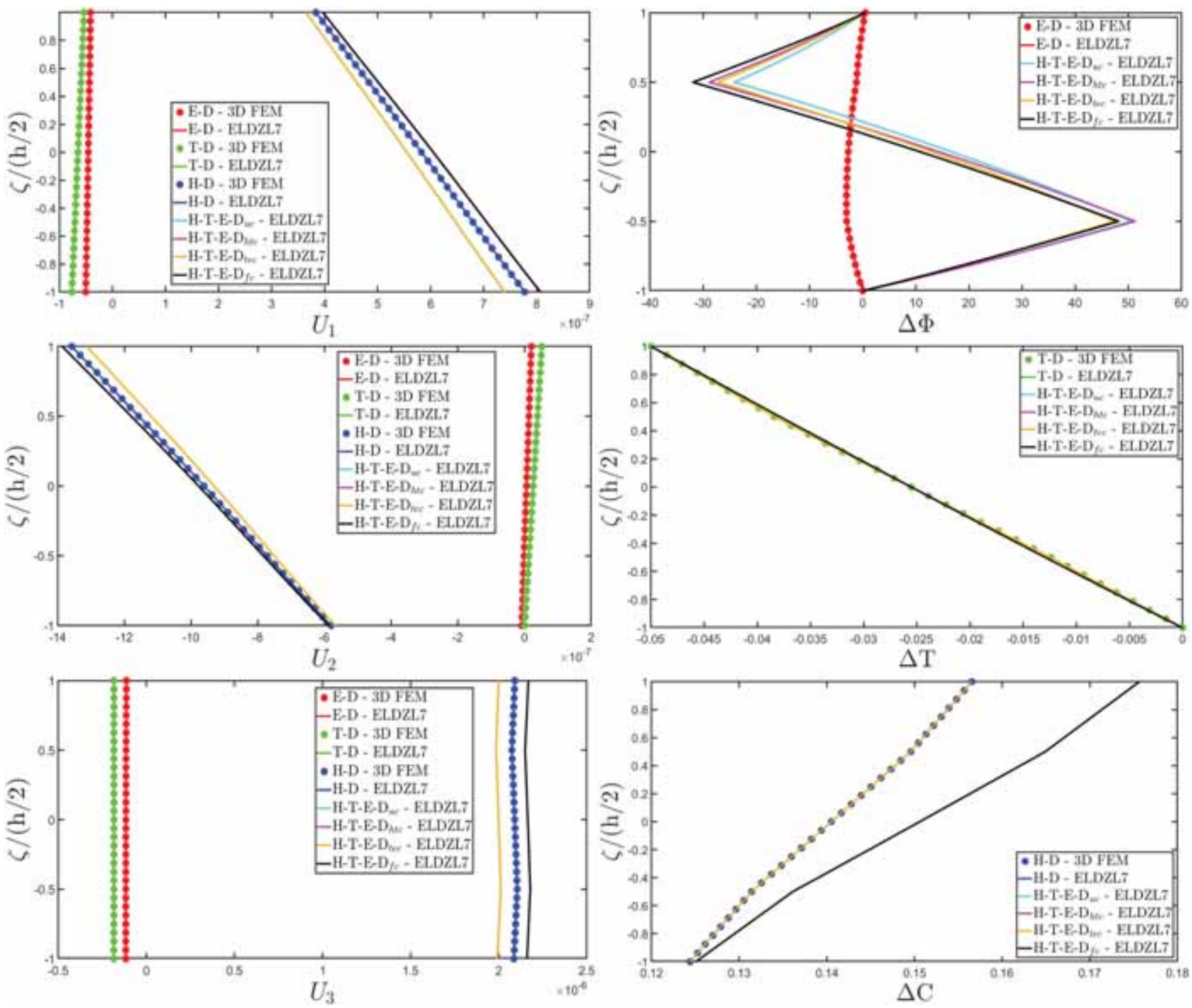

Fig. 4. Representation of the distributions along the thickness direction of the hygro-thermo-electro-mechanical configuration variables of a cylindrical panel-1 for the point located at $(s_1, s_2) = (0.25L_1, 0.25L_2)$. Comparison against 3D FEM results and effect of multifield coupling.

formulation in Eq. (5). This is achieved by introducing the generalized multifield constitutive matrix $\mathbf{A}^{(\tau\eta)\alpha_i\alpha_j}$, associated with any $\tau, \eta = 0, ..., N+1$ and $i, j = 1, ..., 6$. The resulting relation is reported below [58]:

$$\boldsymbol{\Sigma}^{(\tau)\alpha_i} = \sum_{\eta=0}^{N+1}\sum_{j=1}^{6}\left(\sum_{k=1}^{l}\int_{\zeta_k}^{\zeta_{k+1}}\left(\mathbf{Z}^{(k\tau)\alpha_i}\right)^T\overline{\boldsymbol{\Gamma}}^{(k)}\mathbf{Z}^{(k\eta)\alpha_j}H_1H_2\,d\zeta\right)\boldsymbol{\pi}^{(\eta)\alpha_j} = \sum_{\eta=0}^{N+1}\sum_{j=1}^{6}\mathbf{A}^{(\tau\eta)\alpha_i\alpha_j}\boldsymbol{\pi}^{(\eta)\alpha_j} \tag{40}$$

The generalized constitutive matrix $\mathbf{A}^{(\tau\eta)\alpha_i\alpha_j}$ takes the following extended form:

$$\mathbf{A}^{(\tau\eta)\alpha_i\alpha_j} = \begin{bmatrix} \mathbf{A}_{\varepsilon\varepsilon}^{(\tau\eta)\alpha_i\alpha_j} & \mathbf{A}_{\varepsilon\phi}^{(\tau\eta)\alpha_i\alpha_j} & \mathbf{A}_{\varepsilon\mathrm{T}}^{(\tau\eta)\alpha_i\alpha_j} & \mathbf{A}_{\varepsilon\mathrm{C}}^{(\tau\eta)\alpha_i\alpha_j} & \mathbf{0} & \mathbf{0} \\ \mathbf{A}_{\phi\varepsilon}^{(\tau\eta)\alpha_i\alpha_j} & \mathbf{A}_{\phi\phi}^{(\tau\eta)\alpha_i\alpha_j} & \mathbf{A}_{\phi\mathrm{T}}^{(\tau\eta)\alpha_i\alpha_j} & \mathbf{A}_{\phi\mathrm{C}}^{(\tau\eta)\alpha_i\alpha_j} & \mathbf{0} & \mathbf{0} \\ \mathbf{A}_{\mathrm{T}\varepsilon}^{(\tau\eta)\alpha_i\alpha_j} & \mathbf{A}_{\mathrm{T}\phi}^{(\tau\eta)\alpha_i\alpha_j} & \mathbf{A}_{\mathrm{TT}}^{(\tau\eta)\alpha_i\alpha_j} & \mathbf{A}_{\mathrm{TC}}^{(\tau\eta)\alpha_i\alpha_j} & \mathbf{0} & \mathbf{0} \\ \mathbf{A}_{\mathrm{C}\varepsilon}^{(\tau\eta)\alpha_i\alpha_j} & \mathbf{A}_{\mathrm{C}\phi}^{(\tau\eta)\alpha_i\alpha_j} & \mathbf{A}_{\mathrm{CT}}^{(\tau\eta)\alpha_i\alpha_j} & \mathbf{A}_{\mathrm{CC}}^{(\tau\eta)\alpha_i\alpha_j} & \mathbf{0} & \mathbf{0} \\ \mathbf{0} & \mathbf{0} & \mathbf{0} & \mathbf{0} & \mathbf{A}_{\theta\theta}^{(\tau\eta)\alpha_i\alpha_j} & \mathbf{A}_{\theta\lambda}^{(\tau\eta)\alpha_i\alpha_j} \\ \mathbf{0} & \mathbf{0} & \mathbf{0} & \mathbf{0} & \mathbf{A}_{\lambda\theta}^{(\tau\eta)\alpha_i\alpha_j} & \mathbf{A}_{\lambda\lambda}^{(\tau\eta)\alpha_i\alpha_j} \end{bmatrix} \tag{41}$$

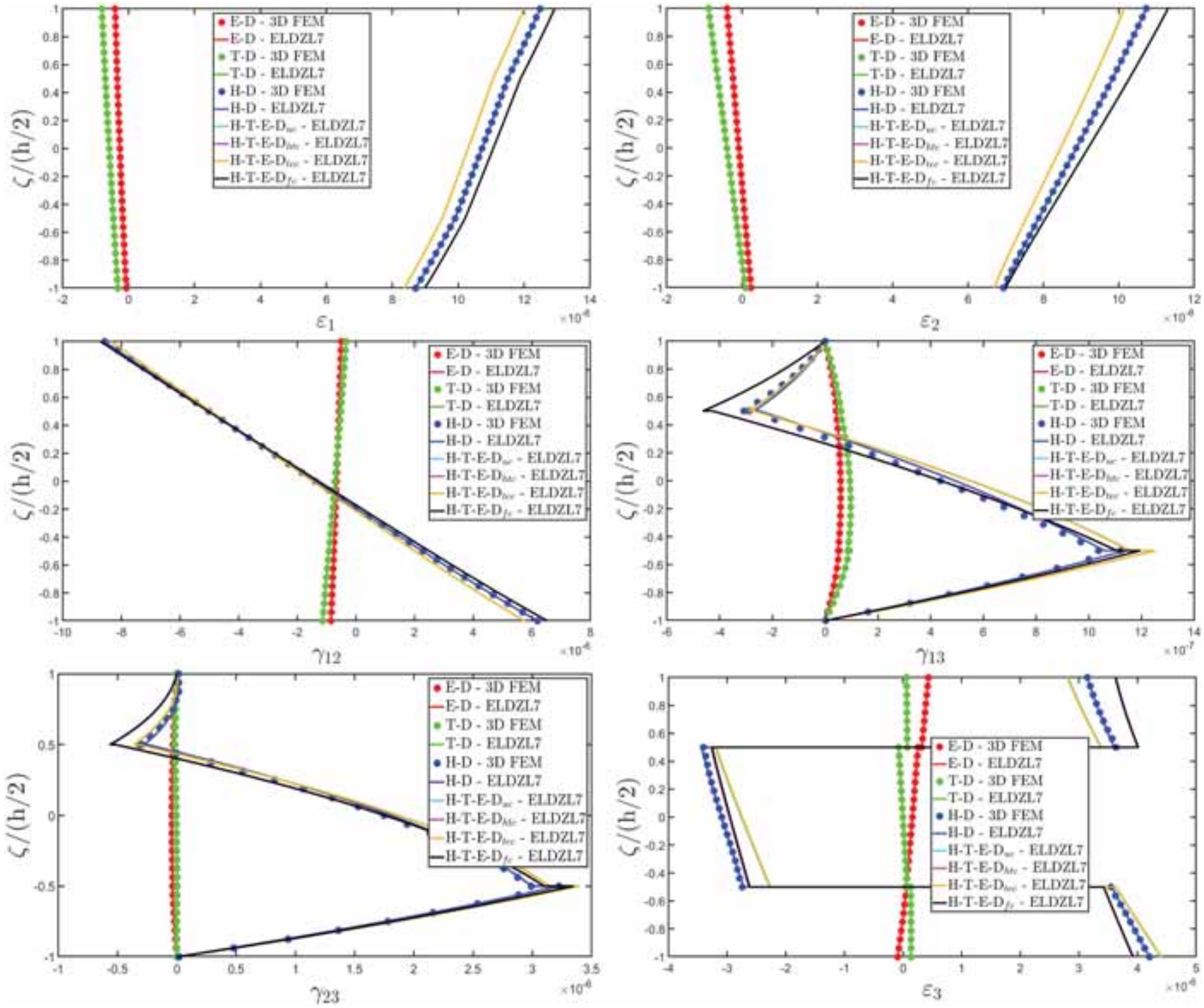

Fig. 5. Representation of the distributions along the thickness direction of 3D strain components of a cylindrical panel-1 for the point located at $(s_1, s_2) = (0.25L_1, 0.25L_2)$. Comparison against 3D FEM results and effect of multifield coupling.

The arbitrary element of the matrix $\mathbf{A}^{(\tau\eta)\alpha_i\alpha_j}$ in Eq. (40) is denoted by $A_{rsnm\ (pq)}^{(\tau\eta)[fg]\ \alpha_i\alpha_j}$ with $r,s = \varepsilon,\phi,\mathrm{T},\mathrm{C},\theta,\lambda$. This quantity can be evaluated at each point within the physical domain according to the following relation, setting $\tau,\eta = 0,\dots,N+1$, $n,m = 1,\dots,20$, $p,q = 0,1,2$, and $i,j = 1,\dots,6$ [58]:

$$A_{rs\,nm\ (pq)}^{(\tau\eta)[fg]\ \alpha_i\alpha_j} = \sum_{k=1}^{l} \int_{\zeta_k}^{\zeta_{k+1}} \overline{\Upsilon}_{nm}^{(k)} \frac{\partial^f F_\tau^{(k)\alpha_i}}{\partial \zeta^f} \frac{\partial^g F_\eta^{(k)\alpha_j}}{\partial \zeta^g} \frac{H_1 H_2}{H_1^p H_2^q} d\zeta \tag{42}$$

where $\overline{\Upsilon}_{nm}^{(k)}$ is a coefficient associated with the 3D constitutive relationship of each k-th layer, as defined in Eq. (22). In particular, this term is expressed as $\overline{\Upsilon}_{nm}^{(k)} = \kappa\overline{\Gamma}_{nm}^{(k)}$, where κ is the shear correction factor. This coefficient is assumed to be $5/6$ for 2D theories with no stretching effects in their kinematic models. However, when higher-order theories are used, the value $\kappa = 1$ is considered. To clarify the position of the elements $A_{rsnm\ (pq)}^{(\tau\eta)[fg]\ \alpha_i\alpha_j}$ within the matrix $\mathbf{A}^{(\tau\eta)\alpha_i\alpha_j}$, the sub-matrices in Eq. (41) are presented in Appendix I in extended form. The higher-order generalized constitutive relationship in Eq. (40) is, then, used to derive the expression for vector $\boldsymbol{\Sigma}^{(\tau)\alpha_i}$ of generalized secondary variables in terms of vector $\boldsymbol{\delta}^{(\tau)}$ of generalized unknown variables in the model. By introducing the higher-order definition of Eq. (18), the following relation is obtained, presented in compact matrix form:

$$\boldsymbol{\Sigma}^{(\tau)\alpha_i} = \sum_{\eta=0}^{N+1} \sum_{j=1}^{6} \mathbf{A}^{(\tau\eta)\alpha_i\alpha_j} \mathbf{D}_\Omega^{\alpha_j} \boldsymbol{\delta}^{(\eta)} = \sum_{\eta=0}^{N+1} \mathbf{O}^{(\tau\eta)\alpha_i} \boldsymbol{\delta}^{(\eta)} \tag{43}$$

The complete expressions of the elements of matrix $\mathbf{O}^{(\tau\eta)\alpha_i}$ for a given $\tau,\eta = 0,\dots,N+1$ kinematic expansion order, are provided in Ref. [58].

As far as the external loads are concerned, the doubly-curved shell solid is subjected to external actions on the top $(+)$ and bottom $(-)$ surfaces, located at $\zeta = h/2$ and $\zeta = -h/2$, respectively. The virtual work associated with these external loads is denoted by $\delta L_s = \delta L_{es} + \delta L_{fs} + \delta Q_{\phi s} + \delta Q_{\mathrm{T}s} + \delta Q_{\mathrm{C}s}$. As can be seen, this work consists of several contributions, including the virtual work δL_{es} from mechanical surface loads $q_{1s}^{(-)}, q_{2s}^{(-)}, q_{3s}^{(-)}$ and $q_{1s}^{(+)}, q_{2s}^{(+)}, q_{3s}^{(+)}$, the virtual work δL_{fs} from the surface actions $q_{1efk}^{(-)}, q_{2efk}^{(-)}, q_{3efk}^{(-)}$ and $q_{1efk}^{(+)}, q_{2efk}^{(+)}, q_{3efk}^{(+)}$ induced by the elastic foundation, which depends on the displacement field components, and the virtual works $\delta Q_{\phi s}$, $\delta Q_{\mathrm{T}s}$, and $\delta Q_{\mathrm{C}s}$ from electric, thermal,

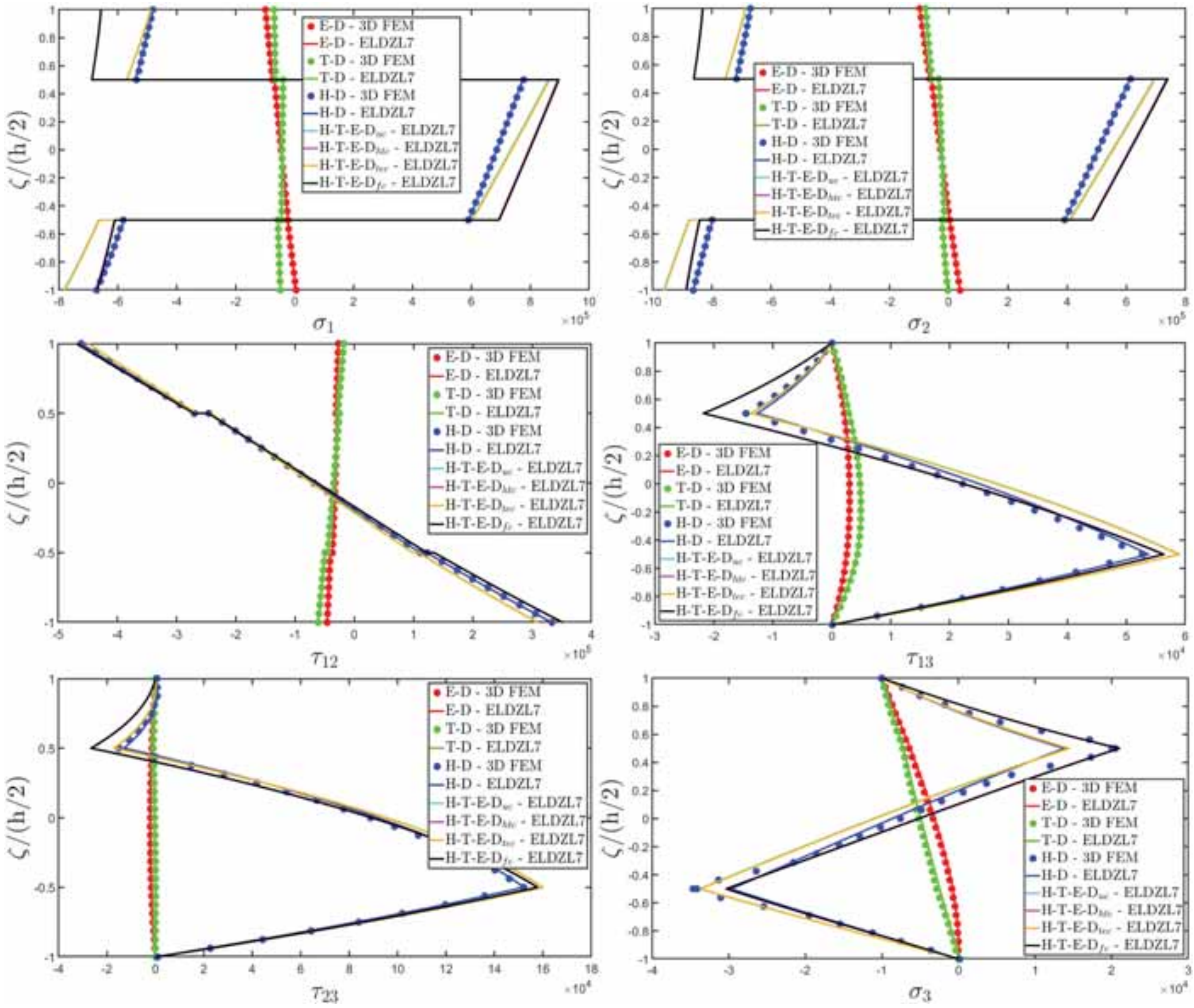

Fig. 6. Representation of the distributions along the thickness direction of 3D stress components of a cylindrical panel-1 for the point located at $(s_1, s_2) = (0.25L_1, 0.25L_2)$. Comparison against 3D FEM results and effect of multifield coupling.

and hygrometric fluxes, here denoted by $q_{\mathrm{D}}^{(-)}, q_{\mathrm{D}}^{(+)}$, $q_{\mathrm{T}}^{(-)}, q_{\mathrm{T}}^{(+)}$, and $q_{\mathrm{C}}^{(-)}$, $q_{\mathrm{C}}^{(+)}$, respectively. The multifield surface loads applied at the top and bottom surfaces of the shell are described by the following relation:

$$q_{\alpha}^{(\pm)} = \overline{q}_{\alpha s}^{(\pm)} \widetilde{q}_{\alpha}^{(\pm)}(\alpha_1, \alpha_2) \tag{44}$$

with $i = 1,2,3,\mathrm{D},\mathrm{T},\mathrm{C}$. Here, $\overline{q}_{\alpha s}^{(\pm)}$ and $\widetilde{q}_{\alpha}^{(\pm)}(\alpha_1, \alpha_2)$ denote the magnitude of the multifield load and its surface distribution at the top and bottom surfaces, respectively. The virtual work δL_s can be computed by integrating the various energetic contributions over the top and bottom surfaces. This leads to the relation reported below [58]:

where $\widetilde{q}_{is}^{(-)} = q_i^{(-)} + q_{iefk}^{(-)}$ and $\widetilde{q}_{is}^{(+)} = q_i^{(+)} + q_{iefk}^{(+)}$ for $i = 1,2,3$ are the global mechanical surface loads. Note that the quantities $H_1^{(-)}, H_2^{(-)}$ and $H_1^{(+)}, H_2^{(+)}$ are the geometric scaling factors introduced in Eq. (4), evaluated at $\zeta = -h/2$ and $\zeta = h/2$, respectively, while $\mathrm{C}_{\infty}^{(k)} = \rho^{(k)} M_{\infty}^{(k)}$ is defined by Eq. (34). By expressing the virtual variation of the 3D multifield configuration variables using the higher-order generalized kinematic model from Eq. (5), the virtual work is, then, expressed in terms of virtual variation of the generalized configuration variables of the theory, accounting for any τ-th kinematic expansion order. In this way, Eq. (45) can be conveniently rewritten as follows:

$$\begin{aligned}\delta L_s = \int_{\alpha_1}\int_{\alpha_2} \Bigg(&\left(\widetilde{q}_{1s}^{(-)} \delta U_1^{(-)} + \widetilde{q}_{2s}^{(-)} \delta U_2^{(-)} + \widetilde{q}_{3s}^{(-)} \delta U_3^{(-)} + q_{\mathrm{D}s}^{(-)} \delta\Delta\phi^{(-)} + \frac{q_{\mathrm{T}s}^{(-)}}{\mathrm{T}_0} \delta\Delta\mathrm{T}^{(-)} + \frac{\mu_{\infty} q_{\mathrm{C}s}^{(-)}}{\mathrm{C}_{\infty}} \delta\Delta\mathrm{C}^{(-)} \right) H_1^{(-)} H_2^{(-)} + \\ + &\left(\widetilde{q}_{1s}^{(+)} \delta U_1^{(+)} + \widetilde{q}_{2s}^{(+)} \delta U_2^{(+)} + \widetilde{q}_{3s}^{(+)} \delta U_3^{(+)} + q_{\mathrm{D}s}^{(+)} \delta\Delta\phi^{(+)} + \frac{q_{\mathrm{T}s}^{(+)}}{\mathrm{T}_0} \delta\Delta\mathrm{T}^{(+)} + \frac{\mu_{\infty} q_{\mathrm{C}s}^{(+)}}{\mathrm{C}_{\infty}} \delta\Delta\mathrm{C}^{(+)} \right) H_1^{(+)} H_2^{(+)} \Bigg) A_1 A_2 d\alpha_1 d\alpha_2\end{aligned} \tag{45}$$

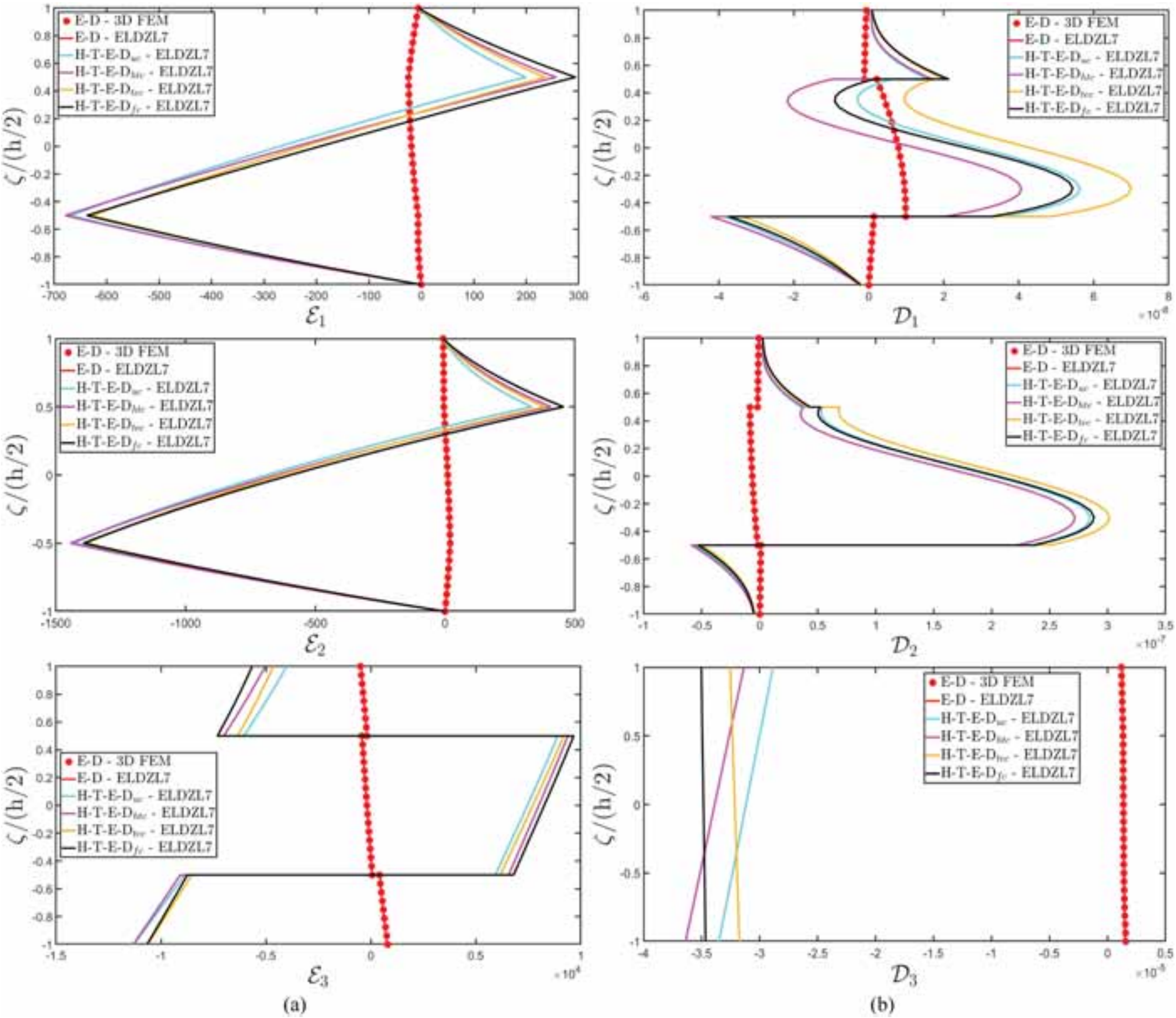

Fig. 7. Representation of the distributions along the thickness direction of 3D electric primary (a) and secondary (b) variables of a cylindrical panel-1 for the point located at $(s_1, s_2) = (0.25L_1, 0.25L_2)$. Comparison against 3D FEM results and effect of multifield coupling.

$$\delta L_s = \int_{\alpha_1}\int_{\alpha_2} \sum_{\tau=0}^{N+1} \left(\widetilde{q}_{1s}^{(\tau)} \delta u_1^{(\tau)} + \widetilde{q}_{2s}^{(\tau)}\delta u_2^{(\tau)} + \widetilde{q}_{3s}^{(\tau)}\delta u_3^{(\tau)} + q_{\mathrm{D}s}^{(\tau)}\delta\phi^{(\tau)} + \frac{q_{\mathrm{T}s}^{(\tau)}}{\mathrm{T}_0}\delta\xi^{(\tau)} + \frac{\mu_\infty q_{\mathrm{C}s}^{(\tau)}}{\mathrm{C}_\infty}\delta\kappa^{(\tau)}\right) A_1 A_2 \, d\alpha_1 d\alpha_2 \tag{46}$$

where $\widetilde{q}_{1s}^{(\tau)}, \widetilde{q}_{2s}^{(\tau)}, \widetilde{q}_{3s}^{(\tau)}, q_{\mathrm{D}s}^{(\tau)}, q_{\mathrm{T}s}^{(\tau)}, q_{\mathrm{C}s}^{(\tau)}$ are the generalized external loads, which are derived at each point of the physical domain for an arbitrary $\tau = 0, \ldots, N+1$ from the following relations:

$$\begin{aligned}
\widetilde{q}_{1s}^{(\tau)} &= q_{1s}^{(-)} F_\tau^{(1)\alpha_1(-)} H_1^{(-)} H_2^{(-)} + q_{1s}^{(+)} F_\tau^{(l)\alpha_1(+)} H_1^{(+)} H_2^{(+)} \\
\widetilde{q}_{2s}^{(\tau)} &= q_{2s}^{(-)} F_\tau^{(1)\alpha_2(-)} H_1^{(-)} H_2^{(-)} + q_{2s}^{(+)} F_\tau^{(l)\alpha_2(+)} H_1^{(+)} H_2^{(+)} \\
\widetilde{q}_{3s}^{(\tau)} &= q_{3s}^{(-)} F_\tau^{(1)\alpha_3(-)} H_1^{(-)} H_2^{(-)} + q_{3s}^{(+)} F_\tau^{(l)\alpha_3(+)} H_1^{(+)} H_2^{(+)} \\
q_{\mathrm{D}s}^{(\tau)} &= q_{\mathrm{D}s}^{(-)} F_\tau^{(1)\alpha_4(-)} H_1^{(-)} H_2^{(-)} + q_{\mathrm{D}s}^{(+)} F_\tau^{(l)\alpha_4(+)} H_1^{(+)} H_2^{(+)} \\
q_{\mathrm{T}s}^{(\tau)} &= q_{\mathrm{T}s}^{(-)} F_\tau^{(1)\alpha_5(-)} H_1^{(-)} H_2^{(-)} + q_{\mathrm{T}s}^{(+)} F_\tau^{(l)\alpha_5(+)} H_1^{(+)} H_2^{(+)} \\
q_{\mathrm{C}s}^{(\tau)} &= q_{\mathrm{C}s}^{(-)} F_\tau^{(1)\alpha_6(-)} H_1^{(-)} H_2^{(-)} + q_{\mathrm{C}s}^{(+)} F_\tau^{(l)\alpha_6(+)} H_1^{(+)} H_2^{(+)}
\end{aligned} \tag{47}$$

The mechanical surface loads $q_{1efk}^{(\pm)}, q_{2efk}^{(\pm)}, q_{3efk}^{(\pm)}$ induced by an elastic foundation at the top and bottom surface of the shell solid are evaluated using the well-known Winkler-Pasternak model [58]. In this model, $k_{1f}^{(\pm)}$, $k_{2f}^{(\pm)}$ and $k_{3f}^{(\pm)}$ represent the elastic stiffnesses of the linear springs oriented along each $\alpha_1, \alpha_2, \zeta$ principal direction, while $G_f^{(\pm)}$ is the shear modulus of the elastic foundation:

$$\begin{aligned}
q_{1efk}^{(\pm)} &= -k_{1f}^{(\pm)} U_1^{(\pm)} \\
q_{2efk}^{(\pm)} &= -k_{2f}^{(\pm)} U_2^{(\pm)} \\
q_{3efk}^{(\pm)} &= -k_{3f}^{(\pm)} U_3^{(\pm)} + G_f^{(\pm)} \nabla_{(\pm)}^2 U_3^{(\pm)}
\end{aligned} \tag{48}$$

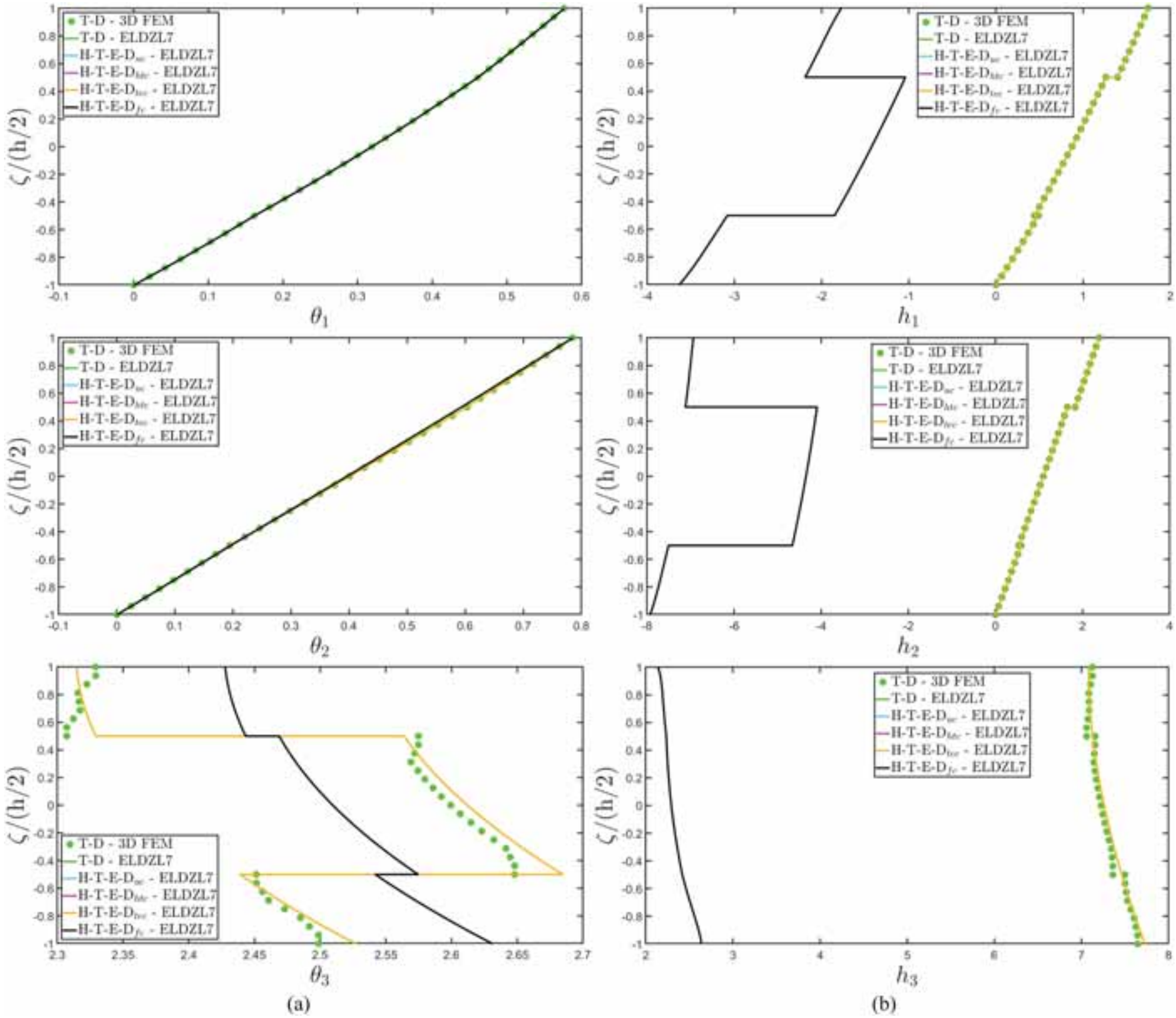

Fig. 8. Representation of the distributions along the thickness direction of 3D thermal primary (a) and secondary (b) variables of a cylindrical panel-1 for the point located at $(s_1, s_2) = (0.25L_1, 0.25L_2)$. Comparison against 3D FEM results and effect of multifield coupling.

As particular case of Eq. (48), the Winkler model for the elastic foundation is obtained by assuming $G_f^{(\pm)} = 0$. The Laplacian operator $\nabla^2_{(\pm)}$ is evaluated at $\zeta = \pm h/2$ using curvilinear principal coordinates, as expressed in the following relation:

By introducing the generalized kinematic model from Eq. (5) to express the displacement field components $U_1^{(\pm)}, U_2^{(\pm)}, U_3^{(\pm)}$ in Eq. (48), the following definition is obtained for the generalized actions $q_{1efk}^{(\tau)}, q_{2efk}^{(\tau)}$,

$$
\begin{aligned}
\nabla^2_{(\pm)} = &\left(\frac{1}{A_1^2\left(H_1^{(\pm)}\right)^2}\frac{\partial^2}{\partial\alpha_1^2} + \frac{1}{A_2^2\left(H_2^{(\pm)}\right)^2}\frac{\partial^2}{\partial\alpha_2^2} + \left(\frac{1}{A_1^2 A_2\left(H_1^{(\pm)}\right)^2}\frac{\partial A_2}{\partial\alpha_1} - \frac{h}{2A_1^2R_2^2\left(H_1^{(\pm)}\right)^2H_2^{(\pm)}}\frac{\partial R_2}{\partial\alpha_1} + \right.\right.\\
&\left. - \frac{1}{A_1^3\left(H_1^{(\pm)}\right)^2}\frac{\partial A_1}{\partial\alpha_1} - \frac{h}{2A_1^2R_1^2\left(H_1^{(\pm)}\right)^3}\frac{\partial R_1}{\partial\alpha_1}\right)\frac{\partial}{\partial\alpha_1} + \left(\frac{1}{A_1A_2^2\left(H_2^{(\pm)}\right)^2}\frac{\partial A_1}{\partial\alpha_2} + \frac{h}{2A_2^2R_1^2\left(H_2^{(\pm)}\right)^2H_1^{(\pm)}}\frac{\partial R_1}{\partial\alpha_2} + \right.\\
&\left.\left. - \frac{1}{A_2^3\left(H_2^{(\pm)}\right)^2}\frac{\partial A_2}{\partial\alpha_2} - \frac{h}{2A_2^2R_2^2\left(H_2^{(\pm)}\right)^3}\frac{\partial R_2}{\partial\alpha_2}\right)\frac{\partial}{\partial\alpha_2}\right)
\end{aligned}
\tag{49}
$$

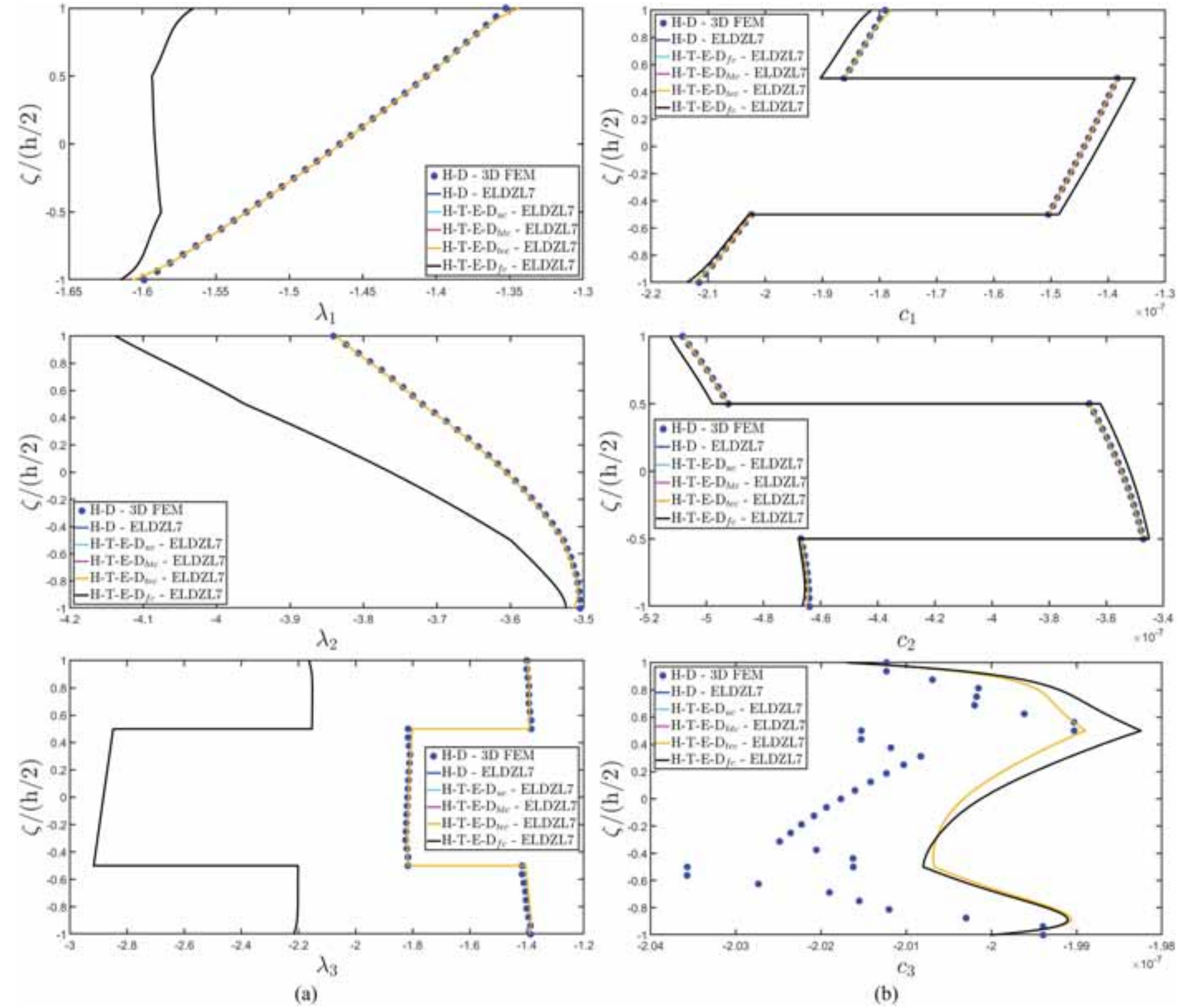

Fig. 9. Representation of the distributions along the thickness direction of 3D hygrometric primary (a) and secondary (b) variables of a cylindrical panel-1 for the point located at $(s_1, s_2) = (0.25L_1, 0.25L_2)$. Comparison against 3D FEM results and effect of multifield coupling.

$q_{3efk}^{(\tau)}$ associated with the elastic foundation for an arbitrary $\tau = 0,\ldots,N+1$:

$$
\begin{aligned}
q_{1efk}^{(\tau)} &= -\left(k_{1f}^{(-)} F_{\eta}^{(1)\alpha_1(-)} F_{\tau}^{(1)\alpha_1(-)} H_1^{(-)} H_2^{(-)} + k_{1f}^{(+)} F_{\eta}^{(l)\alpha_1(+)} F_{\tau}^{(l)\alpha_1(+)} H_1^{(+)} H_2^{(+)}\right) u_1^{(\tau)} = -L_{fm1}^{(\tau\eta)\alpha_1\alpha_1} u_1^{(\tau)} \\
q_{2efk}^{(\tau)} &= -\left(k_{2f}^{(-)} F_{\eta}^{(1)\alpha_2(-)} F_{\tau}^{(1)\alpha_2(-)} H_1^{(-)} H_2^{(-)} + k_{2f}^{(+)} F_{\eta}^{(l)\alpha_2(+)} F_{\tau}^{(l)\alpha_2(+)} H_1^{(+)} H_2^{(+)}\right) u_2^{(\tau)} = -L_{fm2}^{(\tau\eta)\alpha_2\alpha_2} u_2^{(\tau)} \\
q_{3efk}^{(\tau)} &= -\left(\left(k_{3f}^{(-)} - G_f^{(-)} \nabla_{(-)}^2\right) F_{\eta}^{(1)\alpha_3(-)} F_{\tau}^{(1)\alpha_3(-)} H_1^{(-)} H_2^{(-)} + \left(k_{3f}^{(+)} - G_f^{(+)} \nabla_{(+)}^2\right) F_{\eta}^{(l)\alpha_3(+)} F_{\tau}^{(l)\alpha_3(+)} H_1^{(+)} H_2^{(+)}\right) u_3^{(\tau)} = -L_{fm3}^{(\tau\eta)\alpha_3\alpha_3} u_3^{(\tau)}
\end{aligned}
\tag{50}
$$

The generalized surface actions derived in the previous equation are conveniently organized into the vector $\mathbf{q}_{efk}^{(\tau)} = \left[q_{1efk}^{(\tau)} \; q_{2efk}^{(\tau)} \; q_{3efk}^{(\tau)} \; 0 \; 0 \; 0\right]^T$, defined for each $\tau = 0, \ldots, N+1$. The actions associated with mechanical and multifield external loads, which do not depend on the magnitude of configuration variables, are collected into the vector $\mathbf{q}_s^{(\tau)} = \left[q_{1s}^{(\tau)} \; q_{2s}^{(\tau)} \; q_{3s}^{(\tau)} \; q_{Ds}^{(\tau)} \; q_{Ts}^{(\tau)} \; q_{Cs}^{(\tau)}\right]^T$. In this way, the loads derived from Eq. (47) can be expressed in the vector form as $\mathbf{q}^{(\tau)} = \mathbf{q}_s^{(\tau)} + \mathbf{q}_{efk}^{(\tau)}$, which is expressed in expanded form as $\mathbf{q}^{(\tau)} = \left[q_1^{(\tau)} \; q_2^{(\tau)} \; q_3^{(\tau)} \; q_D^{(\tau)} \; q_T^{(\tau)} \; q_C^{(\tau)}\right]^T$. The governing equations of the coupled hygro-thermo-electro-mechanical problem are derived for a stationary configuration of the doubly-curved shell solid under multifield external actions. To this end, we evaluate the virtual variation of the total energy of the system, denoted by δE. Referring to an

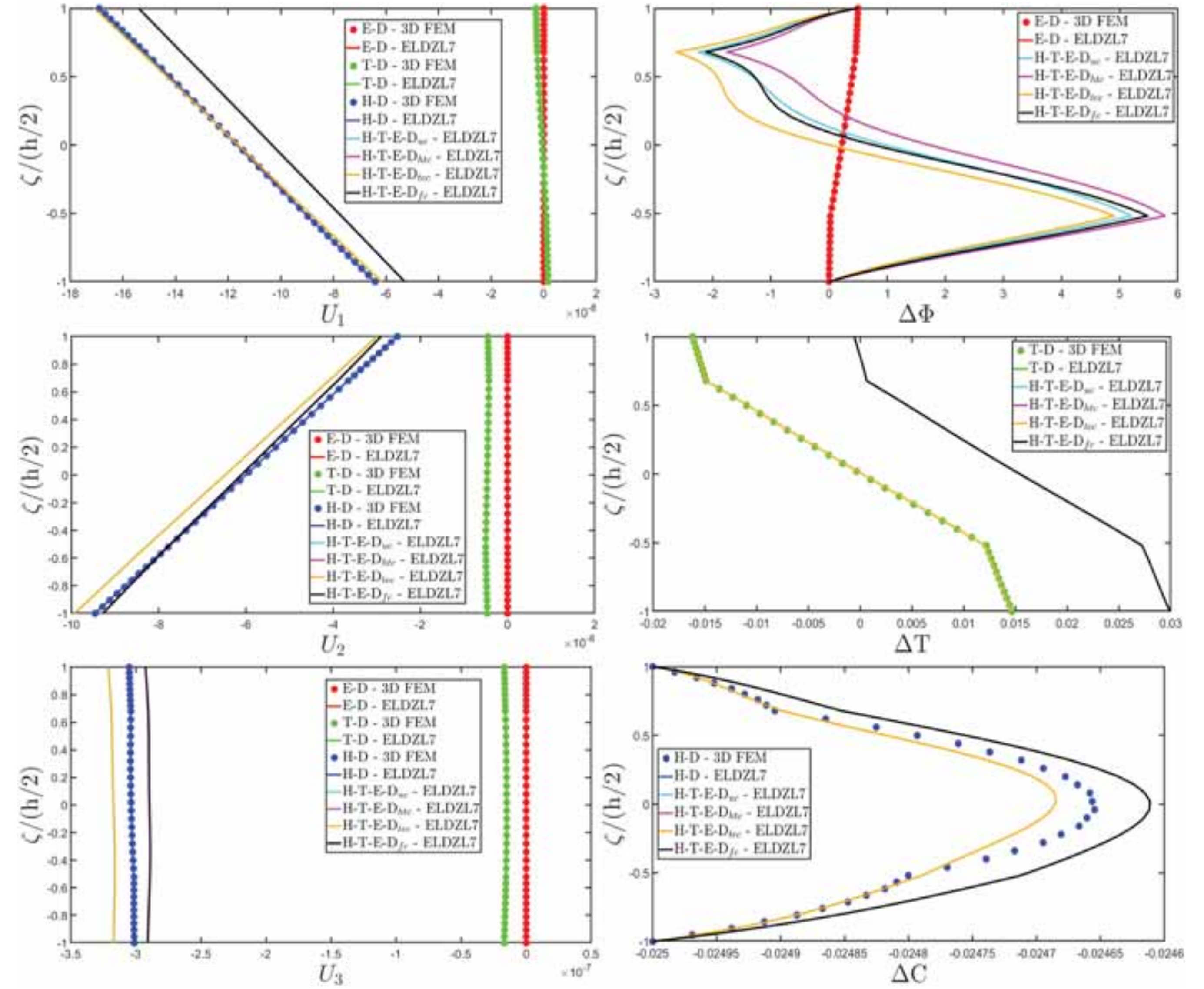

Fig. 10. Representation of the distributions along the thickness direction of the hygro-thermo-electro-mechanical configuration variables of a cylindrical panel-2 for the point located at $(s_1, s_2) = (0.75L_1, 0.25L_2)$. Comparison against 3D FEM results and effect of multifield coupling.

arbitrary time interval $[t_1, t_2]$ with $t_1 < t_2$, the application of the Master Balance principle [58] yields the following relation, where $\delta L = \delta L_T + \delta L_C + \delta L_s$ is the virtual work of the multifield external actions, while δY is the virtual variation of the internal energy of the doubly-curved shell solid, as introduced in Eq. (38):

$$\int_{t_1}^{t_2} \delta E\, dt = \int_{t_1}^{t_2} (\delta Y - \delta L) dt = 0 \tag{51}$$

The virtual work of the external actions consists of three distinct parts: δL_s represents the virtual work of the external surface loads applied at the top and bottom sides of the solid, as derived in Eq. (46), δL_T is the virtual variation of energy associated with the reference entropy of the system, and δL_C is related to the reference chemical potential fixed at an arbitrary point of the shell. These terms are derived from integrating the quantities $\overline{\eta}^{(k)}$ and $\overline{\mu}^{(k)}$ over the entire solid, as shown below, taking into account arbitrary variations in the absolute temperature and the moisture concentration:

$$\begin{aligned} \delta L_T &= -\sum_{k=1}^{l} \int_{\zeta_k}^{\zeta_{k+1}} \int_{\alpha_1} \int_{\alpha_2} \overline{\eta}^{(k)} \delta \Delta T^{(k)} H_1 H_2 A_1 A_2 d\alpha_1 d\alpha_2 d\zeta \\ \delta L_C &= -\sum_{k=1}^{l} \int_{\zeta_k}^{\zeta_{k+1}} \int_{\alpha_1} \int_{\alpha_2} \overline{\mu}^{(k)} \delta \Delta C^{(k)} H_1 H_2 A_1 A_2 d\alpha_1 d\alpha_2 d\zeta \end{aligned} \tag{52}$$

The present formulation is based on thermodynamic equilibrium conditions, which imply that the energy contributions $\delta L_T, \delta L_C$ in the previous equation are set to zero. By introducing the energy contributions from Eqs. (38), (46), and (52) into the Master Balance principle of Eq. (51), and applying the integration by parts rule, the multifield balance equations are derived for doubly-curved shell structures employing higher-order theories. The corresponding boundary conditions are also derived in this procedure [58]. Referring to an arbitrary τ-th order, the following relations are obtained, presented in compact matrix notation:

$$\sum_{i=1}^{6}\mathbf{D}_{\Omega}^{*\alpha_i}\boldsymbol{\Sigma}^{(\tau)\alpha_i}+\mathbf{q}^{(\tau)}=\sum_{i=1}^{6}\mathbf{D}_{\Omega}^{*\alpha_i}\boldsymbol{\Sigma}^{(\tau)\alpha_i}+\mathbf{q}_s^{(\tau)}+\mathbf{q}_{efk}^{(\tau)}=\mathbf{0} \tag{53}$$

where the generalized balance operators $\mathbf{D}_{\Omega}^{*\alpha_i}$ with $i=1,\dots,6$ are:

$$\mathbf{D}_{\Omega}^{*\alpha_1}=\begin{bmatrix}\overline{\mathbf{D}}_{\Omega}^{*\alpha_1}&\mathbf{0}&\mathbf{0}&\mathbf{0}&\mathbf{0}&\mathbf{0}\\\mathbf{0}&\mathbf{0}&\mathbf{0}&\mathbf{0}&\mathbf{0}&\mathbf{0}\\\mathbf{0}&\mathbf{0}&\mathbf{0}&\mathbf{0}&\mathbf{0}&\mathbf{0}\\\mathbf{0}&\mathbf{0}&\mathbf{0}&\mathbf{0}&\mathbf{0}&\mathbf{0}\\\mathbf{0}&\mathbf{0}&\mathbf{0}&\mathbf{0}&\mathbf{0}&\mathbf{0}\\\mathbf{0}&\mathbf{0}&\mathbf{0}&\mathbf{0}&\mathbf{0}&\mathbf{0}\end{bmatrix},\quad \mathbf{D}_{\Omega}^{*\alpha_2}=\begin{bmatrix}\mathbf{0}&\mathbf{0}&\mathbf{0}&\mathbf{0}&\mathbf{0}&\mathbf{0}\\\overline{\mathbf{D}}_{\Omega}^{*\alpha_2}&\mathbf{0}&\mathbf{0}&\mathbf{0}&\mathbf{0}&\mathbf{0}\\\mathbf{0}&\mathbf{0}&\mathbf{0}&\mathbf{0}&\mathbf{0}&\mathbf{0}\\\mathbf{0}&\mathbf{0}&\mathbf{0}&\mathbf{0}&\mathbf{0}&\mathbf{0}\\\mathbf{0}&\mathbf{0}&\mathbf{0}&\mathbf{0}&\mathbf{0}&\mathbf{0}\\\mathbf{0}&\mathbf{0}&\mathbf{0}&\mathbf{0}&\mathbf{0}&\mathbf{0}\end{bmatrix},\quad \mathbf{D}_{\Omega}^{*\alpha_3}=\begin{bmatrix}\mathbf{0}&\mathbf{0}&\mathbf{0}&\mathbf{0}&\mathbf{0}&\mathbf{0}\\\mathbf{0}&\mathbf{0}&\mathbf{0}&\mathbf{0}&\mathbf{0}&\mathbf{0}\\\overline{\mathbf{D}}_{\Omega}^{*\alpha_3}&\mathbf{0}&\mathbf{0}&\mathbf{0}&\mathbf{0}&\mathbf{0}\\\mathbf{0}&\mathbf{0}&\mathbf{0}&\mathbf{0}&\mathbf{0}&\mathbf{0}\\\mathbf{0}&\mathbf{0}&\mathbf{0}&\mathbf{0}&\mathbf{0}&\mathbf{0}\\\mathbf{0}&\mathbf{0}&\mathbf{0}&\mathbf{0}&\mathbf{0}&\mathbf{0}\end{bmatrix},$$
$$\mathbf{D}_{\Omega}^{*\alpha_4}=\begin{bmatrix}\mathbf{0}&\mathbf{0}&\mathbf{0}&\mathbf{0}&\mathbf{0}&\mathbf{0}\\\mathbf{0}&\mathbf{0}&\mathbf{0}&\mathbf{0}&\mathbf{0}&\mathbf{0}\\\mathbf{0}&\mathbf{0}&\mathbf{0}&\mathbf{0}&\mathbf{0}&\mathbf{0}\\\mathbf{0}&\overline{\mathbf{D}}_{\Omega}^{*\alpha_4}&\mathbf{0}&\mathbf{0}&\mathbf{0}&\mathbf{0}\\\mathbf{0}&\mathbf{0}&\mathbf{0}&\mathbf{0}&\mathbf{0}&\mathbf{0}\\\mathbf{0}&\mathbf{0}&\mathbf{0}&\mathbf{0}&\mathbf{0}&\mathbf{0}\end{bmatrix},\quad \mathbf{D}_{\Omega}^{*\alpha_5}=\begin{bmatrix}\mathbf{0}&\mathbf{0}&\mathbf{0}&\mathbf{0}&\mathbf{0}&\mathbf{0}\\\mathbf{0}&\mathbf{0}&\mathbf{0}&\mathbf{0}&\mathbf{0}&\mathbf{0}\\\mathbf{0}&\mathbf{0}&\mathbf{0}&\mathbf{0}&\mathbf{0}&\mathbf{0}\\\mathbf{0}&\mathbf{0}&\mathbf{0}&\mathbf{0}&\mathbf{0}&\mathbf{0}\\\mathbf{0}&\mathbf{0}&\mathbf{0}&\mathbf{0}&\overline{\mathbf{D}}_{\Omega}^{*\alpha_5}&\mathbf{0}\\\mathbf{0}&\mathbf{0}&\mathbf{0}&\mathbf{0}&\mathbf{0}&\mathbf{0}\end{bmatrix},\quad \mathbf{D}_{\Omega}^{*\alpha_6}=\begin{bmatrix}\mathbf{0}&\mathbf{0}&\mathbf{0}&\mathbf{0}&\mathbf{0}&\mathbf{0}\\\mathbf{0}&\mathbf{0}&\mathbf{0}&\mathbf{0}&\mathbf{0}&\mathbf{0}\\\mathbf{0}&\mathbf{0}&\mathbf{0}&\mathbf{0}&\mathbf{0}&\mathbf{0}\\\mathbf{0}&\mathbf{0}&\mathbf{0}&\mathbf{0}&\mathbf{0}&\mathbf{0}\\\mathbf{0}&\mathbf{0}&\mathbf{0}&\mathbf{0}&\mathbf{0}&\mathbf{0}\\\mathbf{0}&\mathbf{0}&\mathbf{0}&\mathbf{0}&\mathbf{0}&\overline{\mathbf{D}}_{\Omega}^{*\alpha_6}\end{bmatrix} \tag{54}$$

The sub-operators $\overline{\mathbf{D}}_{\Omega}^{*\alpha_i}$ with $i=1,\dots,6$ are reported below in extended form:

$$\begin{aligned}
\overline{\mathbf{D}}_{\Omega}^{*\alpha_1}&=\begin{bmatrix}\frac{1}{A_1}\frac{\partial}{\partial\alpha_1}+\frac{1}{A_1A_2}\frac{\partial A_2}{\partial\alpha_1} & -\frac{1}{A_1A_2}\frac{\partial A_2}{\partial\alpha_1} & \frac{1}{A_1A_2}\frac{\partial A_1}{\partial\alpha_2} & \frac{1}{A_2}\frac{\partial}{\partial\alpha_2}+\frac{1}{A_1A_2}\frac{\partial A_1}{\partial\alpha_2} & \frac{1}{R_1} & 0 & -1 & 0 & 0\end{bmatrix}\\
\overline{\mathbf{D}}_{\Omega}^{*\alpha_2}&=\begin{bmatrix}-\frac{1}{A_1A_2}\frac{\partial A_1}{\partial\alpha_2} & \frac{1}{A_2}\frac{\partial}{\partial\alpha_2}+\frac{1}{A_1A_2}\frac{\partial A_1}{\partial\alpha_2} & \frac{1}{A_1}\frac{\partial}{\partial\alpha_1}+\frac{1}{A_1A_2}\frac{\partial A_2}{\partial\alpha_1} & \frac{1}{A_1A_2}\frac{\partial A_2}{\partial\alpha_1} & 0 & \frac{1}{R_2} & 0 & -1 & 0\end{bmatrix}\\
\overline{\mathbf{D}}_{\Omega}^{*\alpha_3}&=\begin{bmatrix}-\frac{1}{R_1} & -\frac{1}{R_2} & 0 & 0 & \frac{1}{A_1}\frac{\partial}{\partial\alpha_1}+\frac{1}{A_1A_2}\frac{\partial A_2}{\partial\alpha_1} & \frac{1}{A_2}\frac{\partial}{\partial\alpha_2}+\frac{1}{A_1A_2}\frac{\partial A_1}{\partial\alpha_2} & 0 & 0 & -1\end{bmatrix}\\
\overline{\mathbf{D}}_{\Omega}^{*\alpha_4}=\overline{\mathbf{D}}_{\Omega}^{*\alpha_5}=\overline{\mathbf{D}}_{\Omega}^{*\alpha_6}&=\begin{bmatrix}\frac{1}{A_1}\frac{\partial}{\partial\alpha_1}+\frac{1}{A_1A_2}\frac{\partial A_2}{\partial\alpha_1} & \frac{1}{A_2}\frac{\partial}{\partial\alpha_2}+\frac{1}{A_1A_2}\frac{\partial A_1}{\partial\alpha_2} & -1\end{bmatrix}
\end{aligned} \tag{55}$$

Performing all matrix multiplications, the generalized balance equations presented in Eq. (53) take the following expressions [58]:

$$\begin{aligned}
&\frac{1}{A_1}\frac{\partial N_1^{(\tau)\alpha_1}}{\partial\alpha_1}+\frac{N_1^{(\tau)\alpha_1}}{A_1A_2}\frac{\partial A_2}{\partial\alpha_1}+\frac{1}{A_2}\frac{\partial N_{21}^{(\tau)\alpha_1}}{\partial\alpha_2}+\frac{N_{21}^{(\tau)\alpha_1}}{A_1A_2}\frac{\partial A_1}{\partial\alpha_2}+\frac{N_{12}^{(\tau)\alpha_1}}{A_1A_2}\frac{\partial A_1}{\partial\alpha_2}\\
&-\frac{N_2^{(\tau)\alpha_1}}{A_1A_2}\frac{\partial A_2}{\partial\alpha_1}+\frac{T_1^{(\tau)\alpha_1}}{R_1}-P_1^{(\tau)\alpha_1}+q_1^{(\tau)}\\
&=0\\[2ex]
&\frac{1}{A_2}\frac{\partial N_2^{(\tau)\alpha_2}}{\partial\alpha_2}+\frac{N_2^{(\tau)\alpha_2}}{A_1A_2}\frac{\partial A_1}{\partial\alpha_2}+\frac{1}{A_1}\frac{\partial N_{12}^{(\tau)\alpha_2}}{\partial\alpha_1}+\frac{N_{12}^{(\tau)\alpha_2}}{A_1A_2}\frac{\partial A_2}{\partial\alpha_1}+\frac{N_{21}^{(\tau)\alpha_2}}{A_1A_2}\frac{\partial A_2}{\partial\alpha_1}\\
&-\frac{N_1^{(\tau)\alpha_2}}{A_1A_2}\frac{\partial A_1}{\partial\alpha_2}+\frac{T_2^{(\tau)\alpha_2}}{R_2}-P_2^{(\tau)\alpha_2}+q_2^{(\tau)}\\
&=0\\[2ex]
&\frac{1}{A_1}\frac{\partial T_1^{(\tau)\alpha_3}}{\partial\alpha_1}+\frac{T_1^{(\tau)\alpha_3}}{A_1A_2}\frac{\partial A_2}{\partial\alpha_1}+\frac{1}{A_2}\frac{\partial T_2^{(\tau)\alpha_3}}{\partial\alpha_2}+\frac{T_2^{(\tau)\alpha_3}}{A_1A_2}\frac{\partial A_1}{\partial\alpha_2}-\frac{N_1^{(\tau)\alpha_3}}{R_1}-\frac{N_2^{(\tau)\alpha_3}}{R_2}-S_3^{(\tau)\alpha_3}\\
&+q_3^{(\tau)}\\
&=0\\[2ex]
&\frac{1}{A_1}\frac{\partial D_1^{(\tau)\alpha_4}}{\partial\alpha_1}+\frac{D_1^{(\tau)\alpha_4}}{A_1A_2}\frac{\partial A_2}{\partial\alpha_1}+\frac{1}{A_2}\frac{\partial D_2^{(\tau)\alpha_4}}{\partial\alpha_2}+\frac{D_2^{(\tau)\alpha_4}}{A_1A_2}\frac{\partial A_1}{\partial\alpha_2}-D_3^{(\tau)\alpha_4}+q_{\mathrm{D}s}^{(\tau)}=0\\
&\frac{1}{A_1}\frac{\partial H_1^{(\tau)\alpha_5}}{\partial\alpha_1}+\frac{H_1^{(\tau)\alpha_5}}{A_1A_2}\frac{\partial A_2}{\partial\alpha_1}+\frac{1}{A_2}\frac{\partial H_2^{(\tau)\alpha_5}}{\partial\alpha_2}+\frac{H_2^{(\tau)\alpha_5}}{A_1A_2}\frac{\partial A_1}{\partial\alpha_2}-H_3^{(\tau)\alpha_5}+q_{\mathrm{T}s}^{(\tau)}=0\\
&\frac{1}{A_1}\frac{\partial C_1^{(\tau)\alpha_6}}{\partial\alpha_1}+\frac{C_1^{(\tau)\alpha_6}}{A_1A_2}\frac{\partial A_2}{\partial\alpha_1}+\frac{1}{A_2}\frac{\partial C_2^{(\tau)\alpha_6}}{\partial\alpha_2}+\frac{C_2^{(\tau)\alpha_6}}{A_1A_2}\frac{\partial A_1}{\partial\alpha_2}-C_3^{(\tau)\alpha_6}+q_{\mathrm{C}s}^{(\tau)}=0
\end{aligned} \tag{56}$$

As previously stated, the boundary conditions derived from Eq. (51), are applied to the four edges of the rectangular parametric domain. These conditions specify particular values for either the generalized configuration variables or the generalized secondary variables. For the edges of the parametric domain located at $\alpha_1 = \alpha_1^0$ or $\alpha_1 = \alpha_1^1$, the following relations are considered:

$$\begin{aligned}
&N_1^{(\tau)\alpha_1} = \overline{N}_1^{(\tau)\alpha_1} \quad \text{or} \quad u_1^{(\tau)} = \overline{u}_1^{(\tau)} \\
&N_{12}^{(\tau)\alpha_2} = \overline{N}_{12}^{(\tau)\alpha_2} \quad \text{or} \quad u_2^{(\tau)} = \overline{u}_2^{(\tau)} \\
&T_1^{(\tau)\alpha_3} = \overline{T}_1^{(\tau)\alpha_3} \quad \text{or} \quad u_3^{(\tau)} = \overline{u}_3^{(\tau)} \\
&D_1^{(\tau)\alpha_4} = \overline{D}_1^{(\tau)\alpha_4} \quad \text{or} \quad \phi^{(\tau)} = \overline{\phi}^{(\tau)} \\
&H_1^{(\tau)\alpha_5} = \overline{H}_1^{(\tau)\alpha_5} \quad \text{or} \quad \xi^{(\tau)} = \overline{\xi}^{(\tau)} \\
&C_1^{(\tau)\alpha_6} = \overline{C}_1^{(\tau)\alpha_6} \quad \text{or} \quad \kappa^{(\tau)} = \overline{\kappa}^{(\tau)}
\end{aligned} \tag{57}$$

where $\overline{u}_1^{(\tau)}, \overline{u}_2^{(\tau)}, \overline{u}_3^{(\tau)}, \overline{\phi}^{(\tau)}, \overline{\xi}^{(\tau)}, \overline{\kappa}^{(\tau)}$ and $\overline{N}_1^{(\tau)\alpha_1}, \overline{N}_{12}^{(\tau)\alpha_2}, \overline{T}_1^{(\tau)\alpha_3}, \overline{D}_1^{(\tau)\alpha_4}, \overline{H}_1^{(\tau)\alpha_5}, \overline{C}_1^{(\tau)\alpha_6}$ denote the prescribed values of configuration and secondary variables, respectively. Following a similar procedure, the boundary conditions for the edges located at $\alpha_2 = \alpha_2^0$ or $\alpha_2 = \alpha_2^1$ within the physical domain are derived, with $\overline{u}_1^{(\tau)}, \overline{u}_2^{(\tau)}, \overline{u}_3^{(\tau)}, \overline{\phi}^{(\tau)}, \overline{\xi}^{(\tau)}, \overline{\kappa}^{(\tau)}$ and $\overline{N}_{21}^{(\tau)\alpha_1}, \overline{N}_2^{(\tau)\alpha_2}, \overline{T}_2^{(\tau)\alpha_3}, \overline{D}_2^{(\tau)\alpha_4}, \overline{H}_2^{(\tau)\alpha_5}, \overline{C}_2^{(\tau)\alpha_6}$ representing the prescribed values of the unknown variables and generalized stress resultants:

$$\begin{aligned}
&N_{21}^{(\tau)\alpha_1} = \overline{N}_{21}^{(\tau)\alpha_1} \quad \text{or} \quad u_1^{(\tau)} = \overline{u}_1^{(\tau)} \\
&N_2^{(\tau)\alpha_2} = \overline{N}_2^{(\tau)\alpha_2} \quad \text{or} \quad u_2^{(\tau)} = \overline{u}_2^{(\tau)} \\
&T_2^{(\tau)\alpha_3} = \overline{T}_2^{(\tau)\alpha_3} \quad \text{or} \quad u_3^{(\tau)} = \overline{u}_3^{(\tau)} \\
&D_2^{(\tau)\alpha_4} = \overline{D}_2^{(\tau)\alpha_4} \quad \text{or} \quad \phi^{(\tau)} = \overline{\phi}^{(\tau)} \\
&H_2^{(\tau)\alpha_5} = \overline{H}_2^{(\tau)\alpha_5} \quad \text{or} \quad \xi^{(\tau)} = \overline{\xi}^{(\tau)} \\
&C_2^{(\tau)\alpha_6} = \overline{C}_2^{(\tau)\alpha_6} \quad \text{or} \quad \kappa^{(\tau)} = \overline{\kappa}^{(\tau)}
\end{aligned} \tag{58}$$

As a particular case of Eqs. (57) and (58), the Simply-supported (S) boundary condition is defined as follows:

$$\begin{aligned}
&N_1^{(\tau)\alpha_1} = 0, \quad u_2^{(\tau)} = u_3^{(\tau)} = \phi^{(\tau)} = \xi^{(\tau)} = \kappa^{(\tau)} = 0 \quad \text{at} \quad \alpha_1 = \alpha_1^0 \ \text{or} \ \alpha_1 = \alpha_1^1 \\
&N_2^{(\tau)\alpha_2} = 0, \quad u_1^{(\tau)} = u_3^{(\tau)} = \phi^{(\tau)} = \xi^{(\tau)} = \kappa^{(\tau)} = 0 \quad \text{at} \quad \alpha_2 = \alpha_2^0 \ \text{or} \ \alpha_2 = \alpha_2^1
\end{aligned} \tag{59}$$

By introducing the expression for the generalized secondary variables $\boldsymbol{\Sigma}^{(\tau)\alpha_i}$ in terms of vector $\boldsymbol{\delta}^{(\tau)}$ as given by Eq. (43) into the higher-order multifield balance relations of Eq. (53), the fundamental equations are derived. These equations relate the unknown field variables vector $\boldsymbol{\delta}^{(\tau)}$ to the vector $\mathbf{q}_s^{(\tau)}$ of multifield surface actions. The following relation is thus obtained [58]:

$$\sum_{\eta=0}^{N+1} \overline{\mathbf{L}}^{(\tau\eta)} \boldsymbol{\delta}^{(\eta)} + \mathbf{q}^{(\tau)} = \sum_{\eta=0}^{N+1} \mathbf{L}^{(\tau\eta)} \boldsymbol{\delta}^{(\eta)} + \mathbf{q}_{efk}^{(\tau)} + \mathbf{q}_s^{(\tau)} = \sum_{\eta=0}^{N+1} \left(\mathbf{L}^{(\tau\eta)} - \mathbf{L}_{fm}^{(\tau\eta)} \right) \boldsymbol{\delta}^{(\eta)} + \mathbf{q}_s^{(\tau)} = \mathbf{0} \tag{60}$$

The fundamental matrix $\overline{\mathbf{L}}^{(\tau\eta)}$ is evaluated at each point within the rectangular parametric domain for each $\tau, \eta = 0, \ldots, N+1$ as follows:

$$\overline{\mathbf{L}}^{(\tau\eta)} = \left[\begin{array}{ccc|c|c|c}
L_{11}^{(\tau\eta)\alpha_1\alpha_1} - L_{fm1}^{(\tau\eta)\alpha_1\alpha_1} & L_{12}^{(\tau\eta)\alpha_1\alpha_2} & L_{13}^{(\tau\eta)\alpha_1\alpha_3} & L_{14}^{(\tau\eta)\alpha_1\alpha_4} & L_{15}^{(\tau\eta)\alpha_1\alpha_5} & L_{16}^{(\tau\eta)\alpha_1\alpha_6} \\
L_{21}^{(\tau\eta)\alpha_2\alpha_1} & L_{22}^{(\tau\eta)\alpha_2\alpha_2} - L_{fm2}^{(\tau\eta)\alpha_2\alpha_2} & L_{23}^{(\tau\eta)\alpha_2\alpha_3} & L_{24}^{(\tau\eta)\alpha_2\alpha_4} & L_{25}^{(\tau\eta)\alpha_2\alpha_5} & L_{26}^{(\tau\eta)\alpha_2\alpha_6} \\
L_{31}^{(\tau\eta)\alpha_3\alpha_1} & L_{32}^{(\tau\eta)\alpha_3\alpha_2} & L_{33}^{(\tau\eta)\alpha_3\alpha_3} - L_{fm3}^{(\tau\eta)\alpha_3\alpha_3} & L_{34}^{(\tau\eta)\alpha_3\alpha_4} & L_{35}^{(\tau\eta)\alpha_3\alpha_5} & L_{36}^{(\tau\eta)\alpha_3\alpha_6} \\
\hline
L_{41}^{(\tau\eta)\alpha_4\alpha_1} & L_{42}^{(\tau\eta)\alpha_4\alpha_2} & L_{43}^{(\tau\eta)\alpha_4\alpha_3} & L_{44}^{(\tau\eta)\alpha_4\alpha_4} & L_{45}^{(\tau\eta)\alpha_4\alpha_5} & L_{46}^{(\tau\eta)\alpha_4\alpha_6} \\
\hline
0 & 0 & 0 & 0 & L_{55}^{(\tau\eta)\alpha_5\alpha_5} & L_{56}^{(\tau\eta)\alpha_5\alpha_6} \\
\hline
0 & 0 & 0 & 0 & L_{65}^{(\tau\eta)\alpha_6\alpha_5} & L_{66}^{(\tau\eta)\alpha_6\alpha_6}
\end{array}\right] =$$

$$= \left[\begin{array}{ccc|c|c|c}
\overline{\mathbf{D}}_\Omega^{*\alpha_1} \mathbf{A}_{uu}^{(\tau\eta)\alpha_1\alpha_1} \overline{\mathbf{D}}_\Omega^{\alpha_1} - L_{fm1}^{(\tau\eta)\alpha_1\alpha_1} & \overline{\mathbf{D}}_\Omega^{*\alpha_1} \mathbf{A}_{uu}^{(\tau\eta)\alpha_1\alpha_2} \overline{\mathbf{D}}_\Omega^{\alpha_2} & \overline{\mathbf{D}}_\Omega^{*\alpha_1} \mathbf{A}_{uu}^{(\tau\eta)\alpha_1\alpha_3} \overline{\mathbf{D}}_\Omega^{\alpha_3} & \overline{\mathbf{D}}_\Omega^{*\alpha_1} \mathbf{A}_{u\phi}^{(\tau\eta)\alpha_1\alpha_4} \overline{\mathbf{D}}_\Omega^{\alpha_4} & \overline{\mathbf{D}}_\Omega^{*\alpha_1} \mathbf{A}_{uT}^{(\tau\eta)\alpha_1\alpha_5} \overline{\mathbf{D}}_\Omega^{\alpha_5} & \overline{\mathbf{D}}_\Omega^{*\alpha_1} \mathbf{A}_{uC}^{(\tau\eta)\alpha_1\alpha_6} \overline{\mathbf{D}}_\Omega^{\alpha_6} \\
\overline{\mathbf{D}}_\Omega^{*\alpha_2} \mathbf{A}_{uu}^{(\tau\eta)\alpha_2\alpha_1} \overline{\mathbf{D}}_\Omega^{\alpha_1} & \overline{\mathbf{D}}_\Omega^{*\alpha_2} \mathbf{A}_{uu}^{(\tau\eta)\alpha_2\alpha_2} \overline{\mathbf{D}}_\Omega^{\alpha_2} - L_{fm2}^{(\tau\eta)\alpha_2\alpha_2} & \overline{\mathbf{D}}_\Omega^{*\alpha_2} \mathbf{A}_{uu}^{(\tau\eta)\alpha_2\alpha_3} \overline{\mathbf{D}}_\Omega^{\alpha_3} & \overline{\mathbf{D}}_\Omega^{*\alpha_2} \mathbf{A}_{u\phi}^{(\tau\eta)\alpha_2\alpha_4} \overline{\mathbf{D}}_\Omega^{\alpha_4} & \overline{\mathbf{D}}_\Omega^{*\alpha_2} \mathbf{A}_{uT}^{(\tau\eta)\alpha_2\alpha_5} \overline{\mathbf{D}}_\Omega^{\alpha_5} & \overline{\mathbf{D}}_\Omega^{*\alpha_2} \mathbf{A}_{uC}^{(\tau\eta)\alpha_2\alpha_6} \overline{\mathbf{D}}_\Omega^{\alpha_6} \\
\overline{\mathbf{D}}_\Omega^{*\alpha_3} \mathbf{A}_{uu}^{(\tau\eta)\alpha_3\alpha_1} \overline{\mathbf{D}}_\Omega^{\alpha_1} & \overline{\mathbf{D}}_\Omega^{*\alpha_3} \mathbf{A}_{uu}^{(\tau\eta)\alpha_3\alpha_2} \overline{\mathbf{D}}_\Omega^{\alpha_2} & \overline{\mathbf{D}}_\Omega^{*\alpha_3} \mathbf{A}_{uu}^{(\tau\eta)\alpha_3\alpha_3} \overline{\mathbf{D}}_\Omega^{\alpha_3} - L_{fm3}^{(\tau\eta)\alpha_3\alpha_3} & \overline{\mathbf{D}}_\Omega^{*\alpha_3} \mathbf{A}_{u\phi}^{(\tau\eta)\alpha_3\alpha_4} \overline{\mathbf{D}}_\Omega^{\alpha_4} & \overline{\mathbf{D}}_\Omega^{*\alpha_3} \mathbf{A}_{uT}^{(\tau\eta)\alpha_3\alpha_5} \overline{\mathbf{D}}_\Omega^{\alpha_5} & \overline{\mathbf{D}}_\Omega^{*\alpha_3} \mathbf{A}_{uC}^{(\tau\eta)\alpha_3\alpha_6} \overline{\mathbf{D}}_\Omega^{\alpha_6} \\
\hline
\overline{\mathbf{D}}_\Omega^{*\alpha_4} \mathbf{A}_{\phi u}^{(\tau\eta)\alpha_4\alpha_1} \overline{\mathbf{D}}_\Omega^{\alpha_1} & \overline{\mathbf{D}}_\Omega^{*\alpha_4} \mathbf{A}_{\phi u}^{(\tau\eta)\alpha_4\alpha_2} \overline{\mathbf{D}}_\Omega^{\alpha_2} & \overline{\mathbf{D}}_\Omega^{*\alpha_4} \mathbf{A}_{\phi u}^{(\tau\eta)\alpha_4\alpha_3} \overline{\mathbf{D}}_\Omega^{\alpha_3} & \overline{\mathbf{D}}_\Omega^{*\alpha_4} \mathbf{A}_{\phi\phi}^{(\tau\eta)\alpha_4\alpha_4} \overline{\mathbf{D}}_\Omega^{\alpha_4} & \overline{\mathbf{D}}_\Omega^{*\alpha_4} \mathbf{A}_{\phi T}^{(\tau\eta)\alpha_4\alpha_5} \overline{\mathbf{D}}_\Omega^{\alpha_5} & \overline{\mathbf{D}}_\Omega^{*\alpha_4} \mathbf{A}_{\phi C}^{(\tau\eta)\alpha_4\alpha_6} \overline{\mathbf{D}}_\Omega^{\alpha_6} \\
\hline
0 & 0 & 0 & 0 & \overline{\mathbf{D}}_\Omega^{*\alpha_5} \mathbf{A}_{\vartheta\vartheta}^{(\tau\eta)\alpha_5\alpha_5} \overline{\mathbf{D}}_\Omega^{\alpha_5} & \overline{\mathbf{D}}_\Omega^{*\alpha_5} \mathbf{A}_{\lambda\vartheta}^{(\tau\eta)\alpha_5\alpha_6} \overline{\mathbf{D}}_\Omega^{\alpha_6} \\
\hline
0 & 0 & 0 & 0 & \overline{\mathbf{D}}_\Omega^{*\alpha_6} \mathbf{A}_{\lambda\vartheta}^{(\tau\eta)\alpha_6\alpha_5} \overline{\mathbf{D}}_\Omega^{\alpha_5} & \overline{\mathbf{D}}_\Omega^{*\alpha_6} \mathbf{A}_{\lambda\lambda}^{(\tau\eta)\alpha_6\alpha_6} \overline{\mathbf{D}}_\Omega^{\alpha_6}
\end{array}\right] \tag{61}$$

Note that the terms $L_{fm1}^{(\tau\eta)\alpha_1\alpha_1}, L_{fm2}^{(\tau\eta)\alpha_2\alpha_2}, L_{fm3}^{(\tau\eta)\alpha_3\alpha_3}$ are evaluated from the higher-order expression of the actions induced by the Winkler-Pasternak elastic foundation, as shown in Eq. (50). The solution of the fundamental Eqs. (60) is determined by using the well-known Navier's method. To this end, the curvilinear abscissa $s_i = s_1, s_2$ with $s_i \in \left[s_i^0, s_i^1\right]$ is considered, where the quantities $L_i = s_i^1 - s_i^0$ for $i = 1, 2$ represent the lengths of the parametric lines along the coordinate directions α_1, α_2. Each element of the unknown field variable vector $\delta^{(\tau)}$ is expanded using a double trigonometric series by setting $\widetilde{N} = \widetilde{M} = +\infty$, thus leading to the following expressions:

$$\begin{aligned}
u_1^{(\tau)}(s_1,s_2) &= \sum_{n=1}^{\tilde N}\sum_{m=1}^{\tilde M} \mathrm{U}_{1nm}^{(\tau)}\cos\left(\frac{n\pi}{L_1}s_1\right)\sin\left(\frac{m\pi}{L_2}s_2\right)\\
u_2^{(\tau)}(s_1,s_2) &= \sum_{n=1}^{\tilde N}\sum_{m=1}^{\tilde M} \mathrm{U}_{2nm}^{(\tau)}\sin\left(\frac{n\pi}{L_1}s_1\right)\cos\left(\frac{m\pi}{L_2}s_2\right)\\
u_3^{(\tau)}(s_1,s_2) &= \sum_{n=1}^{\tilde N}\sum_{m=1}^{\tilde M} \mathrm{U}_{3nm}^{(\tau)}\sin\left(\frac{n\pi}{L_1}s_1\right)\sin\left(\frac{m\pi}{L_2}s_2\right)\\
\phi^{(\tau)}(s_1,s_2) &= \sum_{n=1}^{\tilde N}\sum_{m=1}^{\tilde M} \Phi_{nm}^{(\tau)}\sin\left(\frac{n\pi}{L_1}s_1\right)\sin\left(\frac{m\pi}{L_2}s_2\right)\\
\xi^{(\tau)}(s_1,s_2) &= \sum_{n=1}^{\tilde N}\sum_{m=1}^{\tilde M} \Xi_{nm}^{(\tau)}\sin\left(\frac{n\pi}{L_1}s_1\right)\sin\left(\frac{m\pi}{L_2}s_2\right)\\
\kappa^{(\tau)}(s_1,s_2) &= \sum_{n=1}^{\tilde N}\sum_{m=1}^{\tilde M} \mathrm{K}_{nm}^{(\tau)}\sin\left(\frac{n\pi}{L_1}s_1\right)\sin\left(\frac{m\pi}{L_2}s_2\right)
\end{aligned} \tag{62}$$

In the previous relation, the variables of the formulation are expanded across the physical domain for each $\tau = 0,\dots,N+1$. Therefore, the wave amplitudes $\mathrm{U}_{1nm}^{(\tau)}, \mathrm{U}_{2nm}^{(\tau)}, \mathrm{U}_{3nm}^{(\tau)}, \Phi_{nm}^{(\tau)}, \Xi_{nm}^{(\tau)}, \mathrm{K}_{nm}^{(\tau)}$, introduced for each $n = 1,\dots,\widetilde N$ and $m = 1,\dots,\widetilde M$, are the unknown variables of the problem. Following the same approach, the generalized external surface loads, derived from Eq. (47), are expressed as follows:

$$\begin{aligned}
q_{1s}^{(\tau)}(s_1,s_2) &= \sum_{n=1}^{\tilde N}\sum_{m=1}^{\tilde M} Q_{1snm}^{(\tau)}\cos\left(\frac{n\pi}{L_1}s_1\right)\sin\left(\frac{m\pi}{L_2}s_2\right)\\
q_{2s}^{(\tau)}(s_1,s_2) &= \sum_{n=1}^{\tilde N}\sum_{m=1}^{\tilde M} Q_{2snm}^{(\tau)}\sin\left(\frac{n\pi}{L_1}s_1\right)\cos\left(\frac{m\pi}{L_2}s_2\right)\\
q_{3s}^{(\tau)}(s_1,s_2) &= \sum_{n=1}^{\tilde N}\sum_{m=1}^{\tilde M} Q_{3snm}^{(\tau)}\sin\left(\frac{n\pi}{L_1}s_1\right)\sin\left(\frac{m\pi}{L_2}s_2\right)\\
q_{\mathrm{D}s}^{(\tau)}(s_1,s_2) &= \sum_{n=1}^{\tilde N}\sum_{m=1}^{\tilde M} Q_{\mathrm{D}snm}^{(\tau)}\sin\left(\frac{n\pi}{L_1}s_1\right)\sin\left(\frac{m\pi}{L_2}s_2\right)\\
q_{\mathrm{T}s}^{(\tau)}(s_1,s_2) &= \sum_{n=1}^{\tilde N}\sum_{m=1}^{\tilde M} Q_{\mathrm{T}snm}^{(\tau)}\sin\left(\frac{n\pi}{L_1}s_1\right)\sin\left(\frac{m\pi}{L_2}s_2\right)\\
q_{\mathrm{C}s}^{(\tau)}(s_1,s_2) &= \sum_{n=1}^{\tilde N}\sum_{m=1}^{\tilde M} Q_{\mathrm{C}snm}^{(\tau)}\sin\left(\frac{n\pi}{L_1}s_1\right)\sin\left(\frac{m\pi}{L_2}s_2\right)
\end{aligned} \tag{63}$$

The wave amplitudes from Eq. (63) are collected within the vector $\mathbf{Q}_{snm}^{(\tau)} = \left[Q_{1snm}^{(\tau)} \quad Q_{2snm}^{(\tau)} \quad Q_{3snm}^{(\tau)} \quad Q_{\mathrm{D}snm}^{(\tau)} \quad Q_{\mathrm{T}snm}^{(\tau)} \quad Q_{\mathrm{C}snm}^{(\tau)}\right]^T$. Similarly, the vector $\mathbf{U}_{nm}^{(\eta)} = \left[\mathrm{U}_{1nm}^{(\tau)} \quad \mathrm{U}_{2nm}^{(\tau)} \quad \mathrm{U}_{3nm}^{(\tau)} \quad \Phi_{nm}^{(\tau)} \quad \Xi_{nm}^{(\tau)} \quad \mathrm{K}_{nm}^{(\tau)}\right]^T$ is introduced, which contains the wave amplitudes of the unknown variables of Eq. (62). By substituting Eq. (63) into Eq. (47), an effective expression for the elements of the vector $\mathbf{Q}_{snm}^{(\tau)}$ is obtained, in terms of wave amplitudes $Q_{\alpha snm}^{(-)}$ and $Q_{\alpha snm}^{(+)}$, with $\alpha = 1,2,3,\mathrm{D},\mathrm{T},\mathrm{C}$ and $i = 1,\dots,6$, as obtained from the Fourier expansion of the multifield surface loads at the top and bottom surfaces of the 3D solid. One gets:

$$\begin{aligned}
Q_{1snm}^{(\tau)} &= Q_{1snm}^{(-)}F_\tau^{(1)\alpha_1(-)}H_1^{(-)}H_2^{(-)} + Q_{1snm}^{(+)}F_\tau^{(I)\alpha_1(+)}H_1^{(+)}H_2^{(+)}\\
Q_{2snm}^{(\tau)} &= Q_{2snm}^{(-)}F_\tau^{(1)\alpha_2(-)}H_1^{(-)}H_2^{(-)} + Q_{2snm}^{(+)}F_\tau^{(I)\alpha_2(+)}H_1^{(+)}H_2^{(+)}\\
Q_{3snm}^{(\tau)} &= Q_{3snm}^{(-)}F_\tau^{(1)\alpha_3(-)}H_1^{(-)}H_2^{(-)} + Q_{3snm}^{(+)}F_\tau^{(I)\alpha_3(+)}H_1^{(+)}H_2^{(+)}\\
Q_{\mathrm{D}snm}^{(\tau)} &= Q_{\mathrm{D}snm}^{(-)}F_\tau^{(1)\alpha_4(-)}H_1^{(-)}H_2^{(-)} + Q_{\mathrm{D}snm}^{(+)}F_\tau^{(I)\alpha_4(+)}H_1^{(+)}H_2^{(+)}\\
Q_{\mathrm{T}snm}^{(\tau)} &= Q_{\mathrm{T}snm}^{(-)}F_\tau^{(1)\alpha_5(-)}H_1^{(-)}H_2^{(-)} + Q_{\mathrm{T}snm}^{(+)}F_\tau^{(I)\alpha_5(+)}H_1^{(+)}H_2^{(+)}\\
Q_{\mathrm{C}snm}^{(\tau)} &= Q_{\mathrm{C}snm}^{(-)}F_\tau^{(1)\alpha_6(-)}H_1^{(-)}H_2^{(-)} + Q_{\mathrm{C}snm}^{(+)}F_\tau^{(I)\alpha_6(+)}H_1^{(+)}H_2^{(+)}
\end{aligned} \tag{64}$$

At this point, some assumptions are made regarding the materials within the laminate, as shown in Ref. [58]. In particular, it is assumed that the laminate follows a cross-ply stacking sequence. To achieve this, it is assumed that the material orientation angle, as defined in Eq. (26), is set to either $\vartheta^{(k)} = 0$ or $\vartheta^{(k)} = \pm\pi/2$. In addition, some elements of the matrices introduced in Eq. (23) are assumed null, based on the following expressions:

$$\begin{aligned}
&\overline{\boldsymbol{\Gamma}}_{\mathrm{C}}^{(k)} = \begin{bmatrix} \overline{C}_{11}^{(k)} & \overline{C}_{12}^{(k)} & 0 & 0 & 0 & \overline{C}_{13}^{(k)}\\ \overline{C}_{12}^{(k)} & \overline{C}_{22}^{(k)} & 0 & 0 & 0 & \overline{C}_{23}^{(k)}\\ 0 & 0 & \overline{C}_{66}^{(k)} & 0 & 0 & 0\\ 0 & 0 & 0 & \overline{C}_{44}^{(k)} & 0 & 0\\ 0 & 0 & 0 & 0 & \overline{C}_{55}^{(k)} & 0\\ \overline{C}_{13}^{(k)} & \overline{C}_{23}^{(k)} & 0 & 0 & 0 & \overline{C}_{33}^{(k)} \end{bmatrix}\\
&\overline{\boldsymbol{\Gamma}}_{\mathrm{L}}^{(k)} = \begin{bmatrix} \bar l_{11}^{(k)} & 0 & 0\\ 0 & \bar l_{22}^{(k)} & 0\\ 0 & 0 & \bar l_{33}^{(k)} \end{bmatrix}\\
&\overline{\boldsymbol{\Gamma}}_{\mathrm{P}}^{(k)} = \begin{bmatrix} 0 & 0 & 0 & \bar p_{14}^{(k)} & 0 & 0\\ 0 & 0 & 0 & 0 & \bar p_{25}^{(k)} & 0\\ \bar p_{31}^{(k)} & \bar p_{32}^{(k)} & 0 & 0 & 0 & \bar p_{33}^{(k)} \end{bmatrix}\\
&\overline{\boldsymbol{\Gamma}}_{\mathrm{z}}^{(k)} = \left[\bar z_{11}^{(k)} \;\; \bar z_{22}^{(k)} \;\; 0 \;\; 0 \;\; 0 \;\; \bar z_{33}^{(k)}\right]\\
&\overline{\boldsymbol{\Gamma}}_{\mathrm{e}}^{(k)} = \left[\bar e_{11}^{(k)} \;\; \bar e_{22}^{(k)} \;\; 0 \;\; 0 \;\; 0 \;\; \bar e_{33}^{(k)}\right]\\
&\overline{\boldsymbol{\Gamma}}_{\mathrm{o}}^{(k)} = \left[0 \;\; 0 \;\; \bar o_{33}^{(k)}\right],\; \overline{\boldsymbol{\Gamma}}_{\mathrm{g}}^{(k)} = \left[0 \;\; 0 \;\; \bar g_{33}^{(k)}\right]\\
&\overline{\boldsymbol{\Gamma}}_{\mathrm{K}}^{(k)} = \begin{bmatrix} \bar k_{11}^{(k)} & 0 & 0\\ 0 & \bar k_{22}^{(k)} & 0\\ 0 & 0 & \bar k_{33}^{(k)} \end{bmatrix},\; \overline{\boldsymbol{\Gamma}}_{\mathrm{Y}}^{(k)} = \begin{bmatrix} \bar y_{11}^{(k)} & 0 & 0\\ 0 & \bar y_{22}^{(k)} & 0\\ 0 & 0 & \bar y_{33}^{(k)} \end{bmatrix}\\
&\overline{\boldsymbol{\Gamma}}_{\mathrm{X}}^{(k)} = \begin{bmatrix} \bar x_{11}^{(k)} & 0 & 0\\ 0 & \bar x_{22}^{(k)} & 0\\ 0 & 0 & \bar x_{33}^{(k)} \end{bmatrix},\; \overline{\boldsymbol{\Gamma}}_{\mathrm{S}}^{(k)} = \begin{bmatrix} \bar s_{11}^{(k)} & 0 & 0\\ 0 & \bar s_{22}^{(k)} & 0\\ 0 & 0 & \bar s_{33}^{(k)} \end{bmatrix}\\
&\overline{\boldsymbol{\Gamma}}_{\mathrm{TT}}^{(k)} = \bar\xi_{11}^{(k)},\; \overline{\boldsymbol{\Gamma}}_{\mathrm{TC}}^{(k)} = \bar\xi_{12}^{(k)},\; \overline{\boldsymbol{\Gamma}}_{\mathrm{CC}}^{(k)} = \bar\xi_{22}^{(k)}
\end{aligned} \tag{65}$$

Finally, the geometric properties of the doubly-curved shell solid, are defined accordingly to the ELW approach from Eq. (1). More specifically, it is assumed that the reference surface $\mathbf{r}(\alpha_1,\alpha_2)$ is characterized by uniform principal radii of curvature and Lamé parameters, as defined in Eq. (3):

$$A_i = \mathrm{cost} \Rightarrow \frac{\partial^{n+m}A_i}{\partial s_1^n \partial s_2^m} = 0, \quad R_i = \mathrm{cost} \Rightarrow \frac{\partial^{n+m}R_i}{\partial s_1^n \partial s_2^m} = 0 \tag{66}$$

Under these assumptions, the lengths L_1, L_2 of the parametric lines of the reference surface along α_1,α_2 can be expressed as follows, setting $R_1 = R_2 = R$:

$$\begin{aligned}
s_1 &= R(\varphi - \varphi_0) \;\; \to L_1 = s_1^1 - s_1^0 = R(\varphi_1 - \varphi_0)\\
s_2 &= R(\vartheta - \vartheta_0) \;\; \to L_2 = s_2^1 - s_2^0 = R(\vartheta_1 - \vartheta_0)
\end{aligned} \tag{67}$$

In the previous equation, the 2D parametric domain is assumed to be rectangular with $\left[\alpha_1^0,\alpha_1^1\right] \times \left[\alpha_2^0,\alpha_2^1\right] = \left[\varphi_1^0,\varphi_1^1\right] \times \left[\vartheta_2^0,\vartheta_2^1\right]$. In the case of a circular cylinder with curvature $k_{n2} = 1/R_2 = 0$ and radius $R_1 = R$, the curvilinear abscissae are $s_1 = R(\varphi - \varphi_0)$, $s_2 = y$, while the lengths of the parametric lines are $L_1 = s_1^1 - s_1^0 = R(\varphi_1 - \varphi_0)$ and $L_2 = s_2^1 - s_2^0$. Similarly, for a circular cylinder with curvature $k_{n1} = 1/R_1 = 0$ and $R_2 = R$, it is assumed that $s_1 = y$, $s_2 = R(\vartheta - \vartheta_0)$ and $L_1 = s_1^1 - s_1^0$, $L_2 = s_2^1 - s_2^0 = R(\vartheta_1 - \vartheta_0)$. Finally, for a rectangular plate with null curvatures $1/R_1 = 1/R_2 = 0$, the curvilinear abscissae are denoted by $s_1 = x$, $s_2 = y$, and the parametric lines are characterized by the lengths $L_1 = s_1^1 - s_1^0$, $L_2 = s_2^1 - s_2^0$. It should be noted that the introduction of the

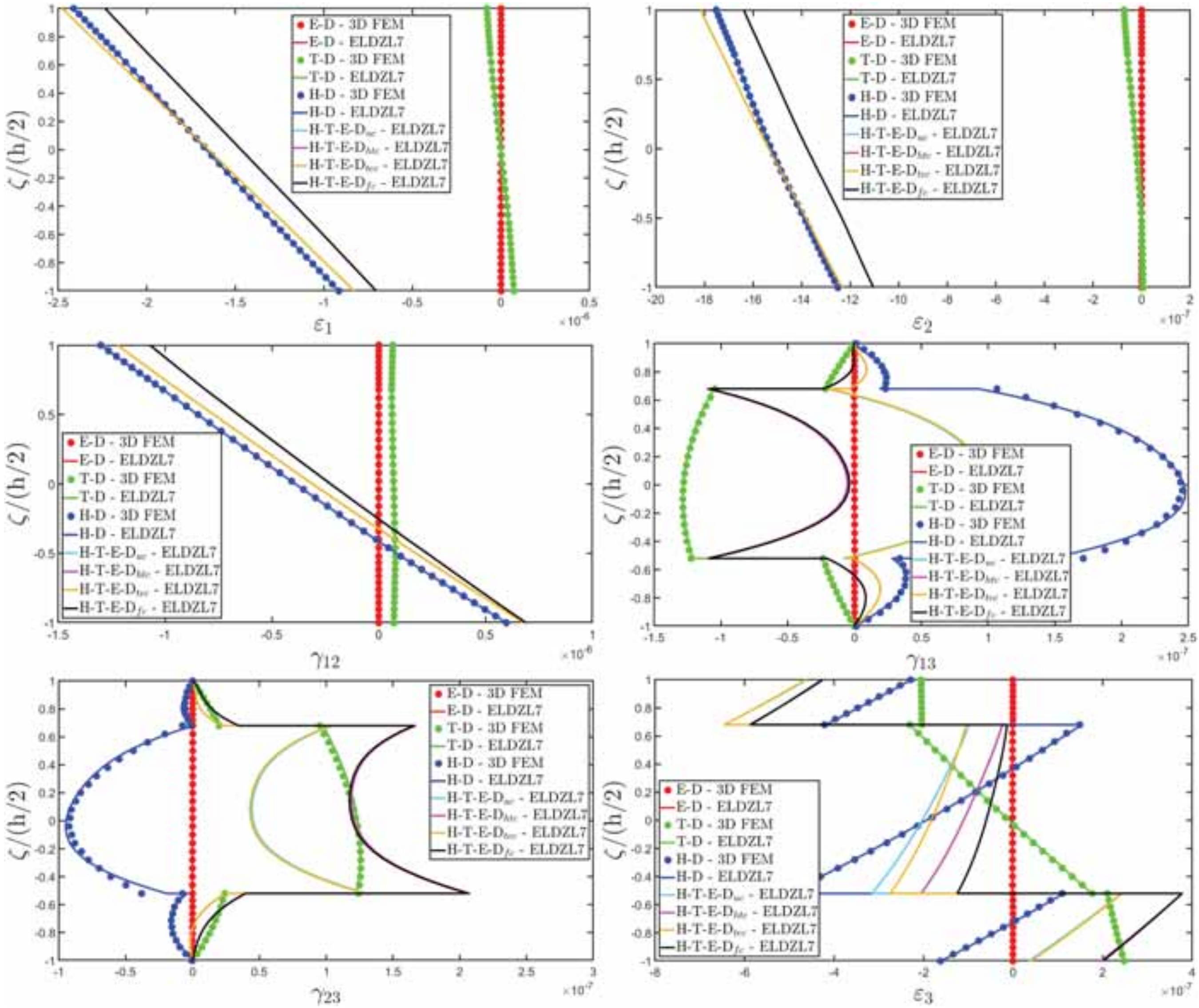

Fig. 11. Representation of the distributions along the thickness direction of 3D strain components of a cylindrical panel-2 for the point located at $(s_1, s_2) = (0.75L_1, 0.25L_2)$. Comparison against 3D FEM results and effect of multifield coupling.

geometric assumptions outlined in Eq. (66) simplifies the expression of the generalized multifield constitutive coefficients $A^{(\tau\eta)[fg]\,\alpha_i\alpha_j}_{rsnm\,(pq)}$, which were introduced in Eq. (42). In this way, the introduction of Eqs. (62)-(63) into the higher-order multifield fundamental Eqs. (60) leads to the following linear algebraic system:

The complete expression of the coefficients $\widetilde{L}^{(\tau\eta)\alpha_i\alpha_j}_{ijnm}$ of the matrix $\widetilde{\mathbf{L}}^{(\tau\eta)}_{nm}$ can be found in Appendix I.

It should be noted that Eq. (68) provides the exact solution of the differential equations for $\widetilde{N} = \widetilde{M} = +\infty$. However, when a finite value is selected for $\widetilde{N}, \widetilde{M}$, a semi-analytical solution is obtained with a sufficient level of accuracy. Using a compact notation, Eq. (68) is expressed as:

$$\sum_{n=1}^{\widetilde{N}}\sum_{m=1}^{\widetilde{M}}\left(\sum_{\eta=0}^{N+1}\left[\begin{array}{ccc|c|c|c}
\widetilde{L}^{(\tau\eta)\alpha_1\alpha_1}_{11nm}-\widetilde{L}^{(\tau\eta)\alpha_1\alpha_1}_{fm1nm} & \widetilde{L}^{(\tau\eta)\alpha_1\alpha_2}_{12nm} & \widetilde{L}^{(\tau\eta)\alpha_1\alpha_3}_{13nm} & \widetilde{L}^{(\tau\eta)\alpha_1\alpha_4}_{14nm} & \widetilde{L}^{(\tau\eta)\alpha_1\alpha_5}_{15nm} & \widetilde{L}^{(\tau\eta)\alpha_1\alpha_6}_{16nm} \\
\widetilde{L}^{(\tau\eta)\alpha_2\alpha_1}_{21nm} & \widetilde{L}^{(\tau\eta)\alpha_2\alpha_2}_{22nm}-\widetilde{L}^{(\tau\eta)\alpha_2\alpha_2}_{fm2nm} & \widetilde{L}^{(\tau\eta)\alpha_2\alpha_3}_{23nm} & \widetilde{L}^{(\tau\eta)\alpha_2\alpha_4}_{24nm} & \widetilde{L}^{(\tau\eta)\alpha_2\alpha_5}_{25nm} & \widetilde{L}^{(\tau\eta)\alpha_2\alpha_6}_{26nm} \\
\widetilde{L}^{(\tau\eta)\alpha_3\alpha_1}_{31nm} & \widetilde{L}^{(\tau\eta)\alpha_3\alpha_2}_{32nm} & \widetilde{L}^{(\tau\eta)\alpha_3\alpha_3}_{33nm}-\widetilde{L}^{(\tau\eta)\alpha_3\alpha_3}_{fm3nm} & \widetilde{L}^{(\tau\eta)\alpha_3\alpha_4}_{34nm} & \widetilde{L}^{(\tau\eta)\alpha_3\alpha_5}_{35nm} & \widetilde{L}^{(\tau\eta)\alpha_3\alpha_6}_{36nm} \\
\hline
\widetilde{L}^{(\tau\eta)\alpha_4\alpha_1}_{41nm} & \widetilde{L}^{(\tau\eta)\alpha_4\alpha_2}_{42nm} & \widetilde{L}^{(\tau\eta)\alpha_4\alpha_3}_{43nm} & \widetilde{L}^{(\tau\eta)\alpha_4\alpha_4}_{44nm} & \widetilde{L}^{(\tau\eta)\alpha_4\alpha_5}_{45nm} & \widetilde{L}^{(\tau\eta)\alpha_4\alpha_6}_{46nm} \\
\hline
\widetilde{L}^{(\tau\eta)\alpha_5\alpha_1}_{51nm} & \widetilde{L}^{(\tau\eta)\alpha_5\alpha_2}_{52nm} & \widetilde{L}^{(\tau\eta)\alpha_5\alpha_3}_{53nm} & \widetilde{L}^{(\tau\eta)\alpha_5\alpha_4}_{54nm} & \widetilde{L}^{(\tau\eta)\alpha_5\alpha_5}_{55nm} & \widetilde{L}^{(\tau\eta)\alpha_5\alpha_6}_{56nm} \\
\hline
\widetilde{L}^{(\tau\eta)\alpha_6\alpha_1}_{61nm} & \widetilde{L}^{(\tau\eta)\alpha_6\alpha_2}_{62nm} & \widetilde{L}^{(\tau\eta)\alpha_6\alpha_3}_{63nm} & \widetilde{L}^{(\tau\eta)\alpha_6\alpha_4}_{64nm} & \widetilde{L}^{(\tau\eta)\alpha_6\alpha_5}_{65nm} & \widetilde{L}^{(\tau\eta)\alpha_6\alpha_6}_{66nm}
\end{array}\right]\begin{bmatrix} \mathrm{U}^{(\eta)}_{1nm} \\ \mathrm{U}^{(\eta)}_{2nm} \\ \mathrm{U}^{(\eta)}_{3nm} \\ \Phi^{(\tau)}_{nm} \\ \Xi^{(\eta)}_{nm} \\ \mathrm{K}^{(\eta)}_{nm} \end{bmatrix} + \begin{bmatrix} Q^{(\tau)}_{1nm} \\ Q^{(\tau)}_{2nm} \\ Q^{(\tau)}_{3nm} \\ Q^{(\tau)}_{\mathrm{D}nm} \\ Q^{(\tau)}_{\mathrm{T}nm} \\ Q^{(\tau)}_{\mathrm{C}nm} \end{bmatrix}\right) = \begin{bmatrix} 0 \\ 0 \\ 0 \\ 0 \\ 0 \\ 0 \end{bmatrix} \tag{68}$$

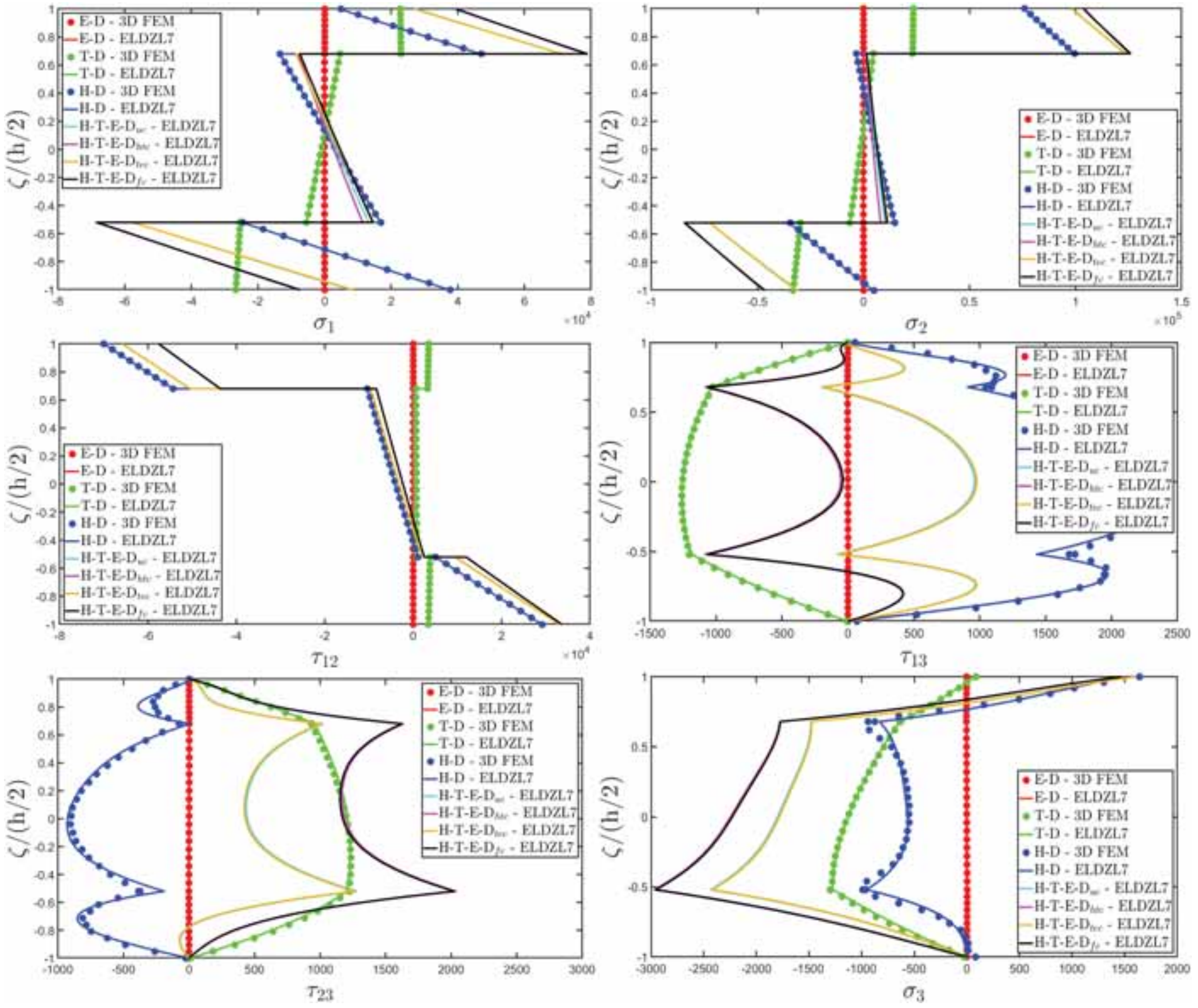

Fig. 12. Representation of the distributions along the thickness direction of 3D stress components of a cylindrical panel-2 for the point located at $(s_1, s_2) = (0.75L_1, 0.25L_2)$. Comparison against 3D FEM results and effect of multifield coupling.

$$\sum_{n=1}^{\tilde{N}}\sum_{m=1}^{\tilde{M}}\left(\sum_{\eta=0}^{N+1}\widetilde{\mathbf{L}}_{nm}^{(\tau\eta)}\mathbf{U}_{nm}^{(\eta)}+\mathbf{Q}_{snm}^{(\tau)}\right)=\mathbf{0} \tag{69}$$

3. Generalized differential and integral quadrature

In the present section, we introduce the fundamental aspects of the GDQ method here used in the post-processing phase of this research. The method is based on the definition of a rectangular computational domain, based on a non-uniform grid distribution of sample points [85]. For this purpose, the well-known Chebyshev–Gauss–Lobatto (CGL) harmonic distribution is employed. Referring to the interval $[a,b]$, if the total number of sample points is I_Q, the position of an arbitrary element x_i with $i=1,\dots,I_Q$ is obtained from that, denoted by,$\bar{x}_i$ on the computational grid, using the following expression:

$$x_i=\frac{x_{I_Q}-x_1}{\bar{x}_{I_Q}-\bar{x}_1}(\bar{x}_i-\bar{x}_1)+x_1=\frac{b-a}{2}\left(1-\cos\left(\frac{i-1}{I_Q-1}\pi\right)\right)+a \tag{70}$$

In this way, the n-th order derivative of an arbitrary smooth function $f=f(x)$ with $x\in[a,b]$ at point x_i, as defined in Eq. (70), is evaluated using the values $f(x_j)$ assumed by the function f at each j-th point of the grid, as follows [85]:

$$f^{(n)}(x_i)=\left.\frac{\partial^n f(x)}{\partial x^n}\right|_{x=x_i}\cong\sum_{j=1}^{I_Q}\varsigma_{ij}^{(n)}f(x_j) \tag{71}$$

In the previous equation, $\varsigma_{ij}^{(n)}$ represents the GDQ weighting coefficients, which are evaluated using a recursive methodology [85] involving the first-order derivative of the Lagrange polynomials, denoted by $\mathscr{L}^{(1)}(x_i)$ and $\mathscr{L}^{(1)}(x_j)$, evaluated at points x_i and x_j, respectively:

$$\begin{aligned}&\varsigma_{ij}^{(1)}=\frac{\mathscr{L}^{(1)}(x_i)}{(x_i-x_j)\mathscr{L}^{(1)}(x_j)},\quad \varsigma_{ij}^{(n)}=n\left(\varsigma_{ij}^{(1)}\varsigma_{ii}^{(n-1)}-\frac{\varsigma_{ij}^{(n-1)}}{x_i-x_j}\right)\quad i\neq j\\ &\varsigma_{ii}^{(n)}=-\sum_{j=1,j\neq i}^{I_Q}\varsigma_{ij}^{(n)}\quad i=j\end{aligned} \tag{72}$$

When Eq. (72) is applied to the computational interval $[-1,1]$, the corresponding weighting coefficients $\tilde{\varsigma}_{ij}^{(n)}$ are transformed into $\varsigma_{ij}^{(n)}$, associated with the interval ,$[a,b]$ by using the coordinate

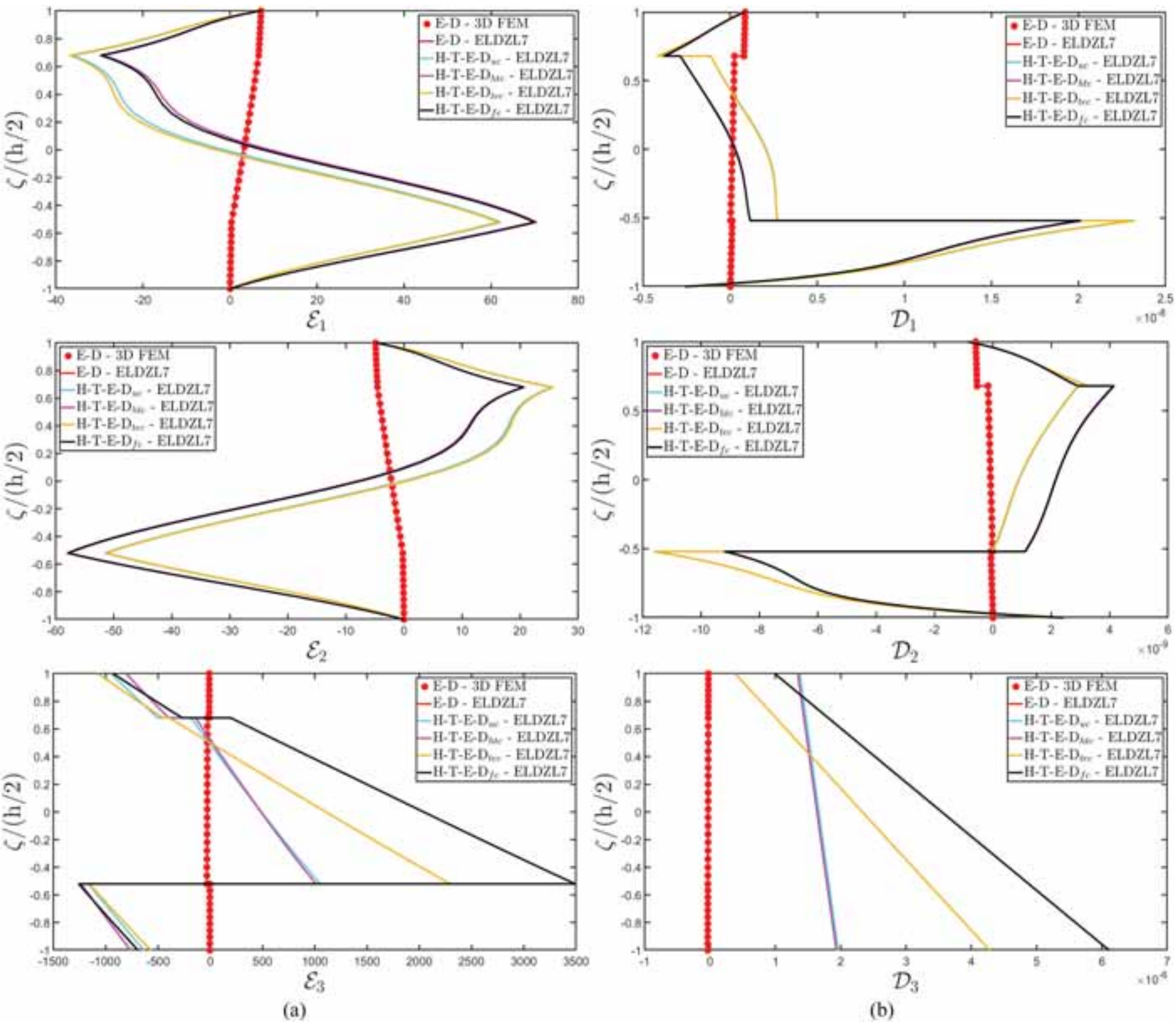

Fig. 13. Representation of the distributions along the thickness direction of 3D electric primary (a) and secondary (b) variables of a cylindrical panel-2 for the point located at $(s_1, s_2) = (0.75L_1, 0.25L_2)$. Comparison against 3D FEM results and effect of multifield coupling.

transformation from Eq. (70). This yields the following expression for $\varsigma_{ij}^{(n)}$:

$$\varsigma_{ij}^{(n)} = \left(\frac{\overline{x}_{I_Q} - \overline{x}_1}{x_{I_Q} - x_1}\right)^n \tilde{\varsigma}_{ij}^{(n)} \tag{73}$$

The integrals in Eq. (42), along with those required during the post-processing phase, are computed using the T-GIQ numerical method. Building on the GDQ rule introduced in Eq. (71), the T-GIQ method [85] employs a Taylor series expansion to approximate the integral of a given function $f = f(x)$ with $x \in [a, b]$ over the interval $[x_i, x_j] \subseteq [a, b]$ with $i, j = 1, \ldots, I_Q$, where I_Q is the number of discrete points. If $f(x_k)$ represents the value of the function at the discrete point x_k, with $k = 1, \ldots, I_Q$, the following relation is used:

$$\int_{x_i}^{x_j} f(x)dx = \sum_{k=1}^{I_Q} w_k^{ij} f(x_k) \tag{74}$$

Here, w_k^{ij} for $k = 1, \ldots, I_Q$ are the T-GIQ coefficients for the quadrature formula. To derive the expression for w_k^{ij}, the integral in Eq. (74) is decomposed into the sum of two integrals, as shown below:

$$\int_{x_i}^{x_j} f(x)dx = \int_{x_i}^{\frac{x_j+x_i}{2}} f(x)dx - \int_{x_j}^{\frac{x_j+x_i}{2}} f(x)dx \tag{75}$$

The integrals in the previous relation are expanded using the Taylor series as follows:

$$\int_{x_i}^{x_j} f(x)dx = \sum_{r=0}^{m-1} \frac{\left(\frac{x_j+x_i}{2} - x_i\right)^{r+1}}{(r+1)!} \left.\frac{d^r f}{dx^r}\right|_{x_i} - \sum_{r=0}^{m-1} \frac{\left(\frac{x_j+x_i}{2} - x_j\right)^{r+1}}{(r+1)!} \left.\frac{d^r f}{dx^r}\right|_{x_j} \tag{76}$$

The derivatives of r-th order in Eq. (76) are numerically computed using the GDQ method from Eq. (71), resulting in the following expression:

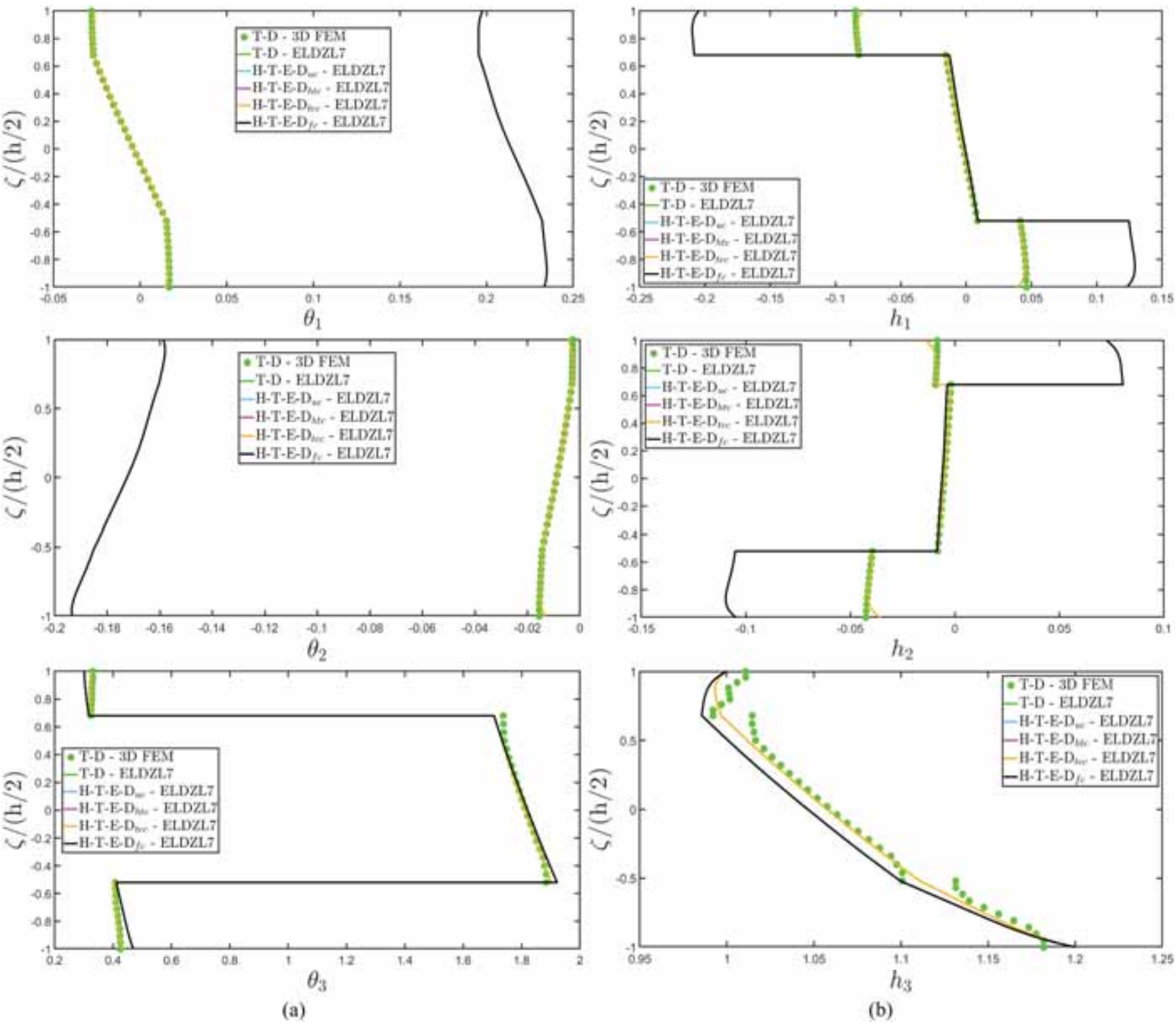

Fig. 14. Representation of the distributions along the thickness direction of 3D thermal primary (a) and secondary (b) variables of a cylindrical panel-2 for the point located at $(s_1, s_2) = (0.75L_1, 0.25L_2)$. Comparison against 3D FEM results and effect of multifield coupling.

$$\int_{x_i}^{x_j} f(x)dx = \sum_{r=0}^{m-1} \frac{(x_j - x_i)^{r+1}}{2^{r+1}(r+1)!} \sum_{k=1}^{N} \varsigma_{ik}^{(r)} f(x_k) - \sum_{r=0}^{m-1} \frac{(x_i - x_j)^{r+1}}{2^{r+1}(r+1)!} \sum_{k=1}^{N} \varsigma_{jk}^{(r)} f(x_k) =$$
$$= \sum_{k=1}^{N} \left(\sum_{r=0}^{m-1} \left(\frac{(x_j - x_i)^{r+1}}{2^{r+1}(r+1)!} \varsigma_{ik}^{(r)} - \frac{(x_i - x_j)^{r+1}}{2^{r+1}(r+1)!} \varsigma_{jk}^{(r)} \right) \right) f(x_k) =$$
$$= \sum_{k=1}^{N} \left(\sum_{r=0}^{m-1} \frac{(x_j - x_i)^{r+1}}{2^{r+1}(r+1)!} \left(\varsigma_{ik}^{(r)} + (-1)^{r+2} \varsigma_{jk}^{(r)} \right) \right) f(x_k) = \sum_{k=1}^{N} w_k^{ij} f(x_k) \tag{77}$$

Recalling that $[x_i, x_j] \subseteq [a, b]$, the integral of the function f over the interval $[a = x_1, b = x_N]$ can be expressed as the sum of all the integrals in Eq. (77) over the interval $[x_i, x_j]$:

$$\int_a^b f(x)dx = \sum_{i=1}^{N-1} \int_{x_i}^{x_{i+1}} f(x)dx = \sum_{i=1}^{N-1} \left(\sum_{k=1}^{N} w_k^{i(i+1)} f(x_k) \right)$$
$$= \sum_{k=1}^{N} \left(\sum_{i=1}^{N-1} w_k^{i(i+1)} \right) f(x_k) = \sum_{k=1}^{N} w_k^{1N} f(x_k) \tag{78}$$

4. Post-processing recovery of multifield variables

Once the solution to the differential Eqs. (69) is obtained, the reconstruction of the multifield response of the 3D solid is performed. To this end, a grid of discrete points of size $I_T \times 1$ is introduced within each k-th layer of the stacking sequence, based on the CGL distribution from Eq. (70), located within the interval $[\zeta_k, \zeta_{k+1}]$ along the thickness

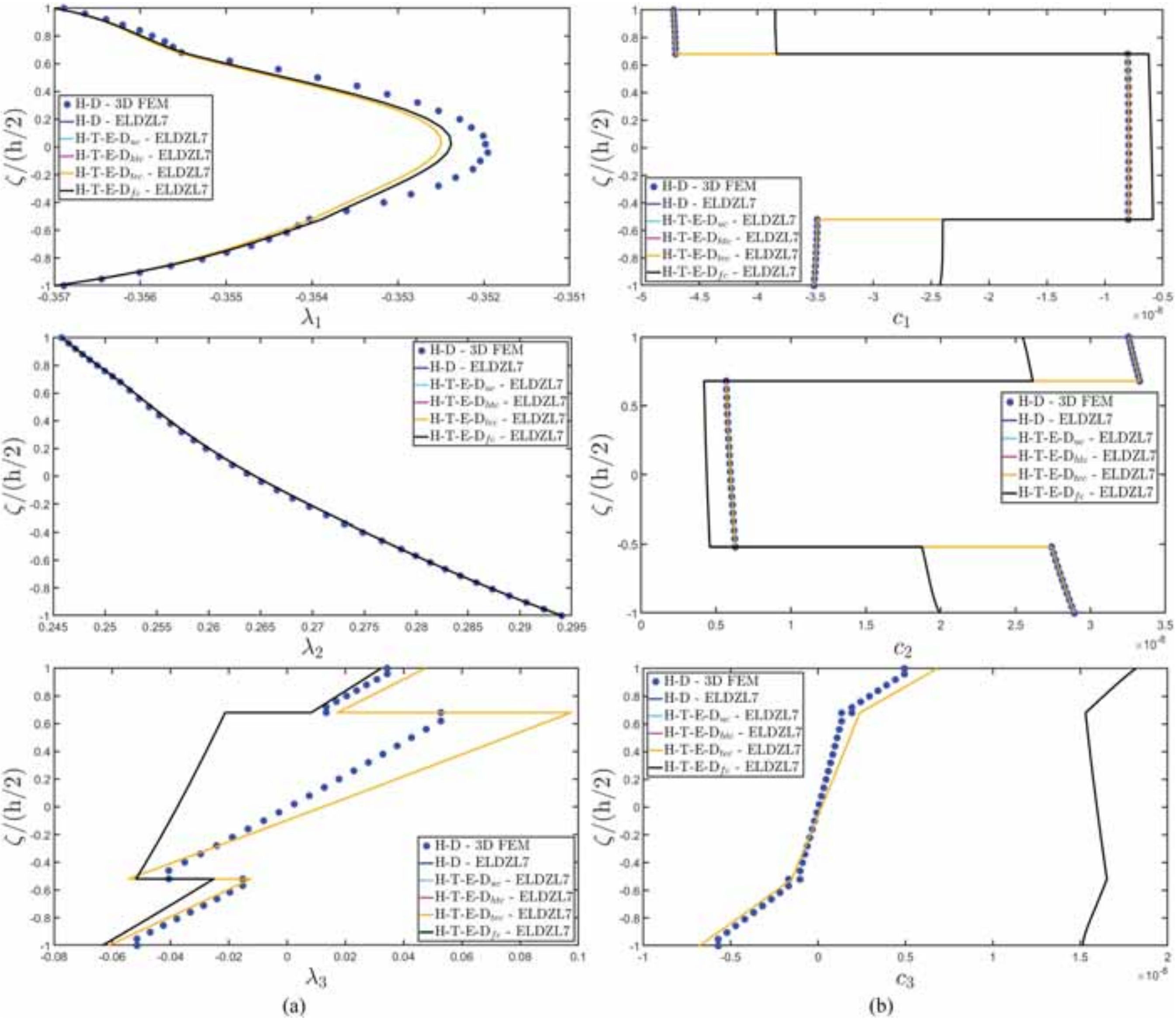

Fig. 15. Representation of the distributions along the thickness direction of 3D hygrometric primary (a) and secondary (b) variables of a cylindrical panel-2 for the point located at $(s_1, s_2) = (0.75L_1, 0.25L_2)$. Comparison against 3D FEM results and effect of multifield coupling.

direction. The arbitrary element of this grid is denoted by $\zeta_{\tilde{m}}^{(k)}$ with $\tilde{m} = 1, ..., I_T$, and it is determined using the following relation [58]:

$$\zeta_{\tilde{m}}^{(k)} = \frac{\zeta_{k+1} - \zeta_k}{2}\overline{x}_{\tilde{m}} + \frac{\zeta_{k+1} + \zeta_k}{2} = \frac{h_k}{2}\overline{x}_{\tilde{m}} + \frac{\zeta_{k+1} + \zeta_k}{2} \tag{79}$$

In this way, the vector $\boldsymbol{\zeta}^{(k)} = \left[\zeta_1^{(k)} \quad \cdots \quad \zeta_{\tilde{m}}^{(k)} \quad \cdots \quad \zeta_{I_T}^{(k)}\right]^T$ is conveniently introduced. This vector is then assembled into the vector $\boldsymbol{\zeta} = [\zeta_1 \ \cdots \ \zeta_m \ \cdots \ \zeta_{l I_T}]^T = [\boldsymbol{\zeta}^{(1)T} \ \cdots \ \boldsymbol{\zeta}^{(k)T} \ \cdots \ \boldsymbol{\zeta}^{(l)T}]$ of size $lI_Q \times 1$, where l denotes the total number of layers. The index m is defined such that $m = (k-1)I_T + \tilde{m}$. It should be noted that the introduction of the discrete grid along the thickness direction, as described in Eq. (70), results in conforming discrete points at each interface between adjacent layers. This is particularly important for reconstructing primary and secondary variables that exhibit stepwise profiles. In other words, the relation $\zeta_{I_T}^{(k)} = \zeta_1^{(k+1)} = \zeta_{kI_T} = \zeta_{(k+1)1}$ is satisfied at the interfaces within the elements of vector $\boldsymbol{\zeta}$. Finally, a 2D discrete grid of size $I_N \times I_M$ is defined within the physical domain, expressed in terms of curvilinear abscissae s_1, s_2, using the CGL grid from Eq. (70). The position (s_{1i}, s_{2j}) of an arbitrary sampling point of this grid is derived by the following expression:

$$s_{1i} = \frac{L_1}{2}\left(1 - \cos\left(\frac{i-1}{I_N - 1}\pi\right)\right), \quad s_{2j} = \frac{L_2}{2}\left(1 - \cos\left(\frac{j-1}{I_M - 1}\pi\right)\right) \tag{80}$$

Note that $s_{1i} \in [0, L_1]$ and $s_{2j} \in [0, L_2]$. Using Eq. (5), it is then possible to obtain the 3D distribution of each element of the vector $\boldsymbol{\Delta}_{(ijm)}^{(k)}$, where $\boldsymbol{\delta}_{(ij)}^{(\tau)}$ is the vector of the unknown configuration variables from the higher-order theory, associated with the τ-th kinematic expansion order and evaluated for the point (s_{1i}, s_{2j}) within the physical domain:

$$\boldsymbol{\Delta}_{(ijm)}^{(k)} = \sum_{\tau=0}^{N+1} \mathbf{F}_{\tau(m)}^{(k)} \boldsymbol{\delta}_{(ij)}^{(\tau)} \tag{81}$$

Following a similar approach, the discrete version of the higher-order definition equations from Eq. (18) is used to derive the elements of the vector $\boldsymbol{\pi}_{(ijm)}^{(k)}$, which represents the 3D multifield primary variables:

$$\boldsymbol{\pi}^{(k)}_{(ijm)} = \sum_{\tau=0}^{N+1} \sum_{i=1}^{6} \mathbf{Z}^{(k\tau)\alpha_i}_{(ijm)} \boldsymbol{\pi}^{(\tau)\alpha_i}_{(ij)} \tag{82}$$

The primary variables derived from Eq. (82) are then used to determine the in-plane multifield secondary variables, which are contained within the vector $\chi^{(k)}$, by applying the 3D constitutive relations from Eq. (22), while taking into account the material assumptions outlined in Eq. (65). The following relations are, thus, obtained:

$$\begin{aligned}
\sigma^{(k)}_{1(ijm)} &= \overline{C}^{(k)}_{11(ijm)}\varepsilon^{(k)}_{1(ijm)} + \overline{C}^{(k)}_{12(ijm)}\varepsilon^{(k)}_{2(ijm)} + \overline{C}^{(k)}_{13(ijm)}\varepsilon^{(k)}_{3(ijm)} - \overline{p}^{(k)}_{31(ijm)}\mathscr{E}^{(k)}_{3(ijm)} - \overline{z}^{(k)}_{11(ijm)}\widehat{\Delta \mathrm{T}}^{(k)}_{(ijm)} - \overline{e}^{(k)}_{11(ijm)}\widehat{\Delta \mathrm{C}}^{(k)}_{(ijm)} \\
\sigma^{(k)}_{2(ijm)} &= \overline{C}^{(k)}_{12(ijm)}\varepsilon^{(k)}_{1(ijm)} + \overline{C}^{(k)}_{22(ijm)}\varepsilon^{(k)}_{2(ijm)} + \overline{C}^{(k)}_{23(ijm)}\varepsilon^{(k)}_{3(ijm)} - \overline{p}^{(k)}_{32(ijm)}\mathscr{E}^{(k)}_{3(ijm)} - \overline{z}^{(k)}_{22(ijm)}\widehat{\Delta \mathrm{T}}^{(k)}_{(ijm)} - \overline{e}^{(k)}_{22(ijm)}\widehat{\Delta \mathrm{C}}^{(k)}_{(ijm)} \\
\tau^{(k)}_{12(ijm)} &= \overline{C}^{(k)}_{66(ijm)}\gamma^{(k)}_{12(ijm)} \\
\mathscr{D}^{(k)}_{1(ijm)} &= \overline{p}^{(k)}_{14(ijm)}\gamma^{(k)}_{13(ijm)} + \overline{l}^{(k)}_{11(ijm)}\mathscr{E}^{(k)}_{1(ijm)} \\
\mathscr{D}^{(k)}_{2(ijm)} &= \overline{p}^{(k)}_{25(ijm)}\gamma^{(k)}_{23(ijm)} + \overline{l}^{(k)}_{22(ijm)}\mathscr{E}^{(k)}_{2(ijm)} \\
h^{(k)}_{1(ijm)} &= \overline{k}^{(k)}_{11(ijm)}\theta^{(k)}_{1(ijm)} + \overline{y}^{(k)}_{11(ijm)}\lambda^{(k)}_{1(ijm)} \\
h^{(k)}_{2(ijm)} &= \overline{k}^{(k)}_{22(ijm)}\theta^{(k)}_{2(ijm)} + \overline{y}^{(k)}_{22(ijm)}\lambda^{(k)}_{2(ijm)} \\
c^{(k)}_{1(ijm)} &= \overline{x}^{(k)}_{11(ijm)}\theta^{(k)}_{1(ijm)} + \overline{s}^{(k)}_{11(ijm)}\lambda^{(k)}_{1(ijm)} \\
c^{(k)}_{2(ijm)} &= \overline{x}^{(k)}_{22(ijm)}\theta^{(k)}_{2(ijm)} + \overline{s}^{(k)}_{22(ijm)}\lambda^{(k)}_{2(ijm)}
\end{aligned} \tag{83}$$

On the other hand, the secondary variables associated with the out-of-plane principal direction ζ are not derived from Eq. (82). Instead, they are obtained from the balance equations for a doubly-curved 3D solid. More specifically, the out-of-plane shear stresses $\tau^{(k)}_{13}$ and $\tau^{(k)}_{23}$ are determined from the 3D equilibrium equations, expressed in curvilinear principal coordinates, referred to the thickness direction ζ [58]:

$$\begin{aligned}
&\frac{\partial \tau^{(k)}_{13}}{\partial \zeta} + \tau^{(k)}_{13}\left(\frac{2}{R_1+\zeta} + \frac{1}{R_2+\zeta}\right) = -\frac{1}{A_1(1+\zeta/R_1)}\frac{\partial \sigma^{(k)}_1}{\partial \alpha_1} + \\
&\quad + \frac{\sigma^{(k)}_2 - \sigma^{(k)}_1}{A_1A_2(1+\zeta/R_2)}\frac{\partial A_2}{\partial \alpha_1} - \frac{1}{A_2(1+\zeta/R_2)}\frac{\partial \tau^{(k)}_{12}}{\partial \alpha_2} - \frac{2\tau^{(k)}_{12}}{A_1A_2(1+\zeta/R_1)}\frac{\partial A_1}{\partial \alpha_2} \\
&\frac{\partial \tau^{(k)}_{23}}{\partial \zeta} + \tau^{(k)}_{23}\left(\frac{1}{R_1+\zeta} + \frac{2}{R_2+\zeta}\right) = -\frac{1}{A_2(1+\zeta/R_2)}\frac{\partial \sigma^{(k)}_2}{\partial \alpha_2} + \\
&\quad + \frac{\sigma^{(k)}_1 - \sigma^{(k)}_2}{A_1A_2(1+\zeta/R_1)}\frac{\partial A_1}{\partial \alpha_2} - \frac{1}{A_1(1+\zeta/R_1)}\frac{\partial \tau^{(k)}_{12}}{\partial \alpha_1} - \frac{2\tau^{(k)}_{12}}{A_1A_2(1+\zeta/R_2)}\frac{\partial A_2}{\partial \alpha_1}
\end{aligned} \tag{84}$$

The boundary conditions associated with the first-order differential equations in Eq. (84) are provided below for the first layer ($k = 1$) in the stacking sequence. These conditions are physically related to the loading conditions at the bottom surface, located at $\zeta = -h/2$:

$$\begin{aligned}
\overline{\tau}^{(1)}_{13(ij1)} &= q^{(-)}_{1s(ij)} \\
\overline{\tau}^{(1)}_{23(ij1)} &= q^{(-)}_{2s(ij)}
\end{aligned} \tag{85}$$

On the other hand, the boundary conditions for an arbitrary k-th layer with $k \neq 1$ of the laminate are expressed in terms of the stress compatibility conditions at the interface between the $(k-1)$-th lamina and the k-th layer:

$$\begin{aligned}
\overline{\tau}^{(k)}_{13\left(ij\left((k-1)I_Q+1\right)\right)} &= \overline{\tau}^{(k-1)}_{13\left(ij\left((k-1)I_Q\right)\right)} \\
\overline{\tau}^{(k)}_{23\left(ij\left((k-1)I_Q+1\right)\right)} &= \overline{\tau}^{(k-1)}_{23\left(ij\left((k-1)I_Q\right)\right)}
\end{aligned} \tag{86}$$

Once the solution of Eq. (84) is obtained through Eqs. (85)–(86), the loading conditions $\overline{\tau}^{(l)}_{13\left(ij\left(lI_Q\right)\right)} = q^{(+)}_{1(ij)}$ and $\overline{\tau}^{(l)}_{23\left(ij\left(lI_Q\right)\right)} = q^{(+)}_{2(ij)}$ at the top surface, corresponding to the in-plane loads, are used to adjust the corrected solution. To this end, the following expressions [58] are considered for any arbitrary point within the 3D solid, located at $\left(s_{1i}, s_{2j}, \zeta_m\right)$ within the discrete domain, where $m = 1, \dots, lI_Q$:

$$\begin{aligned}\tau^{(k)}_{13(ijm)} &= \overline{\tau}^{(k)}_{13(ijm)} + \frac{q^{(+)}_{1(ij)} - \overline{\tau}^{(l)}_{13(ij(lI_Q))}}{h}\left(\zeta_m + \frac{h}{2}\right)\\ \tau^{(k)}_{23(ijm)} &= \overline{\tau}^{(k)}_{23(ijm)} + \frac{q^{(+)}_{2(ij)} - \overline{\tau}^{(l)}_{23(ij(lI_Q))}}{h}\left(\zeta_m + \frac{h}{2}\right)\end{aligned} \tag{87}$$

Once the actual distribution of $\tau^{(k)}_{13}$ and $\tau^{(k)}_{23}$ shear stresses is determined from Eq. (87), the same procedure is applied to obtain the 3D distribution of the normal stress $\sigma^{(k)}_3$. The equilibrium equation reported below is adopted:

$$\begin{aligned}\frac{\partial \sigma^{(k)}_3}{\partial \zeta} + \sigma^{(k)}_3\left(\frac{1}{R_1+\zeta} + \frac{1}{R_2+\zeta}\right) = -\frac{1}{A_1(1+\zeta/R_1)}\frac{\partial \tau^{(k)}_{13}}{\partial \alpha_1} - \frac{\tau^{(k)}_{13}}{A_1A_2(1+\zeta/R_2)}\frac{\partial A_2}{\partial \alpha_1} + \\ - \frac{1}{A_2(1+\zeta/R_2)}\frac{\partial \tau^{(k)}_{23}}{\partial \alpha_2} - \frac{\tau^{(k)}_{23}}{A_1A_2(1+\zeta/R_1)}\frac{\partial A_1}{\partial \alpha_2} + \frac{\sigma^{(k)}_1}{R_1+\zeta} + \frac{\sigma^{(k)}_2}{R_2+\zeta}\end{aligned} \tag{88}$$

Similarly, the 3D balance equations associated with electricity, thermal conduction, and moisture diffusion are solved to determine the through-the-thickness distribution of the out-of-plane electric flux $\sigma^{(k)}_3$, thermal flux $h^{(k)}_3$, and mass concentration flux $c^{(k)}_3$:

$$\begin{aligned}\frac{\partial \mathscr{A}^{(k)}_3}{\partial \zeta} + \mathscr{A}^{(k)}_3\left(\frac{1}{R_1+\zeta} + \frac{1}{R_2+\zeta}\right) = -\frac{1}{A_1(1+\zeta/R_1)}\frac{\partial \mathscr{A}^{(k)}_1}{\partial \alpha_1}\\ -\frac{\mathscr{A}^{(k)}_1}{A_1A_2(1+\zeta/R_2)}\frac{\partial A_2}{\partial \alpha_1} + \\ -\frac{1}{A_2(1+\zeta/R_2)}\frac{\partial \mathscr{A}^{(k)}_2}{\partial \alpha_2} - \frac{\mathscr{A}^{(k)}_2}{A_1A_2(1+\zeta/R_1)}\frac{\partial A_1}{\partial \alpha_2}\end{aligned} \tag{89}$$

with $\mathscr{A}^{(k)}_3 = \mathscr{D}^{(k)}_3, h^{(k)}_3, c^{(k)}_3$. Note that the quantities $\mathscr{A}^{(k)}_1 = \mathscr{D}^{(k)}_1, h^{(k)}_1, c^{(k)}_1$ and $\mathscr{A}^{(k)}_2 = \mathscr{D}^{(k)}_2, h^{(k)}_2, c^{(k)}_2$ are determined from the constitutive relations, as shown in Eq. (83). The boundary conditions associated with the first-order balance equations in Eq. (89), which are derived from the loading conditions at the bottom side and the interface compatibility, are expressed as:

$$\begin{aligned}k = 1 \;\Rightarrow\; &\begin{cases}\overline{\sigma}^{(1)}_{3(ij1)} = q^{(-)}_{3s(ij)}\\ \overline{\mathscr{D}}^{(1)}_{3(ij1)} = q^{(-)}_{Ds(ij)}\\ \overline{h}^{(1)}_{3(ij1)} = q^{(-)}_{Ts(ij)}\\ \overline{c}^{(1)}_{3(ij1)} = q^{(-)}_{Cs(ij)}\end{cases}\\ k \neq 1 \;\Rightarrow\; &\begin{cases}\overline{\sigma}^{(k)}_{3(ij((k-1)I_T+1))} = \overline{\sigma}^{(k-1)}_{3(ij((k-1)I_T))}\\ \overline{\mathscr{D}}^{(k)}_{3(ij((k-1)I_T+1))} = \overline{\mathscr{D}}^{(k-1)}_{3(ij((k-1)I_T))}\\ \overline{h}^{(k)}_{3(ij((k-1)I_T+1))} = \overline{h}^{(k-1)}_{3(ij((k-1)I_T))}\\ \overline{c}^{(k)}_{3(ij((k-1)I_T+1))} = \overline{c}^{(k-1)}_{3(ij((k-1)I_T))}\end{cases}\end{aligned} \tag{90}$$

The solution of the relations in Eq. (89) through Eq. (90) yields the quantities $\overline{\sigma}^{(k)}_{3(ijm)}, \overline{\mathscr{D}}^{(k)}_{3(ijm)}, \overline{h}^{(k)}_{3(ijm)}, \overline{c}^{(k)}_{3(ijm)}$. Finally, the balance under multi-field loads applied at the top surface is satisfied through the following linear correction [58]:

$$\begin{aligned}\sigma^{(k)}_{3(ijm)} &= \overline{\sigma}^{(k)}_{3(ijm)} + \frac{q^{(+)}_{3s(ij)} - \overline{\sigma}^{(l)}_{3(ij(lI_Q))}}{h}\left(\zeta_m + \frac{h}{2}\right)\\ \mathscr{D}^{(k)}_{3(ijm)} &= \overline{\mathscr{D}}^{(k)}_{3(ijm)} + \frac{q^{(+)}_{Ds(ij)} - \overline{\mathscr{D}}^{(l)}_{3(ij(lI_Q))}}{h}\left(\zeta_m + \frac{h}{2}\right)\\ h^{(k)}_{3(ijm)} &= \overline{h}^{(k)}_{3(ijm)} + \frac{q^{(+)}_{Ts(ij)} - \overline{h}^{(l)}_{3(ij(lI_Q))}}{h}\left(\zeta_m + \frac{h}{2}\right)\\ c^{(k)}_{3(ijm)} &= \overline{c}^{(k)}_{3(ijm)} + \frac{q^{(+)}_{Cs(ij)} - \overline{c}^{(l)}_{3(ij(lI_Q))}}{h}\left(\zeta_m + \frac{h}{2}\right)\end{aligned} \tag{91}$$

It should be noted that the 3D balance equations used in the recovery procedure are the first-order differential equations, where $y^{(k)} = y^{(k)}\left(\zeta^{(k)}\right)$ with $\zeta^{(k)} \in [\zeta_k, \zeta_{k+1}]$ is the unknown variable. All these equations can be expressed in a general form as:

$$\frac{\partial y^{(k)}}{\partial \zeta^{(k)}} + a^{(k)}\left(\zeta^{(k)}\right)y^{(k)}\left(\zeta^{(k)}\right) = b^{(k)}\left(\zeta^{(k)}\right) \tag{92}$$

where $a^{(k)} = a^{(k)}\left(\zeta^{(k)}\right)$ and $b^{(k)} = b^{(k)}\left(\zeta^{(k)}\right)$ are the corresponding variable coefficients, which are expressed in terms of the quantities $B^{(k)}_1\left(\zeta^{(k)}\right), B^{(k)}_2\left(\zeta^{(k)}\right)$ as follows, setting $c, d = 1, 2$:

$$\begin{aligned}a^{(k)}\left(\zeta^{(k)}\right) &= \frac{c}{R_1+\zeta^{(k)}} + \frac{d}{R_2+\zeta^{(k)}}\\ b^{(k)}\left(\zeta^{(k)}\right) &= \frac{B^{(k)}_1\left(\zeta^{(k)}\right)}{R_1+\zeta^{(k)}} + \frac{B^{(k)}_2\left(\zeta^{(k)}\right)}{R_2+\zeta^{(k)}}\end{aligned} \tag{93}$$

The solution of Eq. (93) takes the following integral-based form for each $k = 1, \ldots, l$:

$$\begin{aligned}y^{(k)}\left(\zeta^{(k)}\right) &= e^{-A^{(k)}\left(\zeta^{(k)}\right)}\int_{\zeta^{(k)}_1}^{\zeta^{(k)}} e^{A^{(k)}\left(\zeta^{(k)}\right)}b^{(k)}\left(\zeta^{(k)}\right)d\zeta^{(k)} + y^{(k)}_1\\ &= e^{-A^{(k)}\left(\zeta^{(k)}\right)}\int_{\zeta^{(k)}_1}^{\zeta^{(k)}} f\left(\zeta^{(k)}\right)d\zeta^{(k)} + y^{(k)}_1\end{aligned} \tag{94}$$

The term $A^{(k)} = A^{(k)}\left(\zeta^{(k)}\right)$ occurring in the previous relation is a primitive function of the coefficient $a^{(k)} = a^{(k)}\left(\zeta^{(k)}\right)$ from Eq. (93). A closed-form expression for $A^{(k)}$ is provided below:

$$\begin{aligned}A^{(k)}\left(\zeta^{(k)}\right) &= \int a^{(k)}\left(\zeta^{(k)}\right)d\zeta^{(k)}\\ &= \begin{cases}\log\left(\left(R_1+\zeta^{(k)}\right)^c\left(R_2+\zeta^{(k)}\right)^d\right) & R_1 \neq \infty, R_2 \neq \infty\\ \log\left(\left(R_2+\zeta^{(k)}\right)^d\right) & R_1 = \infty, R_2 \neq \infty\\ \log\left(\left(R_1+\zeta^{(k)}\right)^c\right) & R_1 \neq \infty, R_2 = \infty\\ 0 & R_1 = R_2 = \infty\end{cases}\end{aligned} \tag{95}$$

On the other hand, $f^{(k)} = f^{(k)}\left(\zeta^{(k)}\right)$ assumes the following relation:

$$f^{(k)}\left(\zeta^{(k)}\right)=\begin{cases}\left(R_1+\zeta^{(k)}\right)^c\left(R_2+\zeta^{(k)}\right)^d b^{(k)}\left(\zeta^{(k)}\right) & R_1\neq\infty,R_2\neq\infty\\ \left(R_2+\zeta^{(k)}\right)^d b^{(k)}\left(\zeta^{(k)}\right) & R_1=\infty,R_2\neq\infty\\ \left(R_1+\zeta^{(k)}\right)^c b^{(k)}\left(\zeta^{(k)}\right) & R_1\neq\infty,R_2=\infty\\ b^{(k)}\left(\zeta^{(k)}\right) & R_1=R_2=\infty\end{cases}\tag{96}$$

The evaluation of the quantity f according to Eq. (96) at the discrete points ζ_m with $m=1,\dots,lI_T$ along the thickness direction yields the following definition of the column vector $\mathbf{f}$ of size $lI_T\times 1$:

$$\mathbf{f}^{(k)}=\mathbf{g}^{(k)}\odot\mathbf{b}^{(k)}=\mathbf{G}^{(k)}\mathbf{b}^{(k)}\tag{97}$$

where the vector $\mathbf{b}^{(k)}$ of size $I_T\times 1$ contains the discrete values of $b^{(k)}$ as defined in Eq. (93). Furthermore, the symbol $\odot$ denotes the well-known Hadamard product, while $\mathbf{G}^{(k)}=\operatorname{diag}\left(\mathbf{g}^{(k)}\right)$. The arbitrary element $g_m^{(k)}$ of the vector $\mathbf{g}^{(k)}$ is evaluated as follows:

$$g_m^{(k)}=\begin{cases}\left(R_1+\zeta_m^{(k)}\right)^c\left(R_2+\zeta_m^{(k)}\right)^d & R_1\neq\infty,R_2\neq\infty\\ \left(R_2+\zeta_m^{(k)}\right)^d & R_1=\infty,R_2\neq\infty\\ \left(R_1+\zeta_m^{(k)}\right)^c & R_1\neq\infty,R_2=\infty\\ 1 & R_1=R_2=\infty\end{cases}\tag{98}$$

The integral in Eq. (94) is evaluated within each k-th lamina over the interval $[\zeta_k,\zeta_{k+1}]$ using the T-GIQ rule, as presented in Eq. (78):

$$\begin{aligned}\int_{\zeta_1^{(k)}}^{\zeta_i^{(k)}} e^{-A\left(\zeta^{(k)}\right)}b\left(\zeta^{(k)}\right)d\zeta^{(k)}&=\int_{\zeta_1^{(k)}}^{\zeta_i^{(k)}} f\left(\zeta^{(k)}\right)d\zeta^{(k)}=\sum_{\tilde{m}=1}^{I_T}\left(w_{i\tilde{m}}-w_{1\tilde{m}}\right)f\left(\zeta_{\tilde{m}}^{(k)}\right)\\&=\sum_{\tilde{m}=1}^{I_T}w_k^{1i}f\left(\zeta_{\tilde{m}}^{(k)}\right)\end{aligned}\tag{99}$$

being $\zeta_{\tilde{m}}^{(k)}$ a local thickness coordinate. In this way, Eq. (94) takes the following matrix form:

$$y\left(\zeta_{\tilde{m}}^{(k)}\right)=g_{\tilde{m}}\sum_{i=1}^{I_T}w_i^{1\tilde{m}}g_i b\left(\zeta_i^{(k)}\right)+y_1^{(k)}\Rightarrow\mathbf{y}^{(k)}=\left(\mathbf{G}^{(k)}\right)^{-1}\mathbf{W}^{(k)}\mathbf{G}^{(k)}\mathbf{b}^{(k)}+y_1^{(k)}\tag{100}$$

Finally, Eq. (100) is simplified by assuming $\mathbf{G}^{(k)}\cong\mathbf{I}$, based on the fact that $\zeta_i,\zeta_l\ll R_1,R_2$ for an ordinary doubly-curved shell. This leads to the following relation:

$$y\left(\zeta_{\tilde{m}}^{(k)}\right)=\sum_{i=1}^{I_T}w_i^{1\tilde{m}}b\left(\zeta_i^{(k)}\right)+y_1^{(k)}\Rightarrow\mathbf{y}^{(k)}=\mathbf{W}^{(k)}\mathbf{b}^{(k)}+y_1^{(k)}\tag{101}$$

Finally, the out-of-plane primary variables are determined from the 3D constitutive relation by inverting Eq. (22). The following linear system is, thus, considered [58] at each discrete point within the solid:

$$\mathbf{A}_{(ijm)}^{(k)}\mathbf{x}_{(ijm)}^{(k)}=\mathbf{B}_{(ijm)}^{(k)}\Leftrightarrow\begin{bmatrix}\mathbf{A}_{11(ijm)}^{(k)} & \mathbf{0}\\ \mathbf{0} & \mathbf{A}_{22(ijm)}^{(k)}\end{bmatrix}\begin{bmatrix}\mathbf{x}_{1(ijm)}^{(k)}\\ \mathbf{x}_{2(ijm)}^{(k)}\end{bmatrix}=\begin{bmatrix}\mathbf{B}_{1(ijm)}^{(k)}\\ \mathbf{B}_{2(ijm)}^{(k)}\end{bmatrix}\tag{102}$$

As can be seen, the unknown vector $\mathbf{x}_{(ijm)}^{(k)}$ is split in two components, namely $\mathbf{x}_{1(ijm)}^{(k)}=\left[\gamma_{13(ijm)}^{(k)}\ \ \gamma_{23(ijm)}^{(k)}\ \ \varepsilon_{3(ijm)}^{(k)}\ \ \mathscr{E}_{3(ijm)}^{(k)}\right]^T$ and $\mathbf{x}_{2(ijm)}^{(k)}=\left[\theta_{3(ijm)}^{(k)}\ \ \lambda_{3(ijm)}^{(k)}\right]^T$. The coefficient matrices $\mathbf{A}_{11(ijm)}^{(k)}$ and $\mathbf{A}_{22(ijm)}^{(k)}$ take the following form:

$$\begin{gathered}\mathbf{A}_{11(ijm)}^{(k)}=\begin{bmatrix}\overline{C}_{44(ijm)}^{(k)} & \overline{C}_{45(ijm)}^{(k)} & \overline{C}_{34(ijm)}^{(k)} & -\overline{p}_{34(ijm)}^{(k)}\\ \overline{C}_{45(ijm)}^{(k)} & \overline{C}_{55(ijm)}^{(k)} & \overline{C}_{35(ijm)}^{(k)} & -\overline{p}_{35(ijm)}^{(k)}\\ \overline{C}_{34(ijm)}^{(k)} & \overline{C}_{35(ijm)}^{(k)} & \overline{C}_{33(ijm)}^{(k)} & -\overline{p}_{33(ijm)}^{(k)}\\ \overline{p}_{34(ijm)}^{(k)} & \overline{p}_{35(ijm)}^{(k)} & \overline{p}_{33(ijm)}^{(k)} & \overline{l}_{33(ijm)}^{(k)}\end{bmatrix}\\ \mathbf{A}_{22(ijm)}^{(k)}=\begin{bmatrix}\overline{k}_{33(ijm)}^{(k)} & \overline{y}_{33(ijm)}^{(k)}\\ \overline{x}_{33(ijm)}^{(k)} & \overline{s}_{33(ijm)}^{(k)}\end{bmatrix}\end{gathered}\tag{103}$$

Finally, the elements of the vectors $\mathbf{B}_{1(ijm)}^{(k)}=\left[b_{1(ijm)}^{(k)}\ b_{2(ijm)}^{(k)}b_{3(ijm)}^{(k)}b_{4(ijm)}^{(k)}\right]^T$ and $\mathbf{B}_{2(ijm)}^{(k)}=\left[b_{5(ijm)}^{(k)}\ \ b_{6(ijm)}^{(k)}\right]^T$ are evaluated as follows:

$$\begin{aligned}b_{1(ijm)}^{(k)}&=\tau_{13(ijm)}^{(k)}-\overline{C}_{14(ijm)}^{(k)}\varepsilon_{1(ijm)}^{(k)}-\overline{C}_{24(ijm)}^{(k)}\varepsilon_{2(ijm)}^{(k)}-\overline{C}_{46(ijm)}^{(k)}\gamma_{12(ijm)}^{(k)}+\overline{p}_{14(ijm)}^{(k)}\mathscr{E}_{1(ijm)}^{(k)}+\overline{p}_{24(ijm)}^{(k)}\mathscr{E}_{2(ijm)}^{(k)}+\\&\quad+\overline{z}_{13(ijm)}^{(k)}\widehat{\Delta T}_{(ijm)}^{(k)}+\overline{e}_{13(ijm)}^{(k)}\widehat{\Delta C}_{(ijm)}^{(k)}\\ b_{2(ijm)}^{(k)}&=\tau_{23(ijm)}^{(k)}-\overline{C}_{15(ijm)}^{(k)}\varepsilon_{1(ijm)}^{(k)}-\overline{C}_{25(ijm)}^{(k)}\varepsilon_{2(ijm)}^{(k)}-\overline{C}_{56(ijm)}^{(k)}\gamma_{12(ijm)}^{(k)}+\overline{p}_{15(ijm)}^{(k)}\mathscr{E}_{1(ijm)}^{(k)}+\overline{p}_{25(ijm)}^{(k)}\mathscr{E}_{2(ijm)}^{(k)}+\\&\quad+\overline{z}_{23(ijm)}^{(k)}\widehat{\Delta T}_{(ijm)}^{(k)}+\overline{e}_{23(ijm)}^{(k)}\widehat{\Delta C}_{(ijm)}^{(k)}\\ b_{3(ijm)}^{(k)}&=\sigma_{3(ijm)}^{(k)}-\overline{C}_{13(ijm)}^{(k)}\varepsilon_{1(ijm)}^{(k)}-\overline{C}_{23(ijm)}^{(k)}\varepsilon_{2(ijm)}^{(k)}-\overline{C}_{36(ijm)}^{(k)}\gamma_{12(ijm)}^{(k)}+\overline{p}_{13(ijm)}^{(k)}\mathscr{E}_{1(ijm)}^{(k)}+\overline{p}_{23(ijm)}^{(k)}\mathscr{E}_{2(ijm)}^{(k)}+\\&\quad+\overline{z}_{33(ijm)}^{(k)}\widehat{\Delta T}_{(ijm)}^{(k)}+\overline{e}_{33(ijm)}^{(k)}\widehat{\Delta C}_{(ijm)}^{(k)}\\ b_{4(ijm)}^{(k)}&=\mathscr{D}_{3(ijm)}^{(k)}-\overline{p}_{31(ijm)}^{(k)}\varepsilon_{1(ijm)}^{(k)}-\overline{p}_{32(ijm)}^{(k)}\varepsilon_{2(ijm)}^{(k)}-\overline{p}_{36(ijm)}^{(k)}\gamma_{12(ijm)}^{(k)}-\overline{l}_{13(ijm)}^{(k)}\mathscr{E}_{1(ijm)}^{(k)}-\overline{l}_{23(ijm)}^{(k)}\mathscr{E}_{2(ijm)}^{(k)}+\\&\quad-\overline{o}_{33(ijm)}^{(k)}\widehat{\Delta T}_{(ijm)}^{(k)}-\overline{g}_{33(ijm)}^{(k)}\widehat{\Delta C}_{(ijm)}^{(k)}\end{aligned}$$

$$\begin{aligned}b_{5(ijm)}^{(k)}&=h_{3(ijm)}^{(k)}-\overline{k}_{13(ijm)}^{(k)}\theta_{1(ijm)}^{(k)}-\overline{k}_{23(ijm)}^{(k)}\theta_{2(ijm)}^{(k)}-\overline{y}_{13(ijm)}^{(k)}\lambda_{1(ijm)}^{(k)}-\overline{y}_{23(ijm)}^{(k)}\lambda_{2(ijm)}^{(k)}\\ b_{6(ijm)}^{(k)}&=c_{3(ijm)}^{(k)}-\overline{x}_{13(ijm)}^{(k)}\theta_{1(ijm)}^{(k)}-\overline{x}_{23(ijm)}^{(k)}\theta_{2(ijm)}^{(k)}-\overline{s}_{13(ijm)}^{(k)}\lambda_{1(ijm)}^{(k)}-\overline{s}_{23(ijm)}^{(k)}\lambda_{2(ijm)}^{(k)}\end{aligned}\tag{104}$$

Note that the procedure outlined is based on the evaluation of in-plane secondary variables from Eq. (83), starting from the primary variables obtained in Eq. (82), without ensuring the equilibrium along the thickness direction, a-priori. Therefore, the recovery of primary and secondary variables must be repeated by using the primary variables

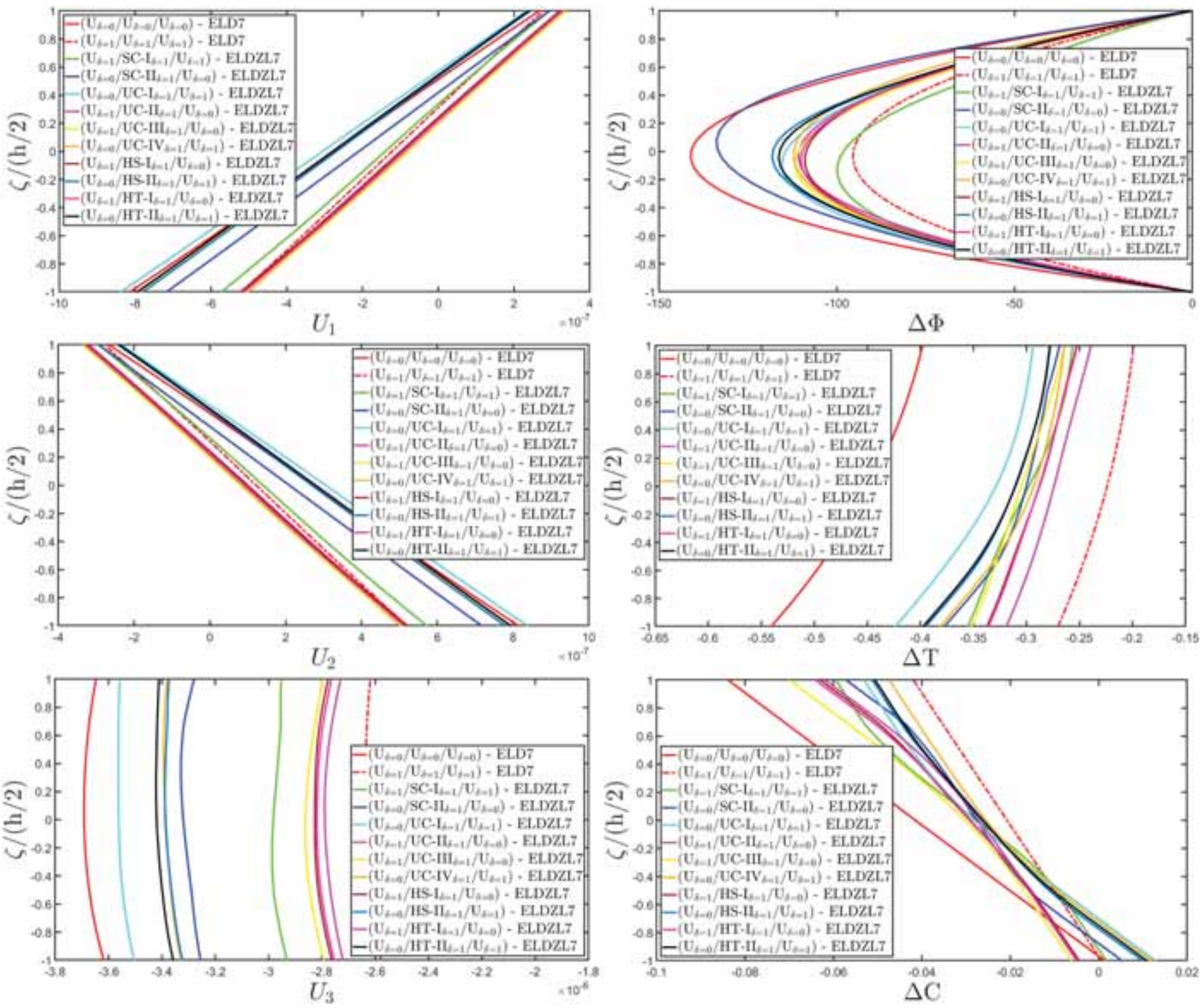

Fig. 16. Representation of the distributions along the thickness direction of the hygro-thermo-electro-mechanical configuration variables of a spherical shallow shell for the point located at $(s_1, s_2) = (0.25L_1, 0.75L_2)$. Comparison against 3D FEM results and effect of material variation.

obtained from Eq. (102) within the constitutive relationship in Eq. (83), until a convergence is achieved between two subsequent iterations of the procedure.

5. Applications and results

In this section, some numerical investigations are presented where the higher-order ELW formulation introduced in the paper is applied to derive the multifield response of curved panels. Following the approach outlined in Eq. (1), the geometry of each panel is fully described from the reference surface equation. In this context, a rectangular plate is described as follows [58]:

$$\mathbf{r}(s_1, s_2) = \mathbf{r}(x, y) = -x\,\mathbf{e}_2 + y\,\mathbf{e}_3 \tag{105}$$

where $(x, y) \in [0, L_1] \times [0, L_2]$, being L_1, L_2 the geometric sizes of the plate. In this case, it is $1/R_1 = 1/R_2 = 0$ and $A_1 = A_2 = 1$. On the other hand, the structure named Cylindrical panel-I, is described by the following reference surface [58], characterized by $1/R_2 = 0$, $R_1 = R$ and $A_1 = R$, $A_2 = 1$:

$$\mathbf{r}(\vartheta, y) = R\cos\vartheta\,\mathbf{e}_1 - y\,\mathbf{e}_2 + R\sin\vartheta\,\mathbf{e}_3 \tag{106}$$

If the α_1 direction is straight with zero curvature, the Cylindrical panel-II is obtained [58], whose reference surface is given as follows:

$$\mathbf{r}(x, \vartheta) = R\cos\vartheta\,\mathbf{e}_1 - R\sin\vartheta\,\mathbf{e}_2 + x\,\mathbf{e}_3 \tag{107}$$

Note that $1/R_1 = 0$, $R_2 = R$ and $A_1 = 1$, $A_2 = R$. Finally, in the case of a spherical shallow shell, the reference surface is characterized by $R_1 = R_2 = R$ and $A_1 = A_2 = R$.

The materials involved in the lamination scheme consist of two phases: cylindrical fibers of barium titanate ($BaTiO_3$), oriented along the thickness direction, and an isotropic matrix of cobalt ferrite ($CoFe_2O_4$) where the fibers are dispersed. The homogenized material properties are derived from the analytical expressions reported in Appendix II, based on Ref. [72], and are collected in Table 2. The homogenized materials are transversely isotropic with $\alpha_1 - \alpha_2$ as the isotropic plane. All the details regarding the geometric dimensions of each panel, as well as the lamination schemes adopted in the simulations, can be found in Fig. 1. Furthermore, in some simulations, arbitrary variations of the material properties have been considered, following the distributions detailed in Table 1. In this way, it is possible to obtain new configurations for the unit cell of the multifield material under consideration, in line with the representation reported in Fig. 2. The through-the-thickness distributions for the variation of the material properties are represented in Fig. 3. The multifield external loads are distributed within the physical domain according to Eq. (44). Following the Navier approach in Eq. (64), the amplitudes $Q_{\alpha snm}^{(-)}, Q_{\alpha snm}^{(+)}$ are evaluated from the Fourier expansion of Eq. (63), reading as:

$$\begin{aligned}
q_{1s}^{(\pm)}(s_1,s_2) &= \sum_{n=1}^{\tilde{N}}\sum_{m=1}^{\tilde{M}} Q_{1snm}^{(\pm)}\cos\left(\frac{n\pi}{L_1}s_1\right)\sin\left(\frac{m\pi}{L_2}s_2\right)\\
q_{2s}^{(\pm)}(s_1,s_2) &= \sum_{n=1}^{\tilde{N}}\sum_{m=1}^{\tilde{M}} Q_{2snm}^{(\pm)}\sin\left(\frac{n\pi}{L_1}s_1\right)\cos\left(\frac{m\pi}{L_2}s_2\right)\\
q_{3s}^{(\pm)}(s_1,s_2) &= \sum_{n=1}^{\tilde{N}}\sum_{m=1}^{\tilde{M}} Q_{3snm}^{(\pm)}\sin\left(\frac{n\pi}{L_1}s_1\right)\sin\left(\frac{m\pi}{L_2}s_2\right)\\
q_{\mathrm{D}}^{(\pm)}(s_1,s_2) &= \sum_{n=1}^{\tilde{N}}\sum_{m=1}^{\tilde{M}} Q_{\mathrm{D}snm}^{(\pm)}\sin\left(\frac{n\pi}{L_1}s_1\right)\sin\left(\frac{m\pi}{L_2}s_2\right)\\
q_{\mathrm{T}}^{(\pm)}(s_1,s_2) &= \sum_{n=1}^{\tilde{N}}\sum_{m=1}^{\tilde{M}} Q_{\mathrm{T}snm}^{(\pm)}\sin\left(\frac{n\pi}{L_1}s_1\right)\sin\left(\frac{m\pi}{L_2}s_2\right)\\
q_{\mathrm{C}}^{(\pm)}(s_1,s_2) &= \sum_{n=1}^{\tilde{N}}\sum_{m=1}^{\tilde{M}} Q_{\mathrm{C}snm}^{(\pm)}\sin\left(\frac{n\pi}{L_1}s_1\right)\sin\left(\frac{m\pi}{L_2}s_2\right)
\end{aligned} \tag{108}$$

Similarly, when a specific value of the unknown variables is enforced at the top and bottom surface, in line with Eq. (9), the following distributions are conveniently introduced, setting $\widetilde{N} = \widetilde{M} = 1$:

$$\begin{aligned}
U_1^{(\pm)}(s_1,s_2) &= \sum_{n=1}^{\tilde{N}}\sum_{m=1}^{\tilde{M}} \overline{U}_{1snm}^{(\pm)}\cos\left(\frac{n\pi}{L_1}s_1\right)\sin\left(\frac{m\pi}{L_2}s_2\right)\\
U_2^{(\pm)}(s_1,s_2) &= \sum_{n=1}^{\tilde{N}}\sum_{m=1}^{\tilde{M}} \overline{U}_{2snm}^{(\pm)}\sin\left(\frac{n\pi}{L_1}s_1\right)\cos\left(\frac{m\pi}{L_2}s_2\right)\\
U_3^{(\pm)}(s_1,s_2) &= \sum_{n=1}^{\tilde{N}}\sum_{m=1}^{\tilde{M}} \overline{U}_{3snm}^{(\pm)}\sin\left(\frac{n\pi}{L_1}s_1\right)\sin\left(\frac{m\pi}{L_2}s_2\right)\\
\Delta\phi^{(\pm)}(s_1,s_2) &= \sum_{n=1}^{\tilde{N}}\sum_{m=1}^{\tilde{M}} \Delta\overline{\phi}_s^{(\pm)}\sin\left(\frac{n\pi}{L_1}s_1\right)\sin\left(\frac{m\pi}{L_2}s_2\right)\\
\Delta\mathrm{T}^{(\pm)}(s_1,s_2) &= \sum_{n=1}^{\tilde{N}}\sum_{m=1}^{\tilde{M}} \Delta\overline{\mathrm{T}}_s^{(\pm)}\sin\left(\frac{n\pi}{L_1}s_1\right)\sin\left(\frac{m\pi}{L_2}s_2\right)\\
\Delta\mathrm{C}^{(\pm)}(s_1,s_2) &= \sum_{n=1}^{\tilde{N}}\sum_{m=1}^{\tilde{M}} \Delta\overline{\mathrm{C}}_s^{(\pm)}\sin\left(\frac{n\pi}{L_1}s_1\right)\sin\left(\frac{m\pi}{L_2}s_2\right)
\end{aligned} \tag{109}$$

A first preliminary investigation is conducted on a simply-supported rectangular plate consisting of four layers with different thicknesses and made of materials with multifield properties. The lamination scheme is (MAT − I\MAT − III\MAT − II\MAT − III), while the homogenized constitutive coefficients, derived from the homogenization procedure outlined in Appendix II, can be found in Table 2, as previously stated. More specifically, MAT-I and MAT-III are characterized by fiber volume fractions equal to $V_f = 0.2$ and $V_f = 0.6$, respectively, while the volume fraction of barium titanate in MAT-II is $V_f = 0.4$. Furthermore, in MAT-II, the homogenized constitutive matrix is multiplied by a scale factor equal to $1/3$. In this way, the lamination scheme contains a softer layer exhibiting stretching effects, leading to complicated deformation behaviors. The structure rests on a Winkler elastic foundation with linear springs of stiffness $k_{3f}^{(-)} = 5\times 10^{10}\,\mathrm{N/m^3}$ and $k_{1f}^{(-)} = k_{2f}^{(-)} = 0\,\mathrm{N/m^3}$ located at the bottom surface. Furthermore, it is subjected to a mechanical pressure of magnitude $\overline{q}_{3s}^{(+)} = -5\times 10^4\,\mathrm{N/m^2}$ with sinusoidal distribution ($n = m = 1$) applied at the top surface. In addition, thermal fluxes with sinusoidal distribution ($n = m = 1$) and magnitudes $\overline{q}_{\mathrm{Ts}}^{(+)} = -1\times 10^2\,\mathrm{J/m^2}$ and $\overline{q}_{\mathrm{Ts}}^{(-)} = -2.7\times 10^1\,\mathrm{J/m^2}$ are applied at $\zeta = h/2$ and $\zeta = -h/2$, respectively. Regarding hygrometric loads, two moisture concentration fluxes with magnitudes $\overline{q}_{\mathrm{Cs}}^{(+)} = 5\times 10^{-7}\,\mathrm{kg/m^2}$ and $\overline{q}_{\mathrm{Cs}}^{(-)} = 1\times 10^{-7}\,\mathrm{kg/m^2}$ are applied to the panel. The rectangular plate is also subjected to sinusoidal distributions of surface charges at the top and bottom surfaces, with $n = m = 1$, characterized by magnitudes equal to $\overline{q}_{\mathrm{Ds}}^{(+)} = 4\times 10^{-6}\,\mathrm{C/m^2}$ and $\overline{q}_{\mathrm{Ds}}^{(-)} = 8\times 10^{-6}\,\mathrm{C/m^2}$, respectively. The present simulation is intended as a preliminary assessment, developed to validate the model against a reference solution. More specifically, thermo-mechanical (T-D), hygro-mechanical (H-D), and electro-mechanical (E-D) 3D models are developed using a 3D FEM commercial software, employing 96768 parabolic brick elements and 408,689 nodes. Furthermore, the higher-order semi-analytical formulation presented here is employed to determine the multifield response of the panel, taking into account the ELDZL7 kinematic model, as described in Eq (6). The thickness functions are developed using Jacobi polynomials, assuming $\gamma = \delta = 0$. The results of the simulations are presented in Tables 3–10, which show the distribution of the 3D configuration variables, as well as the primary and secondary variables, along the thickness direction for the point located at $(0.25L_1, 0.75L_2)$ within the physical domain. As observed, the ELW model, combined with the recovery procedure, accurately predicts the results from 3D FEM while offering a significant reduction in computational cost due to its semi-analytical approach. In particular, Table 3 shows that for electro-mechanical simulations, the out-of-plane configuration variables exhibit slope variations in their profiles, with parabolic distribution within each lamina. This highlights the importance of using zigzag theories and higher-order kinematic models to achieve accurate results. This is also confirmed by the results in terms of 3D strain components in Table 4. While in-plane strains are linearly distributed along the thickness direction, the ε_3 profile follows a piecewise linear distribution. The out-of-plane strain distortion components γ_{13}, γ_{23} exhibit a parabolic distribution, except in the third lamina, where a discontinuity is observed, with polynomial dispersion. All these aspects are well captured by both 3D FEM and ELW models, demonstrating excellent accuracy. Regarding the 3D stress components presented in Table 5, the heterogeneity of the lamination scheme causes the in-plane stress components σ_1, σ_2 and τ_{12} to display significant slope variations in the third lamina, indicating that this layer is the softest region within the laminate. Further observations on the σ_3 distribution along the thickness direction reveal that both 3D FEM and ELW model satisfy the external loading conditions under a mechanical pressure. In addition, the presence of a Winkler-type elastic foundation induces an additional pressure from the bottom side, which depends on the displacement field components at this point, as prescribed by Eq. (48). This factor is very important for applying the post-processing recovery procedure, since the external loads depend on the configuration variables, and require calculating the load magnitude at the selected point before applying the equilibrium conditions at the external surfaces of the solid. As shown in Table 3, the through-the-thickness distribution of the electric potential requires a higher order kinematic model since it is characterized by an arbitrary dispersion with parabolic profiles and slope variations, especially in the third lamina. In any case, the results based on an ELDZL7 model, exhibit an excellent agreement with the 3D solution. Similar considerations can be applied also to the electric primary and secondary variables presented in Table 6. More specifically, the in-plane components of the electric field vector follow a parabolic distribution with slope changes at each interface, while the out-of-plane component shows a stepwise linear distribution. The electric flux components vary significantly between adjacent laminae, especially for in-plane components. The out-of-plane electric flux follows a linear distribution along the thickness direction with a zigzag effect. Above all, this example demonstrates that in fully coupled simulations of laminated structures, higher-order kinematic models with zigzag functions are essential, even when the structure exhibits linear displacement field distributions, since

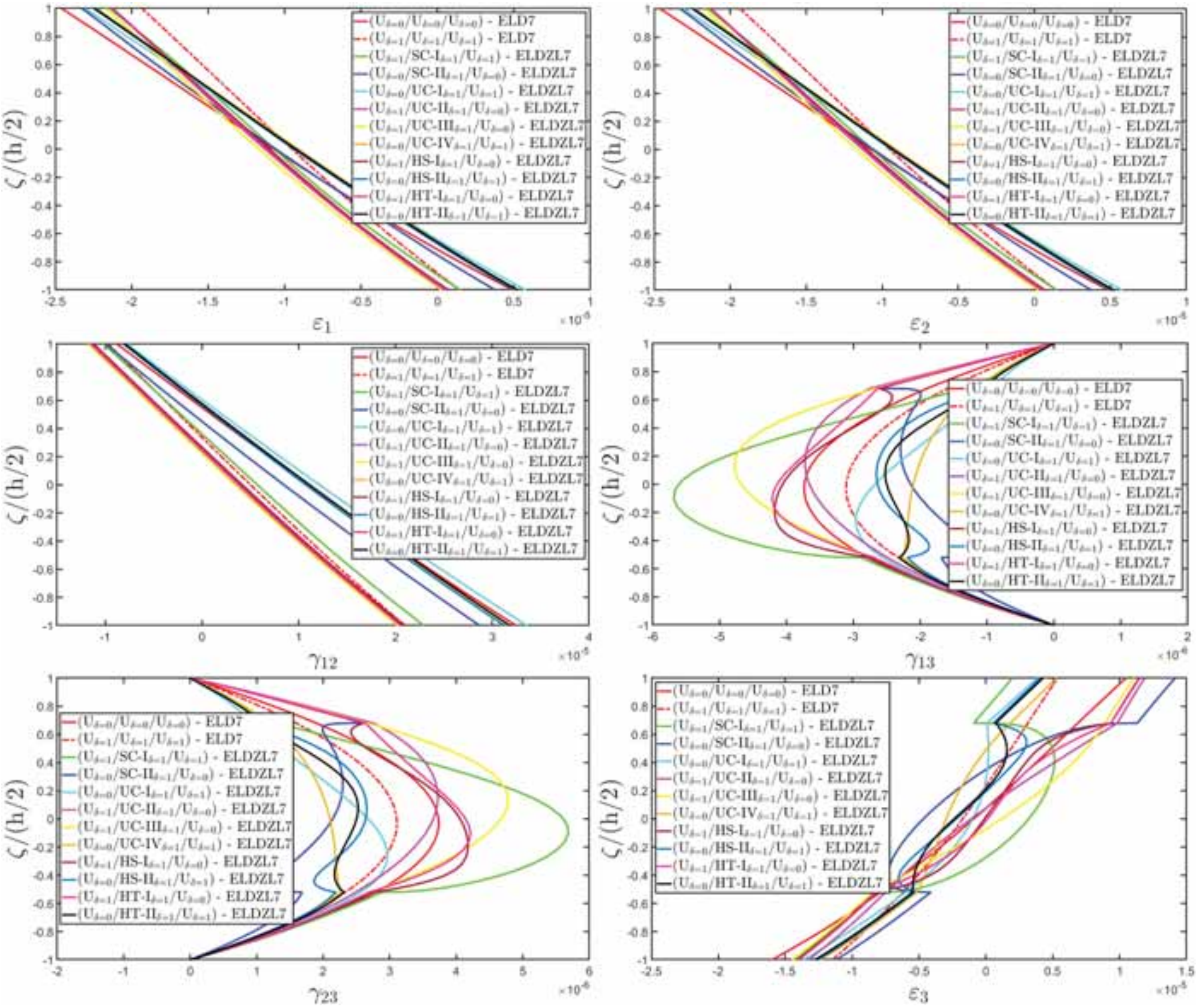

Fig. 17. Representation of the distributions along the thickness direction of 3D strain components of a spherical shallow shell for the point located at $(s_1, s_2) = (0.25L_1, 0.75L_2)$. Comparison against 3D FEM results and effect of material variation.

other configuration variables can exhibit a more complex behavior.

The same plate is then studied under thermo-mechanical loads, with the results presented in Tables 7–10. Unlike the E-D simulation, the T-D analysis reveals a more complex through-the-thickness distribution of displacement field components, especially for the U_3 component, which exhibits a polynomial distribution, as predicted by the 3D FEM solution. The use of the higher-order kinematic model enables an accurate prediction of this behavior, as demonstrated in Table 7. The temperature distribution is linear with different slope variations. The most significative variation in the temperature profile occurs in the third soft layer, which shows the highest level of isolation. As far as the 3D strain components is concerned, Table 8 points out that ε_1 and ε_2 distributions are almost linear, while ε_3 exhibits a linear profile within each layer, with a translation of the distribution from one layer to its adjacent one. Furthermore, in-plane distortion γ_{12} is found to be linearly distributed along the thickness direction, while the out-of-plane components γ_{13} and γ_{23}, derived from the recovery procedure, are characterized by a more complicated distribution, and assume a null value at the top and bottom surface, in line with the 3D finite element solution. It should be noted that the third layer, which is the softest lamina within the lamination scheme, experiences higher strain distortions compared to the other layers. The 3D stresses in Table 9 show a piecewise linear distribution of in-plane components along the thickness due to the heterogeneity of the lamination scheme. On the other hand, the out-of-plane shear stresses τ_{13} and τ_{23} are linear in first and the fourth layers, while a parabolic distribution with slope changes at the interfaces is observed in the second and third laminae. Finally, the σ_3 distribution follows a smooth polynomial pattern along the entire laminate thickness, with the extreme values consistent with the external loading conditions. The primary and secondary variables of the heat conduction problem, derived from both 3D FEM and ELDZL7 model, are reported in Table 10. The temperature gradient components are characterized by a linear distribution with zigzag behavior at each interface, in agreement with the reference results. Moreover, the in-plane secondary variables differ significantly between adjacent laminae due to the high variability in the lamination scheme of the thermal conductivity. As far as the out-of-plane thermal flux component is concerned, a linear distribution is found along the thickness direction, with an evident slope variation in the third lamina. This is due to the fact that the out-of-plane thermal conductivity does not significantly vary between metal and ceramic phase. On the other hand, the thermal conductivity of the central lamina is reduced with a scale factor, therefore thermal flux variations are more

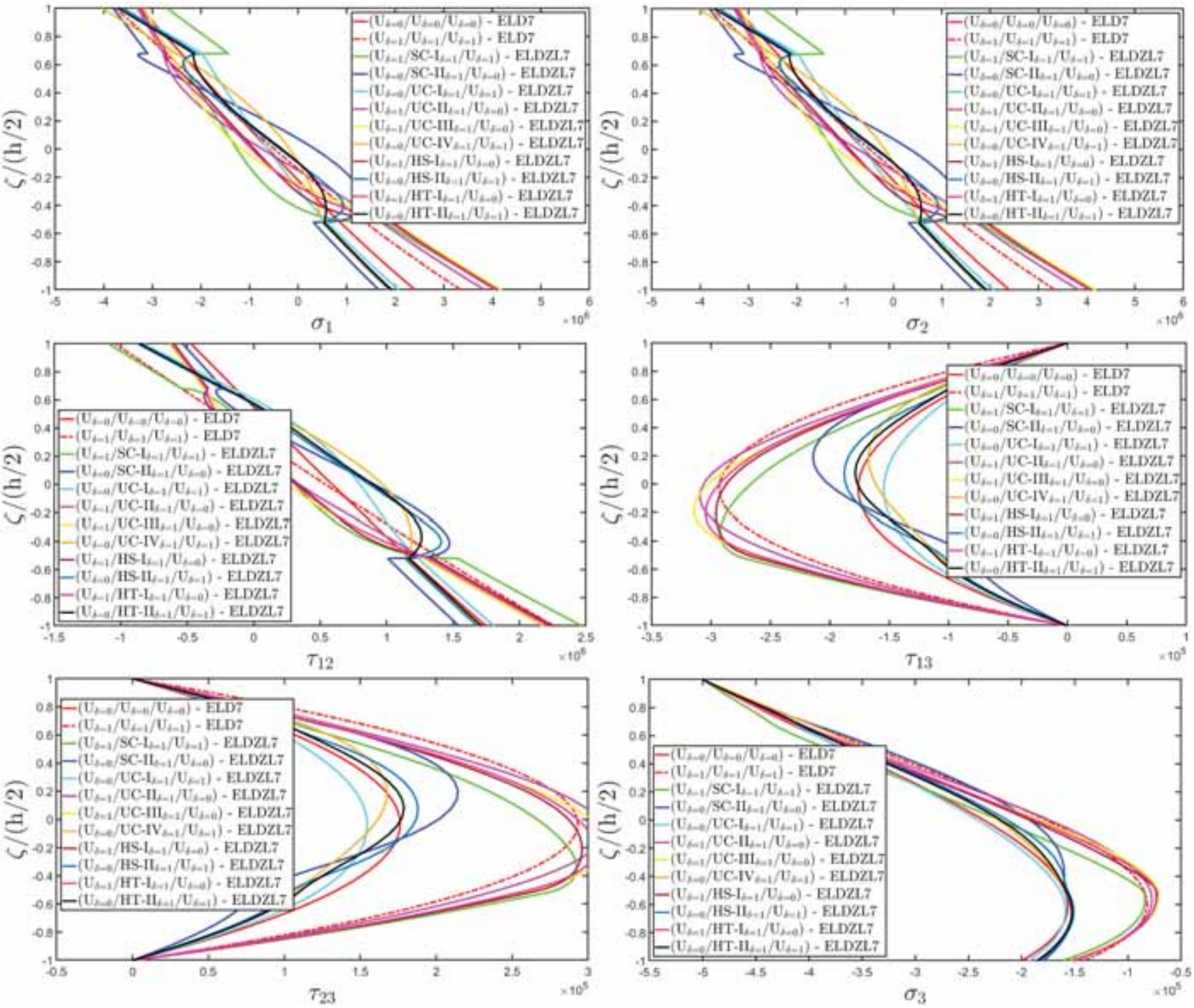

Fig. 18. Representation of the distributions along the thickness direction of 3D stress components of a spherical shallow shell for the point located at $(s_1, s_2) = (0.25L_1, 0.75L_2)$. Comparison against 3D FEM results and effect of material variation.

evident. Next example examines a simply-supported circular cylinder, with a reference surface defined by Eq. (106). The cylinder has a radius equal to $R_1 = 0.12\,\mathrm{m}$, with length $L_2 = 0.20\,\mathrm{m}$, and consists of three layers of smart materials, following the lamination scheme (MAT − I\MAT − III\MAT − I). The structure is subjected to a uniform mechanical pressure of magnitude $\overline{q}_{3s}^{(+)} = -1 \times 10^4\,\mathrm{N/m^2}$ applied to its top surface. In addition, a hydrostatic moisture flux distribution along α_1 axis is applied at the top surface, with magnitudes $\overline{q}_{Cs}^{(+)} = -8 \times 10^{-7}\,\mathrm{kg/m^2}$, while a uniform moisture flux with $\overline{q}_{Cs}^{(-)} = -2 \times 10^{-7}\,\mathrm{kg/m^2}$ is considered at the bottom surface. A sinusoidal distribution with $n = m = 1$ and magnitude $\Delta\overline{\mathrm{T}}_s^{(+)} = -1\,\mathrm{K}$ of temperature variation with respect to the reference absolute temperature T_0 is assigned at the top surface, while the bottom surface is maintained at a constant temperature variation with $\Delta\overline{\mathrm{T}}_s^{(-)} = 0\,\mathrm{K}$. For the electrical boundary conditions, the bottom surface is electrically grounded with an electric potential equal to $\Delta\overline{\phi}_s^{(-)} = 0\,\mathrm{V}$, while the potential $\Delta\overline{\phi}_s^{(+)} = 0.5\,\mathrm{V}$ with sinusoidal distribution is applied at the top surface. The multifield response of the cylinder is evaluated using the ELW semi-analytical formulation by assuming $\widetilde{N} = \widetilde{M} = 150$. Uniform distributions of external loads are modelled within the semi-analytical Navier solution of Eq. (69) by assuming the following expression of the semi-analytical coefficients $Q_{\alpha snm}^{(\pm)}$ with $\alpha = 3, \mathrm{C}$ for each $n = 1, \ldots, \widetilde{N}$ and $m = 1, \ldots, \widetilde{M}$, following the trigonometric expansion of Eq. (64) [58]:

$$Q_{\alpha snm}^{(\pm)} = \frac{4\overline{q}_{\alpha s}^{(\pm)}}{\pi^2 nm}(1-\cos(n\pi))(1-\cos(m\pi)) \tag{110}$$

To model the hydrostatic distribution [58] within the semi-analytical Navier solution, the following expression is used for the quantity $Q_{\alpha snm}^{(\pm)}$ with $s = \mathrm{C}$:

$$Q_{\alpha snm}^{(\pm)} = -\frac{4\overline{q}_{\alpha s}^{(\pm)}}{\pi^2 nm}\cos(n\pi)(1-\cos(m\pi)) \tag{111}$$

When performing multifield simulations, various coupling orders are considered. More specifically, $\mathrm{H}-\mathrm{T}-\mathrm{E}-\mathrm{D}_{fc}$ represents a model where the constitutive matrix of each layer is defined as in Eq. (22). In contrast, $\mathrm{H}-\mathrm{T}-\mathrm{E}-\mathrm{D}_{uc}$ simulations consider hygro-thermo-electro-mechanical interactions by assuming $\overline{\mathbf{\Gamma}}_{\mathrm{o}}^{(k)} = \overline{\mathbf{\Gamma}}_{\mathrm{g}}^{(k)} = \overline{\mathbf{\Gamma}}_{\mathrm{TC}}^{(k)} = \overline{\mathbf{\Gamma}}_{\mathrm{Y}}^{(k)} = \overline{\mathbf{\Gamma}}_{\mathrm{X}}^{(k)} = \mathbf{0}$. In the case of $\mathrm{H}-\mathrm{T}-\mathrm{E}-\mathrm{D}_{htc}$ analysis, the 3D constitutive matrix of Eq. (22) is used with $\overline{\mathbf{\Gamma}}_{\mathrm{o}}^{(k)} = \overline{\mathbf{\Gamma}}_{\mathrm{g}}^{(k)} = \mathbf{0}$, while the assumption $\overline{\mathbf{\Gamma}}_{\mathrm{TC}}^{(k)} = \overline{\mathbf{\Gamma}}_{\mathrm{Y}}^{(k)} = \overline{\mathbf{\Gamma}}_{\mathrm{X}}^{(k)} = \mathbf{0}$ is

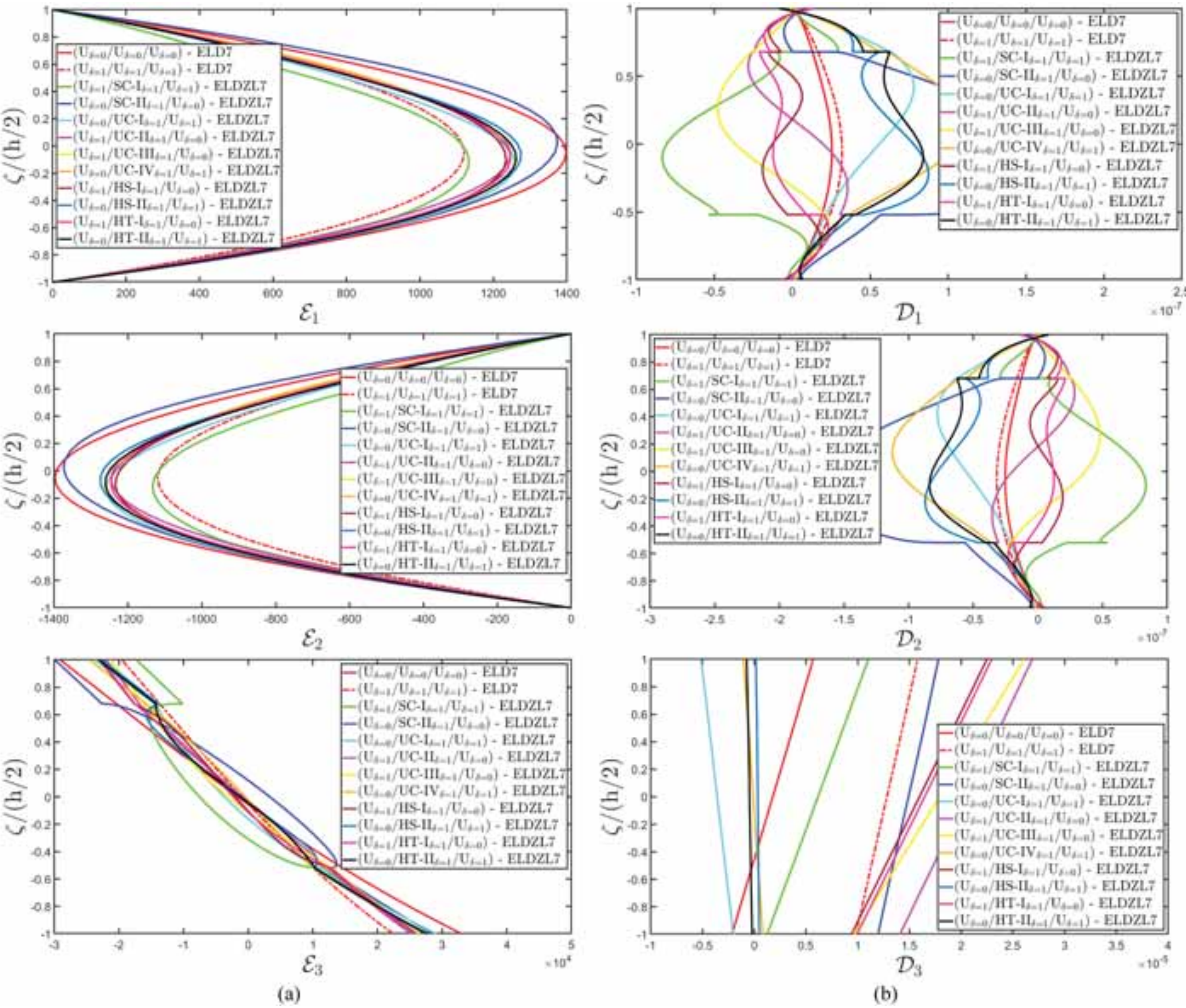

Fig. 19. Representation of the distributions along the thickness direction of 3D electric primary (a) and secondary (b) variables of a spherical shallow shell for the point located at $(s_1, s_2) = (0.25L_1, 0.75L_2)$. Comparison against 3D FEM results and effect of material variation.

made for $H - T - E - D_{tec}$. Results are presented in terms of 3D configuration, primary, and secondary variables at the point $(0.25L_1, 0.25L_2)$ within the rectangular parametric domain, as shown in Figs. 4–9. Model validation is conducted by comparing results to a 3D FEM simulation from commercial software consisting of 81920 parabolic brick elements and 350273 nodes. This analysis explores the coupling between mechanical elasticity and electrostatics (E-D simulation), thermal conduction (T-D simulation), and moisture diffusion (H-D simulation). In addition to these preliminary results, multifield simulations are performed (H-T-E-D), incorporating all these interactions within a single model. Referring to uncoupled simulations ($H - T - E - D_{uc}$), the superposition principle is applied, solving equations without coupling electric and thermal fields, or thermal conduction with moisture diffusion. In contrast, $H - T - E - D_{fc}$ simulation considers the full coupling between mechanical elasticity, thermal conduction, mass diffusion, and electrostatics, taking into account even the pyroelectric, the thermophoretic and the thermal diffusion terms within the total energy of the structure. Finally, $H - T - E - D_{tec}$ and $H - T - E - D_{htc}$ results correspond to multifield simulations considering pyroelectric and hygro-thermal coupling, respectively. The thickness plots of configuration variables are reported in Fig. 4. In E-D, T-D, and H-D simulations the ELDZL7 model aligns closely with the predictions from 3D FEM. In-plane displacement field components are linearly distributed through the laminate thickness, with U_3 showing uniform dispersion in E-D and T-D simulations. However, a characteristic zigzag pattern appears for this quantity in the H-D case. Another interesting aspect is that introducing different couplings in the model affects the overall cylinder deflection, aligning it closely with the H-D simulation configuration. In terms of electric potential variation, a zigzag behavior is observed in E-D problem, becoming very evident in all H-T-E-D simulations. This behavior results in profiles that significantly differ from those associated with simple electro-elasticity. In contrast, temperature profiles remain unaffected by different couplings between physical phenomena, consistently displaying a linear through-the-thickness distribution in each simulation. Similarly, moisture concentration is not influenced by the presence of an electric field within the solid except in the $H - T - E - D_{htc}$ simulation, where an additional moisture concentration variation arises due to thermophoretic effect. For 3D strain components shown in Fig. 5, ε_2 is characterized by a linear distribution in all simulations, similarly to what happens in ε_1 in T-D and E-D analyses. However, H-D and H-T-E-D simulations display a zigzag distribution in these in-plane strain components. The in-plane distortion γ_{12} maintains a linear distribution in all

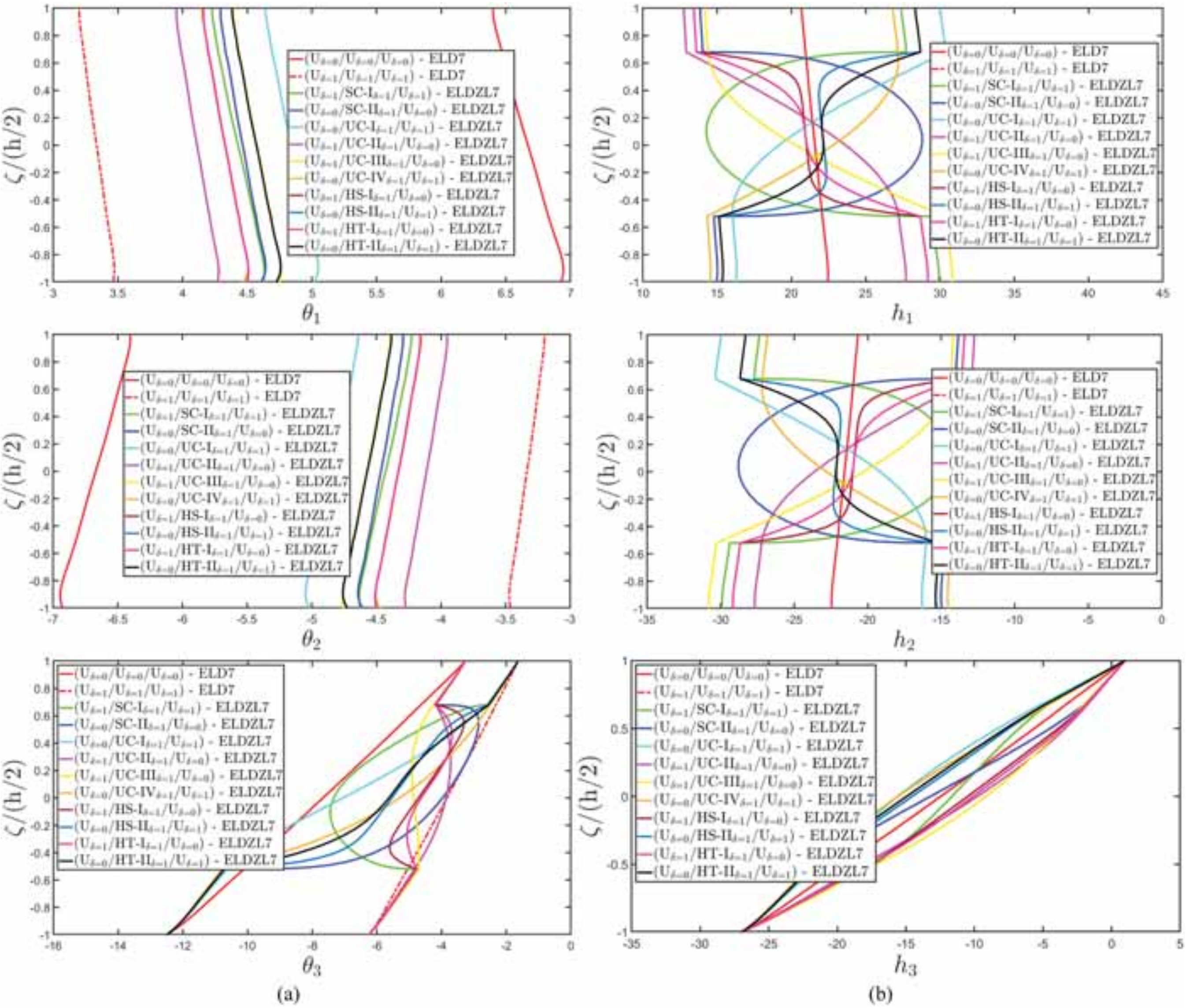

Fig. 20. Representation of the distributions along the thickness direction of 3D thermal primary (a) and secondary (b) variables of a spherical shallow shell for the point located at $(s_1, s_2) = (0.25L_1, 0.75L_2)$. Comparison against 3D FEM results and effect of material variation.

simulations, while ε_3 shows an abrupt variation in the central core, particularly evident in H-D simulation. As a result, multifield simulations are characterized by the same behavior, where various coupling effects affect the ε_3 strain component because a deviation in the profile is observed. In contrast to strains, the 3D stress components in Fig. 6 reveal in-plane normal stresses σ_1 and σ_2 with different values within each lamina, while the out-of-plane stress σ_3 shows a smooth variation consistent with the external loads in E-D and T-D analyses. However, the H-D analysis predicts a significative slope inversion in both 3D FEM and ELW simulations. The in-plane shear stress τ_{12} appears almost linear through the laminate thickness, with abrupt changes at each interface. This aspect is also featured in multifield simulations, particularly between the second and third layers. On the other hand, smooth parabolic profiles are found for the out-of-plane shear stresses in E-D and T-D simulations, while H-T-E-D simulations display τ_{13} and τ_{23} with zigzag patterns and parabolic distributions within each layer. A significant increase in the shear stress magnitude occurs in the bottom layer, with a corresponding decrease in the second lamina. A similar behavior is observed for the in-plane electric field components, reported in Fig. 7, which primarily result from the combined effect of the additional strains induced by thermal expansion. Furthermore, in $\mathrm{H-T-E-D}_{tec}$ and $\mathrm{H-T-E-D}_{fc}$ simulations curves deviate from the results of uncoupled $\mathrm{H-T-E-D}_{uc}$ simulations due to pyroelectricity. In all numerical investigations, electric field components show a linear distribution along the thickness of each layer, while in-plane electric flux vectors exhibit smooth curved profiles within each lamina, with a piecewise distribution across the laminate. The out-of-plane flux component consistently shows a linear distribution in all multifield investigations. Regarding thermal primary and secondary variables in Fig. 8, multifield coupling induces a shift only in the out-of-plane temperature gradient profile, while in-plane quantities θ_1 and θ_2 are linearly distributed in all cases. Each thermal flux component exhibits a variation in its profile due to hygro-thermal coupling, while the electric field does not affect these quantities. Finally, for the mass diffusion problem, the 3D primary and secondary variables in Fig. 9 display smooth linear or parabolic profiles in some simulations, while fully-coupled multifield cases yield a zigzag pattern. The thermophoretic effect in fully-coupled scenarios causes a deviation of both in-plane and out-of-plane mass fluxes, from H-D-based predictions. In addition, since the external mass fluxes are applied at the external sides of the cylinder, the out-of-plane flux c_3 assumes the same

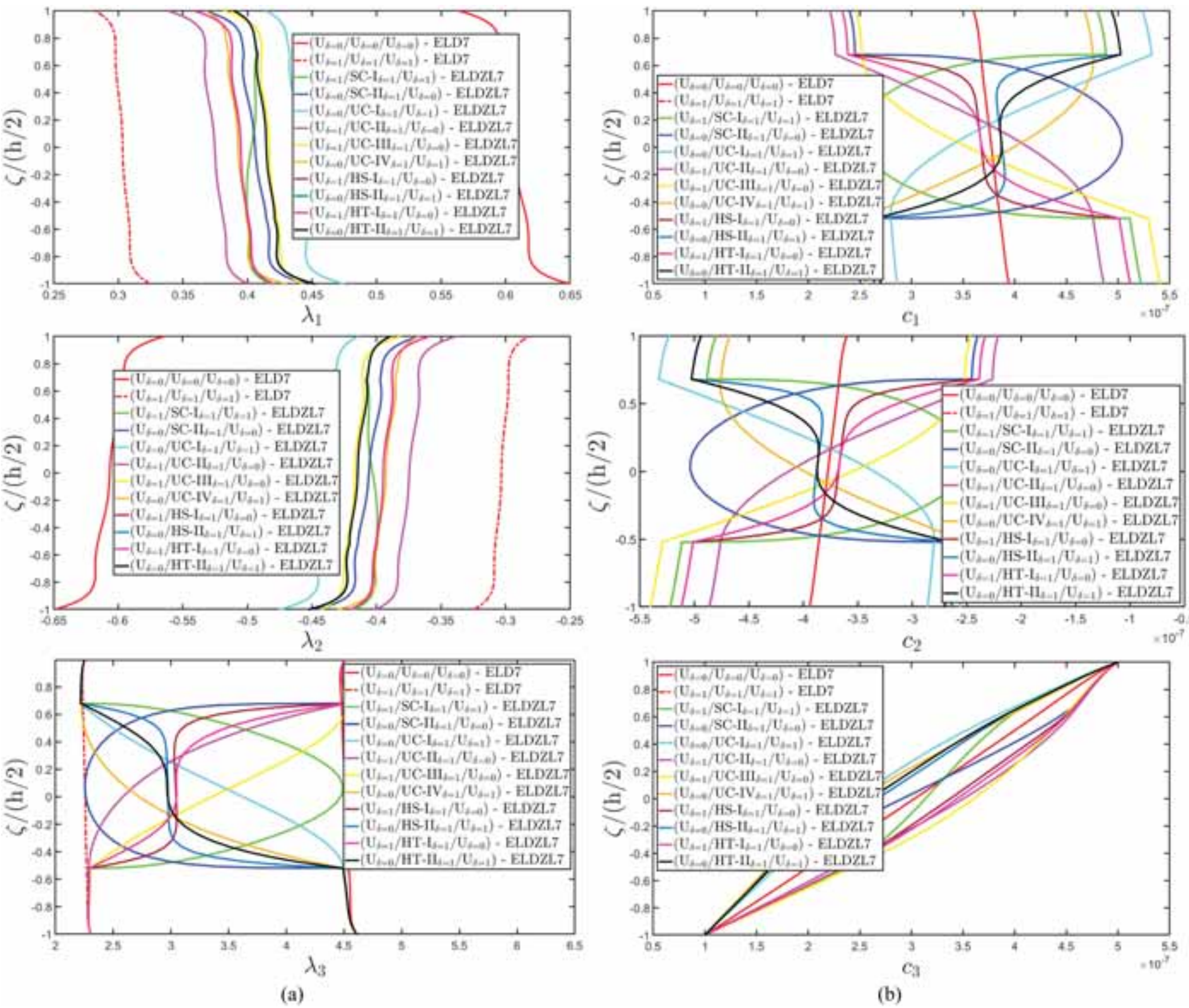

Fig. 21. Representation of the distributions along the thickness direction of 3D hygrometric primary (a) and secondary (b) variables of a spherical shallow shell for the point located at $(s_1, s_2) = (0.25L_1, 0.75L_2)$. Comparison against 3D FEM results and effect of material variation.

value at the extreme surfaces of the cylinder regardless of the coupling between the physical phenomena involved.

A further investigation is conducted on another circular cylinder, named "Cylindrical panel-2″, to explore the coupled response of the laminate under multifield loads. Detailed information about the geometry and lamination scheme can be found in Fig. 1, with the reference surface equation reported in Eq. (107). The top surface is provided with a Winkler elastic foundation, using linear elastic springs oriented along the ζ direction, with a stiffness equal to $k_{3f}^{(+)} = 5 \times 10^9\,\mathrm{N/m^3}$. Electric loads are applied by prescribing a null electric potential at the bottom surface, namely $\Delta\overline{\phi}_s^{(-)} = 0\,\mathrm{V}$, and a sinusoidally distributed electric potential with magnitude $\Delta\overline{\phi}_s^{(+)} = 1\,\mathrm{V}$ at the top surface. Furthermore, the values $\Delta\overline{C}_s^{(-)} = \Delta\overline{C}_s^{(+)} = -0.05\,\mathrm{kg/m^3}$ of moisture concentration are enforced at both the top and bottom surfaces, following a sinusoidal distribution with $n = m = 1$. On the other hand, thermal loads are uniformly distributed at the external surfaces of the shell. The thermal flux magnitudes are equal to $\overline{q}_{\mathrm{Ts}}^{(+)} = 1\,\mathrm{J/m^2}$ and $\overline{q}_{\mathrm{Ts}}^{(-)} = 1.2\,\mathrm{J/m^2}$, with a uniform distribution across the physical domain, following Eq. (110) with $\alpha = \mathrm{T}$, for an arbitrary $n = 1, \ldots, \widetilde{N} = 150$ and $m = 1, \ldots, \widetilde{M} = 150$, for the trigonometric expansion terms. The multifield response of the laminate is evaluated under thermodynamic equilibrium conditions, and the results are represented in Figs. 10–15, showing the through-the-thickness distributions of configuration, primary, and secondary variables at $(0.75L_1, 0.25L_2)$ within the physical domain. The semi-analytical solution is obtained assuming $\widetilde{N} = \widetilde{M} = 150$ and employing the ELDZL7 kinematic model. In addition, 3D FEM models have been developed using commercial software for validation purposes of results for E-D, T-D and H-D simulations. These models consist of 98496 parabolic brick elements with 418071 nodes. As shown in Fig. 10, the adoption of higher-order theories for the kinematic model, along with the Murakami zigzag function, is crucial for accurately predicting the configuration variables. While displacement field components are uniformly or linearly distributed along the thickness of the cylinder, electric potential, temperature variation, and moisture concentration exhibit some complex distributions with slope variations nearby interfaces. The coupling introduction among various fields leads to meaningful variations in the distribution of some variables, which requires the application of a refined kinematic model. The 3D strain components, shown in Fig. 11, exhibit some linear distributions for in-plane components, while more complex profiles are observed for out-of-plane components. The ε_3 strain component follows a piecewise linear distribution across all simulations, while the distortions γ_{13} and γ_{23} show some parabolic profiles within each layer of the laminate. Results from E-D, T-D, and H-D analyses derived from the semi-analytical solution align closely with those from 3D FEM. The introduction of multifield coupling leads to deviations from the distributions associated with uncoupled simulations, especially for the axial strains, where a smooth variation is observed. The effect of pyroelectric coefficients and hygro-thermal constants are less pronounced. Furthermore, deformations due to hygrometric loads are higher than those induced by thermal and electric loads. Fig. 12 presents the through-the-thickness distributions for the 3D stress components. The vertical deflection induced by various loads generates an out-of-plane normal stress near the top surface, attributed to the elastic foundation springs. Parabolic distributions are found in the first and second layers, indicating the presence of a compression state, while a linear distribution of the out-of-plane normal stress is observed in the third lamina which is primarily under tension. The structure undergoes higher in-plane stresses when hygrometric loads are applied, while in-plane normal stresses from E-D, T-D, and H-D cases are comparable in magnitude. These stresses are distributed with linear profiles within each layer. The out-of-plane normal stresses follow the polynomial distributions with their peak values at each interface. The effect of the multifield analysis is particularly evident in Fig. 13, which shows the results in terms of electric flux components. In agreement with 3D FEM predictions for E-D analyses, the curves show significant variations in $\mathrm{H-T-E-D}_{uc}$ analyses, to additional strains induced by other fields, resulting in changes in the electric field and flux. Note that the in-plane components of the electric field exhibit a polynomial distribution within each layer, while ensuring the continuity of the profile. The out-of-plane electric field component $\mathscr{E}_3$, instead, is linearly distributed in all layers, but discontinuous curves are obtained. The hygro-thermo-electric coupling effect is also visible in the primary and secondary variables associated with moisture diffusion. In Fig. 14, the distributions of temperature gradient components θ_1 and θ_2 are translated from the curves associated with the E-D analysis when hygro-thermal coupling is considered. On the other hand, results obtained from the superimposition of various fields, along with the pyroelectric terms, do not significantly affect results. This is reflected in the thickness plots of h_1, h_2 secondary variables, where variations for in-plane thermal fluxes are observed in the first and third layers, while the h_3 component remains largely unaffected by multifield coupling, as also happens for θ_3. Finally, Fig. 15 shows the mass diffusion primary and secondary variables. In-plane moisture gradient components, denoted by λ_1, λ_2, are not significantly affected by multifield loads, as the curves are very similar to those from both the higher-order theory and 3D FEM. However, a variation in the λ_3 profile is observed for multifield simulations within the second layer. The moisture diffusion secondary variables c_1, c_2, c_3 differ the H-D simulations in $\mathrm{H-T-E-D}_{htc}$ and $\mathrm{H-T-E-D}_{fc}$ analyses. On the other hand, $\mathrm{H-T-E-D}_{uc}$ and $\mathrm{H-T-E-D}_{tec}$ results remain consistent with those from H-D simulation.

The final numerical example investigates a doubly-curved spherical panel made of three layers of MAT-I material subjected to hygro-thermo-electro-mechanical loads. The constitutive coefficients of this material are provided in Table 2. MAT-I is derived from the homogenization of smart materials, reported in Appendix II, by assuming a specific value of the volume fraction of fibers, namely $V_f = 0.2$. A representation of the doubly-curved shell solid is shown in Fig. 1. Unlike the previous examples, this model considers an arbitrary grading of the material properties along the thickness direction within each layer. To this end, several distribution profiles are considered, as summarized in Table 1. In this way, the arbitrary element of the 3D multifield material is evaluated according to the relation outlined in Eq. (35). More specifically, a parametric investigation is performed in which the central core of the shell exhibits an arbitrary variation of its constitutive coefficients, setting $\delta_0^{(k)} = 0$ and $\delta^{(k)} = 1$ in all configurations within the core, namely for $k = 2$. On the other hand, in the first ($k = 1$) and third ($k = 3$) layer, a uniform material variation is adopted with $\delta_0^{(k)} = 0$. Within these layers, the scaling parameter is selected to ensure the continuity condition of the material coefficient values. The profiles in Table 1 follow symmetric, antimetric and unsymmetric variations. A Winkler-Pasternak foundation is modelled at the bottom surface, following Eq. (48), with foundation stiffness parameters $k_{3f}^{(-)} = 5 \times 10^{10}\,\mathrm{N/m^3}$ and $G_f^{(-)} = 5 \times 10^6\,\mathrm{N/m^2}$. The loading condition includes uniform distributions of mechanical pressure of magnitude $\overline{q}_{3s}^{(+)} = -5 \times 10^5\,\mathrm{N/m^2}$ applied at the top surface, along with thermal loads of magnitudes $\overline{q}_{Ts}^{(+)} = 1\,\mathrm{J/m^2}$ and $\overline{q}_{Ts}^{(-)} = -27\,\mathrm{J/m^2}$, and moisture fluxes characterized by $\overline{q}_{Cs}^{(+)} = 5 \times 10^{-7}\,\mathrm{kg/m^2}$ and $\overline{q}_{Cs}^{(-)} = 1 \times 10^{-7}\,\mathrm{kg/m^2}$. Electric loads are not directly applied to the panel. Instead, the laminate is modelled by specifying a prescribed value of the electric potential at both the top and bottom surfaces, namely $\Delta\overline{\Phi}_s^{(-)} = 0\,\mathrm{V}$ and $\Delta\overline{\Phi}_s^{(+)} = 0\,\mathrm{V}$, respectively. The through-the-thickness distributions of the multifield configuration variables, along with primary and secondary variables, are shown in Figs. 16–21, evaluated at the point located at $(0.25L_1, 0.75L_2)$. These results are computed using the present higher-order theory with the ELW approach with $N = 7$, employing the ELD7 kinematic model when no variation in the material properties is assumed because a single homogeneous layer is present. The ELDZL7 theory involving the modified zigzag function of Eq. (10) is differently used for variable material properties, due to heterogeneity in the laminate.

Despite the material heterogeneity, all simulations show smooth distributions for the configuration variables with linear or parabolic profiles, as observed in Fig. 16. Note that the kinematic boundary conditions in terms of closed-circuit configuration are perfectly fulfilled by the ELW approach. Another aspect that should be noted is that the structure under external loads undergoes some negative values of the U_3 displacement field component. However, the introduction of a uniform material variation reduces the magnitude of U_3. The results from the other simulations fall between these two extreme curves. The 3D strain components are shown in Fig. 17. In-plane deformations remain unaffected by the material property variations. However, the out-of-plane strains $\gamma_{13}, \gamma_{23}, \varepsilon_3$ vary with the material properties. In particular, the profile of the out-of-plane axial strain, ε_3, follows a linear trend but reflects the distribution of the material variation within the second layer. For uniform material distribution within the lamination scheme, we obtain smooth strain profiles. In Fig. 18, the results of the 3D stress components are presented. The in-plane stress components follow a linear distribution, while the stress variation in the central core is affected by the material distribution. The appropriate selection of the shape parameter for the uniform distributions in the external layers prevents any stress concentration. The post-processing recovery procedure ensures that the distributions of the out-of-plane shear and normal stresses satisfy the equilibrium conditions at both the top and bottom sides. Particular attention must be given to the distribution of the out-of-plane stress σ_3, which turns into the same point at the top surface, where the external mechanical pressures are applied, while they diverge at the bottom side. This is because the displacement field components at the bottom of the panel are influenced by the material variation within the laminate. The 3D electric field components in Fig. 19 are the electric flux components. The in-plane components $\mathscr{E}_1$, $\mathscr{E}_2$ exhibit smooth parabolic distributions, with the maximum value depending on the material distribution. The out-of-plane electric field component $\mathscr{E}_3$ reflects the changes in the constitutive coefficients within the solid, preventing any peak values. The out-of-plane 3D electric flux component $\mathscr{D}_3$ is linearly distributed along the thickness direction, with the lamination scheme affecting only the slope of the curve. In-plane electric flux components $\mathscr{D}_1, \mathscr{D}_2$ show an arbitrary variation in their distribution due to the material heterogeneity in the central core. Fig. 20 also shows the primary and secondary variables related to thermal conduction. The in-plane temperature gradient components exhibit linear distributions which are translated as material properties vary within the shell. On the other hand, the out-of-plane temperature gradient component θ_3 exhibits a zigzag behavior, with profiles that are intermediate between those observed for homogeneous layers, which are smooth linear curves. For the thermal flux components, h_1, h_2 are uniformly distributed in the first and third laminae. In the central core, the distribution follows the material variation. The out-of-plane thermal flux h_3 is essentially linear, but a zigzag distribution is observed when the material properties vary across different layers. Similarly, the moisture concentration gradient components, shown in Fig. 21, follow a behavior similar to that of the temperature gradient components. In case of homogeneous layers, θ_3 is linearly distributed, and λ_3 exhibits a uniform distribution. The in-plane flux components c_1, c_2 show various profiles in the central core, especially for nonlinear variations. The out-of-plane moisture flux component c_3 shows a zigzag slope variation, while the linear curves are derived within each layer of the laminate.

8. Conclusions

A refined ELW model has been developed for the multifield analysis of laminated structures with double curvature under coupled mechanical, electric, thermal, and hygrometric loads, taking into account various assumptions for the description of the unknown variables along the thickness direction. The fundamental equations have been defined in curvilinear principal coordinates ensuring the thermodynamic equilibrium conditions, while also considering the effects of a Winkler-Pasternak elastic foundation. The external loads have been applied by enforcing the secondary variables such as the mechanical pressure, surface charge, thermal and hygrometric fluxes, and by prescribing the configuration variables like displacements, temperature, electric potential, and moisture concentration. A semi-analytical solution procedure has been used in terms of the generalized configuration variables, with a novel post-processing semi-analytical recovery procedure, based on the GIQ, to obtain the multifield 3D response of the solid. The model performance has been evaluated through numerical examples, demonstrating its capability to predict the multifield responses for structures with different curvatures and material compositions using a homogenization approach based on the Mori-Tanaka technique. The validation has been conducted through preliminary simulations, comparing the results from the ELW model with those from 3D models developed in a commercial software. Innovative results have been provided, highlighting the impact of coupling effects on the structural response and the involved physical problems. Furthermore, a parametric analysis has checked the sensitivity of the material variation on the static multifield response of laminates. Future enhancements of the research may involve deriving a numerical implementation for this present theory to overcome the limitations of the semi-analytical approach regarding geometry, lamination scheme, and boundary conditions. This formulation has shown a meaningful computational efficiency, providing an accurate evaluation of the 3D response of the laminate by using a 2D model. Moreover, it introduces new coupling effects not available in conventional commercial software, offering new possibilities for exploring applications in smart materials and structures, in addition to those already considered within existing literature.

CRediT authorship contribution statement

Francesco Tornabene: Writing – review & editing, Visualization, Validation, Supervision, Software, Methodology, Investigation, Formal analysis, Data curation, Conceptualization. **Matteo Viscoti:** Writing – original draft, Validation, Investigation, Formal analysis, Data curation. **Rossana Dimitri:** Writing – review & editing, Validation, Supervision, Methodology, Formal analysis, Data curation. **Timon Rabczuk:** Writing – review & editing, Validation, Methodology, Data curation, Conceptualization.

Declaration of competing interest

The authors declare that they have no known competing financial interests or personal relationships that could have appeared to influence the work reported in this paper.

The author is an Editorial Board Member/Editor-in-Chief/Associate Editor/Guest Editor for *[Journal name]* and was not involved in the editorial review or the decision to publish this article.

The authors declare the following financial interests/personal relationships which may be considered as potential competing interests:

Francesco Tornabene reports financial support was provided by Alexander von Humboldt Foundation. If there are other authors, they declare that they have no known competing financial interests or personal relationships that could have appeared to influence the work reported in this paper.

Acknowledgements

The authors acknowledge the Alexander von Humboldt Foundation and the Friedrich Wilhelm Bessel Research Award that is funding the present research activity.

Appendix I

In this Appendix we provide the extended relations for the semi-analytical fundamental coefficients $\widetilde{L}_{ijnm}^{(\tau\eta)\alpha_i\alpha_j}$ from Eq. (68), for an arbitrary $i,j = 1, ..., 6$ and $\tau,\eta = ,...,N+1$. To this end, the following definitions are considered for the elements of the generalized secondary variables resultants vector $\mathbf{\Sigma}^{(\tau)\alpha_i}$:

$$
\begin{gathered}
N_1^{(\tau)\alpha_i} = \sum_{k=1}^{l} \int_{\zeta_k}^{\zeta_{k+1}} \sigma_1^{(k)} F_\tau^{(k)\alpha_i} H_2 d\zeta, \quad N_2^{(\tau)\alpha_i} = \sum_{k=1}^{l} \int_{\zeta_k}^{\zeta_{k+1}} \sigma_2^{(k)} F_\tau^{(k)\alpha_i} H_1 d\zeta, \quad N_{12}^{(\tau)\alpha_i} = \sum_{k=1}^{l} \int_{\zeta_k}^{\zeta_{k+1}} \tau_{12}^{(k)} F_\tau^{(k)\alpha_i} H_2 d\zeta \\
N_{21}^{(\tau)\alpha_i} = \sum_{k=1}^{l} \int_{\zeta_k}^{\zeta_{k+1}} \tau_{12}^{(k)} F_\tau^{(k)\alpha_i} H_1 d\zeta, \quad T_1^{(\tau)\alpha_i} = \sum_{k=1}^{l} \int_{\zeta_k}^{\zeta_{k+1}} \tau_{13}^{(k)} F_\tau^{(k)\alpha_i} H_2 d\zeta, \quad T_2^{(\tau)\alpha_i} = \sum_{k=1}^{l} \int_{\zeta_k}^{\zeta_{k+1}} \tau_{23}^{(k)} F_\tau^{(k)\alpha_i} H_1 d\zeta \\
P_1^{(\tau)\alpha_i} = \sum_{k=1}^{l} \int_{\zeta_k}^{\zeta_{k+1}} \tau_{13}^{(k)} \frac{\partial F_\tau^{(k)\alpha_i}}{\partial \zeta} H_1 H_2 d\zeta, \quad P_2^{(\tau)\alpha_i} = \sum_{k=1}^{l} \int_{\zeta_k}^{\zeta_{k+1}} \tau_{23}^{(k)} \frac{\partial F_\tau^{(k)\alpha_i}}{\partial \zeta} H_1 H_2 d\zeta, \quad S_3^{(\tau)\alpha_i} = \sum_{k=1}^{l} \int_{\zeta_k}^{\zeta_{k+1}} \sigma_3^{(k)} \frac{\partial F_\tau^{(k)\alpha_i}}{\partial \zeta} H_1 H_2 d\zeta \\
D_1^{(\tau)\alpha_i} = \sum_{k=1}^{l} \int_{\zeta_k}^{\zeta_{k+1}} \mathscr{D}_1^{(k)} F_\tau^{(k)\alpha_i} H_2 d\zeta, \quad D_2^{(\tau)\alpha_i} = \sum_{k=1}^{l} \int_{\zeta_k}^{\zeta_{k+1}} \mathscr{D}_2^{(k)} F_\tau^{(k)\alpha_i} H_1 d\zeta, \quad D_3^{(\tau)\alpha_i} = \sum_{k=1}^{l} \int_{\zeta_k}^{\zeta_{k+1}} \mathscr{D}_3^{(k)} \frac{\partial F_\tau^{(k)\alpha_i}}{\partial \zeta} H_1 H_2 d\zeta \\
H_1^{(\tau)\alpha_i} = \sum_{k=1}^{l} \int_{\zeta_k}^{\zeta_{k+1}} h_1^{(k)} F_\tau^{(k)\alpha_i} H_2 d\zeta, \quad H_2^{(\tau)\alpha_i} = \sum_{k=1}^{l} \int_{\zeta_k}^{\zeta_{k+1}} h_2^{(k)} F_\tau^{(k)\alpha_i} H_1 d\zeta, \quad H_3^{(\tau)\alpha_i} = \sum_{k=1}^{l} \int_{\zeta_k}^{\zeta_{k+1}} h_3^{(k)} \frac{\partial F_\tau^{(k)\alpha_i}}{\partial \zeta} H_1 H_2 d\zeta \\
C_1^{(\tau)\alpha_i} = \sum_{k=1}^{l} \int_{\zeta_k}^{\zeta_{k+1}} c_1^{(k)} F_\tau^{(k)\alpha_i} H_2 d\zeta, \quad C_2^{(\tau)\alpha_i} = \sum_{k=1}^{l} \int_{\zeta_k}^{\zeta_{k+1}} c_2^{(k)} F_\tau^{(k)\alpha_i} H_1 d\zeta, \quad C_3^{(\tau)\alpha_i} = \sum_{k=1}^{l} \int_{\zeta_k}^{\zeta_{k+1}} c_3^{(k)} \frac{\partial F_\tau^{(k)\alpha_i}}{\partial \zeta} H_1 H_2 d\zeta \\
E^{(\tau)\alpha_i} = \sum_{k=1}^{l} \int_{\zeta_k}^{\zeta_{k+1}} \eta^{(k)} F_\tau^{(k)\alpha_i} H_1 H_2 d\zeta, \quad M^{(\tau)\alpha_i} = \sum_{k=1}^{l} \int_{\zeta_k}^{\zeta_{k+1}} \mu^{(k)} F_\tau^{(k)\alpha_i} H_1 H_2 d\zeta
\end{gathered}
\tag{A.1}
$$

In addition, the sub-matrices of the higher-order constitutive matrix $\mathbf{A}^{(\tau\eta)\alpha_i\alpha_j}$ in Eq. (41) are reported below in extended form:

$$
\mathbf{A}_{\varepsilon\varepsilon}^{(\tau\eta)\alpha_i\alpha_j} = \left[\left(A_{\varepsilon\varepsilon nm(pq)}^{(\tau\eta)[fg]\alpha_i\alpha_j} \right)_{hs} \right]_{\substack{h=1,\dots,9 \\ s=1,\dots,9}} =
\left[\begin{array}{cccccc|ccc}
A_{11(20)}^{(\tau\eta)[00]\alpha_i\alpha_j} & A_{12(11)}^{(\tau\eta)[00]\alpha_i\alpha_j} & A_{16(20)}^{(\tau\eta)[00]\alpha_i\alpha_j} & A_{16(11)}^{(\tau\eta)[00]\alpha_i\alpha_j} & A_{14(20)}^{(\tau\eta)[00]\alpha_i\alpha_j} & A_{15(11)}^{(\tau\eta)[00]\alpha_i\alpha_j} & A_{14(10)}^{(\tau\eta)[01]\alpha_i\alpha_j} & A_{15(10)}^{(\tau\eta)[01]\alpha_i\alpha_j} & A_{13(10)}^{(\tau\eta)[01]\alpha_i\alpha_j} \\
A_{12(11)}^{(\tau\eta)[00]\alpha_i\alpha_j} & A_{22(02)}^{(\tau\eta)[00]\alpha_i\alpha_j} & A_{26(11)}^{(\tau\eta)[00]\alpha_i\alpha_j} & A_{26(02)}^{(\tau\eta)[00]\alpha_i\alpha_j} & A_{24(11)}^{(\tau\eta)[00]\alpha_i\alpha_j} & A_{25(02)}^{(\tau\eta)[00]\alpha_i\alpha_j} & A_{24(01)}^{(\tau\eta)[01]\alpha_i\alpha_j} & A_{25(01)}^{(\tau\eta)[01]\alpha_i\alpha_j} & A_{23(01)}^{(\tau\eta)[01]\alpha_i\alpha_j} \\
A_{16(20)}^{(\tau\eta)[00]\alpha_i\alpha_j} & A_{26(11)}^{(\tau\eta)[00]\alpha_i\alpha_j} & A_{66(20)}^{(\tau\eta)[00]\alpha_i\alpha_j} & A_{66(11)}^{(\tau\eta)[00]\alpha_i\alpha_j} & A_{46(20)}^{(\tau\eta)[00]\alpha_i\alpha_j} & A_{56(11)}^{(\tau\eta)[00]\alpha_i\alpha_j} & A_{46(10)}^{(\tau\eta)[01]\alpha_i\alpha_j} & A_{56(10)}^{(\tau\eta)[01]\alpha_i\alpha_j} & A_{36(10)}^{(\tau\eta)[01]\alpha_i\alpha_j} \\
A_{16(11)}^{(\tau\eta)[00]\alpha_i\alpha_j} & A_{26(02)}^{(\tau\eta)[00]\alpha_i\alpha_j} & A_{66(11)}^{(\tau\eta)[00]\alpha_i\alpha_j} & A_{66(02)}^{(\tau\eta)[00]\alpha_i\alpha_j} & A_{46(11)}^{(\tau\eta)[00]\alpha_i\alpha_j} & A_{56(02)}^{(\tau\eta)[00]\alpha_i\alpha_j} & A_{46(01)}^{(\tau\eta)[01]\alpha_i\alpha_j} & A_{56(01)}^{(\tau\eta)[01]\alpha_i\alpha_j} & A_{36(01)}^{(\tau\eta)[01]\alpha_i\alpha_j} \\
A_{14(20)}^{(\tau\eta)[00]\alpha_i\alpha_j} & A_{24(11)}^{(\tau\eta)[00]\alpha_i\alpha_j} & A_{46(20)}^{(\tau\eta)[00]\alpha_i\alpha_j} & A_{46(11)}^{(\tau\eta)[00]\alpha_i\alpha_j} & A_{44(20)}^{(\tau\eta)[00]\alpha_i\alpha_j} & A_{45(11)}^{(\tau\eta)[00]\alpha_i\alpha_j} & A_{44(10)}^{(\tau\eta)[01]\alpha_i\alpha_j} & A_{45(10)}^{(\tau\eta)[01]\alpha_i\alpha_j} & A_{34(10)}^{(\tau\eta)[01]\alpha_i\alpha_j} \\
A_{15(11)}^{(\tau\eta)[00]\alpha_i\alpha_j} & A_{25(02)}^{(\tau\eta)[00]\alpha_i\alpha_j} & A_{56(11)}^{(\tau\eta)[00]\alpha_i\alpha_j} & A_{56(02)}^{(\tau\eta)[00]\alpha_i\alpha_j} & A_{45(11)}^{(\tau\eta)[00]\alpha_i\alpha_j} & A_{55(02)}^{(\tau\eta)[00]\alpha_i\alpha_j} & A_{45(01)}^{(\tau\eta)[01]\alpha_i\alpha_j} & A_{55(01)}^{(\tau\eta)[01]\alpha_i\alpha_j} & A_{35(01)}^{(\tau\eta)[01]\alpha_i\alpha_j} \\
\hline
A_{14(10)}^{(\tau\eta)[10]\alpha_i\alpha_j} & A_{24(01)}^{(\tau\eta)[10]\alpha_i\alpha_j} & A_{46(10)}^{(\tau\eta)[10]\alpha_i\alpha_j} & A_{46(01)}^{(\tau\eta)[10]\alpha_i\alpha_j} & A_{44(10)}^{(\tau\eta)[10]\alpha_i\alpha_j} & A_{45(01)}^{(\tau\eta)[10]\alpha_i\alpha_j} & A_{44(00)}^{(\tau\eta)[11]\alpha_i\alpha_j} & A_{45(00)}^{(\tau\eta)[11]\alpha_i\alpha_j} & A_{34(00)}^{(\tau\eta)[11]\alpha_i\alpha_j} \\
A_{15(10)}^{(\tau\eta)[10]\alpha_i\alpha_j} & A_{25(01)}^{(\tau\eta)[10]\alpha_i\alpha_j} & A_{56(10)}^{(\tau\eta)[10]\alpha_i\alpha_j} & A_{56(01)}^{(\tau\eta)[10]\alpha_i\alpha_j} & A_{45(10)}^{(\tau\eta)[10]\alpha_i\alpha_j} & A_{55(01)}^{(\tau\eta)[10]\alpha_i\alpha_j} & A_{45(00)}^{(\tau\eta)[11]\alpha_i\alpha_j} & A_{55(00)}^{(\tau\eta)[11]\alpha_i\alpha_j} & A_{35(00)}^{(\tau\eta)[11]\alpha_i\alpha_j} \\
A_{13(10)}^{(\tau\eta)[10]\alpha_i\alpha_j} & A_{23(01)}^{(\tau\eta)[10]\alpha_i\alpha_j} & A_{36(10)}^{(\tau\eta)[10]\alpha_i\alpha_j} & A_{36(01)}^{(\tau\eta)[10]\alpha_i\alpha_j} & A_{34(10)}^{(\tau\eta)[10]\alpha_i\alpha_j} & A_{35(01)}^{(\tau\eta)[10]\alpha_i\alpha_j} & A_{34(00)}^{(\tau\eta)[11]\alpha_i\alpha_j} & A_{35(00)}^{(\tau\eta)[11]\alpha_i\alpha_j} & A_{33(00)}^{(\tau\eta)[11]\alpha_i\alpha_j}
\end{array}\right]
$$

$$
\mathbf{A}_{\varphi\varphi}^{(\tau\eta)\alpha_i\alpha_j} = \left[\left(A_{\varphi\varphi nm(pq)}^{(\tau\eta)[fg]\alpha_i\alpha_j} \right)_{hs} \right]_{\substack{h=1,2,3 \\ s=1,2,3}} =
\left[\begin{array}{cc|c}
\Gamma_{11(20)}^{(\tau\eta)[00]\alpha_i\alpha_j} & \Gamma_{12(11)}^{(\tau\eta)[00]\alpha_i\alpha_j} & \Gamma_{13(10)}^{(\tau\eta)[01]\alpha_i\alpha_j} \\
\Gamma_{12(11)}^{(\tau\eta)[00]\alpha_i\alpha_j} & \Gamma_{22(02)}^{(\tau\eta)[00]\alpha_i\alpha_j} & \Gamma_{23(01)}^{(\tau\eta)[01]\alpha_i\alpha_j} \\
\hline
\Gamma_{13(10)}^{(\tau\eta)[10]\alpha_i\alpha_j} & \Gamma_{23(01)}^{(\tau\eta)[10]\alpha_i\alpha_j} & \Gamma_{33(00)}^{(\tau\eta)[11]\alpha_i\alpha_j}
\end{array}\right]
$$

$$
\mathbf{A}_{\varepsilon\varphi}^{(\tau\eta)\alpha_i\alpha_j} = \left[\left(A_{\varepsilon\varphi nm(pq)}^{(\tau\eta)[fg]\alpha_i\alpha_j} \right)_{hs} \right]_{\substack{h=1,\dots,9 \\ s=1,2,3}} = -
\left[\begin{array}{cccccc|ccc}
P_{11(20)}^{(\tau\eta)[00]\alpha_i\alpha_j} & P_{12(11)}^{(\tau\eta)[00]\alpha_i\alpha_j} & P_{16(20)}^{(\tau\eta)[00]\alpha_i\alpha_j} & P_{16(11)}^{(\tau\eta)[00]\alpha_i\alpha_j} & P_{14(20)}^{(\tau\eta)[00]\alpha_i\alpha_j} & P_{15(11)}^{(\tau\eta)[00]\alpha_i\alpha_j} & P_{14(10)}^{(\tau\eta)[10]\alpha_i\alpha_j} & P_{15(10)}^{(\tau\eta)[10]\alpha_i\alpha_j} & P_{13(10)}^{(\tau\eta)[10]\alpha_i\alpha_j} \\
P_{21(11)}^{(\tau\eta)[00]\alpha_i\alpha_j} & P_{22(02)}^{(\tau\eta)[00]\alpha_i\alpha_j} & P_{26(11)}^{(\tau\eta)[00]\alpha_i\alpha_j} & P_{26(02)}^{(\tau\eta)[00]\alpha_i\alpha_j} & P_{24(11)}^{(\tau\eta)[00]\alpha_i\alpha_j} & P_{25(02)}^{(\tau\eta)[00]\alpha_i\alpha_j} & P_{24(01)}^{(\tau\eta)[10]\alpha_i\alpha_j} & P_{25(01)}^{(\tau\eta)[10]\alpha_i\alpha_j} & P_{23(01)}^{(\tau\eta)[10]\alpha_i\alpha_j} \\
\hline
P_{31(10)}^{(\tau\eta)[01]\alpha_i\alpha_j} & P_{32(01)}^{(\tau\eta)[01]\alpha_i\alpha_j} & P_{36(10)}^{(\tau\eta)[01]\alpha_i\alpha_j} & P_{36(01)}^{(\tau\eta)[01]\alpha_i\alpha_j} & P_{34(10)}^{(\tau\eta)[01]\alpha_i\alpha_j} & P_{35(01)}^{(\tau\eta)[01]\alpha_i\alpha_j} & P_{34(00)}^{(\tau\eta)[11]\alpha_i\alpha_j} & P_{35(00)}^{(\tau\eta)[11]\alpha_i\alpha_j} & P_{33(00)}^{(\tau\eta)[11]\alpha_i\alpha_j}
\end{array}\right]^T
$$

$$\mathbf{A}_{\phi\varepsilon}^{(\tau\eta)\alpha_i\alpha_j} = \left[\left(A_{\phi\varepsilon nm(pq)}^{(\tau\eta)[fg]\alpha_i\alpha_j}\right)_{hs}\right]_{\substack{h=1,2,3\\ s=1,\ldots,9}} = \left[\begin{array}{cccccc|ccc} P_{11(20)}^{(\tau\eta)[00]\alpha_i\alpha_j} & P_{12(11)}^{(\tau\eta)[00]\alpha_i\alpha_j} & P_{16(20)}^{(\tau\eta)[00]\alpha_i\alpha_j} & P_{16(11)}^{(\tau\eta)[00]\alpha_i\alpha_j} & P_{14(20)}^{(\tau\eta)[00]\alpha_i\alpha_j} & P_{15(11)}^{(\tau\eta)[00]\alpha_i\alpha_j} & P_{14(10)}^{(\tau\eta)[01]\alpha_i\alpha_j} & P_{15(10)}^{(\tau\eta)[01]\alpha_i\alpha_j} & P_{13(10)}^{(\tau\eta)[01]\alpha_i\alpha_j} \\ P_{21(11)}^{(\tau\eta)[00]\alpha_i\alpha_j} & P_{22(02)}^{(\tau\eta)[00]\alpha_i\alpha_j} & P_{26(11)}^{(\tau\eta)[00]\alpha_i\alpha_j} & P_{26(02)}^{(\tau\eta)[00]\alpha_i\alpha_j} & P_{24(11)}^{(\tau\eta)[00]\alpha_i\alpha_j} & P_{25(02)}^{(\tau\eta)[00]\alpha_i\alpha_j} & P_{24(01)}^{(\tau\eta)[01]\alpha_i\alpha_j} & P_{25(01)}^{(\tau\eta)[01]\alpha_i\alpha_j} & P_{23(01)}^{(\tau\eta)[01]\alpha_i\alpha_j} \\ \hline P_{31(10)}^{(\tau\eta)[10]\alpha_i\alpha_j} & P_{32(01)}^{(\tau\eta)[10]\alpha_i\alpha_j} & P_{36(10)}^{(\tau\eta)[10]\alpha_i\alpha_j} & P_{36(01)}^{(\tau\eta)[10]\alpha_i\alpha_j} & P_{34(10)}^{(\tau\eta)[10]\alpha_i\alpha_j} & P_{35(01)}^{(\tau\eta)[10]\alpha_i\alpha_j} & P_{34(00)}^{(\tau\eta)[11]\alpha_i\alpha_j} & P_{35(00)}^{(\tau\eta)[11]\alpha_i\alpha_j} & P_{33(00)}^{(\tau\eta)[11]\alpha_i\alpha_j} \end{array}\right]$$

$$\mathbf{A}_{\varepsilon\mathrm{T}}^{(\tau\eta)\alpha_i\alpha_j} = \left[\left(\mathrm{A}_{\varepsilon\mathrm{T}nm(pq)}^{(\tau\eta)[fg]\,\alpha_i\alpha_j}\right)_{hs}\right]_{\substack{h=1,\ldots,9\\ s=1}} = -\left[\begin{array}{ccccccccc} Z_{11(10)}^{(\tau\eta)[00]\alpha_i\alpha_j} & Z_{22(01)}^{(\tau\eta)[00]\alpha_i\alpha_j} & Z_{12(10)}^{(\tau\eta)[00]\alpha_i\alpha_j} & Z_{12(01)}^{(\tau\eta)[00]\alpha_i\alpha_j} & Z_{13(10)}^{(\tau\eta)[00]\alpha_i\alpha_j} & Z_{23(01)}^{(\tau\eta)[00]\alpha_i\alpha_j} & Z_{13(00)}^{(\tau\eta)[10]\alpha_i\alpha_j} & Z_{23(00)}^{(\tau\eta)[10]\alpha_i\alpha_j} & Z_{33(00)}^{(\tau\eta)[10]\alpha_i\alpha_j} \end{array}\right]^{\mathrm{T}}$$

$$\mathbf{A}_{\mathrm{T}\varepsilon}^{(\tau\eta)\alpha_i\alpha_j} = \left[\left(\mathrm{A}_{\mathrm{T}\varepsilon nm(pq)}^{(\tau\eta)[fg]\,\alpha_i\alpha_j}\right)_{hs}\right]_{\substack{h=1\\ s=1,\ldots,9}} = \left[\begin{array}{ccccccccc} Z_{11(10)}^{(\tau\eta)[00]\alpha_i\alpha_j} & Z_{22(01)}^{(\tau\eta)[00]\alpha_i\alpha_j} & Z_{12(10)}^{(\tau\eta)[00]\alpha_i\alpha_j} & Z_{12(01)}^{(\tau\eta)[00]\alpha_i\alpha_j} & Z_{13(10)}^{(\tau\eta)[00]\alpha_i\alpha_j} & Z_{23(01)}^{(\tau\eta)[00]\alpha_i\alpha_j} & Z_{13(00)}^{(\tau\eta)[01]\alpha_i\alpha_j} & Z_{23(00)}^{(\tau\eta)[01]\alpha_i\alpha_j} & Z_{33(00)}^{(\tau\eta)[01]\alpha_i\alpha_j} \end{array}\right]$$

$$\mathbf{A}_{\varepsilon\mathrm{C}}^{(\tau\eta)\alpha_i\alpha_j} = \left[\left(\mathrm{A}_{\varepsilon\mathrm{C}nm(pq)}^{(\tau\eta)[fg]\,\alpha_i\alpha_j}\right)_{hs}\right]_{\substack{h=1,\ldots,9\\ s=1}} = -\left[\begin{array}{ccccccccc} E_{11(10)}^{(\tau\eta)[00]\alpha_i\alpha_j} & E_{22(01)}^{(\tau\eta)[00]\alpha_i\alpha_j} & E_{12(10)}^{(\tau\eta)[00]\alpha_i\alpha_j} & E_{12(01)}^{(\tau\eta)[00]\alpha_i\alpha_j} & E_{13(10)}^{(\tau\eta)[00]\alpha_i\alpha_j} & E_{23(01)}^{(\tau\eta)[00]\alpha_i\alpha_j} & E_{13(00)}^{(\tau\eta)[10]\alpha_i\alpha_j} & E_{23(00)}^{(\tau\eta)[10]\alpha_i\alpha_j} & E_{33(00)}^{(\tau\eta)[10]\alpha_i\alpha_j} \end{array}\right]^{\mathrm{T}}$$

$$\mathbf{A}_{\mathrm{C}\varepsilon}^{(\tau\eta)\alpha_i\alpha_j} = \left[\left(\mathrm{A}_{\mathrm{C}\varepsilon nm(pq)}^{(\tau\eta)[fg]\,\alpha_i\alpha_j}\right)_{hs}\right]_{\substack{h=1\\ s=1,\ldots,9}} = \left[\begin{array}{ccccccccc} E_{11(10)}^{(\tau\eta)[00]\alpha_i\alpha_j} & E_{22(01)}^{(\tau\eta)[00]\alpha_i\alpha_j} & E_{12(10)}^{(\tau\eta)[00]\alpha_i\alpha_j} & E_{12(01)}^{(\tau\eta)[00]\alpha_i\alpha_j} & E_{13(10)}^{(\tau\eta)[00]\alpha_i\alpha_j} & E_{23(01)}^{(\tau\eta)[00]\alpha_i\alpha_j} & E_{13(00)}^{(\tau\eta)[01]\alpha_i\alpha_j} & E_{23(00)}^{(\tau\eta)[01]\alpha_i\alpha_j} & E_{33(00)}^{(\tau\eta)[01]\alpha_i\alpha_j} \end{array}\right]$$

$$\mathbf{A}_{\phi\mathrm{T}}^{(\tau\eta)\alpha_i\alpha_j} = \left[\left(A_{\phi\mathrm{T}nm(pq)}^{(\tau\eta)[fg]\,\alpha_i\alpha_j}\right)_{hs}\right]_{\substack{h=1,2,3\\ s=1}} = \left[\begin{array}{ccc} O_{11(10)}^{(\tau\eta)[00]\alpha_i\alpha_j} & O_{22(01)}^{(\tau\eta)[00]\alpha_i\alpha_j} & O_{33(00)}^{(\tau\eta)[01]\alpha_i\alpha_j} \end{array}\right]^{T}$$

$$\mathbf{A}_{\mathrm{T}\phi}^{(\tau\eta)\alpha_i\alpha_j} = \left[\left(A_{\mathrm{T}\phi nm(pq)}^{(\tau\eta)[fg]\,\alpha_i\alpha_j}\right)_{hs}\right]_{\substack{h=1\\ s=1,2,3}} = \left[\begin{array}{ccc} O_{11(10)}^{(\tau\eta)[00]\alpha_i\alpha_j} & O_{22(01)}^{(\tau\eta)[00]\alpha_i\alpha_j} & O_{33(00)}^{(\tau\eta)[10]\alpha_i\alpha_j} \end{array}\right]$$

$$\mathbf{A}_{\phi\mathrm{C}}^{(\tau\eta)\alpha_i\alpha_j} = \left[\left(A_{\phi\mathrm{C}nm(pq)}^{(\tau\eta)[fg]\,\alpha_i\alpha_j}\right)_{hs}\right]_{\substack{h=1,2,3\\ s=1}} = \left[\begin{array}{ccc} G_{11(10)}^{(\tau\eta)[00]\alpha_i\alpha_j} & G_{22(01)}^{(\tau\eta)[00]\alpha_i\alpha_j} & G_{33(00)}^{(\tau\eta)[01]\alpha_i\alpha_j} \end{array}\right]^{T}$$

$$\mathbf{A}_{\mathrm{C}\phi}^{(\tau\eta)\alpha_i\alpha_j} = \left[\left(A_{\mathrm{C}\phi nm(pq)}^{(\tau\eta)[fg]\,\alpha_i\alpha_j}\right)_{hs}\right]_{\substack{h=1\\ s=1,2,3}} = \left[\begin{array}{ccc} G_{11(10)}^{(\tau\eta)[00]\alpha_i\alpha_j} & G_{22(01)}^{(\tau\eta)[00]\alpha_i\alpha_j} & G_{33(00)}^{(\tau\eta)[10]\alpha_i\alpha_j} \end{array}\right]$$

$$\mathbf{A}_{\mathrm{TT}}^{(\tau\eta)\alpha_i\alpha_j} = \left[\left(A_{\mathrm{TT}nm(pq)}^{(\tau\eta)[fg]\,\alpha_i\alpha_j}\right)_{hs}\right]_{\substack{h=1\\ s=1}} = C_{11(00)}^{(\tau\eta)[00]\alpha_i\alpha_j}$$

$$\mathbf{A}_{\mathrm{CC}}^{(\tau\eta)\alpha_i\alpha_j} = \left[\left(A_{\mathrm{CC}nm(pq)}^{(\tau\eta)[fg]\,\alpha_i\alpha_j}\right)_{hs}\right]_{\substack{h=1\\ s=1}} = T_{11(00)}^{(\tau\eta)[00]\alpha_i\alpha_j}$$

$$\mathbf{A}_{\mathrm{TC}}^{(\tau\eta)\alpha_i\alpha_j} = \mathbf{A}_{\mathrm{CT}}^{(\tau\eta)\alpha_i\alpha_j} = \left[\left(A_{\mathrm{TC}nm(pq)}^{(\tau\eta)[fg]\,\alpha_i\alpha_j}\right)_{hs}\right]_{\substack{h=1\\ s=1}} = B_{11(00)}^{(\tau\eta)[00]\alpha_i\alpha_j}$$

$$\mathbf{A}_{\theta\theta}^{(\tau\eta)\alpha_i\alpha_j} = \left[\left(A_{\theta\theta nm(pq)}^{(\tau\eta)[fg]\alpha_i\alpha_j}\right)_{hs}\right]_{\substack{h=1,2,3\\ s=1,2,3}} = \left[\begin{array}{cc|c} K_{11(20)}^{(\tau\eta)[00]\alpha_i\alpha_j} & K_{12(11)}^{(\tau\eta)[00]\alpha_i\alpha_j} & K_{13(10)}^{(\tau\eta)[01]\alpha_i\alpha_j} \\ K_{12(11)}^{(\tau\eta)[00]\alpha_i\alpha_j} & K_{22(02)}^{(\tau\eta)[00]\alpha_i\alpha_j} & K_{23(01)}^{(\tau\eta)[01]\alpha_i\alpha_j} \\ \hline K_{13(10)}^{(\tau\eta)[10]\alpha_i\alpha_j} & K_{23(01)}^{(\tau\eta)[10]\alpha_i\alpha_j} & K_{33(00)}^{(\tau\eta)[11]\alpha_i\alpha_j} \end{array}\right]$$

$$\mathbf{A}_{\lambda\lambda}^{(\tau\eta)\alpha_i\alpha_j} = \left[\left(A_{\lambda\lambda nm(pq)}^{(\tau\eta)[fg]\alpha_i\alpha_j}\right)_{hs}\right]_{\substack{h=1,2,3\\ s=1,2,3}} = \left[\begin{array}{cc|c} S_{11(20)}^{(\tau\eta)[00]\alpha_i\alpha_j} & S_{12(11)}^{(\tau\eta)[00]\alpha_i\alpha_j} & S_{13(10)}^{(\tau\eta)[01]\alpha_i\alpha_j} \\ S_{12(11)}^{(\tau\eta)[00]\alpha_i\alpha_j} & S_{22(02)}^{(\tau\eta)[00]\alpha_i\alpha_j} & S_{23(01)}^{(\tau\eta)[01]\alpha_i\alpha_j} \\ \hline S_{13(10)}^{(\tau\eta)[10]\alpha_i\alpha_j} & S_{23(01)}^{(\tau\eta)[10]\alpha_i\alpha_j} & S_{33(00)}^{(\tau\eta)[11]\alpha_i\alpha_j} \end{array}\right]$$

$$\mathbf{A}_{\lambda\theta}^{(\tau\eta)\alpha_i\alpha_j} = \left[\left(A_{\lambda\theta nm(pq)}^{(\tau\eta)[fg]\alpha_i\alpha_j}\right)_{hs}\right]_{\substack{h=1,2,3\\ s=1,2,3}} = \left[\begin{array}{cc|c} X_{11(20)}^{(\tau\eta)[00]\alpha_i\alpha_j} & X_{12(11)}^{(\tau\eta)[00]\alpha_i\alpha_j} & X_{13(10)}^{(\tau\eta)[01]\alpha_i\alpha_j} \\ X_{12(11)}^{(\tau\eta)[00]\alpha_i\alpha_j} & X_{22(02)}^{(\tau\eta)[00]\alpha_i\alpha_j} & X_{23(01)}^{(\tau\eta)[01]\alpha_i\alpha_j} \\ \hline X_{13(10)}^{(\tau\eta)[10]\alpha_i\alpha_j} & X_{23(01)}^{(\tau\eta)[10]\alpha_i\alpha_j} & X_{33(00)}^{(\tau\eta)[11]\alpha_i\alpha_j} \end{array}\right]$$

$$\mathbf{A}_{\theta\lambda}^{(\tau\eta)\alpha_i\alpha_j} = \left[\left(A_{\theta\lambda nm(pq)}^{(\tau\eta)[fg]\alpha_i\alpha_j}\right)_{hs}\right]_{\substack{h=1,2,3\\ s=1,2,3}} = \left[\begin{array}{cc|c} Y_{11(20)}^{(\tau\eta)[00]\alpha_i\alpha_j} & Y_{12(11)}^{(\tau\eta)[00]\alpha_i\alpha_j} & Y_{13(10)}^{(\tau\eta)[01]\alpha_i\alpha_j} \\ Y_{12(11)}^{(\tau\eta)[00]\alpha_i\alpha_j} & Y_{22(02)}^{(\tau\eta)[00]\alpha_i\alpha_j} & Y_{23(01)}^{(\tau\eta)[01]\alpha_i\alpha_j} \\ \hline Y_{13(10)}^{(\tau\eta)[10]\alpha_i\alpha_j} & Y_{23(01)}^{(\tau\eta)[10]\alpha_i\alpha_j} & Y_{33(00)}^{(\tau\eta)[11]\alpha_i\alpha_j} \end{array}\right] \tag{A.2}$$

The expression of the coefficients $\widetilde{L}_{ijnm}^{(\tau\eta)\alpha_i\alpha_j}$ is thus derived for a given set of wave numbers n, m used in the harmonic expansion of the unknown variables, as defined in Eq. (62), following the well-known Navier approach. In addition we provide the semi-analytical expression for the coefficients $L_{fminm}^{(\tau\eta)\alpha_i}$, with $i = 1,2,3$, which appear in Eq. (68). These coefficients are associated with the stiffness contribution from the Winkler-Pasternak elastic foundation.

$$L_{fm1nm}^{(\tau\eta)\alpha_1} = k_{1f}^{(-)} F_\eta^{(1)\alpha_1(-)} F_\tau^{(1)\alpha_1(-)} H_1^{(-)} H_2^{(-)} + k_{1f}^{(+)} F_\eta^{(l)\alpha_1(+)} F_\tau^{(l)\alpha_1(+)} H_1^{(+)} H_2^{(+)}$$

$$L_{fm2nm}^{(\tau\eta)\alpha_2} = k_{2f}^{(-)} F_\eta^{(1)\alpha_2(-)} F_\tau^{(1)\alpha_2(-)} H_1^{(-)} H_2^{(-)} + k_{2f}^{(+)} F_\eta^{(l)\alpha_2(+)} F_\tau^{(l)\alpha_2(+)} H_1^{(+)} H_2^{(+)}$$

$$L_{fm3nm}^{(\tau\eta)\alpha_3} = \left(k_{3f}^{(-)} + G_f^{(-)}\left(\frac{1}{\left(H_1^{(-)}\right)^2}\left(\frac{n\pi}{L_1}\right)^2 + \frac{1}{\left(H_2^{(-)}\right)^2}\left(\frac{m\pi}{L_2}\right)^2\right)\right) F_\eta^{(1)\alpha_3(-)} F_\tau^{(1)\alpha_3(-)} H_1^{(-)} H_2^{(-)} +$$
$$+ \left(k_{3f}^{(+)} + G_f^{(+)}\left(\frac{1}{\left(H_1^{(+)}\right)^2}\left(\frac{n\pi}{L_1}\right)^2 + \frac{1}{\left(H_2^{(+)}\right)^2}\left(\frac{m\pi}{L_2}\right)^2\right)\right) F_\eta^{(l)\alpha_3(+)} F_\tau^{(l)\alpha_3(+)} H_1^{(+)} H_2^{(+)}$$

$$\widetilde{L}_{11nm}^{(\tau\eta)\alpha_1\alpha_1} = -A_{11(20)}^{(\tau\eta)[00]\alpha_1\alpha_1}\left(\frac{n\pi}{L_1}\right)^2 - A_{66(02)}^{(\tau\eta)[00]\alpha_1\alpha_1}\left(\frac{m\pi}{L_2}\right)^2 - \frac{A_{44(20)}^{(\tau\eta)[00]\alpha_1\alpha_1}}{R_1^2} + \frac{A_{44(10)}^{(\tau\eta)[01]\alpha_1\alpha_1} + A_{44(10)}^{(\tau\eta)[10]\alpha_1\alpha_1}}{R_1} - A_{44(00)}^{(\tau\eta)[11]\alpha_1\alpha_1}$$

$$\widetilde{L}_{12nm}^{(\tau\eta)\alpha_1\alpha_2} = -\left(A_{12(11)}^{(\tau\eta)[00]\alpha_1\alpha_2} + A_{66(11)}^{(\tau\eta)[00]\alpha_1\alpha_2}\right)\left(\frac{n\pi}{L_1}\right)\left(\frac{m\pi}{L_2}\right)$$

$$\widetilde{L}_{13nm}^{(\tau\eta)\alpha_1\alpha_3} = \left(A_{13(10)}^{(\tau\eta)[01]\alpha_1\alpha_3} - A_{44(10)}^{(\tau\eta)[10]\alpha_1\alpha_3} + \frac{A_{11(20)}^{(\tau\eta)[00]\alpha_1\alpha_3} + A_{44(20)}^{(\tau\eta)[00]\alpha_1\alpha_3}}{R_1} + \frac{A_{12(11)}^{(\tau\eta)[00]\alpha_1\alpha_3}}{R_2}\right)\left(\frac{n\pi}{L_1}\right)$$

$$\widetilde{L}_{14nm}^{(\tau\eta)\alpha_1\alpha_4} = \left(P_{31(10)}^{(\tau\eta)[01]\alpha_1\alpha_4} - P_{14(10)}^{(\tau\eta)[10]\alpha_1\alpha_4} + \frac{P_{14(20)}^{(\tau\eta)[00]\alpha_1\alpha_4}}{R_1}\right)\left(\frac{n\pi}{L_1}\right)$$

$$\widetilde{L}_{15nm}^{(\tau\eta)\alpha_1\alpha_5} = -Z_{11(10)}^{(\tau\eta)[00]\alpha_1\alpha_5}\left(\frac{n\pi}{L_1}\right)$$

$$\widetilde{L}_{16nm}^{(\tau\eta)\alpha_1\alpha_6} = -E_{11(10)}^{(\tau\eta)[00]\alpha_1\alpha_6}\left(\frac{n\pi}{L_1}\right)$$

$$\widetilde{L}_{21nm}^{(\tau\eta)\alpha_2\alpha_1} = -\left(A_{12(11)}^{(\tau\eta)[00]\alpha_2\alpha_1} + A_{66(11)}^{(\tau\eta)[00]\alpha_2\alpha_1}\right)\left(\frac{n\pi}{L_1}\right)\left(\frac{m\pi}{L_2}\right)$$

$$\widetilde{L}_{22nm}^{(\tau\eta)\alpha_2\alpha_2} = -A_{66(20)}^{(\tau\eta)[00]\alpha_2\alpha_2}\left(\frac{n\pi}{L_1}\right)^2 - A_{22(02)}^{(\tau\eta)[00]\alpha_2\alpha_2}\left(\frac{m\pi}{L_2}\right)^2 - \frac{A_{55(02)}^{(\tau\eta)[00]\alpha_2\alpha_2}}{R_2^2} + \frac{A_{55(01)}^{(\tau\eta)[01]\alpha_2\alpha_2} + A_{55(01)}^{(\tau\eta)[10]\alpha_2\alpha_2}}{R_2} - A_{55(00)}^{(\tau\eta)[11]\alpha_2\alpha_2}$$

$$\widetilde{L}_{23nm}^{(\tau\eta)\alpha_2\alpha_3} = \left(A_{23(01)}^{(\tau\eta)[01]\alpha_2\alpha_3} - A_{55(01)}^{(\tau\eta)[10]\alpha_2\alpha_3} + \frac{A_{22(02)}^{(\tau\eta)[00]\alpha_2\alpha_3} + A_{55(02)}^{(\tau\eta)[00]\alpha_2\alpha_3}}{R_2} + \frac{A_{12(11)}^{(\tau\eta)[00]\alpha_2\alpha_3}}{R_1}\right)\left(\frac{m\pi}{L_2}\right)$$

$$\widetilde{L}_{24nm}^{(\tau\eta)\alpha_2\alpha_4} = \left(P_{32(01)}^{(\tau\eta)[01]\alpha_2\alpha_4} - P_{25(01)}^{(\tau\eta)[10]\alpha_2\alpha_4} + \frac{P_{25(02)}^{(\tau\eta)[00]\alpha_2\alpha_4}}{R_2}\right)\left(\frac{m\pi}{L_2}\right)$$

$$\widetilde{L}_{25nm}^{(\tau\eta)\alpha_2\alpha_5} = -Z_{22(01)}^{(\tau\eta)[00]\alpha_2\alpha_5}\left(\frac{m\pi}{L_2}\right)$$

$$\widetilde{L}_{26nm}^{(\tau\eta)\alpha_2\alpha_6} = -E_{22(01)}^{(\tau\eta)[00]\alpha_2\alpha_6}\left(\frac{m\pi}{L_2}\right)$$

$$\widetilde{L}_{31nm}^{(\tau\eta)\alpha_3\alpha_1} = \left(A_{13(10)}^{(\tau\eta)[10]\alpha_3\alpha_1} - A_{44(10)}^{(\tau\eta)[01]\alpha_3\alpha_1} + \frac{A_{11(20)}^{(\tau\eta)[00]\alpha_3\alpha_1} + A_{44(20)}^{(\tau\eta)[00]\alpha_3\alpha_1}}{R_1} + \frac{A_{12(11)}^{(\tau\eta)[00]\alpha_3\alpha_1}}{R_2}\right)\left(\frac{n\pi}{L_1}\right)$$

$$\widetilde{L}_{32nm}^{(\tau\eta)\alpha_3\alpha_2} = \left(A_{23(01)}^{(\tau\eta)[10]\alpha_3\alpha_2} - A_{55(01)}^{(\tau\eta)[01]\alpha_3\alpha_2} + \frac{A_{12(11)}^{(\tau\eta)[00]\alpha_3\alpha_2}}{R_1} + \frac{A_{22(02)}^{(\tau\eta)[00]\alpha_3\alpha_2} + A_{55(02)}^{(\tau\eta)[00]\alpha_3\alpha_2}}{R_2}\right)\left(\frac{m\pi}{L_2}\right)$$

$$\widetilde{L}_{33nm}^{(\tau\eta)\alpha_3\alpha_3} = -A_{44(20)}^{(\tau\eta)[00]\alpha_3\alpha_3}\left(\frac{n\pi}{L_1}\right)^2 - A_{55(02)}^{(\tau\eta)[00]\alpha_3\alpha_3}\left(\frac{m\pi}{L_2}\right)^2 - \frac{A_{11(20)}^{(\tau\eta)[00]\alpha_3\alpha_3}}{R_1^2} - \frac{A_{22(02)}^{(\tau\eta)[00]\alpha_3\alpha_3}}{R_2^2} - \frac{2A_{12(11)}^{(\tau\eta)[00]\alpha_3\alpha_3}}{R_1 R_2} +$$
$$- \frac{A_{13(10)}^{(\tau\eta)[01]\alpha_3\alpha_3} + A_{13(10)}^{(\tau\eta)[10]\alpha_3\alpha_3}}{R_1} - \frac{A_{23(01)}^{(\tau\eta)[01]\alpha_3\alpha_3} + A_{23(01)}^{(\tau\eta)[10]\alpha_3\alpha_3}}{R_2} - A_{33(00)}^{(\tau\eta)[11]\alpha_3\alpha_3}$$

$$\widetilde{L}_{34nm}^{(\tau s)\alpha_3\alpha_4} = -P_{14(20)}^{(\tau\eta)[00]\alpha_3\alpha_4}\left(\frac{n\pi}{L_1}\right)^2 - P_{25(02)}^{(\tau\eta)[00]\alpha_3\alpha_4}\left(\frac{m\pi}{L_2}\right)^2 - \frac{P_{31(10)}^{(\tau\eta)[01]\alpha_3\alpha_4}}{R_1} - \frac{P_{32(01)}^{(\tau\eta)[01]\alpha_3\alpha_4}}{R_2} - P_{33(00)}^{(\tau\eta)[11]\alpha_3\alpha_4}$$

$$\widetilde{L}^{(\tau\eta)\alpha_3\alpha_5}_{35nm} = \frac{Z^{(\tau\eta)[00]\alpha_3\alpha_5}_{11(10)}}{R_1} + \frac{Z^{(\tau\eta)[00]\alpha_3\alpha_5}_{22(01)}}{R_2} + Z^{(\tau\eta)[10]\alpha_3\alpha_5}_{33(00)}$$

$$\widetilde{L}^{(\tau\eta)\alpha_3\alpha_6}_{36nm} = \frac{E^{(\tau\eta)[00]\alpha_3\alpha_6}_{11(10)}}{R_1} + \frac{E^{(\tau\eta)[00]\alpha_3\alpha_6}_{22(01)}}{R_2} + E^{(\tau\eta)[10]\alpha_3\alpha_6}_{33(00)}$$

$$\widetilde{L}^{(\tau\eta)\alpha_4\alpha_1}_{41nm} = -\left(P^{(\tau\eta)[01]\alpha_4\alpha_1}_{14(10)} - P^{(\tau\eta)[10]\alpha_4\alpha_1}_{31(10)} - \frac{P^{(\tau\eta)[00]\alpha_4\alpha_1}_{14(20)}}{R_1}\right)\left(\frac{n\pi}{L_1}\right)$$

$$\widetilde{L}^{(\tau\eta)\alpha_4\alpha_2}_{42nm} = -\left(P^{(\tau\eta)[01]\alpha_4\alpha_2}_{25(01)} - P^{(\tau\eta)[10]\alpha_4\alpha_2}_{32(01)} - \frac{P^{(\tau\eta)[00]\alpha_4\alpha_2}_{25(02)}}{R_2}\right)\left(\frac{m\pi}{L_2}\right)$$

$$\widetilde{L}^{(\tau\eta)\alpha_4\alpha_3}_{43nm} = -P^{(\tau\eta)[00]\alpha_4\alpha_3}_{14(20)}\left(\frac{n\pi}{L_1}\right)^2 - P^{(\tau\eta)[00]\alpha_4\alpha_3}_{25(02)}\left(\frac{m\pi}{L_2}\right)^2 - \frac{P^{(\tau\eta)[10]\alpha_4\alpha_3}_{31(10)}}{R_1} - \frac{P^{(\tau\eta)[10]\alpha_4\alpha_3}_{32(01)}}{R_2} - P^{(\tau\eta)[11]\alpha_4\alpha_3}_{33(00)}$$

$$\widetilde{L}^{(\tau\eta)\alpha_4\alpha_4}_{44nm} = L^{(\tau\eta)[00]\alpha_4\alpha_4}_{11(20)}\left(\frac{n\pi}{L_1}\right)^2 + L^{(\tau\eta)[00]\alpha_4\alpha_4}_{22(02)}\left(\frac{m\pi}{L_2}\right)^2 + L^{(\tau\eta)[11]\alpha_4\alpha_4}_{33(00)}$$

$$\widetilde{L}^{(\tau\eta)\alpha_4\alpha_5}_{45nm} = -O^{(\tau\eta)[01]\alpha_4\alpha_5}_{33(00)}$$

$$\widetilde{L}^{(\tau\eta)\alpha_4\alpha_6}_{46nm} = -G^{(\tau\eta)[01]\alpha_4\alpha_6}_{33(00)}$$

$$\widetilde{L}^{(\tau\eta)\alpha_5\alpha_1}_{51nm} = 0, \quad \widetilde{L}^{(\tau\eta)\alpha_5\alpha_2}_{52nm} = 0, \quad \widetilde{L}^{(\tau\eta)\alpha_5\alpha_3}_{53nm} = 0, \quad \widetilde{L}^{(\tau\eta)\alpha_5\alpha_4}_{54nm} = 0$$

$$\widetilde{L}^{(\tau\eta)\alpha_5\alpha_5}_{55nm} = K^{(\tau\eta)[00]\alpha_5\alpha_5}_{11(20)}\left(\frac{n\pi}{L_1}\right)^2 + K^{(\tau\eta)[00]\alpha_5\alpha_5}_{22(02)}\left(\frac{m\pi}{L_2}\right)^2 + K^{(\tau\eta)[11]\alpha_5\alpha_5}_{33(00)}$$

$$\widetilde{L}^{(\tau\eta)\alpha_5\alpha_6}_{56nm} = Y^{(\tau\eta)[00]\alpha_5\alpha_6}_{11(20)}\left(\frac{n\pi}{L_1}\right)^2 + Y^{(\tau\eta)[00]\alpha_5\alpha_6}_{22(02)}\left(\frac{m\pi}{L_2}\right)^2 + Y^{(\tau\eta)[11]\alpha_5\alpha_6}_{33(00)}$$

$$\widetilde{L}^{(\tau\eta)\alpha_6\alpha_1}_{61nm} = 0, \quad \widetilde{L}^{(\tau\eta)\alpha_6\alpha_2}_{62nm} = 0, \quad \widetilde{L}^{(\tau\eta)\alpha_6\alpha_3}_{63nm} = 0, \quad \widetilde{L}^{(\tau\eta)\alpha_6\alpha_4}_{64nm} = 0$$

$$\widetilde{L}^{(\tau\eta)\alpha_5\alpha_6}_{65nm} = X^{(\tau\eta)[00]\alpha_6\alpha_5}_{11(20)}\left(\frac{n\pi}{L_1}\right)^2 + X^{(\tau\eta)[00]\alpha_6\alpha_5}_{22(02)}\left(\frac{m\pi}{L_2}\right)^2 + X^{(\tau\eta)[11]\alpha_6\alpha_5}_{33(00)}$$

$$\widetilde{L}^{(\tau\eta)\alpha_6\alpha_6}_{66nm} = S^{(\tau\eta)[00]\alpha_6\alpha_6}_{11(20)}\left(\frac{n\pi}{L_1}\right)^2 + S^{(\tau\eta)[00]\alpha_6\alpha_6}_{22(02)}\left(\frac{m\pi}{L_2}\right)^2 + S^{(\tau\eta)[11]\alpha_6\alpha_6}_{33(00)} \tag{A.3}$$

Appendix II

This Appendix presents the analytical expressions for the homogenization of a smart multifield material with hygro-thermo-electro-elastic constitutive properties, using the Mori-Tanaka approach, as derived from Ref. [65]. The unit cell of the homogenized material consists of a cylindrical inclusion with a volume fraction V_f, oriented along the ζ direction, and embedded in an isotropic matrix with a volume fraction V_m. It is assumed that there are no voids within the heterogeneous solid, therefore $V_m + V_f = 1$. The homogenization in hand is based on the full coupling, between mechanical elasticity, electrostatic and magnetostatic fields, as well as hygro-thermal properties. In fact, the following constitutive relationship is considered for the homogenized smart material, being $\widehat{\varepsilon}_1, \widehat{\varepsilon}_2, \widehat{\varepsilon}_3, \widehat{\gamma}_{12}, \widehat{\gamma}_{13}, \widehat{\gamma}_{23}$ and $\widehat{\sigma}_1, \widehat{\sigma}_2, \widehat{\sigma}_3, \widehat{\tau}_{12}, \widehat{\tau}_{13}, \widehat{\tau}_{23}$ the strain and stress components, $\widehat{\mathscr{E}}_1, \widehat{\mathscr{E}}_2, \widehat{\mathscr{E}}_3$ and $\widehat{\mathscr{D}}_1, \widehat{\mathscr{D}}_2, \widehat{\mathscr{D}}_3$ the electric field components and the electric flux components, $\widehat{\mathscr{H}}_1, \widehat{\mathscr{H}}_2, \widehat{\mathscr{H}}_3$ and $\widehat{\mathscr{B}}_1, \widehat{\mathscr{B}}_2, \widehat{\mathscr{B}}_3$ the primary and secondary variables of magnetostatic equations. Furthermore, $\widehat{\theta}_1, \widehat{\theta}_2, \widehat{\theta}_3$ and $\widehat{h}_1, \widehat{h}_2, \widehat{h}_3$ are the primary and secondary variables associated with thermal conduction, whereas $\widehat{\lambda}_1, \widehat{\lambda}_2, \widehat{\lambda}_3$ and $\widehat{c}_1, \widehat{c}_2, \widehat{c}_3$ denote the moisture concentration gradient and the moisture flux components, respectively:

$$
\begin{bmatrix} \hat{\sigma}_1 \\ \hat{\sigma}_2 \\ \hat{\tau}_{12} \\ \hat{\tau}_{13} \\ \hat{\tau}_{23} \\ \hat{\sigma}_3 \\ \hat{\mathcal{D}}_1 \\ \hat{\mathcal{D}}_2 \\ \hat{\mathcal{D}}_3 \\ \hat{\mathcal{B}}_1 \\ \hat{\mathcal{B}}_2 \\ \hat{\mathcal{B}}_3 \\ \eta \\ \mu \\ \hat{h}_1 \\ \hat{h}_2 \\ \hat{h}_3 \\ \hat{c}_1 \\ \hat{c}_2 \\ \hat{c}_3 \end{bmatrix}
=
\left[\begin{array}{cccccc|ccc|ccc|c|c|ccc|ccc}
C_{11} & C_{12} & 0 & 0 & 0 & C_{13} & 0 & 0 & -p_{31} & 0 & 0 & -q_{31} & -z_{11} & -e_{11} & 0 & 0 & 0 & 0 & 0 & 0 \\
C_{12} & C_{22} & 0 & 0 & 0 & C_{23} & 0 & 0 & -p_{32} & 0 & 0 & -q_{32} & -z_{22} & -e_{22} & 0 & 0 & 0 & 0 & 0 & 0 \\
0 & 0 & \overline{C}_{66} & 0 & 0 & 0 & 0 & 0 & 0 & 0 & 0 & 0 & 0 & 0 & 0 & 0 & 0 & 0 & 0 & 0 \\
0 & 0 & 0 & C_{44} & 0 & 0 & -p_{14} & 0 & 0 & -q_{14} & 0 & 0 & 0 & 0 & 0 & 0 & 0 & 0 & 0 & 0 \\
0 & 0 & 0 & 0 & C_{55} & 0 & 0 & -p_{25} & 0 & 0 & -q_{25} & 0 & 0 & 0 & 0 & 0 & 0 & 0 & 0 & 0 \\
C_{13} & C_{23} & 0 & 0 & 0 & C_{33} & 0 & 0 & -p_{33} & 0 & 0 & -q_{33} & -z_{33} & -e_{33} & 0 & 0 & 0 & 0 & 0 & 0 \\
\hline
0 & 0 & 0 & p_{14} & 0 & 0 & l_{11} & 0 & 0 & d_{11} & 0 & 0 & 0 & 0 & 0 & 0 & 0 & 0 & 0 & 0 \\
0 & 0 & 0 & 0 & p_{25} & 0 & 0 & l_{22} & 0 & 0 & d_{22} & 0 & 0 & 0 & 0 & 0 & 0 & 0 & 0 & 0 \\
p_{31} & p_{32} & 0 & 0 & 0 & p_{33} & 0 & 0 & l_{33} & 0 & 0 & d_{33} & o_{33} & g_{33} & 0 & 0 & 0 & 0 & 0 & 0 \\
\hline
0 & 0 & 0 & q_{14} & 0 & 0 & d_{11} & 0 & 0 & m_{11} & 0 & 0 & 0 & 0 & 0 & 0 & 0 & 0 & 0 & 0 \\
0 & 0 & 0 & 0 & q_{25} & 0 & 0 & d_{22} & 0 & 0 & m_{22} & 0 & 0 & 0 & 0 & 0 & 0 & 0 & 0 & 0 \\
q_{31} & q_{32} & 0 & 0 & 0 & q_{33} & 0 & 0 & d_{33} & 0 & 0 & m_{33} & w_{33} & f_{33} & 0 & 0 & 0 & 0 & 0 & 0 \\
\hline
z_{11} & z_{22} & 0 & 0 & 0 & z_{33} & 0 & 0 & o_{33} & 0 & 0 & w_{33} & \xi_{11} & \xi_{12} & 0 & 0 & 0 & 0 & 0 & 0 \\
\hline
e_{11} & e_{22} & 0 & 0 & 0 & e_{33} & 0 & 0 & g_{33} & 0 & 0 & f_{33} & \xi_{12} & \xi_{22} & 0 & 0 & 0 & 0 & 0 & 0 \\
\hline
0 & 0 & 0 & 0 & 0 & 0 & 0 & 0 & 0 & 0 & 0 & 0 & 0 & 0 & k_{11} & 0 & 0 & y_{11} & 0 & 0 \\
0 & 0 & 0 & 0 & 0 & 0 & 0 & 0 & 0 & 0 & 0 & 0 & 0 & 0 & 0 & k_{22} & 0 & 0 & y_{22} & 0 \\
0 & 0 & 0 & 0 & 0 & 0 & 0 & 0 & 0 & 0 & 0 & 0 & 0 & 0 & 0 & 0 & k_{33} & 0 & 0 & y_{33} \\
\hline
0 & 0 & 0 & 0 & 0 & 0 & 0 & 0 & 0 & 0 & 0 & 0 & 0 & 0 & x_{11} & 0 & 0 & s_{11} & 0 & 0 \\
0 & 0 & 0 & 0 & 0 & 0 & 0 & 0 & 0 & 0 & 0 & 0 & 0 & 0 & 0 & x_{22} & 0 & 0 & s_{22} & 0 \\
0 & 0 & 0 & 0 & 0 & 0 & 0 & 0 & 0 & 0 & 0 & 0 & 0 & 0 & 0 & 0 & x_{33} & 0 & 0 & s_{33}
\end{array}\right]
\begin{bmatrix} \hat{\varepsilon}_1 \\ \hat{\varepsilon}_2 \\ \hat{\gamma}_{12} \\ \hat{\gamma}_{13} \\ \hat{\gamma}_{23} \\ \hat{\varepsilon}_3 \\ \hat{\mathcal{E}}_1 \\ \hat{\mathcal{E}}_2 \\ \hat{\mathcal{E}}_3 \\ \hat{\mathcal{H}}_1 \\ \hat{\mathcal{H}}_2 \\ \hat{\mathcal{H}}_3 \\ \Delta T \\ \Delta C \\ \hat{\theta}_1 \\ \hat{\theta}_2 \\ \hat{\theta}_3 \\ \hat{\lambda}_1 \\ \hat{\lambda}_2 \\ \hat{\lambda}_3 \end{bmatrix}
\tag{A.4}
$$

In the analytical expressions for homogenization, the constitutive coefficients of the matrix are denoted with the subscript "m", while those of the cylindrical fiber are characterized by the subscript "f".

Preliminary computations

$$j = 2V_f \frac{C_{44m} l_{11m} m_{11m} + p_{14m}^2 m_{11m} + l_{11m} q_{14m}^2 - 2 d_{11m} p_{14m} - d_{11m}^2 C_{44m}}{(ic - gb)h + (fb - ia)e + (ga - fc)d}$$

$$a = V_m\Big(\big(q_{14f} - q_{14m}\big)\big(l_{11m} m_{11m} - d_{11m}^2\big) - \big(d_{11f} - d_{11m}\big)\big(p_{14m} m_{11m} - d_{11m} q_{14m}\big) - \big(m_{11f} - m_{11m}\big)\big(q_{14m} l_{11m} - d_{11m} p_{14m}\big)\Big)$$

$$b = V_m\Big(\big(p_{14f} - p_{14m}\big)\big(l_{11m} m_{11m} - d_{11m}^2\big) - \big(d_{11f} - d_{11m}\big)\big(q_{14m} l_{11m} - d_{11m} p_{14m}\big) - \big(l_{11f} - l_{11m}\big)\big(p_{14m} m_{11m} - d_{11m} q_{14m}\big)\Big)$$

$$c = V_m\Big(\big(C_{44f} - C_{44m}\big)\big(l_{11m} m_{11m} - d_{11m}^2\big) + \big(p_{14f} - p_{14m}\big)\big(p_{14m} m_{11m} - d_{11m} q_{14m}\big) + \big(q_{14f} - q_{14m}\big)\big(q_{14m} l_{11m} - d_{11m} p_{14m}\big)\Big) +$$
$$+ \frac{j}{V_f}\big((ic - gb)h + (fb - ia)e + (ga - fc)d\big)$$

$$d = V_m\Big(- \big(d_{11f} - d_{11m}\big)\big(d_{11m} C_{44m} + p_{14m} q_{14m}\big) + \big(p_{14f} - p_{14m}\big)\big(p_{14m} m_{11m} - d_{11m} q_{14m}\big) + \big(l_{11f} - l_{11m}\big)\big(q_{14m}^2 + C_{44m} m_{11m}\big)\Big) +$$
$$+ \frac{j}{V_f}\big((ic - gb)h + (fb - ia)e + (ga - fc)d\big)$$

$$e = V_m\Big(\big(q_{14f} - q_{14m}\big)\big(d_{11m} C_{44m} + p_{14m} q_{14m}\big) + \big(C_{44f} - C_{44m}\big)\big(p_{14m} m_{11m} - d_{11m} q_{14m}\big) - \big(p_{14f} - p_{14m}\big)\big(q_{14m}^2 + C_{44m} m_{11m}\big)\Big)$$

$$f = V_m\Big(- \big(d_{11f} - d_{11m}\big)\big(d_{11m} C_{44m} + p_{14m} q_{14m}\big) + \big(q_{14f} - q_{14m}\big)\big(q_{14m} l_{11m} - d_{11m} p_{14m}\big) + \big(m_{11f} - m_{11m}\big)\big(p_{14m}^2 + C_{44m} l_{11m}\big)\Big) +$$
$$+ \frac{j}{V_f}\big((ic - gb)h + (fb - ia)e + (ga - fc)d\big)$$

$$g = V_m\Big(\big(p_{14f} - p_{14m}\big)\big(d_{11m} C_{44m} + p_{14m} q_{14m}\big) + \big(C_{44f} - C_{44m}\big)\big(q_{14m} l_{11m} - d_{11m} p_{14m}\big) - \big(q_{14f} - q_{14m}\big)\big(p_{14m}^2 + C_{44m} l_{11m}\big)\Big)$$

$$h = V_m\Big(- \big(m_{11f} - m_{11m}\big)\big(d_{11m} C_{44m} - p_{14m} q_{14m}\big) + \big(q_{14f} - q_{14m}\big)\big(p_{14m} m_{11m} - d_{11m} q_{14m}\big) + \big(d_{11f} - d_{11m}\big)\big(q_{14m}^2 + C_{44m} m_{11m}\big)\Big)$$

$$i = V_m\Big(- \big(l_{11f} - l_{11m}\big)\big(d_{11m} C_{44m} + p_{14m} q_{14m}\big) + \big(p_{14f} - p_{14m}\big)\big(q_{14m} l_{11m} - d_{11m} p_{14m}\big) + \big(d_{11f} - d_{11m}\big)\big(p_{14m}^2 + C_{44m} l_{11m}\big)\Big) \tag{A.5}$$

Density

$$\rho = V_m \rho_m + V_f \rho_f \tag{A.6}$$

Elastic stiffness coefficients

$$k = \frac{k_m k_f + V_f m_m k_f + V_m m_m k_m}{V_m k_f + V_f k_m + m_m}$$

$$m = \frac{m_m \left(k_m m_f + V_f k_m m_f + V_m k_m m_m + 2 m_m m_f\right)}{V_m k_m m_f + k_m m_m + V_f k_m m_m + 2 V_m m_m m_f + 2 V_f m_m^2}$$

$$C_{11} = C_{22} = k + m$$

$$C_{12} = k - m$$

$$C_{13} = C_{23} = C_{13m} + \frac{V_f \left(C_{13f} - C_{13m}\right)\left(k_m + m_m\right)}{V_m k_f + V_f k_m + m_m}$$

$$C_{33} = C_{33m} + V_f \left(C_{33f} - C_{33m} - \frac{V_m \left(C_{13m} - C_{13f}\right)^2}{V_m k_f + V_f k_m + m_m}\right)$$

$$C_{44} = C_{55} = C_{44m} + j\left(\left(p_{14f} - p_{14m}\right)(fe - gh) + \left(C_{44f} - C_{44m}\right)(ih - fd) + \left(q_{14f} - q_{14m}\right)(gd - ie)\right) \tag{A.7}$$

Piezoelectric coefficients

$$p_{31} = p_{32} = p_{31m} + \frac{V_f \left(p_{31f} - p_{31m}\right)\left(k_m + m_m\right)}{V_m k_f + V_f k_m + m_m}$$

$$p_{33} = p_{33m} + V_f \left(p_{33f} - p_{33m} + \frac{V_m \left(C_{13m} - C_{13f}\right)\left(p_{31f} - p_{31m}\right)}{V_m k_f + V_f k_m + m_m}\right)$$

$$p_{14} = p_{25} = p_{14m} + j\left(\left(p_{14f} - p_{14m}\right)(ga - fc) + \left(C_{44f} - C_{44m}\right)(fb - ia) + \left(q_{14f} - q_{14m}\right)(ic - gb)\right) \tag{A.8}$$

Dielectric permittivity coefficients

$$\begin{aligned} l_{11} &= l_{22} = l_{11m} + j\left(\left(l_{11f} - l_{11m}\right)(ga - fc) + \left(p_{14f} - p_{14m}\right)(ia - fb) + \left(d_{11f} - d_{11m}\right)(ic - gb)\right) \\ l_{33} &= l_{33m} + V_f \left(l_{33f} - l_{33m} + \frac{V_m \left(p_{31f} - p_{31m}\right)^2}{V_m k_f + V_f k_m + m_m}\right) \end{aligned} \tag{A.9}$$

Thermal expansion coefficients

$$\begin{aligned} a_{11} &= \frac{V_f E_f a_f + V_m E_m a_m}{E_1} \\ a_{22} &= a_{33} = (1 + \nu_f) a_f V_f + (1 + \nu_m) a_m V_m - \nu_{12} a_{11} \end{aligned} \tag{A.10}$$

Hygroscopic expansion coefficients

$$\begin{aligned} b_{11} &= \frac{V_f E_f b_f + V_m E_m b_m}{E_1} \\ b_{22} &= b_{33} = (1 + \nu_f) b_f V_f + (1 + \nu_m) b_m V_m - \nu_{12} b_{11} \end{aligned} \tag{A.11}$$

Pyroelectric coefficient

$$o_{33} = V_m o_{33m} + V_f o_{33f} - V_m V_f \frac{\left(p_{31f} - p_{31m}\right)\left(z_{11f} - z_{11m}\right)}{C_{11m} + V_m k_f - V_m k_m} \tag{A.12}$$

Hygroelectric coefficient

$$g_{33} = V_m g_{33m} + V_f g_{33f} - V_m V_f \frac{\left(p_{31f} - p_{31m}\right)\left(e_{11f} - e_{11m}\right)}{C_{11m} + V_m k_f - V_m k_m} \tag{A.13}$$

Specific heat capacity

$$c_p = \frac{V_f \rho_f c_{pf} + V_m \rho_m c_{pm}}{\rho} \tag{A.14}$$

Equilibrium moisture content

$$M_\infty = \frac{V_m \rho_m M_{\infty m} + V_f \rho_f M_{\infty f}}{\rho} \tag{A.15}$$

Thermal conductivity

$$k_{11} = k_{22} = \frac{k_m k_f}{V_f k_m + V_m k_f}$$
$$k_{33} = V_m k_m + V_f k_f = (1 - V_f) k_m + V_f k_f = (k_f - k_m) V_f + k_m \tag{A.16}$$

Diffusion coefficients

$$s_{11} = s_{22} = \frac{s_m s_f}{V_f s_m + V_m s_f}$$
$$s_{33} = V_m s_m + V_f s_f = (1 - V_f) s_m + V_f s_f = (s_f - s_m) V_f + s_m \tag{A.17}$$

Thermodiffusion (Dufour) coefficients

$$y_{11} = \nu\rho c s_{11} = \nu u_d k_{11}, \quad y_{22} = \nu\rho c s_{22} = \nu u_d k_{22}, \quad y_{33} = \nu\rho c s_{33} = \nu u_d k_{33} \tag{A.18}$$

Thermophoretic (Soret) coefficients

$$x_{11} = \frac{\lambda}{\rho c} k_{11}, \quad x_{22} = \frac{\lambda}{\rho c} k_{22}, \quad x_{33} = \frac{\lambda}{\rho c} k_{33} \tag{A.19}$$

Data availability

No data was used for the research described in the article.

References

[1] A.L. Kalamkarov, A.V. Georgiades, Modeling of smart composites on account of actuation, thermal conductivity and hygroscopic absorption, Compos. B: Eng. 33 (2002) 141–152.
[2] H. Zhou, et al., Numerical simulation of failure of composite coatings due to thermal and hygroscopic stresses, Coatings 9 (2019) 243.
[3] B.C. Ray, Temperature effect during humid ageing on interfaces of glass and carbon fibers reinforced epoxy composites, J. Colloid Interface Sci. 298 (2006) 111–117.
[4] D. Gay, Composite materials: Design And Applications, CRC Press, Boca Raton, 2022.
[5] R.M. Jones, Mechanics of Composite Materials, CRC Press, Philadelphia, 1999.
[6] F. Ali, et al., Piezoelectric energy harvesters for biomedical applications, Nano Energy 57 (2019) 879–902.
[7] P. Jiao, et al., Piezoelectric sensing techniques in structural health monitoring: a state-of-the-art review, Sensors 20 (2020) 3730.
[8] S. Wang, et al., Tooth backlash inspired comb-shaped single-electrode triboelectric nanogenerator for self-powered condition monitoring of gear transmission, Nano Energy 123 (2024) 109429.
[9] Y. Wu, Y. Ma, H. Zheng, S. Ramakrishna, Piezoelectric materials for flexible and wearable electronics: a review, Mater. Des. 211 (2021) 110164.
[10] H.S. Tzou, Piezoelectric Shells, Springer Science & Business Media, Dordrecht, 1993.
[11] N.N. Rogacheva, The Theory Of Piezoelectric Shells And Plates, CRC Press, Boca Raton, 2020.
[12] T. Peret, A. Clément, S. Fréour, F. Jacquemin, Numerical transient hygro-elastic analyses of reinforced Fickian and non-Fickian polymers, Compos. Struct. 116 (2014) 395–403.
[13] I.B.C.M. Rocha, et al., A multiscale and multiphysics numerical framework for modelling of hygrothermal ageing in laminated composites, Int. J. Numer. Methods Eng. 112 (2017) 360–379.
[14] B.P. Patel, M. Ganapathi, D.P. Makhecha, Hygrothermal effects on the structural behaviour of thick composite laminates using higher-order theory, Compos. Struct. 56 (2002) 25–34.
[15] C.D. Shirrell Moisture diffusion in advanced composite resin matrix laminates, AFML Progress Report, Bergamo Center, 1977.
[16] N. Roe, et al., Advanced moisture modeling of polymer composites, J. Reinf. Plast. Compos. 32 (2013) 437–449.
[17] G. King, A.B.D. Cassie, S. Baxter, Propagation of temperature changes through textiles in humid atmospheres, Trans. Faraday Soc. 35 (1940) 445–465.
[18] G.C. Sih, J. Michopoulos, S.C. Chou, Hygrothermoelasticity, Springer Science & Business Media, 2012.
[19] G.C. Sih, M.T. Shih, S.C. Chou, Transient hygrothermal stresses in composites: coupling of moisture and heat with temperature varying diffusivity, Int. J. Eng. Sci. 18 (1980) 19–42.
[20] G.C. Sih, A. Ogawa, Transient thermal change on a solid surface: coupled diffusion of heat and moisture, J. Therm. Stress. 5 (1982) 265–282.
[21] L. Onsager, Reciprocal relations in irreversible processes. I-II, Phys. Rev. 37 (1931) 405.
[22] S. Brischetto, Hygrothermoelastic analysis of multilayered composite and sandwich shells, J. Sandw. Struct. Mater. 15 (2013) 168–202.
[23] Y. Zhao, et al., Excellent angular and electrical performance damage tolerance of wave-absorbing laminate via gradient ATA design, Compos. Commun. 46 (2024) 101838.
[24] S. Guo, et al., A flexible impact sensor of interpenetrating-phase composite architecture with high mechanical stability and energy-absorbing capability, Adv. Funct. Mater. (2025) 2419882.
[25] F. Meftah, S. Dal Pont, B.A. Schrefler, A three-dimensional staggered finite element approach for random parametric modeling of thermo-hygral coupled phenomena in porous media, Int. J. Numer. Anal. Methods Geomech. 36 (2012) 574–596.
[26] Z. Liu, J. Reinoso, M. Paggi, Hygro-thermo-mechanical modeling of thin-walled photovoltaic laminates with polymeric interfaces, J. Mech. Phys. Solids 169 (2022) 105056.
[27] S. Brischetto, R. Torre, 3D shell model for the thermo-mechanical analysis of FGM structures via imposed and calculated temperature profiles, Aerosp. Sci. Technol. 85 (2019) 125–149.
[28] S. Brischetto, D. Cesare, R. Torre, A layer-wise coupled thermo-elastic shell model for 3D stress analysis of functionally graded material structures, Technologies 11 (2023) 35.
[29] F. Tornabene, M. Viscoti, R. Dimitri, Hygro-Thermo-mechanical equivalent layer-Wise theory of laminated shell structures, Comput. Model. Eng. Sci. 142 (2024) 1697.
[30] A.K. Noor, M. Malik, An assessment of five modeling approaches for thermo-mechanical stress analysis of laminated composite panels, Comput. Mech. 25 (2000) 43–58.
[31] G.A. Holzapfel, Nonlinear Solid Mechanics: A Continuum Approach For Engineering Science, John Wiley & Sons, 2002.
[32] F. Moleiro, E. Carrera, A.J.M. Ferreira, J.N. Reddy, Hygro-thermo-mechanical modelling and analysis of multilayered plates with embedded functionally graded material layers, Compos. Struct. 233 (2020) 111442.
[33] F. Moleiro, V.F. Correia, A.J.M. Ferreira, J.N. Reddy, Fully coupled thermo-mechanical analysis of multilayered plates with embedded FGM skins or core layers using a layerwise mixed model, Compos. Struct. 210 (2019) 971–996.
[34] D. Li, Layerwise theories of laminated composite structures and their applications: a review, Arch. Comput. Methods Eng. 28 (2021) 577–600.
[35] J.N. Reddy, An evaluation of equivalent-single-layer and layerwise theories of composite laminates, Compos. Struct. 25 (1993) 21–35.
[36] J.N. Reddy, D.H. Robbins Jr, Theories and computational models for composite laminates, Appl. Mech. Rev. 47 (1994) 147–169.
[37] Y. Qu, X. Long, S. Wu, G. Meng, A unified formulation for vibration analysis of composite laminated shells of revolution including shear deformation and rotary inertia, Compos. Struct. 98 (2013) 169–191.
[38] K.M. Liew, Z.Z. Pan, L.W. Zhang, An overview of layerwise theories for composite laminates and structures: development, numerical implementation and application, Compos. Struct. 216 (2019) 240–259.
[39] J.N. Reddy, On refined theories of composite laminates, Meccanica 25 (1990) 230–238.
[40] J.N. Reddy, C.M. Wang, An overview of the relationships between solutions of the classical and shear deformation plate theories, Compos. Sci. Technol. 60 (2000) 2327–2335.
[41] R. Khandan, S. Noroozi, P. Sewell, J. Vinney, The development of laminated composite plate theories: a review, J. Mater. Sci. 47 (2012) 5901–5910.
[42] C.M. Wang, J.N. Reddy, K.H. Lee, Shear Deformable Beams And Plates: Relationships With Classical Solutions, Elsevier, Amsterdam, 2000.
[43] E. Carrera, S. Brischetto, M. Cinefra, M. Soave, Effects of thickness stretching in functionally graded plates and shells, Compos. B: Eng. 42 (2) (2011) 123–133.
[44] V.L. Nguyen, M.T. Tran, S. Limkatanyu, H. Mohammad-Sedighi, J. Rungamornrat, Reddy's third-order shear deformation shell theory for free vibration analysis of rotating stiffened advanced nanocomposite toroidal shell segments in thermal environments, Acta Mech. 233 (2022) 4659–4684.
[45] J.N. Reddy, C. Liu, A higher-order shear deformation theory of laminated elastic shells, Int. J. Eng. Sci. 23 (1985) 319–330.

[46] A. Chikh, A. Tounsi, H. Hebali, S.R. Mahmoud, Thermal buckling analysis of cross-ply laminated plates using a simplified HSDT, Smart Struct. Syst. 19 (2017) 289–297.
[47] A. Bouhadra, et al., Improved HSDT accounting for effect of thickness stretching in advanced composite plates, Struct. Eng. Mech. 66 (2018) 61–73.
[48] T. Ye, G. Jin, Y. Zhang, Vibrations of composite laminated doubly-curved shells of revolution with elastic restraints including shear deformation, rotary inertia and initial curvature, Compos. Struct. 133 (2015) 202–225.
[49] H. Murakami, Laminated composite plate theory with improved in-plane responses, J. Appl. Mech. 53 (1986) 661–666.
[50] A. Toledano, H. Murakami, A high-order laminated plate theory with improved in-plane responses, Int. J. Solids Struct. 23 (1987) 111–131.
[51] F. Tornabene, M. Viscoti, R. Dimitri, J.N. Reddy, Higher order theories for the vibration study of doubly-curved anisotropic shells with a variable thickness and isogeometric mapped geometry, Compos. Struct. 267 (2021) 113829.
[52] A. Tessler, M. Di Sciuva, M. Gherlone, Refined zigzag theory for laminated composite and sandwich plates, NASA Tech. Publ. (2009), 20090007494.
[53] A. Tessler, M. Di Sciuva, M. Gherlone, A consistent refinement of first-order shear deformation theory for laminated composite and sandwich plates using improved zigzag kinematics, J. Mech. Mater. Struct. 5 (2010) 341–367.
[54] K. Washizu, Variational Methods in Elasticity & Plasticity, Pergamon Press, Oxford, 1975.
[55] J.N. Reddy, A generalization of two-dimensional theories of laminated composite plates, Commun. Appl. Numer. Methods 3 (1987) 173–180.
[56] F. Tornabene, N. Fantuzzi, M. Bacciocchi, J.N. Reddy, An equivalent layer-wise approach for the free vibration analysis of thick and thin laminated and sandwich shells, Appl. Sci. 7 (2016) 17.
[57] J. Wang, J. Yang, Higher-order theories of piezoelectric plates and applications, Appl. Mech. Rev. 53 (2000) 87–99.
[58] F. Tornabene, Hygro-Thermo-Magneto-Electro-Elastic Theory of Anisotropic Doubly-curved Shells, Esculapio, Bologna, 2023.
[59] F. Tornabene, M. Viscoti, R. Dimitri, Equivalent layer-wise theory for the hygro-thermo-magneto-electro-elastic analysis of laminated curved shells, Thin-Walled Struct. 198 (2024) 111751.
[60] X. Liang, et al., Roadmap on magnetoelectric materials and devices, IEEE Trans. Magn. 57 (2021) 1–57.
[61] H.S. Kim, S.I. Hong, S.J. Kim, On the rule of mixtures for predicting the mechanical properties of composites with homogeneously distributed soft and hard particles, J. Mater. Process. Technol. 112 (2001) 109–113.
[62] T. Mori, K. Tanaka, Average stress in matrix and average elastic energy of materials with misfitting inclusions, Acta Metall. 21 (1973) 571–574.
[63] J.D. Eshelby, The determination of the elastic field of an ellipsoidal inclusion, and related problems, Proc. R. Soc. Lond. 241 (1957) 376–396.
[64] A.C. Gavazzi, D.C. Lagoudas, On the numerical evaluation of Eshelby's tensor and its application to elastoplastic fibrous composites, Comput. Mech. 7 (1990) 13–19.
[65] J.Y. Li, M.L. Dunn, Anisotropic coupled-field inclusion and inhomogeneity problems, Philos. Mag. A 77 (1998) 1341–1350.
[66] T. Mura, Micromechanics of Defects in Solids, Martinus Nijhoff Publishers, The Hague, 1982.
[67] T. Mura, Inclusion problems, Appl. Mech. Rev. 41 (1988) 15–20.
[68] S. Trotta, F. Marmo, L. Rosati, Analytical expression of the Eshelby tensor for arbitrary polygonal inclusions in two-dimensional elasticity, Compos. B: Eng. 106 (2016) 48–58.
[69] S. Trotta, F. Marmo, L. Rosati, Evaluation of the Eshelby tensor for polygonal inclusions, Compos. B: Eng. 115 (2017) 170–181.
[70] S.I. Kundalwal, M.C. Ray, Effect of carbon nanotube waviness on the elastic properties of the fuzzy fiber reinforced composites, J. Appl. Mech. 80 (2013) 021010.
[71] D.L. Shi, et al., The effect of nanotube waviness and agglomeration on the elastic property of carbon nanotube-reinforced composites, J. Eng. Mater. Technol. 126 (2004) 250–257.
[72] F. Tornabene, M. Viscoti, R. Dimitri, Free vibration analysis of laminated anisotropic doubly-curved shell structures reinforced with three-phase polymer/CNT/fiber material, Eng. Anal. Bound. Elem. 164 (2024) 105762.
[73] M.L. Dunn, M. Taya, Micromechanics predictions of the effective electroelastic moduli of piezoelectric composites, Int. J. Solids Struct. 30 (1993) 161–175.
[74] J.Y. Li, M.L. Dunn, Micromechanics of magnetoelectroelastic composite materials: average fields and effective behavior, J. Intell. Mater. Syst. Struct. 9 (1998) 404–416.
[75] K.M. Gupta, Engineering Materials: Research, Applications And Advances, CRC Press, Boca Raton, 2014.
[76] A. Garg, M.O. Belarbi, H.D. Chalak, A. Chakrabarti, A review of the analysis of sandwich FGM structures, Compos. Struct. 258 (2021) 113427.
[77] Ö. Civalek, A.K. Baltacıoglu, Free vibration analysis of laminated and FGM composite annular sector plates, Compos. B: Eng. 157 (2019) 182–194.
[78] P.M. Ramteke, K. Mehar, N. Sharma, S.K. Panda, Numerical prediction of deflection and stress responses of functionally graded structure for grading patterns (power-law, sigmoid, and exponential) and variable porosity (even/uneven), Sci. Iran. 28 (2021) 811–829.
[79] F. Tornabene, Free vibration analysis of functionally graded conical, cylindrical shell and annular plate structures with a four-parameter power-law distribution, Comput. Methods Appl. Mech. Eng. 198 (2009) 2911–2935.
[80] M.S. El-Wazery, A.R. El-Desouky, A review on functionally graded ceramic-metal materials, J. Mater. Environ. Sci. 6 (2015) 1369–1376.
[81] F. Tornabene, M. Viscoti, R. Dimitri, Effect of porosity on the modal response of doubly-curved laminated shell structures made of functionally graded materials employing higher order theories, Structures 60 (2024) 105848.
[82] J.N. Reddy, An Introduction To The Finite Element Method, McGraw-Hill, New York, 2005.
[83] W.B. Zimmerman, Multiphysics Modeling With Finite Element Methods, World Scientific Publishing Company, Singapore, 2006.
[84] F. Tornabene, M. Viscoti, R. Dimitri, Static analysis of anisotropic doubly-curved shells with arbitrary geometry and variable thickness resting on a Winkler-Pasternak support and subjected to general loads, Eng. Anal. Bound. Elem. 140 (2022) 618–673.
[85] F. Tornabene, Generalized Differential and Integral Quadrature, Esculapio, Bologna, 2023.
[86] C. Shu, Y.T. Chew, On the equivalence of generalized differential quadrature and highest order finite difference scheme, Comput. Methods Appl. Mech. Eng. 155 (1998) 249–260.
[87] F. Tornabene, M. Viscoti, R. Dimitri, M.A. Aiello, Higher-order modeling of anisogrid composite lattice structures with complex geometries, Eng. Struct. 244 (2021) 112686.
[88] F. Tornabene, M. Viscoti, R. Dimitri, M.A. Aiello, Higher order formulations for doubly-curved shell structures with a honeycomb core, Thin-Walled Struct. 164 (2021) 107789.
[89] C. Shu, B.E. Richards, Application of generalized differential quadrature to solve two-dimensional incompressible Navier-Stokes equations, Int. J. Numer. Methods Fluids 15 (1992) 791–798.
[90] C. Shu, H. Du, Free vibration analysis of laminated composite cylindrical shells by DQM, Compos. B: Eng. 28 (1997) 267–274.
[91] A. Szekrenyes, Application of differential quadrature method to delaminated first-order shear deformable composite plates, Thin-Walled Struct. 166 (2021) 108028.
[92] F. Tornabene, R. Dimitri, E. Viola, Transient dynamic response of generally-shaped arches based on a GDQ-time-stepping method, Int. J. Mech. Sci. 114 (2016) 277–314.
[93] Y. Hao, L. Sun, W. Zhang, H. Li, Active traveling wave vibration control of elastic supported conical shells with smart micro fiber composites based on the differential quadrature method, Appl. Math. Mech. 46 (2025) 305–322.
[94] Y.X. Hao, et al., Nonlinear vibration of porous truncated conical shell under unified boundary condition and mechanical load, Thin-Walled Struct. 195 (2024) 111355.
[95] C.W. Bert, M. Malik, Differential quadrature method in computational mechanics: a review, Appl. Mech. Rev. 49 (1996) 1–28.
[96] F. Tornabene, N. Fantuzzi, F. Ubertini, E. Viola, Strong formulation finite element method based on differential quadrature: a survey, Appl. Mech. Rev. 67 (2015) 020801.
[97] C. Shu, Differential Quadrature And Its Application In Engineering, Springer Verlag, Berlin, 2000.
[98] P. Sharma, Numerical study of grid distribution effect on accuracy of GDQ method of FGPM actuator, Mater. Today: Proc. 45 (2021) 5706–5708.
[99] F. Tornabene, M. Viscoti, R. Dimitri, Equivalent single layer higher order theory based on a weak formulation for the dynamic analysis of anisotropic doubly-curved shells with arbitrary geometry and variable thickness, Thin-Walled Struct. 174 (2022) 109119.
[100] S. Brischetto, D. Cesare, A coupled hygro-elastic 3D model for steady-state analysis of functionally graded plates and shells, Curved Layer. Struct. 10 (2023) 20220216.
[101] W. Ye, et al., A new semi-analytical solution of bending, buckling and free vibration of functionally graded plates using scaled boundary finite element method, Thin-Walled Struct. 163 (2021) 107776.
[102] Z. Jing, Semi-analytical optimal solution for maximum buckling load of simply supported orthotropic plates, Int. J. Mech. Sci. 187 (2020) 105930.
[103] R.A. Chaudhuri, On boundary-discontinuous double fourier series solution to a system of completely coupled P.D.E.`s, Int. J. Eng. Sci. 27 (1989) 1005–1022.
[104] R.A. Chaudhuri, On the roles of complementary and admissible boundary constraints in fourier solutions to boundary-value problems of completely coupled rth order P.D.E.`s, J. Sound Vib. 251 (2002) 261–313.
[105] F. Tornabene, M. Viscoti, R. Dimitri, On the importance of the recovery procedure in the semi-analytical solution for the static analysis of curved laminated panels: comparison with 3D finite elements, Materials 17 (2024) 588.
[106] X. Peng, et al., Stacking sequence optimization of variable thickness composite laminated plate based on multi-peak stacking sequence table, Compos. Struct. 356 (2025) 118886.
[107] X. Zhang, et al., Dispersion and attenuation characteristics of Lamb waves in multilayered piezoelectric semiconductor plates with imperfect interfaces, Mech. Adv. Mater. Struct. 32 (2025) 1–14.